Author:
Seow, Cui

Title:
Microstructure and the characterisation of mechanical properties of Wire + Arc Additively Manufactured nickel-base superalloys

Microstructure and the characterisation of mechanical properties of Wire + Arc Additively Manufactured nickel-base superalloys

Cui Er Seow

A dissertation submitted to the University of Bristol in accordance with the requirements for award of the degree of Doctor of Philosophy in the Faculty of Engineering, School of Civil, Aerospace and Mechanical Engineering.

April 2021

(34,600 words)

Abstract

Additive manufacturing of large structures has the potential to shorten production lead times and reduce material wastage. One technique is Wire + Arc Additive Manufacturing (WAAM), a high-deposition rate process that uses an electric arc and wire feedstock to deposit material layer-by-layer into a desired geometry. Nickel-base superalloys 718 and 625 are two alloys which have been successfully deposited using WAAM, but their as-deposited microstructures contain detrimental Laves phase and long columnar grains with a strong fibre texture. The effect of these microstructural inhomogeneities on the material's response to heat treatment and their subsequent mechanical properties are not yet well understood.

This work demonstrates, that WAAM Alloys 625 and 718 have micro-, meso- and macro-scale characteristics that are inherently different from their conventional equivalents, and consideration of microstructure and anisotropy is important in optimising and characterising the properties of these materials.

Although the as-deposited microstructure provides an unfavourable starting point, specialised heat treatments are crucial to optimising the tensile properties of WAAM Alloy 718. A modified heat treatment is effective in addressing microstructural inhomogeneities and reducing anisotropy in grain structure, resulting in near-isotropic elevated temperature tensile properties. In addition, unfavourable deposition conditions can lead to the formation of extensive crack-like defects in WAAM Alloy 718. These defects have hot cracking characteristics and result in "semi-stable" crack extension during fracture testing. Toughness values are direction dependent, attributed to interaction of the main crack with defects. Finally, the unique grain structure of WAAM Alloys 718 and 625 presented challenges in the use of neutron diffraction techniques. A new crystallite tracking method was developed to account for crystallite movement during in-situ loading, allowing for experimental determination of crack-tip strain fields. The results demonstrate that it may not be appropriate to treat WAAM materials as homogeneous or isotropic continua when predicting their mechanical behaviour.

(300 words)

Keywords: Additive manufacturing, Nickel-base superalloy, microstructure, heat treatment, defects, tensile properties, fracture toughness, crack-tip strain field, neutron diffraction.

~

To my partner Verner,

my parents Poh Leok and Gek Huang,

my sisters Ying, Shu, and Ching,

and all of my friends,

for their love, patience, and support,

without whom this journey would not have been possible.

~

Acknowledgements

Firstly, I would like to acknowledge the financial support from Lloyd's Register Foundation, TWI Ltd and the University of Bristol, which enabled me to undertake this PhD with the National Structural Integrity Research Centre (NSIRC) at TWI Ltd.

I am immensely grateful to my academic supervisor, Dr Harry Coules, for his unwavering guidance and encouragement throughout this PhD. Despite having to put up with teleconference calls as the main means of communication during supervisory meetings for 2.5 years, Harry did not compromise on the depth of our technical discussions and always made sure my questions were addressed. His support on the various neutron experiments and help with Crystal Plasticity Finite Element modelling have also been invaluable to this work.

I am also indebted to the staff at TWI Ltd who have supported me throughout this PhD: Dr Guiyi Wu, for his guidance and support as the industrial supervisor; Dr Raja Khan, for his supervision and help with designing heat treatment parameters; Marcus Young, for his help with coordinating various lab activities at TWI Ltd; Adrian Addison, for supplying WAAM Alloy 625 material; Jerry Godden, Jack Bradford, Phillip Cossey and Alex Pargeter, for their help with tensile testing, fracture testing and data analysis; William Spicer, for his help with X-ray radiography; Kim Hayward and Daniel Davies, for their help with liquid penetrant testing; Dr David Griffiths and Dr Michael Dodge for their help with Electron Backscatter Diffraction; Ashley Spencer, Diane Shaw and Ramin Taheri for their help with metallography and hardness testing; Sheila Stevens for her help with Scanning Electron Microscopy; Mark Tinkler, for his help with Digital Image Correlation small-scale tensile testing; Cliff Hart, Tom Woolhouse for their assistance with specimen machining at The Test House; Dr Muntasir Hashim, Dr Jazeel Chukkan, Dr Yin Jin Janin, Matthew Haslett, and many others for their engagement in technical discussions.

I also owe thanks to Prof. Stewart Williams, Dr Jialuo Ding, Dr Xiangfang Xu, Flemming Nielsen and Zsolt Pinter at Cranfield University, for supplying the material, equipment, and expertise for WAAM Alloy 718 sample manufacture, and for guiding me through the WAAM process at their laboratory.

Special thanks to Dr Thilo Pirling, Dr Sandra Cabeza and Sergio Martinez from the Institute Laue Langevin (ILL) for their help on the SALSA instrument during the neutron experiments.

My gratitude also goes to collaborators, colleagues, and friends at the University of Bristol: Dr Zhang Jie, for his help with ultrasonic testing and analysis; Dr Christopher Jones, for his help with X-ray computed tomography; Dr Mahmoud Mostafavi, for his advice during my yearly PhD reviews; and Molly Probert, for her help on the various neutron experiments and support outside of the PhD.

To my colleagues at NSIRC and now closest friends, who have shared this incredible journey with me, Drs Kostas Georgilas, Yao Ren, Jialin Tang, Dorothy Winful, Lisa Blanchard, Dibakor Boruah, and soon-to-be Drs Xu Liu, Rosa Griñon Echaniz, Andrew Sandeman, Ana Antelava, thank you for being there through thick and thin, you have made my PhD experience a truly memorable one.

Lastly, I am eternally grateful to my partner and family, who have been remarkably patient and supportive during my PhD journey. To Verner, thanks for bearing with my antics, especially when I was writing up this thesis while employed in a full-time position. To my parents and sisters, thanks for the care and support throughout this time, I am exceptionally thankful for the emotional and mental support since the start of the Covid-19 pandemic.

Author’s declaration

I declare that the work in this dissertation was carried out in accordance with the requirements of the University's Regulations and Code of Practice for Research Degree Programmes and that it has not been submitted for any other academic award. Except where indicated by specific reference in the text, the work is the candidate's own work. Work done in collaboration with, or with the assistance of, others, is indicated as such. Any views expressed in the dissertation are those of the author.

SIGNED: ..... DATE:.....

List of Publications

The following publications were produced during this work:

Seow C E, Coules H and Khan R (2018) 'Effect of Crack Orientation on Fracture Behaviour of Wire + Arc Additively Manufactured (WAAM) Nickel-Base Superalloy', in American Society of Mechanical Engineers, Pressure Vessels and Piping Division (Publication) PVP, p. V005T10A016. doi: 10.1115/pvp2018-84090.

Seow C E, Coules H E, Wu G, Khan R H U, Xu X, et al. (2019) 'Wire + Arc Additively Manufactured Inconel 718: Effect of post-deposition heat treatments on microstructure and tensile properties', Materials and Design, 183. doi: 10.1016/j.matdes.2019.108157.

Seow C E, Zhang J, Coules H E, Wu G, Jones C, et al. (2020) 'Effect of crack-like defects on the fracture behaviour of Wire + Arc Additively Manufactured nickel-base Alloy 718', Additive Manufacturing, 36, p. 101578. doi: 10.1016/j.addma.2020.101578.

Table of Contents

List of Tables

List of Figures

Introduction

Metal additive manufacturing for large engineering components is of great interest to industry, due to the potential for more versatility in the production of parts conventionally made via capital-intensive methods such as casting or forging. Wire + Arc Additive Manufacturing (WAAM) is one example of a high deposition rate, near-net shape technique that can produce large engineering components. An electric arc is used to simultaneously melt and deposit wire feedstock layer-by-layer into a three-dimensional part geometry. The final deposited part requires fewer machining operations and results in less material wastage than conventional methods, which are desirable benefits for specialist materials with high raw costs, such as nickel-base superalloys, titanium alloys and maraging steels.

Nickel-base alloys are known for their high temperature strength and corrosion resistance, their low temperature ductility and toughness, as well as their versatility in welding. Several conventional production routes exist for these alloys, ranging from melting, conversion, forging, investment casting, powder metallurgy to joining methods. However, each route has its limitations, such as high die manufacturing costs and inflexibility to design changes; requiring large raw material volumes; imparting undesirable microstructures at the joint; and requiring extensive post-processing. WAAM offers solutions to some of these limitations and Inconel (IN) 625 and 718 are two nickel-base superalloys that can be deposited using WAAM. However, WAAM IN625 and IN718 are susceptible to elemental micro-segregation, leading to undesirable secondary phases in the microstructure. They also tend to form large columnar grains with strong crystallographic texture. This microstructural inhomogeneity and anisotropic grain structure could be detrimental for mechanical properties. Furthermore, defects may also form

under unfavourable deposition conditions, and the effects of these microstructural characteristics on the mechanical behaviour of WAAM materials are not yet well understood. This understanding is especially important for safety critical applications of WAAM materials because it is the first step towards treating them fairly in design codes or structural integrity assessments. An understanding of how the properties of WAAM materials differ from that of conventional material helps in developing standards to incorporate their safe and appropriate use in industry.

This research aims to determine the unique microstructural characteristics of WAAM nickel-base superalloys IN625 and IN718, and understand their role in mechanical behaviour. To achieve this aim, the following objectives were defined:

1. Characterise the microstructural properties and mechanical behaviour (i.e. tensile, fracture, surface and lattice strain around a crack tip) of WAAM nickel-base superalloys, and compare their performance against those of equivalent conventional processed materials.
2. Characterise the defects which may occur during unfavourable deposition conditions and determine their effects on mechanical behaviour of WAAM nickel-base superalloys.
3. Investigate how direction dependency manifests in the microstructural properties and mechanical behaviour of WAAM nickel-base superalloys.
4. Determine the suitability of neutron diffraction techniques for measuring lattice strain in WAAM nickel-base superalloys and investigate the feasibility of novel adaptations to these techniques.

The following chapters provide better understanding of the microstructural characteristics and mechanical behaviour of WAAM materials, using IN625 and IN718 as case studies. Chapter 1 provides a background of metal additive manufacturing and a literature review of WAAM processes and material characteristics. Chapter 2 offers a metallurgical perspective on nickel-base superalloys and discusses the role of WAAM in consideration of the conventional processing routes. Chapter 3 presents a new specialised post-deposition heat treatment and discusses its importance in improving the microstructure and mechanical properties of WAAM IN718. Chapter 4 presents an investigation of crack-like defects in WAAM IN718 and their effects on apparent fracture toughness. Lastly, Chapter 5 presents a new method of experimental determination of strain fields around a crack tip using diffraction techniques, which circumvents some issues posed by the unfavourable microstructure in WAAM IN625 and IN718.

Chapter 1 The drive for metal additively manufactured components

This chapter provides an overview of additive manufacturing. It discusses the drivers behind the rise of additive manufacturing and the prospect of using them to produce large metallic components. This is followed by a summary of the process, microstructure, and mechanical property characteristics of additively manufactured metallic materials, and a discussion of comparisons with the closely related field of welding. Lastly, a brief introduction to Wire + Arc Additive Manufacturing and the current state of the art is described.

1.1 A brief history of Additive Manufacturing

Additive Manufacturing (AM) is the "process of joining materials to make parts from 3D model data, usually layer upon layer, as opposed to subtractive manufacturing and formative manufacturing technologies". This definition is stated in ISO/ASTM 52900:2015 [1], which outlines the standard terminology for AM and its processes. In a non-technical context, terms such as 3D printing and rapid prototyping, are often used synonymously with AM, despite their different technical definitions. Historical terms such as layer manufacturing, additive processes and solid freeform fabrication are also commonly found in publications predating the formal adoption of AM terminology in 2009 [2].

The concept of AM has been around for several decades. Bourell [2] describes the historical developments of AM in three eras: (i) prehistory – additive approaches which were developed long before the invention of the computer; (ii) precursor – processes with all the features of modern AM technologies but developed before the widespread use of modern computing; and (iii) modern process – AM process which have been successfully commercialised. Instances of AM prehistory date back to the 1860s, where techniques like photosculpting, topography and ornamental weld deposition [3] (see Figure 1.1a) were used for artistic and visualisation purposes. AM precursors began development in the 1950s but were never commercialised due to the lack of an intuitive computer-based user interface. In the 1980s, the most influential patents of modern AM processes were filed. Of which, the most notable is a patent for a stereolithography apparatus filed by Hull [4], which led to the first commercial AM entity, 3D Systems [5] in 1986. Various other AM technologies were developed and commercialised shortly after, such as fused deposition modelling by Stratasys [6] and polymer laser sintering from DTM Corporation (later merged with 3D Systems).

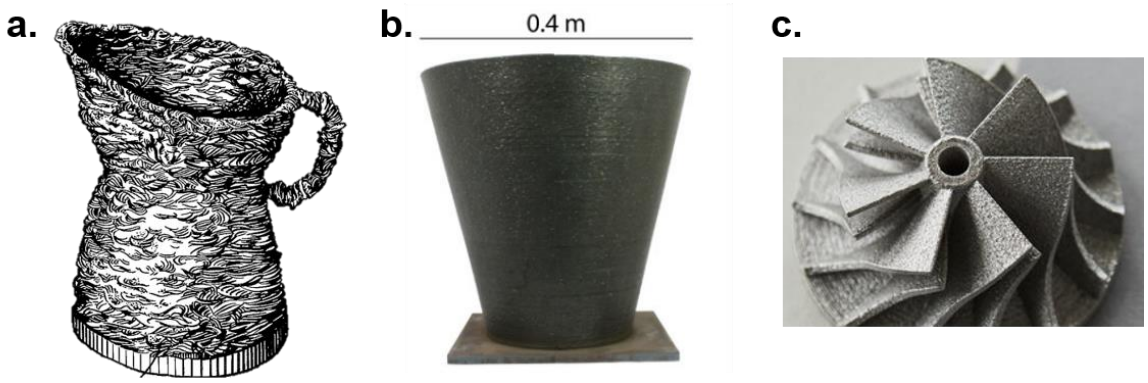

Figure 1.1: Examples of (a) ornamental weld deposition, (b) wire + arc additive manufacturing, and (c) powder bed fusion. Images adapted from [3], [7], [8].

Although most of these early developments were focused on the manufacture of polymers, they laid the groundwork for the development of metal AM technologies. In the mid 1990s, the first metal AM systems, such as selective laser sintering (SLS), direct laser metal sintering (DLMS) and laser-engineered net shaping (LENS), began to enter the market. By the 2000s, many other powder bed (SLM solutions [9]) and blown powder processes emerged. In parallel, wire-feed systems were being developed, drawing from expertise in the related field of welding. By the 2010s, early developments of wire-based metal AM emerged. Examples of modern metal AM components are shown in Figure 1.1b,c. A list by Wohlers and Gornet [10] provides a detailed

chronology of commercial developments in AM. In the last decade, the growth of AM technologies has been fuelled by three main factors: (i) development of low cost-printers, (ii) increased accessibility to computer-based 3D modelling software, and (iii) the expiry of key patents. Today, there are numerous commercial and academic developments in AM, whose processes can be classified into one of seven categories, described in Section 1.3.

Despite being initially developed for visualisation and prototyping, AM has started to find its applications in end-use manufacturing in a wide range of industries. Although also driven by greater design freedom of complex geometries (e.g. lattice structures [11]), the main drive for end-use AM is the prospect of streamlining the production process [12], which can be achieved through: (i) the use of 3D model data throughout the design and production process; (ii) fewer stages between the 3D model to the manufacturing of the part; and (iii) reduction in the number of construction steps and resources that would otherwise be needed with more conventional processes.

The shift towards end-use AM has resulted in a stronger focus on characterising and predicting the performance of the final build. This is especially important in load bearing structures which may be safety critical. A pre-cursor to this is understanding the relationships between the AM processes and material properties, and the relationships of those with the final structure built using AM.

1.2 The drive for large-scale metal AM

Large metal components are mostly used in heavy industries such as transport, power, oil and gas, shipbuilding, and construction machinery. Production of such components via conventional means is usually capital-intensive and requires long periods from planning to production, making it costly to produce small quantities of parts. In addition, conventional processes can result in large amounts of material wastage, driving up the cost of components, particularly those manufactured from specialist materials. Large components are also usually intended to be in service for long periods of time (decades), during which inevitably requires maintenance and repair that is sometimes reliant on the availability of spare parts. However, holding stock of large components requires space and can be costly in the long run. The alternative, which is to fabricate spare components when necessary using conventional means, brings about cost and logistical challenges, especially when a small number of parts are needed quickly.

Against this backdrop, large-scale metal AM presents several potential solutions to these production and supply chain challenges. A streamlined production process with less component-specific equipment allows for shorter lead times and more versatility in manufacturing of large metallic components. The near-net shape nature of large-scale AM processes reduces the need for large machining operations and material wastage. The smaller footprint of AM equipment, combined with the potential to fabricate on-demand, may replace the need for large warehouses holding stock of spare components. These potential benefits have been demonstrated in several case studies in the aerospace [13]–[15] marine [16], [17], [18] and construction machinery [19] industries. In addition, the widespread adoption of AM has the potential to overhaul global supply chains through decentralised manufacturing [20]. However, as the characteristics of AM materials are different from those of conventional counterparts, a like-for-like replacement may not be appropriate. Therefore, there is a need to understand the characteristics of large-scale AM materials and how they differ from their conventional counterparts.

1.3 Metal AM processes and their characteristics

1.3.1 Classification of AM processes

As the properties of AM materials are often process-specific, it is important to first establish an understanding of the various process types. Classification schemes provide a useful way of grouping AM processes with similar characteristics. Although convenient, classification by material or feedstock type (i.e. powder vs. wire) can lead to grouping of very different processes together. One classification scheme which circumvents this is based on machine architecture and the way materials are deposited and fused together [21]. This scheme is provided in ISO/ASTM 52900:2015 [1] and a summary is shown in Table 1.1.

Metals are generally used in two process categories: powder bed fusion (PBF) and directed energy deposition (DED). PBF involves raking a layer of powder over a bed or substrate, then using laser or electron beam systems to selectively melt areas of the pre-laid powder. This is usually carried out in an enclosed vacuum chamber, as shown in Figure 1.2a. In contrast, DED involves feeding material (which can be either powder or wire) directly to the area where it is desired, and melting it using laser, electron beam or an electric arc, as shown in Figure 1.2b,c. Although the two categories share some characteristics, the key difference lies in the timing of material melting and deposition. For DED, material is deposited, melted and fused *simultaneously;* whereas for PBF, material is first laid, then melted and fused.

Table 1.1: Overview of AM classification scheme in ISO/ASTM 52900:2015 [1].

Process category	Defining characteristics	Feedstock		Energy source
		Material	Type	
Directed energy deposition (DED)	Focused thermal energy is used to fuse materials by melting as they are deposited.	Metal	Powder, wire	Electric arc, laser, electron beam
Powder bed fusion (PBF)	Thermal energy selectively fuses regions of a powder bed.	Metal, ceramic, polymer	Powder	Laser, electron beam
Sheet lamination	Sheets of material are bonded to form a part.	Metal, polymer	Sheet	Thermo-mechanical, chemical
Material extrusion	Material is selectively dispensed through a nozzle.	Polymer	Filament	Thermo-mechanical
Material jetting	Droplets of build material are selectively deposited.	Polymer (incl. photopolymer), ceramic, metal	Liquid	Thermo-mechanical, chemical
Binder jetting	Liquid bonding agent is selectively deposited to join powder materials.	Polymer	Liquid (binder), powder	Chemical
Vat polymerisation	Liquid photopolymer in a vat is selectively cured by light-activated polymerisation	Photopolymer	Liquid	Chemical (UV-induced)

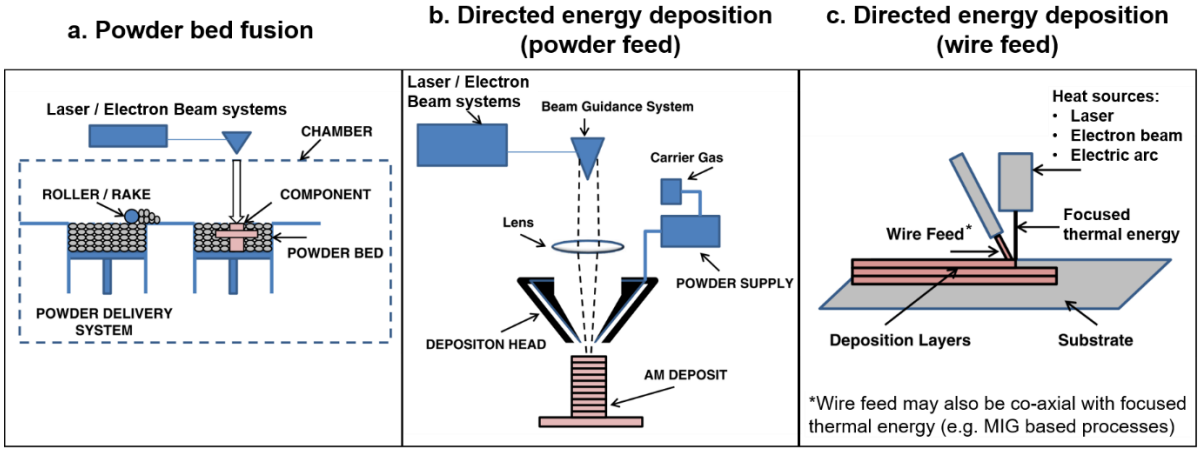

Figure 1.2: Illustration of (a) powder bed fusion and directed energy deposition systems with (b) powder and (c) wire feedstock. Images adapted from [22].

1.3.2 Process characteristics

Metal PBF and DED have processes characteristics that address different requirements, and therefore should be viewed as complementary processes. These characteristics are summarised in Table 1.2. The advantages and disadvantages of these characteristics are well documented by various authors (e.g. Frazier [22], Sames et al. [23], DebRoy et al. [24]). In general, the PBF systems have smaller build volumes, tend to use lower beam power, and have smaller layer thicknesses than DED systems. The higher beam/arc power of DED systems enables these processes to achieve higher deposition rates; but results in poorer surface finishing and feature definition. Therefore, PBF processes are well suited for smaller components of complex geometries requiring high part resolution and good surface finishing, whereas DED techniques are more appropriate for large components of medium to low complexity, and may require post-deposition machining to achieve desired surface finishing.

Table 1.2: Comparison of powder bed fusion (PBF) and directed energy deposition (DED) process characteristics, adapted from DebRoy et al. [24], and Sames et al. [23].

Characteristics	PBF	DED		
	Powder	Powder	Wire	
Heat source	Laser/ Electron beam	Laser	Electron beam	Electric arc
Power (W)	50–1000	100–3000	500–2000	1000–3000
Feed rate (g/s)	–	0.1–1.0	0.1–2.0	0.2–2.8
Max. build vol. (mm×mm× mm)	500× 280× 320	2000× 1500× 750	2000× 1500× 750	5000× 3000× 1000
Production time	Long	Long	Medium	Short
Dimensional accuracy (mm)	0.04–0.2	0.5–1.0	1.0–1.5	Intricate features are not possible
Surface roughness (μm)	7–20	4–10	8–15	–
Layer thickness (μm)	10-50	~250	500-3000	~3000
Post-process machining	Not usually required	Not usually required	For better finish	Essential for dimensional accuracy

1.3.3 Defects and microstructural characteristics

Metals and alloys processed via PBF and DED have unique microstructures that are generally distinct from their conventionally processed counterparts. In general, inappropriate process parameters or melt pool conditions often lead to defects, such as porosity [25], [26] (due to lack-

of-fusion or gas entrapment) and micro-cracking [27]. Their grain structures are usually finer than castings, due to the comparatively rapid solidification [28], [29]; but coarser than wrought product (e.g. hot-rolled sheet or bar), due to the lack of work hardening to promote recrystallisation (if no additional grain refinement techniques are applied) [30]. Directional heat extraction typically results in columnar or elongated grain structures [22]; and complex thermal cycling [23] results in subgrain structures containing meta-stable phases and non-equilibrium phase compositions, depending on the specific alloy composition [31]. These microstructural features can vary within the same deposit (i.e. location-dependence), due to geometry-induced local thermal effects [32]. A summary of the various ways in which anisotropy and heterogeneity can manifest in AM metallic materials is provided by Kok et al. [33]; they can be broadly categorised into: grain morphology; crystallographic texture; lack-of-fusion defects; phase transformation; heterogeneous recrystallization; layer banding and microstructural coarsening.

In addition, process-specific trends in microstructure have also been observed. PBF and powder-feed DED materials tend to be more susceptible to porosity defects, due to inherent porosity and other inconsistencies occurring in powder feedstock [34] that do not usually occur in wire feedstock. The longer and shallower melt pool created during PBF usually results in finer grains with growth directions not always parallel to the build direction (often angled towards scanning direction), whereas the shorter and deeper melt pool created during DED may result in large columnar grains with the growth direction, i.e. near-parallel to the build direction [24]. Columnar grain growth is often more severe in wire feed DED materials due to the larger thermal gradients resulting from higher heat inputs [35].

1.3.4 Mechanical properties

Based on the currently available data, the tensile properties of as-deposited AM metallic materials generally approach the minimum requirements for, and in some cases even exceed conventional wrought or cast equivalents [36], despite the presence of heterogeneity and anisotropy in the microstructures [22], [32], [33]. Although promising, the mechanical properties data currently available for AM metallic materials fall short of the required range typically required for structural applications. In their 2016 review, Lewandowski and Seifi [32] reported that majority of the published work is focused on tensile and hardness properties, and very limited data exists for low cycle fatigue, fatigue crack growth, fracture toughness, impact, creep, creep fatigue, multiaxial testing, or environmental effects. Furthermore, not many are

based on standard samples or test methods, which makes comparison of measured properties from different studies challenging. In addition, heterogeneity (which can result location-dependent mechanical properties [37]) and anisotropy in the microstructure (which can lead to weaker tensile properties in the build direction [22]), adds complexity to the characterisation of mechanical properties of AM metallic materials. In a 2018 review paper, DebRoy et al. [24] concluded that: *"... compositional, microstructural and stress gradients are common to AM parts. The approach of treating structure and properties as homogeneous is clearly not appropriate for understanding the behaviour of AM components. There are opportunities to develop new theory and methodology to evaluate microstructure, properties and performance of AM parts in the presence of various gradients."*

Although there have been significant efforts in each of these areas, the relationship between process, microstructure (including defects) and mechanical properties of AM metallic materials is not yet well understood. More thorough understanding of process-microstructure relationships are needed to prevent variation in properties from machine to machine for the same process [36], [38]. Microstructure-property relationships may also help to explain complex interactions between defect-dominated and microstructure-dominated contributions to mechanical properties, which can lead to conflicting results [32]. In addition, these microstructural features can also interact with structural and residual stresses [24], which complicates the measurement of dynamic mechanical properties such as fatigue [39]. Although some process-microstructure modelling efforts [23] are underway, developing a thorough understanding of the interrelation between process, structure, properties and performance still requires a large knowledge base on the properties of AM metallic materials [24]. Interestingly, Yates et al. [39] note that where fatigue properties are measured for AM materials, they are often quantified in a way that "would be familiar to engineers in the 19th century". The authors also argue that although the methods to predict the fatigue response of AM materials theoretically exist in the open literature, their practical applications are hindered by the fact that the complexity of AM microstructures and the dominant length scales of their interactions with defects and stress distributions remain yet to be well understood. To this end, it is imperative that process- and material-specific characterisation of mechanical properties and microstructure are continuously carried out for AM metallic materials.

1.3.5 Comparisons to welding

Perhaps important insights can be drawn from the closely related field of welding. Welding, which is commonly used to join conventionally processed materials (e.g. sheet, tube) or semi-finished products into complex assemblies, is a well-established field with a good general understanding of process-structure-property relationships, as well as various standards which guide their use in industry. Oliveira et al. [35] conducted a detailed review of fundamental fusion welding concepts and demonstrated that the thermal effects, solidification mechanisms, and chemical reactions within the melted region, distortion and residual stresses, that occur in welding (especially multipass) share similarities with those observed in AM of metallic materials; and that techniques used to model, characterise and mitigate against these issues can be adapted from welding to AM.

One example is the concept of weldability, which describes how some alloys are easier to weld (i.e. less prone to defects) than others, and the critical range of parameters within which welds are free from physical and metallurgical defects. An example of a weldability map for nickel Alloy 718 [40] is shown in Figure 1.3a. Although no formal terminology or definitions have been established yet, the concept equivalent for AM is printability [24] which is the ability of a particular feedstock or material to be successfully deposited without severe defects. Dass and Moridi [34] proposed the use of optimal processing maps, shown in Figure 1.3b, to describe a range of key parameters (i.e. optimal processing window) in which the AM deposited material can meet mechanical or metallurgical requirements.

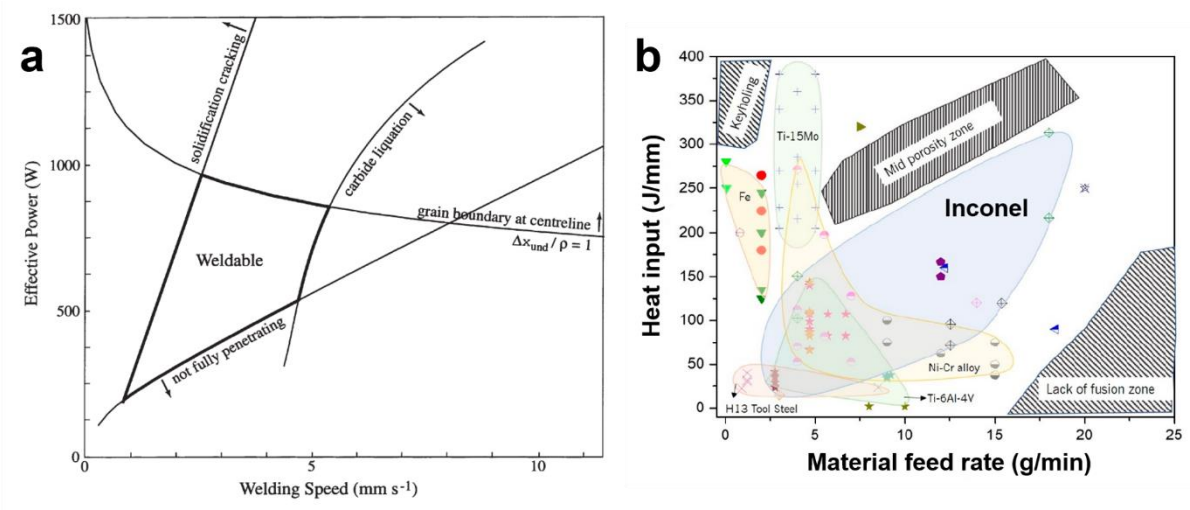

Figure 1.3: Examples of (a) weldability map (for nickel Alloy 718) from Dye et al. [40] and (b) AM DED printability processing map from Dass and Moridi [34].

It must be recognised that there are some fundamental differences between welding and AM which affect how existing welding knowledge can be applied to AM. Firstly, a deep melt pool shape is often preferred in welding, so as to achieve good depth of penetration [41]. Deep melt pools in AM can cause excessive re-melting of previously deposited layers and in some cases lead to keyhole porosity [24]. Instead, a melt pool with shallow penetration, good bead height and width is preferred in AM to achieve better deposition rates.

Secondly, in welding, heat extraction (i.e. heat sink effects) is mostly provided by the parent material, which tends to be adjacent to the weld metal. In contrast, for AM, heat extraction is provided either by the substrate plate and previously deposited material (for DED), or by surrounding unfused powders (for PBF). Figure 1.4 illustrates this difference in heat extraction directions. This difference in heat extraction direction often results in different metallurgical observations between welding and AM.

Thirdly, the parent material of a weld always forms part of the final component, whereas the substrate plate of an AM build may not. As a result, post-processing techniques such as post-weld heat treatments, which are designed in consideration of effects on parent metal, may not always be appropriate for AM metallic materials. In addition, comparisons of weld metal properties against parent material properties is essential in welded structures (to prevent strength mismatch that could compromise the integrity of the structure), but may not always be applicable in AM components, especially if the substrate plates are to be removed. Therefore, assessing the suitability of mechanical properties of AM metallic materials requires a different approach to that of welding, with stronger emphasis on the properties of the deposited beads themselves and the overall structural context in which these parts are to be used.

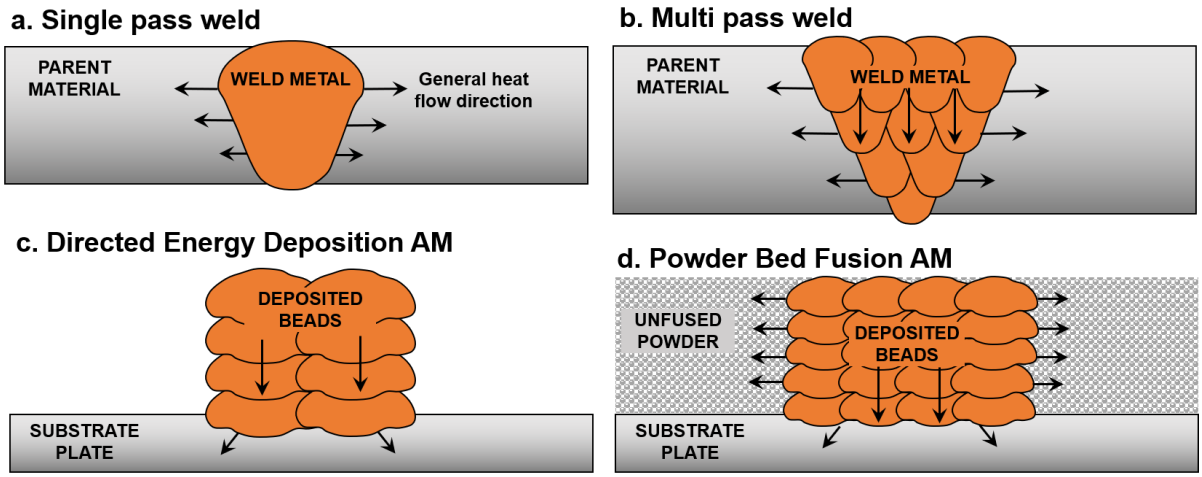

Figure 1.4: Schematic illustration of general heat flow directions in (a) single pass and (b) multi pass weldments, (c) DED and (d) PBF AM deposits.

1.4 Wire + Arc Additive Manufacturing (WAAM)

1.4.1 Overview

One type of wire feed DED suitable for large-scale AM is Wire + Arc Additive Manufacturing (WAAM), which uses an electric arc as a heat source and wire as feedstock to simultaneously melt and deposit metal onto a substrate plate, building up a desired part geometry layer-by-layer. Other terminology used to describe this process include: 3D-welding [42], weld deposition [43]–[45], shaped metal deposition [46], [47], and microcasting [48]. For simplicity, examples in the literature using any of these terms will be referred to as WAAM in this work. WAAM has a high-deposition rate, enabling large components to be built relatively quickly. Industrial interest in WAAM (and large-scale AM in general, described in Section 1.2) is mainly driven by the potential for material savings (of up to 500 kg per part [7]) and shortening of production lead times, especially for parts which are conventionally manufactured through casting, forging and machining.

From a practicality viewpoint, arc-based equipment (example shown in Figure 1.5) is more available than laser or electron beam systems and many manufacturers have welding facilities which can be adapted for WAAM. Wire feedstock also has simpler handling considerations than metal powder [49]. Various alloys have been successfully deposited using WAAM, such as titanium (Ti-6Al-4V), steels (low alloy and stainless), aluminium, nickel-base superalloys, duplex stainless steels and maraging steels. Some examples of WAAM studies in each alloy group are provided in Table 1.3. Specific alloy compositions and grades are selected according to the intended applications and the alloy's weldability.

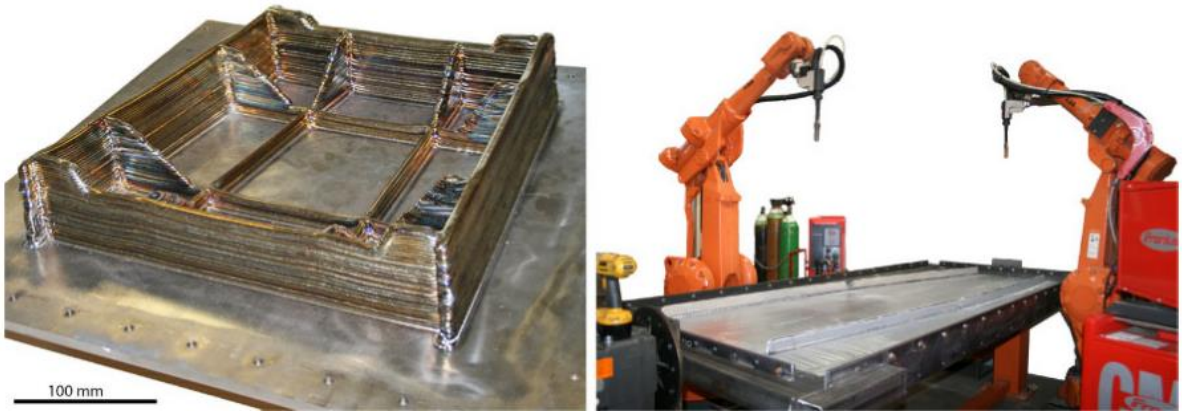

Figure 1.5: Example WAAM part and arc equipment, from Williams et al. [7].

Table 1.3 : Examples of WAAM studies, sorted by material.

Material	Application	Industry	WAAM process	Ref.
Ti-6Al-4V	Wing spar, landing gear	Aerospace, Defence	PAW, GTAW	[47], [7], [50]
Aluminium	Wing spar, stiffened panels	Aerospace Automobile	CMT (incl. variants)	[7], [51]
Steel	Propeller (WAAMpeller), Bridge (MX3D), Projectiles	Aerospace, Marine, Civil, Tooling, Defence	MIG, CMT	[52], [53], [54], [17]
Nickel-base alloys	Combustor outer casing, Tubular components	Aerospace, Nuclear, Oil and Gas	PAW, CMT	[46], [55]
Duplex stainless steel	Impeller blade	Oil and Gas	CMT	[56], [57]
Maraging steel	-	Aerospace, Defence, Tooling	CMT	[58], [59]
Tantalum	-	Nuclear	GTAW (TIG)	[60]

There are various process considerations for WAAM that can influence the final build quality (i.e. microstructure and mechanical properties). These process factors range from the selection of the wire consumables, substrates, build strategy, and process parameters, to the use of in-situ heat transfer and inter-layer cold rolling techniques to obtain tailored microstructures. These factors can be classified into primary and secondary (or ancillary) processes, as first proposed by Cunningham et al. [61] and summarised in Figure 1.6.

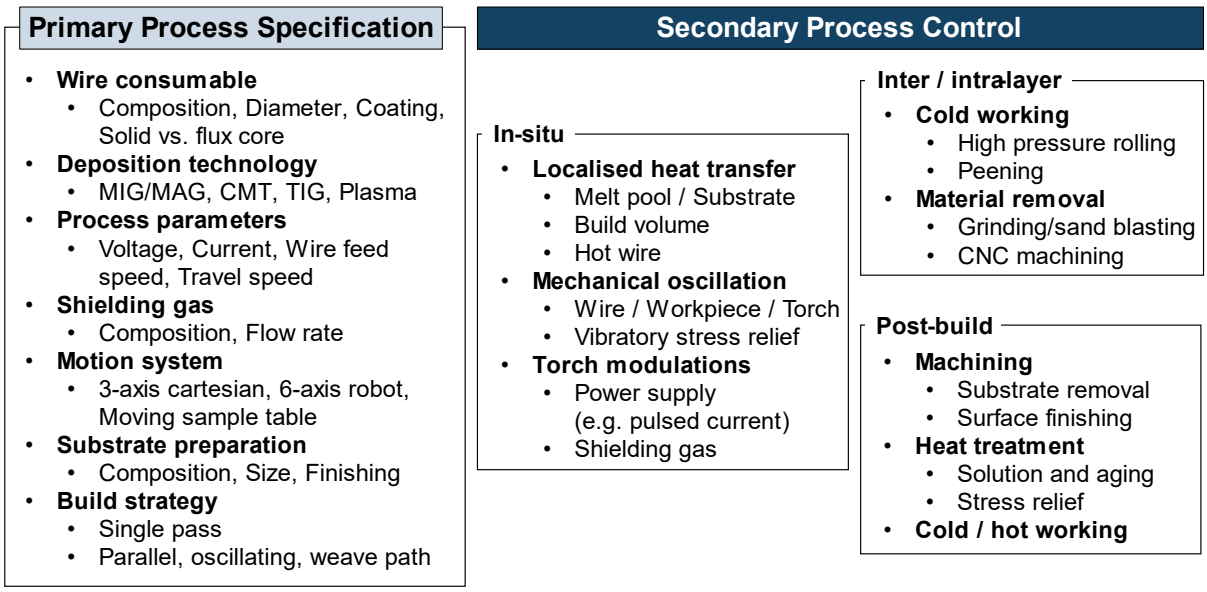

Figure 1.6: Summary of process considerations for WAAM that can influence the characteristics of the final build, adapted from [61].

Primary process specifications typically determine the deposition rate and geometrical properties (e.g. surface waviness and dimensional accuracy) of the final build. Secondary processes, which can be applied either in-situ, inter-/intra-layer, or post-build, are generally used to fine-tune physical and microstructural properties, such as heat distribution, distortion, and grain structure. A few key process considerations are reviewed and discussed in the following sections.

1.4.2 Deposition technology

Selection of the appropriate arc-based deposition systems for WAAM is largely dependent on the material, required deposition rate, and complexity of geometry. Gas Metal Arc systems such as Metal Inert/Active Gas (MIG/MAG) and Cold Metal Transfer (CMT) are generally more versatile and can be used with most materials with high deposition rates [62]. These systems also have a co-axial wire electrode and benefit from simpler deposition path planning. In contrast, Tungsten Inert Gas (TIG) and Plasma Arc (PA) systems have an external wire feed, which can complicate the deposition path and introduce additional process parameters such as wire feed angle [63]. However, TIG and PA systems benefit from having independent control of wire feed speed, which enables better fine-tuning of process parameters (see Section 1.4.4) and therefore higher quality builds.

1.4.3 Build strategy

Selecting a build strategy for WAAM usually depends on the part geometry. Simple geometries such as walls, cylinders, or box sections, can be deposited with basic deposition patterns. Thin-walled structures are typically deposited using a single bead strategy (i.e. single pass wall). Thicker sections may adopt parallel, oscillating, or weave bead strategies [58], [64] as illustrated in Figure 1.7. Outline and infill patterns, often used in PBF [65], have also been adopted in WAAM builds [44], [66]. Large blocks may also be built using spiral-in or spiral-out patterns [66]. Geometries involving intersections, such as T-sections [67], may require different deposition patterns from layer to layer, to prevent uneven build up of material leading to concavity. For more complex geometries, modular path planning methods [68] may be useful in determining the appropriate combination of deposition patterns; and assigning specific deposition parameters to different “zones” of the build geometry. This is useful because apart from geometrical considerations, the build strategy can also result in different thermal histories, which influences the defect rate [67], microstructure [68], and residual stress profiles [66] in

the final parts. The control of residual stress and distortion can also be achieved using a "back-to-back" build strategy [7], as shown in Figure 1.8.

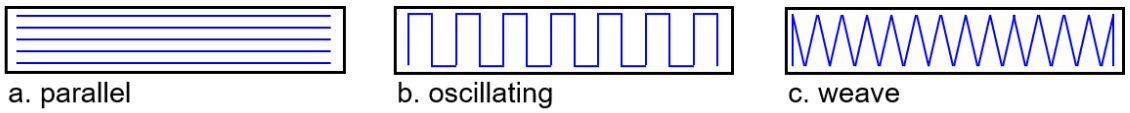

Figure 1.7: Illustration of basic (a) parallel, (b) oscillating and (c) weave deposition patterns adopted in various WAAM studies [17], [58], [67], [68].

Figure 1.8: Example of WAAM component built using back-to-back strategy. Image from [7].

1.4.4 Process parameters

The selection and control of process parameters are crucial to the quality of a WAAM build. The main parameters are voltage, current, travel speed (TS) and wire feed speed (WFS). Whilst the effects of these parameters on weld deposition is generally well understood, that for WAAM requires more investigation due to differences in thermal profile of the melt pool as discussed in Section 1.3.5, and development of this knowledge is still underway. Varying the waveforms of current and voltage can have an impact on the metal transfer mode [69], [70], [71] which affects arc stability. Within the range of arc stability, TS and WFS has an effect on surface roughness [72], bead height [73] and melt through depth [73]. In addition, inter-layer temperature has also been identified by several authors as a key parameter influencing surface quality [72] and porosity [74]. Numerous trials are often required to optimise these process parameters for the desired build characteristics, although more advanced techniques such as a Gaussian Process Regression model presented by Lee [70] may be used to optimise process parameters for the desired deposited bead shape more efficiently. Furthermore, optimised process parameters can be more consistently implemented with the use of monitoring and feedback control methods [19], [75], especially if the optimal parameters vary with part geometry.

1.4.5 Inter-layer cold rolling

One example of a secondary process control method is interlayer cold rolling, which involves applying a downward force, large enough to induce plastic deformation, on the WAAM deposit after every layer (or every few layers) [76]. This method uses a roller fork behind the WAAM deposition torch as shown in Figure 1.9. This method has been demonstrated to reduce peak residual stress [76], reduce porosity in Al deposits [77], achieve grain refinement [78], [79], [80] and therefore improve mechanical properties [81] of various WAAM materials.

However, interlayer cold rolling increases the overall build time, as deposition is paused whilst rolling is carried out. There may also be additional wait time for the part to cool (e.g. to below 50 °C [76]) prior to rolling. Rolling also imparts a slight change to the build geometry, resulting in a shorter and wider deposit [76], which must be accounted for in the original build to achieve the required dimensional accuracy. In addition, Xu et al. [82] has demonstrated that the grain refinement effects of cold rolling can vary from layer to layer, resulting in banding of columnar and equiaxed grains. This indicates that interlayer cold rolling may not be straightforward to implement consistently, especially with more complex part geometry.

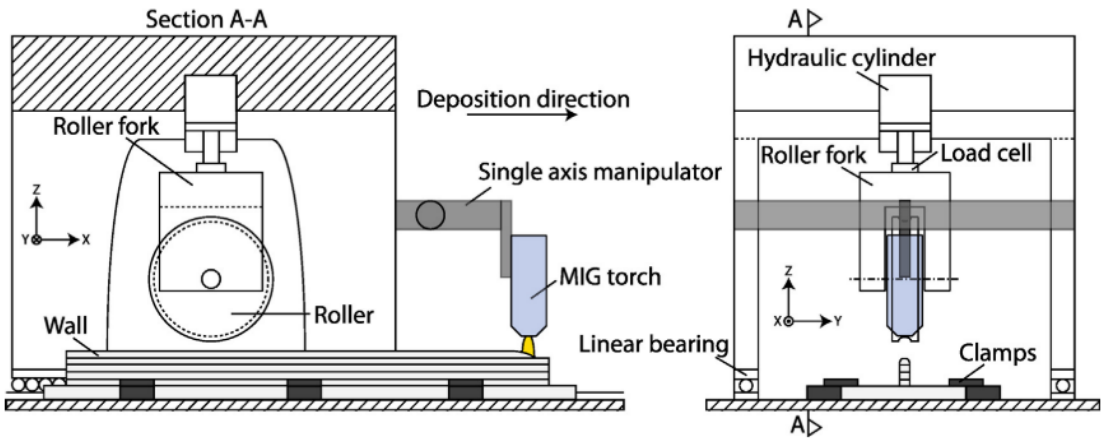

Figure 1.9: Schematic of interlayer cold rolling equipment. Image from [76].

1.4.6 Post-build heat treatments

Another example of a secondary process control method is post-build heat treatment. In general, heat treatments can be used to achieve microstructural homogenisation, annealing, precipitation strengthening or stress relieving effects in WAAM materials, depending on the treatment parameters and the material composition. For example, Baufeld et al. [87] found that

for Ti-6Al-4V, a standard treatment at 600 °C relieved stresses in the deposit without altering the microstructure, and an annealing treatment at 834 °C increased the strain at failure significantly. For 2219 Al alloys, Gu et al. [83] reported that a T6 heat treatment provided a larger strength increase (attributed to precipitation hardening) than interlayer cold rolling. For 2024 Al alloys, Qi et al. [84] reported that T4 and T6 heat treatments homogenised the dendritic microstructure, which led to improvements in hardness and strength. Similarly, for low alloy steel ER70S-6, Vahedi Nemani et al. [85] found that normalising (i.e. homogenisation) heat treatments improved the microstructure by dissolving meta-stable phases, whereas a hardening treatment (i.e. water quenching) preserved bainite and acicular ferrite in the microstructure, leading to a 20% increase in tensile strength.

However, the effects of heat treatment on the properties of WAAM materials are not yet well understood. Although welding or materials specification standards are often referenced when selecting treatment parameters, various studies have demonstrated that these may not always be appropriate for WAAM materials as they have a different starting microstructure to conventional products. For example, Vahedi Nemani et al. [85] observed that the hardening heat treatment applied to WAAM ER70S-6 low alloy steel resulted in poorer elongation in the build direction than in the vertical direction (i.e. increased anisotropy). Gu et al. [77] found that in 2319 and 5087 Al alloys, pores eliminated during interlayer cold rolling were re-opened during heat treatments, attributed to the precipitation of hydrogen pores. In nickel-based alloy Inconel 718, Xu et al. [82], [87] and Kindermann et al. [88] observed that standard solution and aging heat treatments led to partial dissolution of Laves phase and precipitation of δ-phase in microstructure, which are detrimental for mechanical properties.

1.5 General characteristics of WAAM materials

The characteristics of WAAM materials depend on the primary and secondary processing methods described in Section 1.4. This section summarises the general characteristics observed in WAAM materials across the different processing methods which can be applied.

1.5.1 Macro-scale build characteristics

Macro-scale features, such as excessive spatter [86], sloping [58] and build collapse [87] (see Figure 1.10 a-c), are often observed in WAAM materials which have been built using inappropriate processing parameters. Excessive spatter is typically a result of undesirable globular transfer which can be addressed by fine-tuning the current, voltage and wire feed speed. A mono-directional build path can result in sloping at one end, due to build up of material at the start, and accumulation of craters at the end of the deposition path. Overly high heat inputs can result in excessive melting of the previous layers, eventually leading to build collapse.

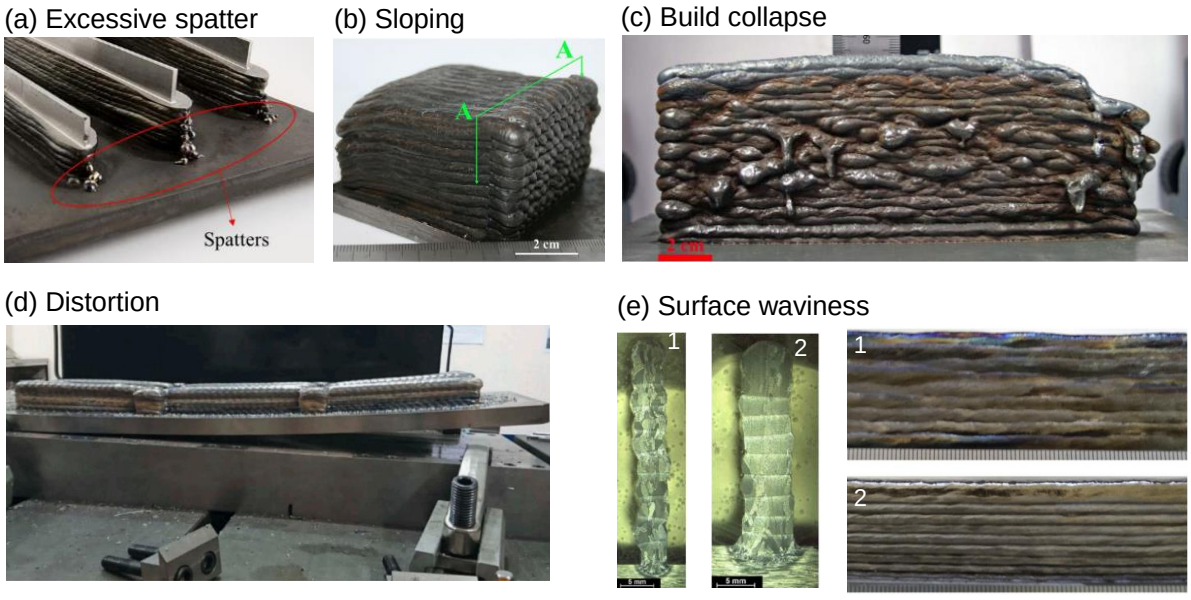

Figure 1.10: Typical build characteristics observed in WAAM materials. Images taken from: (a) excessive spatter [86], (b) sloping [58], (c) build collapse [87], (d) distortion [88], (e) surface waviness [89].

However, even with well controlled process parameters, WAAM builds are still susceptible to distortion [88] and surface waviness [89] (see Figure 1.10 d-e). Distortion results from the build

up of residual stresses (described in Section 1.5.7) which occurs gradually throughout deposition. Clamping of the substrate plate adds restraint, but distortion can still occur after removal of the clamps. Processing variants such as "back-to-back" building (see Figure 1.8) and interlayer cold rolling (described in Section 1.4.5) can balance or reduce peak residual stresses [76] and prevent excessive distortion. Surface waviness results from the natural spread of molten material towards the edges of the build and can be exacerbated by arc wandering. Pradal et al. [89] demonstrated that the use of concentric lasers can stabilise the arc, leading to reduced surface waviness.

1.5.2 Meso-scale defects

Lack-of-fusion defects (Figure 1.11 a) have also been observed in WAAM deposits. Xu et al. [58] reported lack-of-fusion defects in maraging steel builds, deposited using oscillating, parallel and weave bead strategies. These defects were observed between adjacent tracks (i.e. side of bead) as well as between layers (i.e. inter-run). The weave bead strategy was found to achieve the fewest defects, which the authors attributed to the flatter bead profile providing a more favourable starting point for the fusion of subsequent layers. In welding, lack of fusion defects are typically attributed to poor technique and inappropriate parameters, such as current too low, travel speed too high and inadequate surface or inter-pass cleaning [90].

Although WAAM materials are generally less susceptible to porosity than powder-based AM materials, porosity is often observed in Al alloys deposited via WAAM [77], [91], [92], [93]. Al alloys are more susceptible than other materials to hydrogen pores, due to the large difference in hydrogen solubility between liquid and solid Al. Selection of the deposition technology and processing parameters can mitigate porosity; for example, CMT has been observed to achieve lower porosity than pulsed-MIG techniques, attributed to the lower arc energy and smaller melt pool in the CMT process [92], [93]. However, secondary processing techniques such as interlayer cold rolling may be required to completely eliminate pores [77].

Whilst some WAAM materials are crack-free [27], Clark et al. [46] observed the presence of crack-like defects (see Figure 1.11 c) in WAAM nickel-base Alloy 718 deposited via MIG. They attributed the formation of these crack-like defects to dense regions of micro-segregated phases (e.g. Laves) in the microstructure.

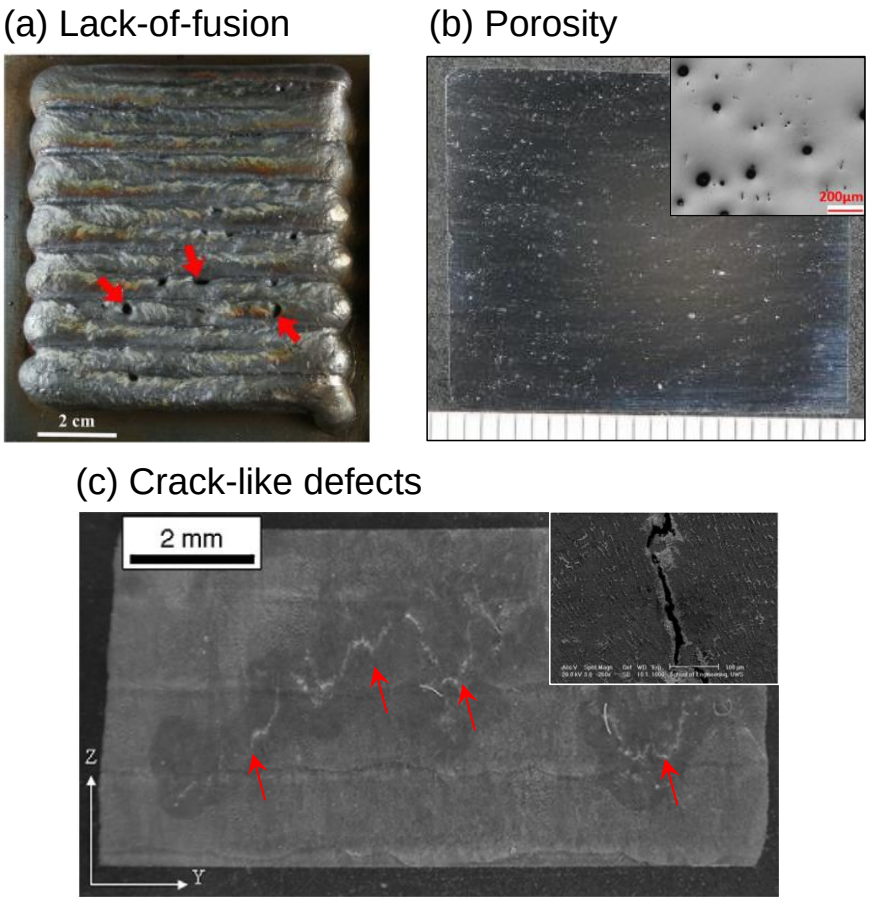

Figure 1.11: Types of meso-scale defects observed in WAAM materials. (a) lack-of-fusion [58], (b) porosity [74], [92]**, (c) crack-like defects [46].**

1.5.3 Microstructural characteristics

From a microstructural perspective, WAAM materials are susceptible to the formation of large columnar grains due to the large thermal gradient set up in the build direction. The grains tend to be larger at the top of the build [78], resulting from competitive epitaxial grain growth across many layers (see Figure 1.12 a). In addition, the grains are also strongly textured as shown in the electron backscatter diffraction maps and pole figures in Figure 1.12 a. WAAM deposited Ti-6Al-4V [78], nickel superalloys Inconel 625 [94] and 718 [82] often exhibit this type of grain structure, especially if no process control methods (e.g. interlayer cold rolling) are applied to induce grain refinement.

Microstructural banding in WAAM materials often appears in metallurgical macrographs as alternating light and dark bands [78], [95], as shown for Ti-6Al-4V deposits in Figure 1.12 b. Ho et al. [95] demonstrated that these horizontal bands (also known as HAZ bands) correspond to

fine and coarse α-lamellar spacings respectively. They also reported the presence of curved segregation bands which displayed compositional variation (i.e. reduced Fe and V) from the rest of the microstructure, although these bands were comparatively weaker in contrast and required careful etching to be revealed. On a smaller scale, WAAM materials can be susceptible to dendrite formation, leading to micro-segregation (see Figure 1.12 c). This has been observed in Inconel 625 [96], Inconel 718 [82] and maraging steel [59] WAAM deposits. This can result in the formation of undesirable phases (e.g. Laves), in the interdendritic regions.

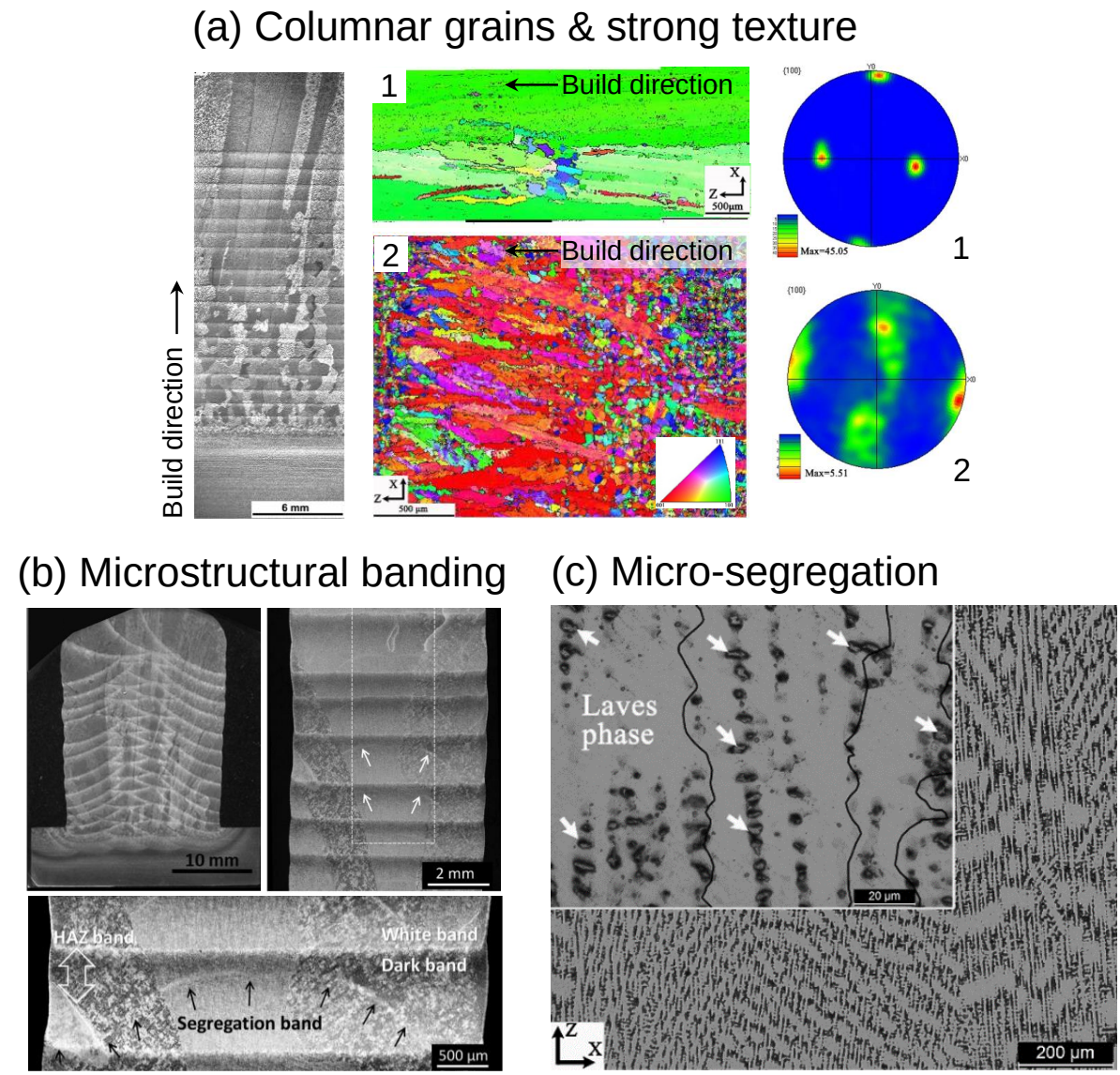

Figure 1.12: Summary of microstructural characteristics observed in WAAM materials. Images adapted from: (a) columnar grains and strong texture in as-deposited condition (1), and semi-refined grain structure after inter-layer cold rolling (2) [78], [82], (b) microstructural banding [95], and (c) micro-segregation [82].

1.5.4 Tensile properties

The tensile properties of WAAM materials are most dependent on the alloy group and chemical composition. Figure 1.13 shows a plot of reported tensile properties various WAAM materials [17], [45], [55], [59], [71], [81], [82], [84], [96]–[104], summarised in Table A.1. The tensile properties reported thus far are of materials with standard compositions (i.e. commercially available feedstock). From this plot, it can be observed that WAAM Al alloys tend to have the lowest Yield and Ultimate Tensile Strengths (YS and UTS respectively), whereas Maraging steels have the highest. Heat treatments have a large effect on the YS and UTS of WAAM materials, as shown by the increase in YS and UTS for heat-treated AA2024, Alloy 718 and Maraging steel. Inter-layer cold rolling also provided an additional increase to the YS and UTS of heat-treated Alloy 718 and Maraging steel, likely due to grain refinement induced by plastic deformation during rolling. Weak direction dependence of YS and UTS can also be observed in the heat-treated samples, where the properties measured in the other directions are very slightly higher than that of the build direction.

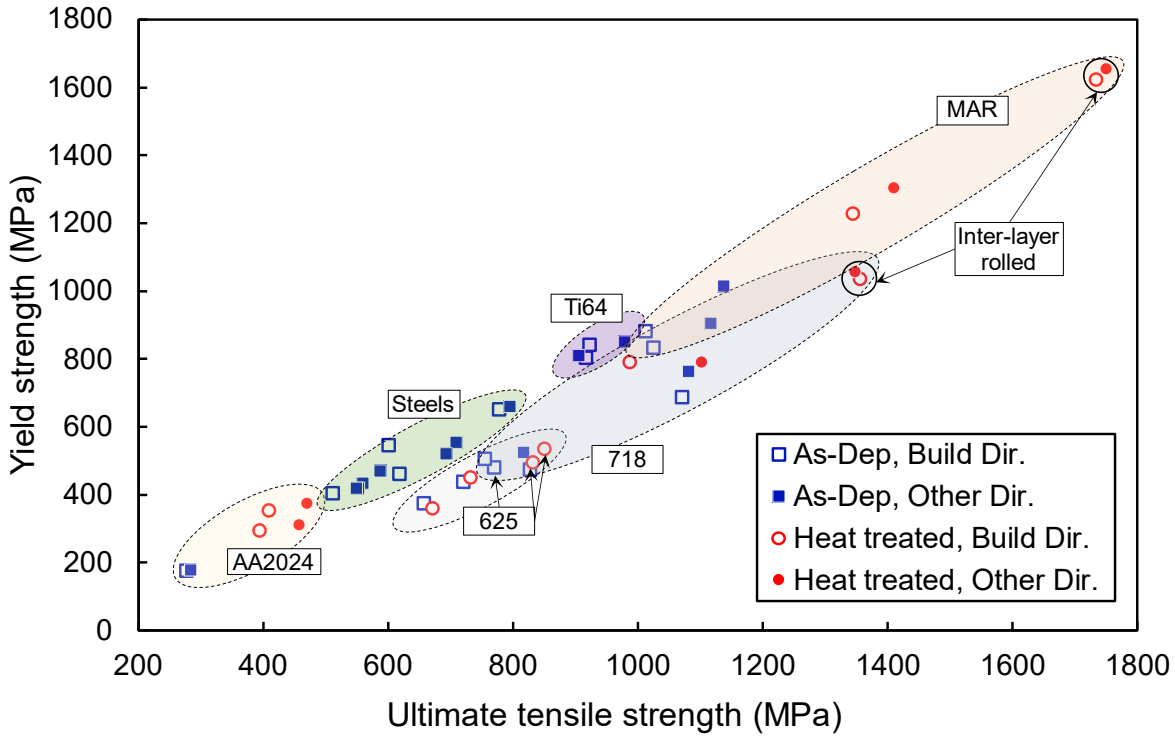

Figure 1.13: Plot of yield and ultimate tensile strengths of various WAAM materials; data and references in Table A.1.

In terms of elongation (see Figure 1.14), WAAM nickel Alloy 625 displays the highest elongation of over 35 %, whereas Al alloy AA2024 and Maraging steel display elongation of not more than 15 %. Ductility generally worsens after heat treatments, as shown by the lower in elongation of heat-treated Alloy 625, Alloy 718 and Maraging steel, in comparison to their as-deposited counterparts. This is likely due to the embrittling effect of precipitation hardening induced by the aging heat treatments, or the formation of brittle zones in the microstructure (for Alloy 625). The only exception is the custom heat treated WAAM Alloy 718, which displayed good elongation of 30-35 %. Although there is some scatter in elongation between the build and other (i.e. longitudinal and thickness) directions, no consistent trend in direction dependency can be observed from the plot.

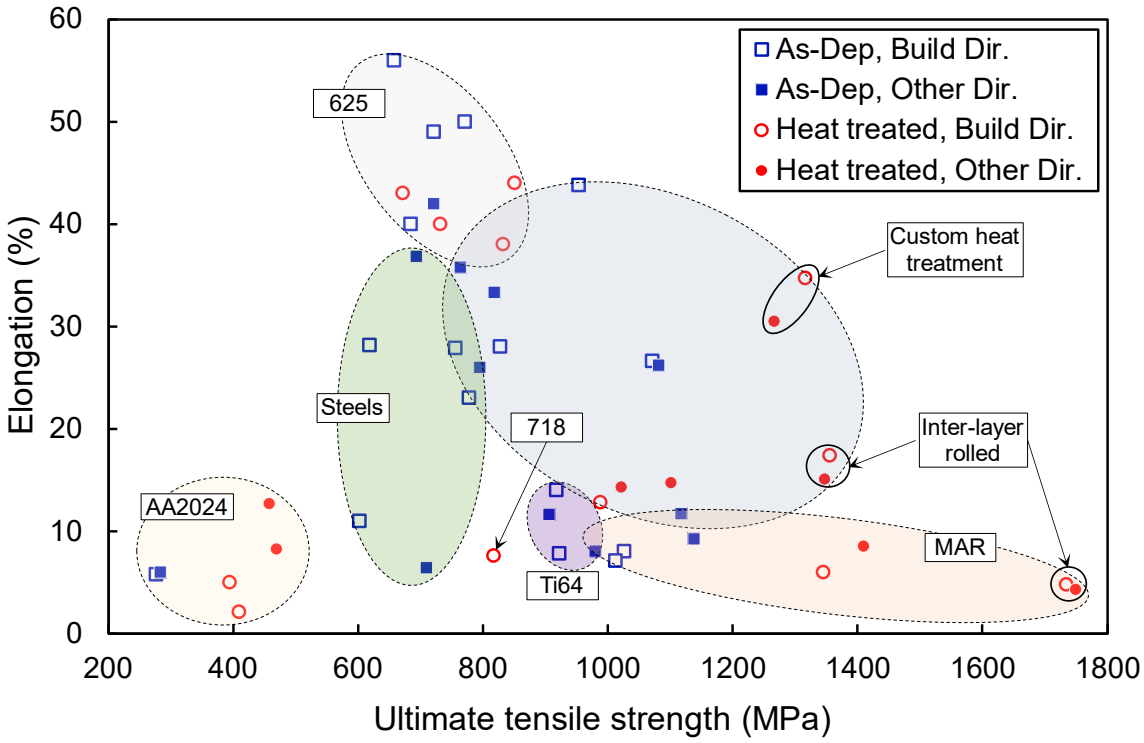

Figure 1.14: Plot of elongation and ultimate tensile strengths of various WAAM materials; data and references in Table A.1.

1.5.5 Fracture behaviour

The fracture behaviour of materials can be characterised by various parameters, such as Charpy impact energy, K- and J-based fracture toughness. These parameters describe the resistance of a material to cracking and are important inputs to structural integrity assessments. At present, although there are a just a handful of studies focusing on the fracture behaviour of WAAM

materials, the initial results show that WAAM materials display toughness properties comparable to that of conventional wrought material. However, the fracture behaviour of WAAM materials are also susceptible to effects of location dependence and anisotropy, which have largely been attributed to the effects of microstructure.

Charpy impact energy of WAAM low alloy steel ER70S-6 at room temperature was found to lie on the upper shelf, with values comparable to conventional steel of similar carbon equivalent; and was weakly anisotropic between the build and longitudinal directions [105], [106]. Similar findings were observed in WAAM C-Mn steels [17],[75]; and additionally the ductile to brittle transition temperature increased from -36 °C to -17 °C with increasing build height [75], which the authors attributed to microstructural and hardness variations.

Weak anisotropy has also been observed in K-based linear-elastic fracture toughness, which is typically used to characterise fracture of brittle materials. Zhang et al. [107] found that K_Q and K_{IC} measurements (ASTM E399 [108]) of WAAM Ti-6Al-4V were comparable with or greater than that of wrought material (measured with the same specimen dimensions); and the values were weakly anisotropic, with toughness higher in the build direction (see Figure 1.15a). These have been attributed to the greater fracture resistance provided by the larger α-lamellae along the crack path of specimens notched in the build direction.

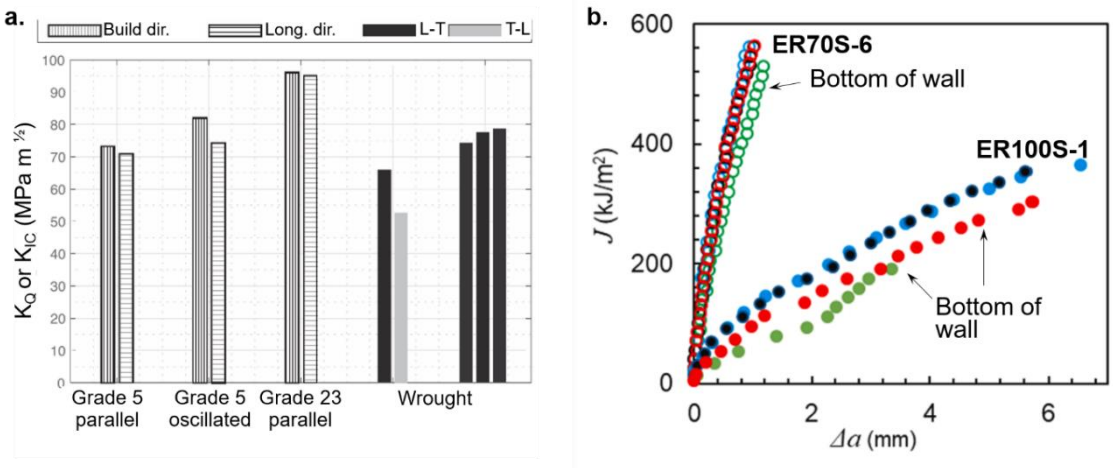

Figure 1.15: (a) K-based fracture toughness of WAAM Ti-6Al-4V, ref. [107]**, and (b) J-based fracture resistance curves of WAAM low alloy steels, ref.** [109]**.**

For J-based elastic-plastic fracture toughness, which is typically used to characterise fracture of ductile materials, Ermakova et al. [109] reported location dependency and weak anisotropy in

WAAM ER70S-6 and ER100S-1. Between the two materials, ER70S-6 displayed higher J_{IC} measurements (ASTM E1820 [110]) and toughening behaviour (i.e. steeper resistance curve, see Figure 1.15b) than ER100S-1, attributed to the higher tensile strength of the latter. Additionally, the ER100S-1 specimens displayed location dependence, where the specimens from the bottom of the wall displayed poorer toughness than the specimens from the top of the wall. Although the authors postulated that this may be due to microstructural variations caused by higher number of thermal cycles experienced at the lower parts of the wall, detailed microstructural analysis was not performed. Similarly, Dirisu et al. [111] compared the fracture toughness of three different WAAM steels, ER70S-6, ER90S-B3 and ER120S-G, each sampled with three notch orientations (i.e. build, longitudinal and thickness directions). ER70S-6, which has the lowest tensile strength, displayed the highest J_Q (ASTM E1820 [110]). In addition, J_Q was found to be the highest in the build direction for all three steels, which the authors attributed to the smaller grain size and therefore higher density of grain boundaries in the build direction. One limitation of both J-based fracture toughness studies is the small sample size, where one fracture test was carried out for each material, location, or orientation. Given the variability of the microstructure of WAAM materials, the reported fracture toughness results may be susceptible to the effects of material scatter. Therefore, there is a need to carry out fracture studies with larger sample sizes to verify if the observations of location and direction dependency of fracture toughness are related to the material's anisotropic microstructure.

1.5.6 Fatigue behaviour

Fatigue properties, which characterise the dynamic behaviour of materials, are crucial inputs into structural integrity assessments. However, there are only a few studies on the fatigue properties of WAAM materials, and most have focused on high cycle fatigue. Although initial results show that properties such as fatigue crack growth rate and fatigue life of WAAM materials are comparable to those of wrought materials, the results also show that there is much less consensus on the direction dependence of fatigue properties. In addition, there are several other factors such as heat treatment, porosity, surface finishing and testing environment which could affect the results. These factors are discussed in more detail in the following paragraphs.

The fatigue crack growth rate of WAAM Ti-6Al-4V was observed by Zhang et al. [107] to be lower than that of equivalent wrought material, but higher than cast material, as shown in Figure 1.16a. Slight anisotropy was also observed, where the fatigue crack growth rate was slightly higher in the build direction, although the authors attributed this to data scatter. In a

separate study, Xie et al. [103] observed that the fatigue crack growth rate was up to 5% higher in the build direction for WAAM Ti-6Al-4V at low stress intensity factor ranges, where the effects of microstructure dominate. At higher stress intensity factor ranges, the fatigue crack growth rate was almost isotropic. Similarly, Gordon et al. [112] found that WAAM austenitic stainless steel 304L displayed lower fatigue crack growth rate compared to conventional wrought alloy. Although the fatigue crack growth rate was observed to be slightly lower in the build direction for the as-deposited specimens, the heat treated specimens displayed almost no direction dependence, which the authors attributed to the changes in microstructure and residual stress distributions from the heat treatment.

For fatigue life, Brandl et al. [113] and Baufeld et al. [114] found that the WAAM Ti-6Al-4V had between $2{\cdot}10^5$ – $2{\cdot}10^6$ cycles to failure and a fatigue limit of 760-780 MPa, which is comparable to that of wrought plate material. Despite the higher static tensile properties in the longitudinal direction, the fatigue properties were found to be isotropic. Wang et al. [102] made similar observations, concluding that "no statistically valid relationship could be demonstrated between a specimen's orientation and location". The authors also noted that a small number of specimens failed prematurely ($< 1{\cdot}10^6$ cycles), attributed to the presence of gas porosity. Gordon et al. [115] also found that the fatigue life of WAAM 304L to be longer than that of a powder DED equivalent (see Figure 1.16b), and the run-out specimens displayed a similar fatigue limit to wrought material. The authors attributed this to extrinsic toughening mechanisms, specifically the tortuous crack path resulting from the material's microstructure. However, specimens loaded in the build direction at 85 % UTS displayed a longer fatigue life than those in the longitudinal direction. The specimens also displayed high levels of strain localisation, which was observed from surface strain measurements using digital image correlation. At the regions of final failure, phase analysis indicated that the deformation-induced phase transformations may have led to the observed anisotropy in the fatigue life in the WAAM specimens.

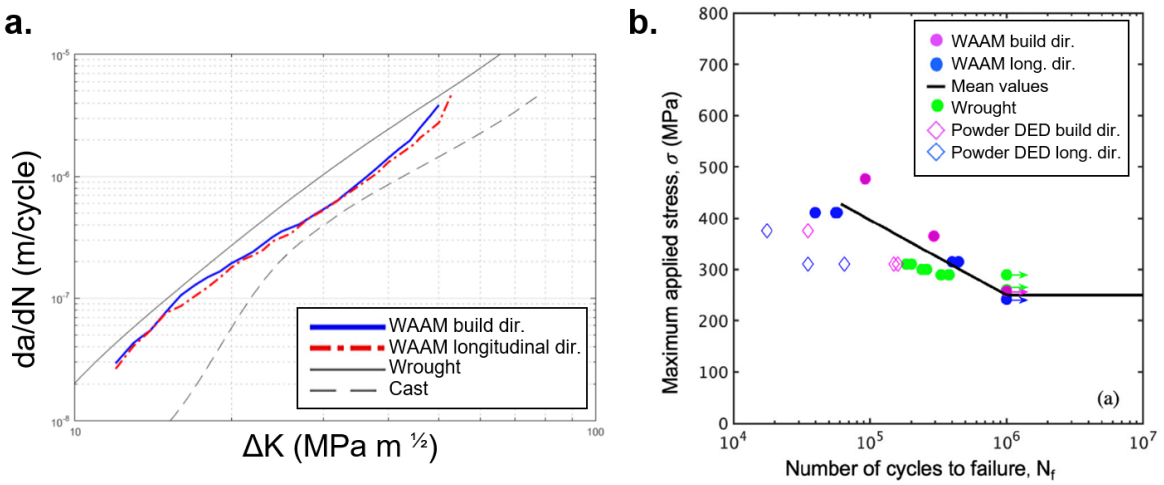

Figure 1.16: (a) Fatigue crack growth rate curves of WAAM Ti-6Al-4V in comparison with wrought and cast equivalents, adapted from ref. [107]**, and (b) S-N curves of WAAM austenitic stainless steel 304L in comparison with wrought and powder-based DED equivalents, adapted from ref** [115]**.**

Large pores have been observed by Biswal et al. [116] to cause a stress concentration effect, resulting in local stress ratios of up to 10 times that of the applied stress ratio. They conducted interrupted fatigue testing with periodic X-ray computed tomography (CT) on WAAM Ti-6Al-4V specimens and found that cyclic plastic deformation of a tension-compression nature occurred at the pore root, resulting in growth of pores to almost double their original sizes (see Figure 1.17a). The authors also found fine slip lines on the internal surfaces of the expanded pores, which have been attributed to the accumulation of dislocations at the free surfaces (see Figure 1.17b, c).

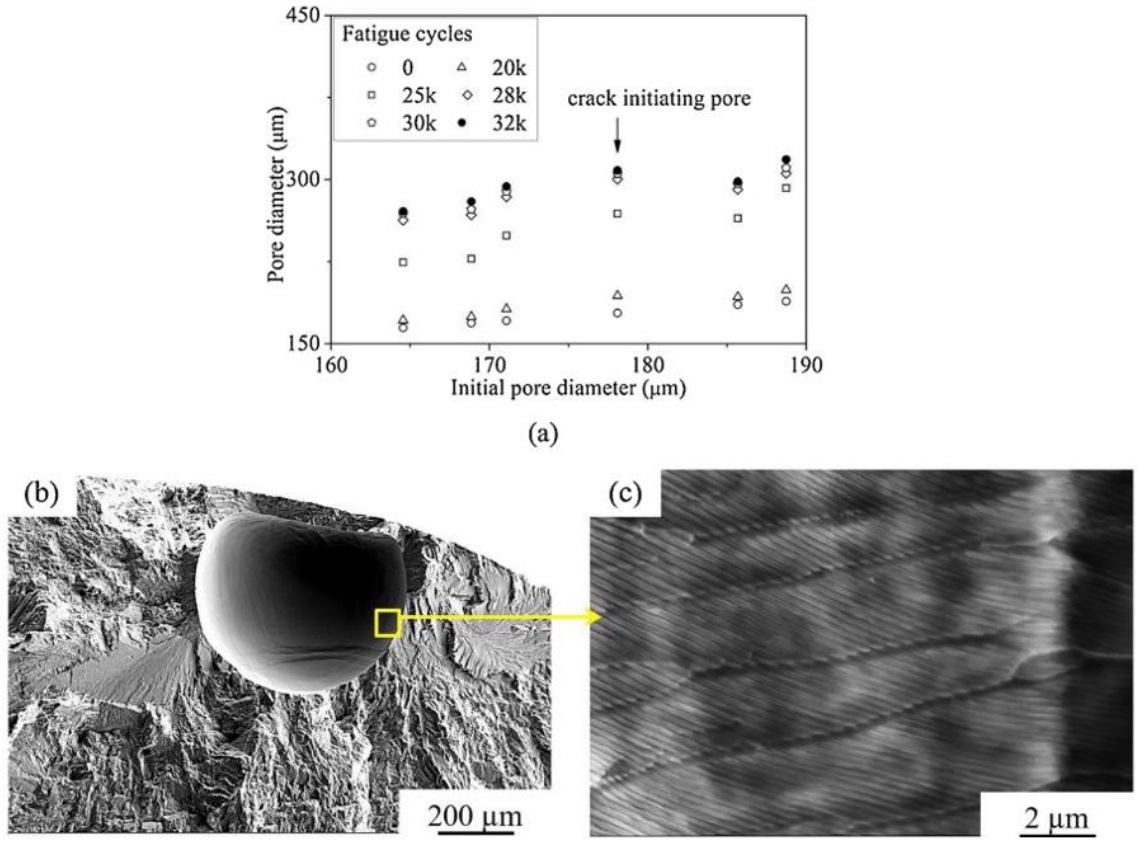

Figure 1.17: (a) Plot showing increase in pore diameter before and after fatigue cycling. Fractographic images showing (b) crack initiation at pore and (b) pore internal surface. Images taken from [116]**.**

Although most WAAM materials require machining as a finishing operation, in some instances this may not always be feasible. Under these circumstances, the surface waviness of the WAAM deposit can influence the fatigue response. Dirisu et al. [117] demonstrated that reducing the surface waviness via inter-layer cold rolling improved the high cycle fatigue life of WAAM ER70S-6 to the level of a machined specimen. The authors attributed this to the combination of smaller surface imperfections which reduces the stress concentration effect at the surface, and the introduction of a surface compressive residual stress which may be beneficial for fatigue life.

The fatigue response of WAAM materials can also be affected by adjacent materials with different microstructures. For example, Zhang et al. [118], [119] investigated the fatigue crack growth rate of WAAM Ti-6Al-4V specimens notched in five different locations and orientations with respect to the WAAM-substrate interface, and found that fatigue cracks tend to propagate

towards the wrought substrate. The authors attributed this to three main factors – (i) the more equiaxed microstructure in the substrate having weaker resistance to fatigue crack growth; (ii) the asymmetric residual stress distributions across the WAAM-substrate interface which promotes crack propagation into the substrate; and (iii) the mechanical property mismatch between the WAAM and substrate materials, all of which contributing to the preferential fatigue crack growth towards the substrate than the WAAM material.

Lastly, the operating environment also has a large influence on the fatigue response of WAAM materials. Ron et al. [120] found that the fatigue strength of WAAM ER70S-6 was considerably lower than that of the wrought equivalent when tested in a 3.5% NaCl solution, despite displaying similar fatigue strength when tested in air.

1.5.7 Residual stress and distortion

Residual stresses can be problematic for large structures, as they can lead to part distortion during fabrication and can also affect the part's susceptibility to fracture and fatigue. Large tensile residual stresses can occur in a WAAM part, due to the large and complex thermal variation that arises in a WAAM deposit. These stresses often build up during deposition and are redistributed upon unclamping the part from the sample table, which often leads to distortion in the longitudinal direction [121] (see in Figure 1.18). In the unclamped state, the longitudinal residual stresses are highest at close to the substrate [121], [122], as shown in Figure 1.19a. The stresses in the transverse and build directions have been found to be almost negligible in single pass walls [123].

There are several methods to reduce the large longitudinal residual stresses in WAAM components. If the baseplate is sacrificial, stresses can be reduced by removal of the baseplate [124], although this may cause redistribution of the stresses elsewhere in complex geometries. Inter-layer cold rolling has also been found to be effective in reducing the peak residual stresses (see Figure 1.19 b, c), through plastic deformation of the deposited material. Martina et al. [122] demonstrated that a higher rolling force applied downwards towards the substrate led to lower peak tensile residual stresses, although the residual stresses were not completely eliminated and the rolled components still displayed some distortion. Hönnige et al. [121], found that sideways rolling (i.e. pinch rolling) in directions parallel to the substrate plate was more effective at reducing residual stresses than downward rolling. However, sideway rolling can be more

complicated to apply, for example, the surface waviness of the wall may inhibit access to the deposited material.

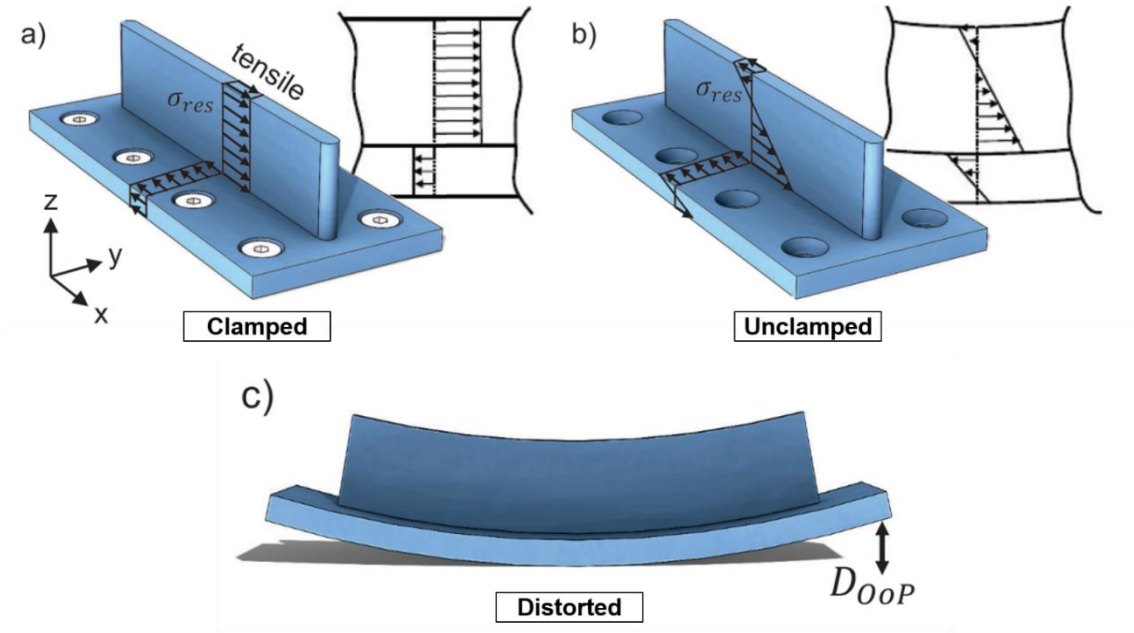

Figure 1.18: Schematic of residual stress profiles in (a) clamped and (b) unclamped WAAM walls, and the resulting (c) distortion, images taken from [121]**.**

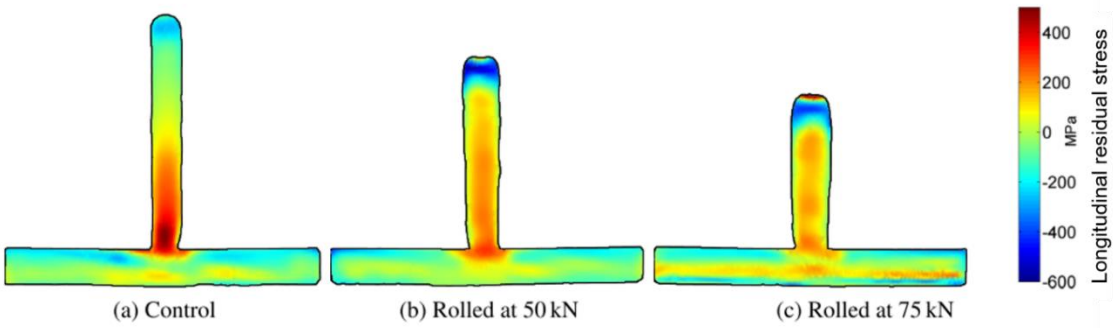

Figure 1.19: Residual stress maps measured by contour methods, taken from [122]**.**

Stress relieving heat treatment is another way to reduce residual stress in WAAM materials. Hönnige et al. [125] demonstrated that stress relieving heat treatments can reduce residual stresses where inter-layer rolling may not be so effective. The residual stress profiles in Figure 1.20 show that in all three measurement directions, the heat treated samples displayed significantly lower residual stresses than their non-heat treated counterparts.

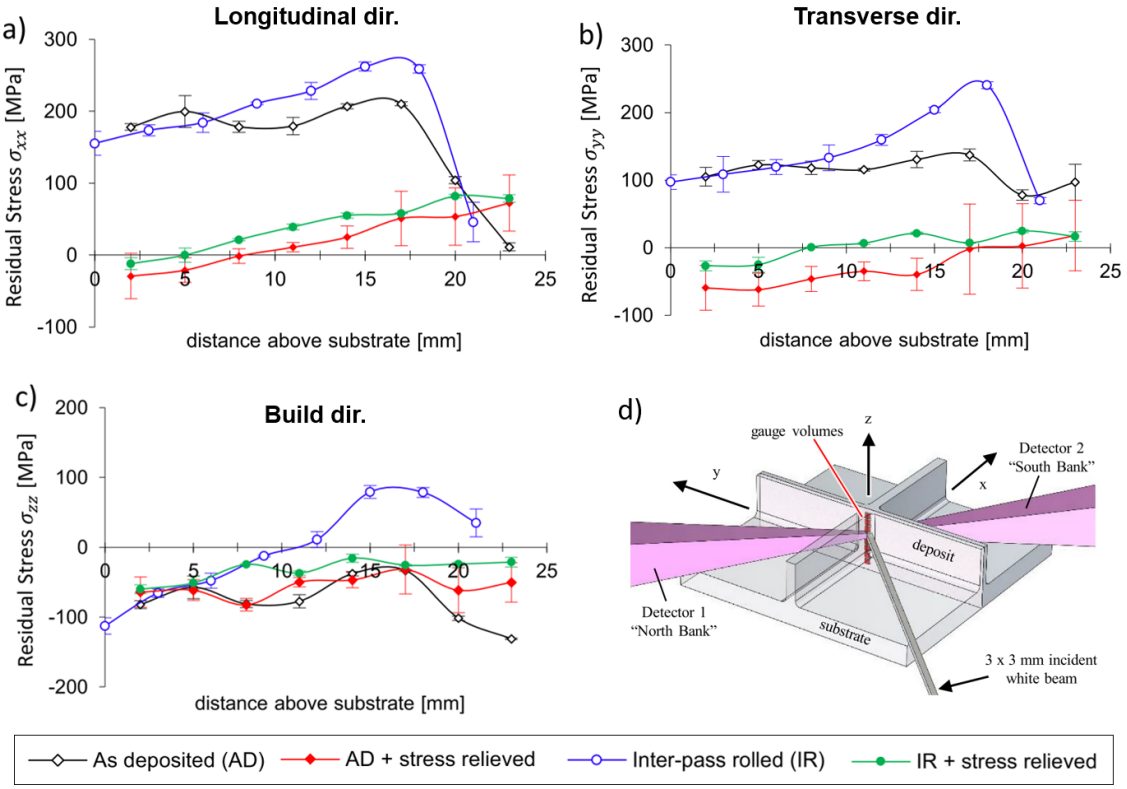

Figure 1.20: Residual stress profiles of WAAM Ti-6Al-4V cruciform component in the as-deposited, stress relieved heat treated and inter-layer rolled conditions, in (a) longitudinal, (b) transverse and (c) build directions, measured by neutron diffraction at locations shown in (d), images taken from [125].

1.5.8 Modelling and simulation

Various methods of thermo-mechanical modelling have been used to predict the residual stress and distortion that develops during the WAAM process [60]. If validated, these models can be very useful in understanding the key factors influencing residual stress and therefore facilitates the development of effective mitigation methods. In general, these models require several inputs, such as part geometry, materials properties, thermal and mechanical boundary conditions, meshing strategy and governing equations, to generate the computed temperature fields, residual stress and distortion distributions.

Reviewing the modelling efforts for WAAM to date, Srivastava et al. [126] concluded that the efforts have revolved around simple geometries and short scanning paths, which are simpler to validate and may not be applicable to more complex geometries and longer scanning paths that would be more relevant to WAAM. In addition, majority of the modelling efforts have used conventional methods, which are not efficient for simulating large-scale WAAM structures.

Nonetheless, based on the available studies, the authors summarised the main factors influencing residual stress in WAAM components as: (i) temperature distribution, (ii) substrate preheat temperature, (iii) substrate thickness, (iv) deposition strategy, (v) power and heat input, (vi) layer thickness and (vii) inter-layer deposition time.

One way to improve computational efficiency is proposed by Ding et al. [127]. The authors first used a conventional transient thermomechanical finite element model to determine the relationship between peak temperature and residual stress, then developed an efficient "engineering" model based on this relationship. The "engineering" model reduced computational time by 99 % and produced distortion and residual stress predictions that were almost identical to the original transient model. The predictions were also validated by experimental results.

In addition, machine learning methods may also provide a more efficient way to identify the fundamental factors influencing residual stress in WAAM materials. Wu et al. [128] proposed that the most influential factors on residual stress may not be the process parameters which are easy to measure, but instead complex thermo-mechanical variables more representative of complex physical mechanisms involved. Using two hundred and forty-three datasets on residual stresses for single layer deposits of three alloys in random forest and neural network-based machine learning, the authors identified preheat temperature as the most important process variable influencing residual stress, followed by the arc power, substrate thickness and scanning speed (see Figure 1.21a). Further, five thermo-mechanical variables were identified to be more representative of the complex mechanisms of evolution of residual stresses than individual WAAM process variables. The difference between solidus and preheat temperature was found to be the most influential on the residual stress, followed by liquid pool volume, heat input, substrate rigidity, and the product of elastic modulus and coefficient of thermal expansion (see Figure 1.21b). Although this type of analysis for WAAM materials is still relatively new, it indicates that there might be a possibility of minimising the residual stress in WAAM materials through the control of a few key process parameters.

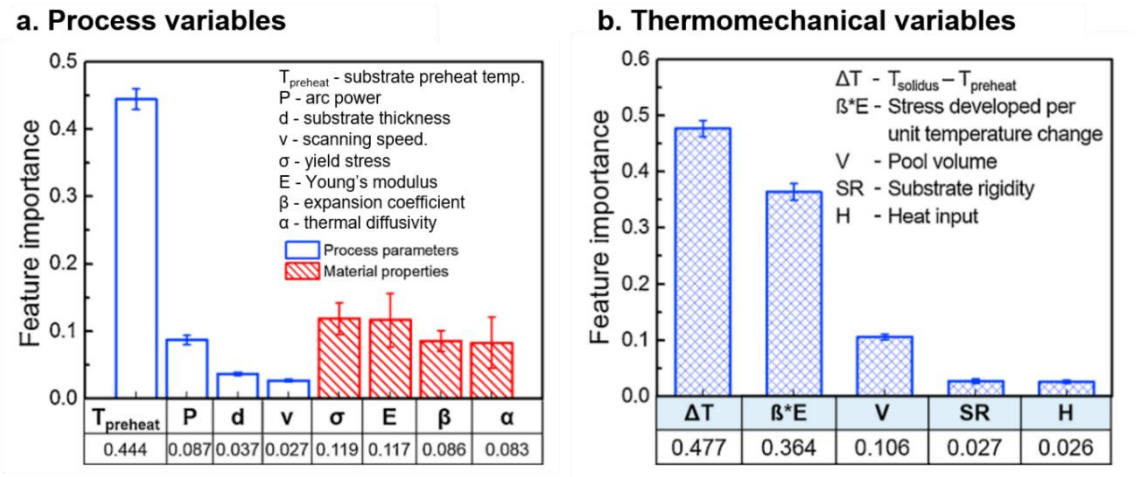

Figure 1.21: Plots showing feature importance derived from machine learning methods for various (a) WAAM process variables and (b) thermomechanical variables, images taken from [128].

1.6 Current state of the art

In summary, the shift towards end-use metal AM has led to a need for a better understanding of the characteristics of metal AM materials, such as their process characteristics, defects, microstructure, and mechanical properties, in the as-deposited and various post-processed conditions. These characteristics are especially important for large-scale metal AM parts, which tend to be load bearing and safety critical. Amongst the available AM techniques, WAAM is well-suited to large-scale AM due to its high deposition rates and large build volumes. There are many deposition technologies and build strategies which have been successfully implemented, and process parameters play a crucial role in determining deposition stability. In addition, there are many secondary processes which can be implemented in-situ to optimise deposition conditions. These process specifications and control methods can greatly influence the characteristics of a WAAM deposit, and therefore these must be carefully considered and reported in WAAM studies.

Although the use of favourable process parameters can produce WAAM material that is largely free of defects, the use of unfavourable process parameters can cause a wide range of undesirable macro-, meso- and micro-scale characteristics. Common characteristics include large columnar grains, strong crystallographic texture, microstructural banding, elemental segregation, and in some cases porosity and crack-like defects. Whilst these characteristics may be minimised through further process improvements, through either in-situ control or post-build processing

methods, more importantly, there is a need to understand the impact of these undesirable characteristics on the mechanical properties of WAAM materials.

The mechanical properties of WAAM materials are generally between those of conventional cast and wrought equivalents. Tensile properties for various commercially available alloy compositions are available in the literature. Post-build heat treatments can greatly improve the yield and ultimate tensile strengths of many WAAM materials, especially when used in conjunction with inter-pass rolling, although some compromise on ductility is often observed. Customised heat treatments have the potential to achieve a balance between strength and ductility, however at present there are very limited studies in this area for WAAM materials. There are also very limited studies on the fracture and fatigue behaviour of WAAM materials, and initial results indicate that these are susceptible to the effects of location dependence and anisotropy, largely attributable to the materials unique microstructure. However, there is a general lack of consensus on what effects microstructure have on the mechanical properties of WAAM materials, and there is also a general lack of focus on the effects of defects on mechanical behaviour, despite the wide range of possible undesirable characteristics which could arise from sub-optimal processing conditions. In addition, despite their highly anisotropic microstructures, WAAM materials generally display weak direction dependency in mechanical properties, and the fundamental reasons for this are not yet well understood in several material systems.

WAAM materials are susceptible to large tensile residual stresses, especially near the WAAM-substrate interface. There are several methods to reduce the peak residual stresses, such as inter-layer rolling and stress relief heat treatments. Thermo-mechanical modelling efforts can help to identify the most important factors influencing residual stress thereby facilitating the development of mitigation strategies. However, at present these efforts are largely focused on simple geometries, short scanning paths, and use conventional transient methods which are not computationally efficient. There is a need to develop computationally efficient models for more complex geometries, and corresponding experiments for validation of such models.

Chapter 2 Nickel-base superalloys: the case for Additive Manufacturing

This chapter provides a metallurgical perspective on Ni-base superalloys. It begins with the classification of Ni-base superalloys, followed by a description of the conventional production routes. Two alloys in particular, Alloys 625 and 718, are introduced from a historical perspective. Their phase composition and heat treatments are then discussed in relation to their suitability for additive manufacturing. This is followed by an overview of the existing work on WAAM Alloys 718 and 625, which demonstrates that using the technique with these materials is viable, although careful control of build parameters is required to avoid defects. This chapter brings together the characteristics of nickel-base alloys and the complexities of large-scale additive manufacturing for engineering components.

2.1 Introduction to Ni-base superalloys

Ni-base superalloys are an important class of engineering materials. They are used in a wide range of environments and industries, such as aerospace, power generation, nuclear, oil and gas. Known for their high temperature strength and corrosion resistance, low temperature ductility and toughness, Ni-base superalloys are also very versatile in welding, where they are often used to weld Ni-steels, cast irons and dissimilar joints of carbon steels and austenitic stainless steels, to provide good combinations of welded strength and ductility.

Ni-base superalloys are the most widely used of the superalloy family (the other two members are Co- and Fe-based superalloys), and are usually the material of choice in strength-based applications at operating temperatures around 1204 to 1371 °C [129]. They can be further classified into solid-solution strengthened, precipitation strengthened, or "other specialty alloys" [130], as shown in Figure 2.1.

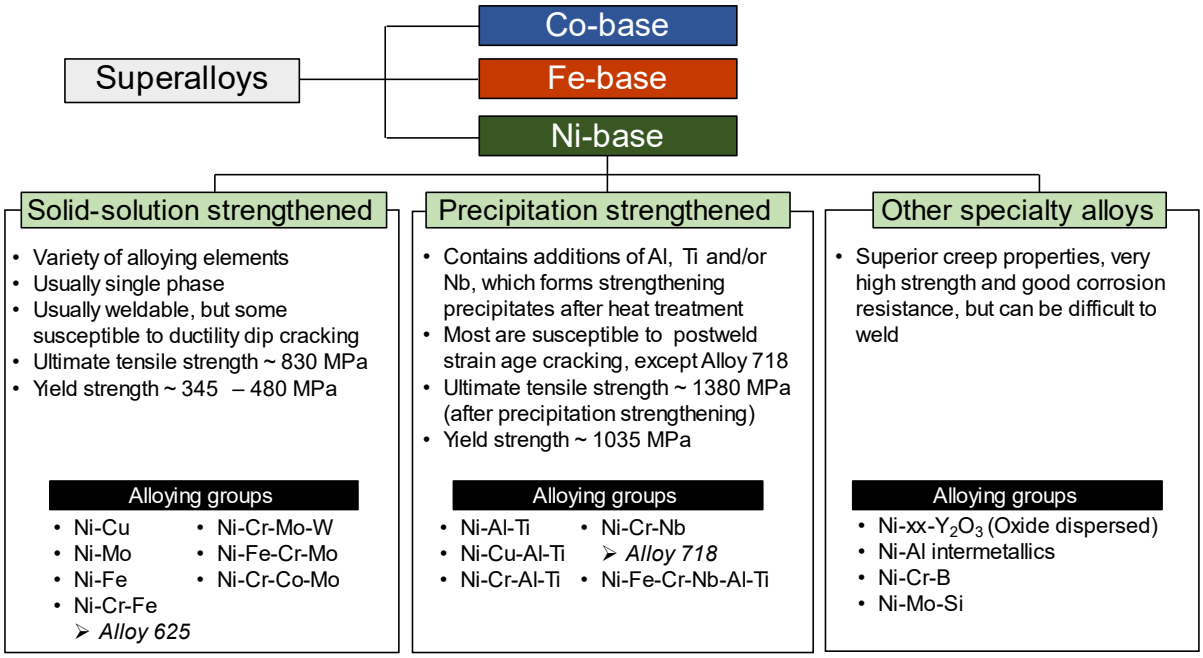

Figure 2.1: Classification of Ni-base superalloys, adapted from DuPont et al. [130].

Solid-solution strengthened Ni-base superalloys are typically alloyed with substitutional elements Cu, Mo, Fe, and/or Cr. They have a single-phase austenitic matrix and are reasonably weldable. Their maximum ultimate tensile strength values at room temperature approach 830 MPa, and yield strength values are in the range of 345 – 480 MPa [130].

Precipitation strengthened Ni-base superalloys are alloyed with similar substitutional elements but contain additions of Al, Ti and/or Nb, which form strengthening precipitates γ′ and γ″ (described in Section 2.3.2). Appropriate heat treatments (described in Section 2.3.3) are required for the strengthening precipitates to form within the austenite matrix. These precipitates, which are coherent with the austenite matrix (under most conditions), strain the matrix such that the strength of the alloy increases [130]. The ultimate tensile strength at room temperature of precipitation strengthened Ni-base superalloys can reach over 1380 MPa, and yield strength over 1035 MPa [130].

The last category, “other specialty alloys” include superalloys that have impressive high temperature creep strength, such as MA6000 and MA754, which are oxide dispersion strengthened. This category of superalloys exhibits high strength and corrosion resistance, but are typically very difficult to weld, as they have poor ductility over a wide temperature range [130].

The general characteristics of most Ni-base superalloys are well established with several reference books existing on the topic, provide detailed descriptions of the physical metallurgy of Ni-base superalloys (e.g. phase composition, strengthening mechanisms, crystallographic structure, mechanical behaviour), but each has a different focus. For example, Donachie and Donachie [129] focuses on the processing routes of superalloys (from melting and conversion, to casting, machining and finishing operations), and the resulting metallurgical characteristics imparted by each of these processes. Reed [131] addresses the topic in the context of their use in turbine blades and discs, with particular emphasis on the operating conditions and environmental degradation such components are exposed to. Lastly, DuPont, Lippold and Kiser [130] presents the topic from a welding perspective, paying particular attention to defects and microstructural characteristics formed at the weld (i.e. fusion and heat affected zones) and their formation mechanisms. The following sections will reiterate aspects of Ni-base superalloys relevant to the next chapters.

2.2 Conventional production routes

The conventional production routes for Ni-base superalloys are melting and conversion, forging and forming, investment casing, joining, and powder metallurgy, as summarised in Figure 2.2. Each of these routes are described comprehensively in Donachie and Donachie [129], and will be briefly described in Sections 2.2.1 to 2.2.5.

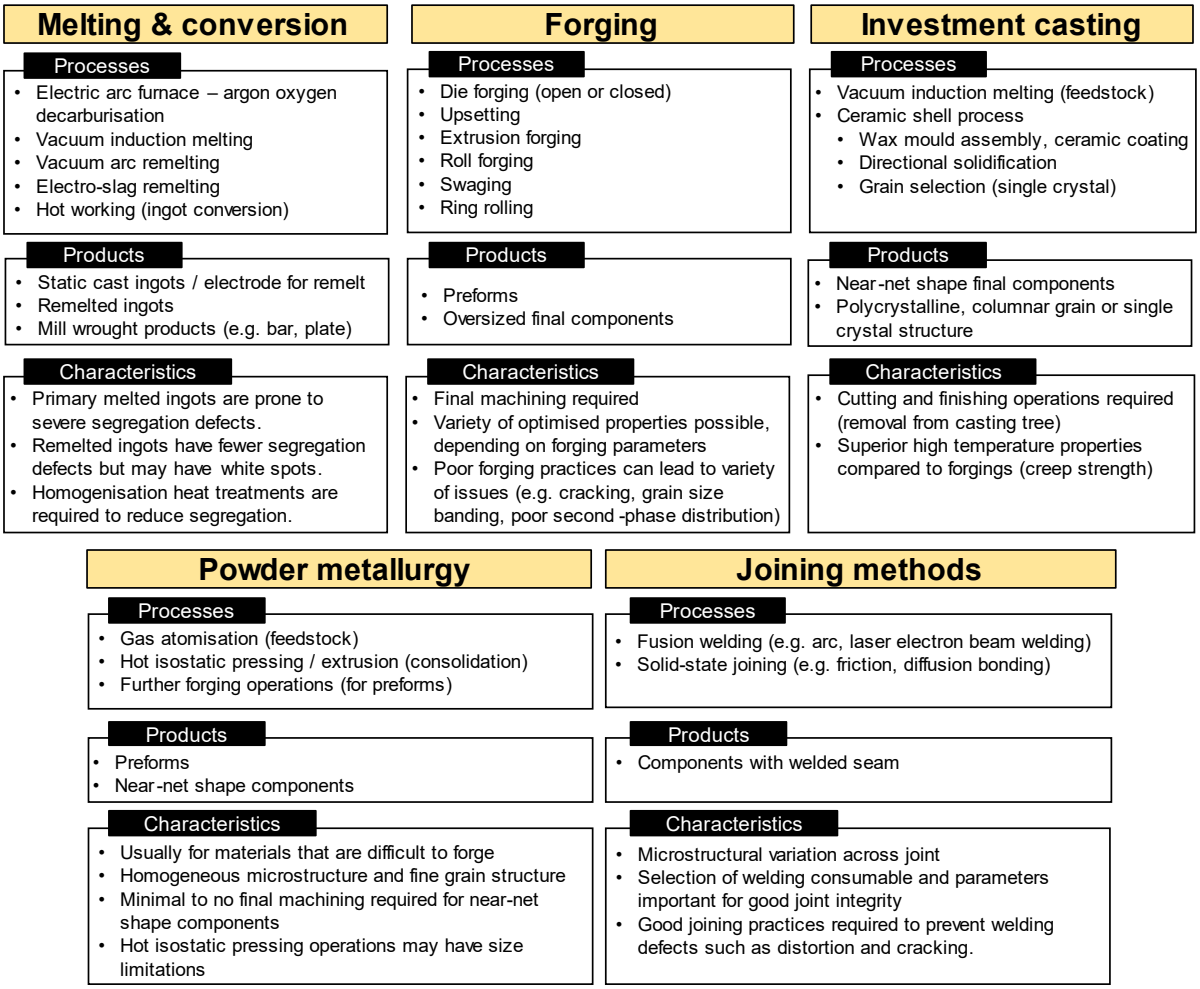

Figure 2.2: Overview of the common processing routes for superalloys, adapted from [129].

2.2.1 Melting and conversion

Melting and conversion is usually the starting point for most superalloys. These processes provide the cast ingots and mill products that are required for forging, forming, or joining methods. Schlatter [132] provides a detailed review of various melting and refining processes, describing that selection of melting methods are mainly dependent on economics, melt

segregation requirements and degree of chemistry control required. Melting methods such as Electric Arc Furnace – Argon Oxygen Decarburisation (EAF-AOD) and Vacuum Induction Melting (VIM) are primarily used for static casting, which involves pouring a large volume of molten metal into a mould, with solidification conditions largely controlled by mould design and metal feed rate to eliminate porosity. Although the open-air EAF-AOD has lower raw material costs and reduced melting times in comparison to VIM, vacuum processes provide a considerable reduction in O and N contents, providing greatly improved compositional control and microstructural cleanliness [132]. Therefore, VIM is the primary melting method used to provide feedstock for investment casting (see Section 2.2.3) and powder metallurgy (see Section 2.2.4). However, with both methods, low solidification rates often result in unacceptable segregation defects (e.g. freckles), especially for highly alloyed materials [133]. Hence, static cast ingots often undergo a second (and sometimes third) melting process (i.e. remelting), which can be carried out under more controlled conditions to achieve a more homogenised macrostructure.

The two main remelting processes are Vacuum Arc Remelting (VAR) and Electroslag Remelting (ESR). Both methods involve remelting a previously static cast ingot into a water-cooled copper crucible, by means of connecting the crucible and ingot in an electric circuit, then withdrawing the ingot slightly from the bottom of the crucible to create an arc, essentially turning the ingot into a consumable electrode. Remelting conditions are controlled through parameters such as current and voltage, and may be optimised using numerical modelling techniques [134]. Some critical components require triple-melting (i.e. VIM, followed by ESR, and finally VAR) to achieve the required level of cleanliness and homogeneity [133]. More specialised remelting techniques such as Electron Beam Cold Hearth Remelting (EBCHR) may also be used to achieve better cleanliness [135]. Nonetheless, remelted ingots are still susceptible to white spot defects and dendritic microstructures [136], and their presence must be accounted for when selecting this production route. Homogenisation heat treatments are usually required to minimise effects of segregation. Cast ingots can be converted into wrought mill products via various hot working operations, such as cogging, extrusion and rolling, to produce billets, bars, rod plate and sheet products. Wrought mill products may undergo further thermomechanical processing (i.e. forging, see Section 2.2.2).

2.2.2 Forging

Forging is a form of wrought processing which involves shaping solid metal (usually a billet) via thermomechanical deformation to impart desirable properties. There are various forging methods (see Figure 2.2), and several methods may be used in sequence; to achieve uniform grain refinement, control of second-phase morphology, controlled grain flow and structural soundness in the final product. These characteristics are controlled by the level and rate of dimensional reduction (i.e. strain and strain rate), as well as the temperature of the workpiece at any time during forging [137]. These factors influence the level of recrystallisation and hence grain size and uniformity in the final product [138]. Due to their high strength at elevated temperatures, superalloys (especially precipitation hardenable ones) are more difficult to forge than most other metals; resulting in the need for more preforms, often made by open-die forging, upsetting, roll forging or extruding, for subsequent forging in closed dies. Closed dies are better for complex shapes but die manufacture can be very costly with long lead times and are therefore inflexible to design changes. Forgings are typically oversized and require post-forge machining to achieve the final dimensional accuracy.

Poor forging practices can result in a variety of problems. Forging temperatures that are too low, or too great a size reduction, can result in surface and internal cracking. Unintended temperature variations and overly high forging temperatures can result in non-uniform recrystallisation, leading to poor grain size control and grain size banding. Inappropriate forging temperatures can also lead to incomplete homogenisation, leading to poor carbide or second-phase morphology distribution. Although some Ni-base superalloys are more forgeable than others, in general they have a relatively narrow hot-working range [137], [139] and require accurate temperature and process control. Therefore, forging techniques are often developed with process modelling [140], enabling the optimisation of temperature, strain and strain rate conditions for the required grain size and final mechanical properties. However, forging techniques developed for one shape cannot be applied directly to another shape, development time is usually required for re-optimising forging conditions.

2.2.3 Investment casting

The dominant method of investment casting Ni-base superalloys is the ceramic shell process. This involves first creating a wax mould assembly (or “tree”) in a closed die, followed by applying a ceramic coating over the wax assembly. The wax is then removed, leaving a hollow cavity in

the ceramic shell, into which molten metal can be poured into. After solidification, the ceramic shell is destroyed to retrieve the component tree, which undergoes cutting and finishing processes to obtain the final component. Investment casting can produce components with high dimensional accuracy and fine surface finishing, and is therefore often used for components with highly complex geometries (e.g. turbine blades with internal cooling passages). However, mould design can be challenging as they must be strong enough to withstand induced forces during solidification; thermally stable to maintain dimensional accuracy; sufficiently permeable to allow for displacement of gas through the mould; and not react with the molten alloy [141]. Further, the shrinkage of the molten metal mass could compromise on dimensional accuracy, and can be difficult to predict for complex geometries as its behaviour is highly non-linear [142], [143]. Under unfavourable conditions, investment cast components are susceptible to dimensional discrepancies, warping inclusions, porosity, coarse grain sizes. Some components are subsequently subject to Hot Isostatic Pressing (HIP) techniques to reduce porosity defects [144], to improve fatigue and creep life.

Investment cast Ni-base superalloy components can have different grain structures depending on the solidification conditions. Under static solidification, components have a polycrystalline grain structure. With directional solidification, components can have columnar grain or single-crystal structures, the latter achieved with the use of specialised grain selectors [145]. As directionally solidified and single-crystal components have fewer grain boundaries than their polycrystalline counterparts, they are more resistant to grain boundary sliding and have superior high temperature creep properties [131]. However, these components also have a higher scrap rate, due to their susceptibility to grain structure related defects (e.g. separately nucleated grains, grain misorientation, freckle grains, surface recrystallisation).

2.2.4 Powder metallurgy

Powder Metallurgy (PM) techniques are typically used for high strength compositions which are difficult to forge by conventional methods. PM involves the consolidation of metal powder into preforms or near-net shape components. Metal powders are typically made via gas-atomisation and are consolidated via hot isostatic pressing or extrusion. PM preforms benefit from having superplastic properties which allow for greatly reduced force requirements for near-net forgings [146]. PM parts have superior microstructural homogeneity and hence more uniform mechanical properties due to the elimination of macro-segregation and the ability to achieve finer grain sizes. PM preforms require fewer processing steps than conventional

forgings, and near-net shape PM parts require fewer machining operations. However, the cost of PM parts generally exceeds that of conventional cast or forged parts due to higher input material (powder) costs. Therefore, PM is generally used only where the component can not be made conventionally or where a property advantage is gained [147].

2.2.5 Joining methods

Large and complex structures will almost invariably require some form of joining. The main joining technique used is fusion welding. Fusion welding, by arc, laser or electron beam, involves melting a filler metal (consumable electrode) and/or part of the base materials, to create a metallurgical bond. This introduces a cast microstructure at the welded joint, with properties dependent on the consumable selected and the process parameters. Other joining methods such as solid-state processes (e.g. friction) and brazing are also commonly used, particularly in applications where a fusion welded microstructure at the joint is unacceptable, or where the alloys are un-weldable using fusion welding [148]. Good joining practices are required to retain most of the strength of the base alloy(s) while preventing joint cracking, distortion, and other defects [149].

Solid solution strengthened Ni-base superalloys (e.g. Alloy 625) have good fusion weldability and are straightforward to weld, as they usually do not require special pre-heat, post-heat or control of inter-pass temperature. In contrast, precipitation strengthened Ni-base superalloys, particularly those with high Al and Ti contents, are considerably more difficult to weld than their solid solution strengthened counterparts as they are more susceptible to post-weld strain-age cracking[1] [149], [150]. One exception to this is Alloy 718 (described in Section 2.3), which was specifically developed to overcome this issue [151]. Furthermore, fusion welding leads to the dissolution of hardening phases and their reprecipitation in less desirable forms in the matrix [152]. Therefore, precipitation strengthened alloys are often fusion welded in the (solution) annealed condition and subsequently heat treated to precipitate the strengthening phases.

[1] A solid-state cracking phenomenon most often observed in the heat affected zone just adjacent to the fusion boundary.

2.3 Alloys 625 and 718

2.3.1 A brief history

Alloys 625 and 718 were developed as part of the Inconel® family of alloys in the 1960s by the International Nickel Company (INCO), now Special Metals Corporation. Eiselstein and Tillack [153] describe the developmental history of these alloys in their 1991 paper. Initial development work on Alloy 625 was driven by applications in supercritical steam power plants, which required the alloy to be weldable, resistant to creep, and non-age hardening (for metallurgical stability). As the individual strengthening effects of the common alloying elements (Cr, Nb and Mo) in a Ni base were not particularly impressive, various combinations of Nb and Mo were trialled with increasing levels of Ni. These samples were given a simple aging heat treatment and tested at room temperature, which was intended to demonstrate any tendencies for age hardening. Surprisingly, these trials demonstrated that a combination of Nb and Mo in a Ni base, gave rise to an age-hardenable alloy that displayed significant improvements in yield strength. Although this was not the intended outcome for Alloy 625, it became the basis of subsequent development work of Alloy 718, which is a precipitation strengthened alloy with good strength and ductility, improved weldability, and resistance to strain-age cracking, and was patented in 1962 [154]. Alloy 625 was further developed through increased additions of Cr and Mo, which improved its room temperature strength and corrosion resistance. Both alloys quickly became widely used in the aerospace, nuclear, power generation and chemical processing industries.

Inconel® is a registered trademark of Special Metals Corporation. There are many other manufacturers for Alloys 625 and 718, whose compositions are governed by UNS designations N06625 and N07718 respectively. In this work, Inconel® alloys are referred to as IN625 and IN718, and material from other manufacturers are referred to as Alloys 625 and 718 respectively.

2.3.2 Phase composition

A summary of the phases in Alloys 625 and 718 is shown in Table 2.1. Alloys 625 and 718 have an austenitic γ-matrix, which has a face-centred cubic (fcc) lattice structure. They have a very small amount of the secondary phase γ′, $Ni_3(Al,Ti)$ (which is the dominant strengthening precipitate in many precipitation-strengthened Ni-base superalloys), due to the low Ti and Al contents in their composition. This also greatly improves their weldability (see Figure 2.3) and

minimises their susceptibility to strain-age cracking. Alloy 625 is typically classed as a solid-solution strengthened alloy, hardened primarily by the addition of Cr, Fe and Mo as substitutional alloying elements, which results in the expansion of the fcc lattice, providing a net strengthening of the γ-matrix [131]. However, precipitation strengthening is occasionally used in Alloy 625 to provide additional strength in specialised applications [155]–[157]. Alloy 718 is precipitation strengthened predominantly by the secondary phase precipitate γ′′, Ni_3Nb, which is coherent with the γ-matrix and is formed following a series of aging heat treatments (described in Section 2.3.3).

Carbides phases are also present in Alloys 625 and 718, typically precipitating along the grain boundaries. In Alloy 625, carbides are mostly of the $M_{23}C_6$ and M_6C types; whereas in Alloy 718, carbides are predominantly a Nb-rich MC type [158], [159]. These carbides are sometimes observed to nucleate from TiN inclusions in the alloy microstructure, resulting in a composite "carbonitride" particle with a TiN core and NbC shell [159].

In castings and weldments of Alloys 625 and 718 with dendritic microstructures, Laves phase, $(Ni, Fe)_2Nb$, is often observed in the interdendritic regions [129], [130]. Laves phase has an island-like morphology and forms because of segregation of Nb. Thus, the formation of Laves phase depletes the remaining γ-matrix of Nb. In Alloy 718, this is can reduce the available Nb required for precipitation of strengthening phase γ′′, which can be undesirable for tensile strength. Typically for castings, a homogenisation heat treatment is required to dissolve Laves phase back into the matrix, prior to the application of precipitation hardening heat treatments. However, in weldments, homogenisation heat treatments may not always be practicable without sacrificing strength in the parent material, as treatment temperatures above 1040 °C can cause grain coarsening [160]. Therefore, careful selection of welding parameters is required to prevent excessive formation of Laves phase.

In forgings and some wrought products of Alloys 625 and 718, δ-phase is precipitated along the grain boundaries in small quantities for grain size control. Although δ has the same composition as γ′′, Ni_3Nb, it has an orthorhombic crystal structure that is incoherent with the γ-matrix, and thus does not provide strengthening effects in large quantities [129]. Careful control of heat treatment is required to ensure the right balance of δ and γ′′ to achieve the appropriate strengthening effects. In addition, as δ is a more thermodynamically stable form of γ′′, long-time exposure to very high service temperatures (above 650 °C) [161] or multiple post-weld heat

treatment and repair cycles [162] can cause the transformation of γ′′ into δ, leading to depletion in strength and embrittlement effects. This is an important consideration when designing and fabricating Alloy 718 components for very high temperature applications.

Table 2.1 Summary of phases present in Alloys 625 and 718, adapted from [131]**.**

Phase	Morphology	Composition	Crystal structure
γ-matrix	Continuous matrix	Ni, Cr, Mo, Fe	Face centred cubic
γ′	Cuboidal, semi-spherical	$Ni_3(Al,Ti)$	Primitive cubic
γ′′	Disc-shaped	Ni_3Nb	Body centred tetragonal
Carbides	Globular, blocky, script	MC, $M_{23}C_6$, M_6C	Face centred cubic, Complex cubic
Laves	Island-like, globular	$(Ni, Fe)_2Nb$	Topologically close-packed
δ	Acicular, plate-like	Ni_3Nb	Orthorhombic

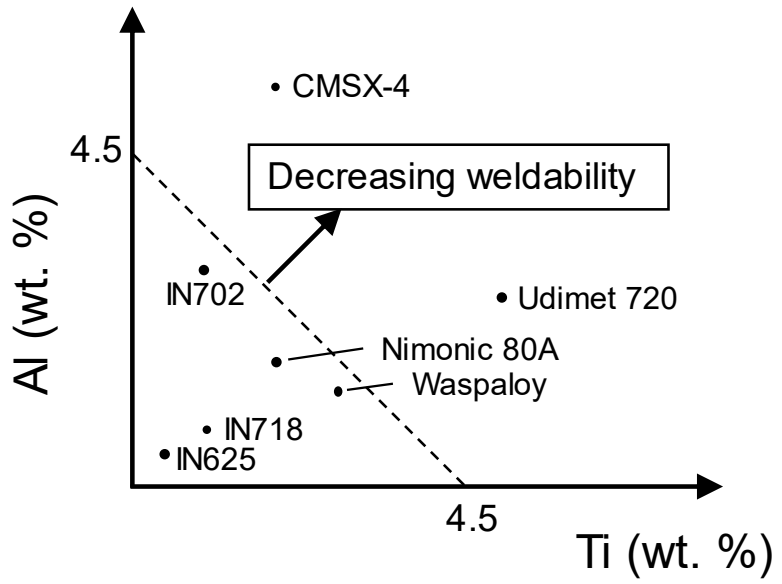

Figure 2.3: Weldability chart of various Ni-base superalloys, adapted from [129]**.**

2.3.3 Role of heat treatments

Heat treatments are an essential aspect of superalloy production. In general, heat treatment refers to the application of heat to a material/component for an amount of time sufficient to cause macro-scale (e.g. reduce stresses) or microstructural (e.g. dissolve phases, promote grain growth) changes to the material. The effects of heat treatment are largely dependent on the alloy's chemistry, heat treatment temperature and duration. Stress relieving heat treatments are applied below the alloy's annealing temperature to avoid affecting the alloy's microstructure.

Homogenisation, solution, or aging treatments are designed based on an alloy's time-temperature-transformation (TTT) curves, as shown in Figure 2.4. The TTT curves depict the temperature and duration at which different phases precipitate within an alloy's microstructure, and are used to determine the "sweet spot" where strengthening phases such as γ'' can be precipitated without excessive formation of less desirable phases such as δ.

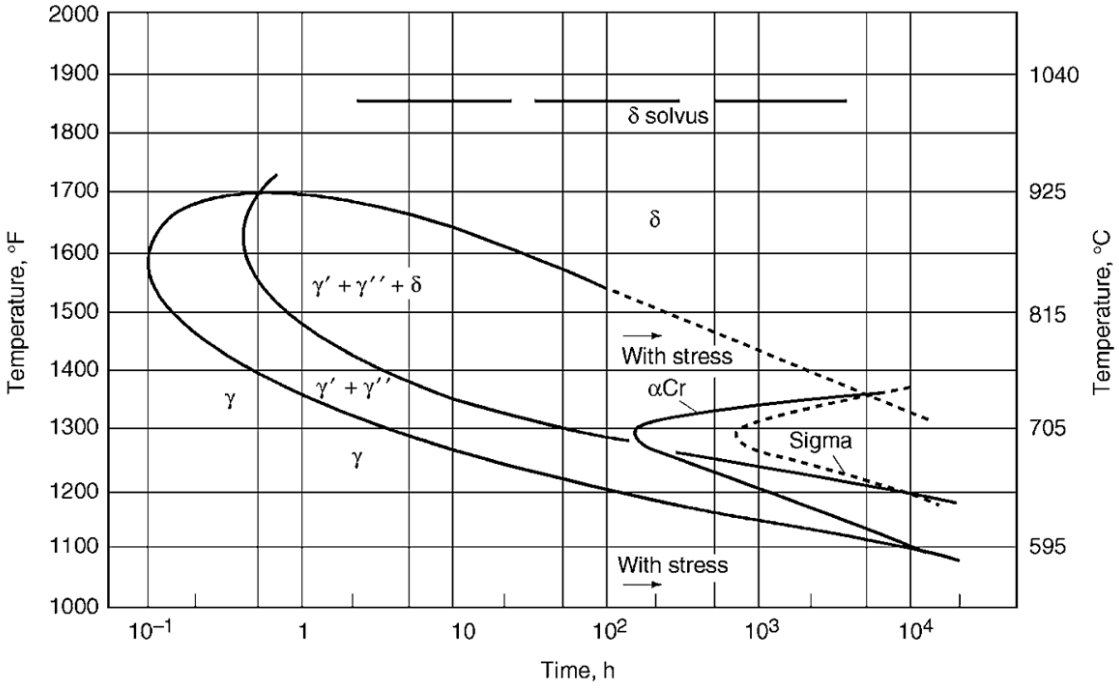

Figure 2.4: Time-temperature-transformation curves of IN718, taken from [129].

Typical recommendations for heat treatment of Alloy 718 are solution treating, aging, stress relieving and annealing; the specific temperatures and durations are detailed elsewhere by Chandler [163]. In addition to the required final microstructure and material properties, the alloy's prior processing route should also be considered when selecting heat treatment schedules. For example, cast Alloy 718 with dendritic microstructures will require additional solution (or homogenisation) treatments than their wrought counterparts, to dissolve any secondary phases (i.e. Laves phase) into solid solution prior to aging treatments. This requirement is also specified in AMS 5383 [164] for investment castings, and AMS 5662 [165] for forgings and other wrought products. Homogenisation heat treatment temperatures can be determined using Differential scanning calorimetry (DCS) curves, such as the one in Figure 2.5, which indicates the solidification/dissolution temperatures of some segregated phases in cast

Alloy 718. Laves phase dissolves between 1171 °C and 1186 °C, and this forms the basis of the modified heat treatment temperatures described in Chapter 3.

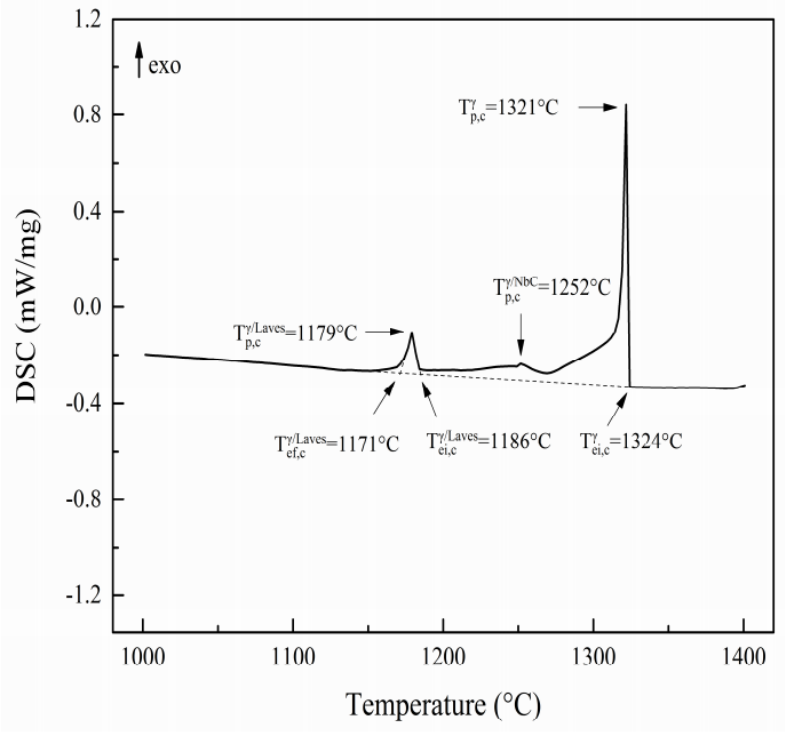

Figure 2.5: Differential canning calorimetry curve for cast IN718, taken from [166].

2.3.4 Suitability for Wire + Arc Additive Manufacturing

Relative to other γ′ strengthened Ni-base alloys, Alloys 625 and 718 have good weldability and are therefore well suited for WAAM. This has been demonstrated in several studies using various welding technologies. For Alloy 625, Xu et al. [97] deposited thick (~ 50 mm) blocks using a plasma-based system and a parallel bead strategy, and reported that the WAAM deposits were free of cracks and pores. Although the tensile strength of as-deposited material was slightly lower than that of conventional wrought material, the yield strength and elongation were almost equal. Post-build heat treatments were found to improve the tensile strength, albeit at the expense of elongation. Similar results were reported by Tanvir et al. [167], [99], who deposited a single-pass box section with using CMT, and Wang et al. [96], who deposited single-pass walls using a TIG-based deposition system.

For Alloy 718, Baufeld [55] deposited single-pass box sections using a TIG based system, and reported that the deposit was free from pores, cracks or fissures, with tensile strengths (in the

build direction) higher than as-cast material but lower than wrought or other AM methods (e.g. PBF). Similar results were also reported by Xu et al. [82], who also deposited single-pass walls using plasma arc based systems. In addition, they found that inter-layer rolling could improve the tensile strength of the deposited Alloy 718 to a level comparable with that of wrought alloy. Using CMT, Kindermann et al. [168] also deposited single-pass walls and reported that the hardness levels (after aging heat treatments) were comparable to those of wrought and other AM materials.

In all these studies of Alloys 625 and 718, the as-deposited WAAM materials displayed large columnar grains and dendritic microstructures, with Laves phase and MC-type carbides in the interdendritic regions. This type of microstructure is unlike that of conventional wrought product, but more like those of directionally solidified cast material and weld fusion zones. The as-deposited microstructure may be altered through secondary processing methods. For example, inter-layer cold rolling can impart grain refinement effects [82], and post-build heat treatment can result in dissolution of Laves and precipitation of δ-phase [82], [99], [167], [169], in addition to the precipitation of γ′′ during aging treatments.

In a small number of studies of Alloy 718, crack-like defects have been observed and attributed to unfavourable deposition conditions. Clark et al. [46] found sinuous crack-like defects in cylindrical walls deposited using a MIG-based system and a parallel-bead strategy. The cracks were described as “closed” and “not evident until close to the end of the manufacturing route”, despite their relatively large microstructural features relative to forgings. The cracks were attributed to Laves phase found in the interdendritic regions of the microstructure. Similarly, Artaza et al. [170] observed hot cracking defects in single-pass walls deposited via a plasma-based system, although their formation was attributed to the use of deposition parameters that resulted in large thermal gradients. Cracks were not observed in the samples which were deposited using parameters with lower thermal gradients. The effects of these crack-like defects on mechanical properties were not investigated in these studies.

2.4 Conclusions

There are several existing production routes for Ni-base superalloys, ranging from melting, conversion, forging, investment casting, powder metallurgy to joining methods. These conventional production routes have been used for decades to achieve various the characteristics of Ni-base superalloys for their wide range of industrial applications. However,

for complex geometries, forging dies and casting moulds may be difficult to produce, and once they are made, are inflexible to design changes. Joining methods may help to achieve complex shapes without the need for dies, but fusion welding can impart undesirable microstructures at the joint. In addition, conventional methods of casting, forging and machining generally require much more raw material than near-net shape methods such as powder metallurgy or AM. Powder metallurgy (and powder-based AM) has a high raw material cost, and typically requires hot isostatic pressing for consolidation, which has size limitations and may be costly to run on production scale. WAAM presents many potential solutions to the limitations of conventional production methods, enabling production of near-net shape parts with available raw materials, without the need for hot isostatic pressing for consolidation.

Alloys 625 and 718 are particularly well suited to the WAAM process, due to their good weldability. Although their tensile properties have been demonstrated to be comparable to that of conventional equivalents, they have an inhomogeneous microstructure which may be detrimental for properties such as fracture toughness and fatigue resistance. Furthermore, a better understanding of the effects of their anisotropic grain structure on the direction dependency of mechanical properties is needed. In addition, unfavourable WAAM processing conditions can lead to defects, and their effects on mechanical properties are poorly understood.

2.5 Summary of WAAM Alloy 718 material in this work

A total of 4 WAAM walls (Walls 1-4) of Alloy 718 material were used in the work reported in Chapters 3-5. The manufacturing methods and microstructural characteristics for Wall 1 is described in Chapter 3, and that of Walls 2-4 is described in Chapter 4. All tensile specimens tested were extracted from Wall 1 and these results are reported in Chapter 3. Five compact tension C(T) fracture specimens were extracted from Wall 1; the results from three specimens are reported in Chapter 4, and two in Chapter 5. Ten C(T) fracture specimens were extracted from Walls 2 and 3, and these results are reported in Chapter 4. Samples used for liquid penetrant inspection and ultrasonic testing were extracted from Walls 3 and 4. No mechanical test specimens were extracted from Wall 4. Detailed specimen lists and extraction locations can be found in Appendix A.

Chapter 3 Effect of post-deposition heat treatments on microstructure and tensile properties of WAAM IN718

This chapter describes a new modified heat treatment which was found to be effective in addressing these microstructural inhomogeneities in WAAM IN718. It also argues that the modified heat treatment has reduced the anisotropy in grain structure, resulting in almost isotropic elevated temperature tensile properties. However, the as-deposited microstructure provides an unfavourable starting point for the improvement of tensile properties to the level of conventional wrought material.

This chapter is based on the following publication:

Seow C E, Coules H E, Wu G, Khan R H U, Xu X, et al. (2019) 'Wire + Arc Additively Manufactured Inconel 718: Effect of post-deposition heat treatments on microstructure and tensile properties', Materials and Design, 183. doi: 10.1016/j.matdes.2019.108157.

3.1 Introduction

Deposition of nickel-base alloy IN718 using WAAM techniques has been demonstrated to be viable in several studies using metal-inert-gas (MIG) [46], tungsten-inert-gas (TIG) [171], [55], [172] and cold metal transfer (CMT) [173], although careful control of build parameters is necessary to prevent porosity and crack-like defects. In the as-deposited condition, WAAM IN718 has a dendritic microstructure decorated with Laves phase $(Ni,Cr,Fe)_2(Nb,Mo,Ti)$ and carbides [46], [171], [55], [172], [173]. Laves phase is generally deemed detrimental for mechanical properties, as its formation depletes the matrix of Nb for γ" precipitation and its presence may have an embrittling effect on the material. There are two possible ways of dealing with Laves phase – (i) preventing its formation during deposition, and (ii) dissolving it back into the matrix through homogenisation heat treatments. The formation of Laves phase, due to elemental segregation of heavier elements into the interdendritic regions, is governed by thermal conditions during deposition. At present, this is difficult to monitor and control due to the complex thermal cycling that the part undergoes during the WAAM process [61]. Therefore, post-deposition heat treatment is currently the most viable way of managing Laves phase in the

as-deposited microstructure. However, standard heat treatment schedules, which are designed for cast or wrought IN718, may not be suitable for WAAM materials as they have a different starting microstructure. The extent of Laves phase in the as-deposited microstructure may be dependent on specific WAAM deposition parameters, therefore it is important to characterise the as-deposited microstructure, which is the starting microstructure for subsequent post-deposition heat treatment, using conventional metallography techniques.

The mechanical properties of WAAM materials at elevated temperature are especially important for IN718 since this material is most commonly used for high temperature applications. Whilst tensile properties of WAAM IN718 at room temperature have been shown to be comparable to cast material [55] but short of wrought material [173], the properties at elevated temperature remain largely unknown.

WAAM IN718 in the as-deposited condition has been found to have large columnar grains and a strong crystallographic texture [172], [173]. Unlike fine-grained polycrystalline wrought materials, the grain structure of WAAM IN718 is highly anisotropic which could lead to direction dependent mechanical properties. It is important to assess the extent of anisotropy and reveal the relationship between the grain structure and mechanical properties, as knowledge of this structure-property relationship is critical in understanding the underlying mechanisms which govern the mechanical behaviour of WAAM materials. Although separate tensile properties for WAAM IN718 loaded in different directions have been reported [173], the extent of their anisotropy has not been quantified, and their relationship with the anisotropic grain structure remains unclear.

Post-deposition heat treatment can be a convenient way of improving the microstructure and grain structure of WAAM materials. However, little is known about the effects of heat treatments on grain size and texture, and the resulting mechanical properties of WAAM IN718. Although the use of high-pressure cold rolling [76], [78], [80] has been found to mitigate the formation of large columnar grains through recrystallisation, rolling requires expensive tooling, increases overall deposition time, places additional limitations on part geometry, and the levels of recrystallisation could vary across the height of the build [82]. Therefore, alternative ways of improving the grain structure of as-deposited material must be developed and the resulting direction dependency on mechanical properties must be examined.

In this work, the effectiveness of heat treatments in improving the microstructure and tensile properties of WAAM IN718 material was investigated, and the extent of anisotropy in tensile properties in relation to its microstructure was assessed. This was performed by comparing the (i) microstructure, (ii) grain size and texture, (iii) tensile properties at room and elevated temperature, of WAAM IN718 material in both the as-deposited and heat-treated conditions.

3.2 Methodology

3.2.1 WAAM IN718 manufacture and sample extraction

A WAAM wall specimen was built using a Migatronic 320 A AC/DC plasma controller with a water-cooled plasma torch in an argon filled glove box, as shown in Figure 3.1. Purified argon was used to produce the plasma and for shielding. The position of the torch was controlled using a three-axis linear CNC system. IN718 wire, manufactured by INCO Alloys Limited, with diameter of 1.2 mm and chemical composition detailed in Section 3.2.5, was guided through a jig to the tip of the torch.

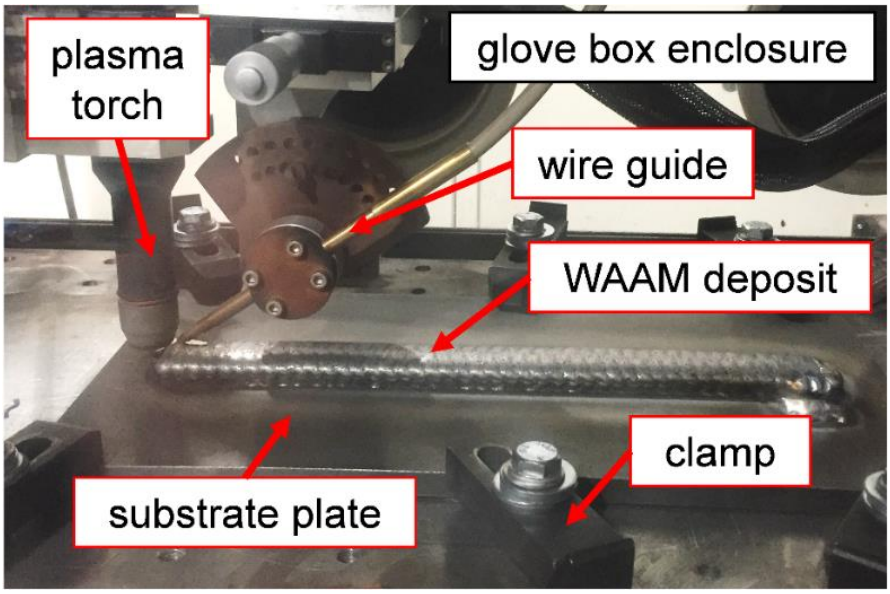

Figure 3.1: WAAM equipment setup within the glove box.

Each layer of the WAAM wall was deposited in an oscillating pattern about the wall axis. WAAM build parameters were selected based on previous work by Xu et al. [82]. The distance from the torch to the deposition surface was maintained at 8mm. The current used was 240 A for the initial layers and was gradually decreased to 200 A after 18 layers. The torch travel speed was 6.5 mm/s, and the wire feed speed was adjusted between 1.5 to 2 m/min. The final build dimensions are 300 mm length by 27 mm thickness by 68 mm height (Figure 3.2). No defects were observed from X-ray radiographs of the wall, although the minimum detectable size is 1.2 mm. Metallographic slices and cylindrical tensile specimens were extracted from the wall as shown in Figure 3.2.

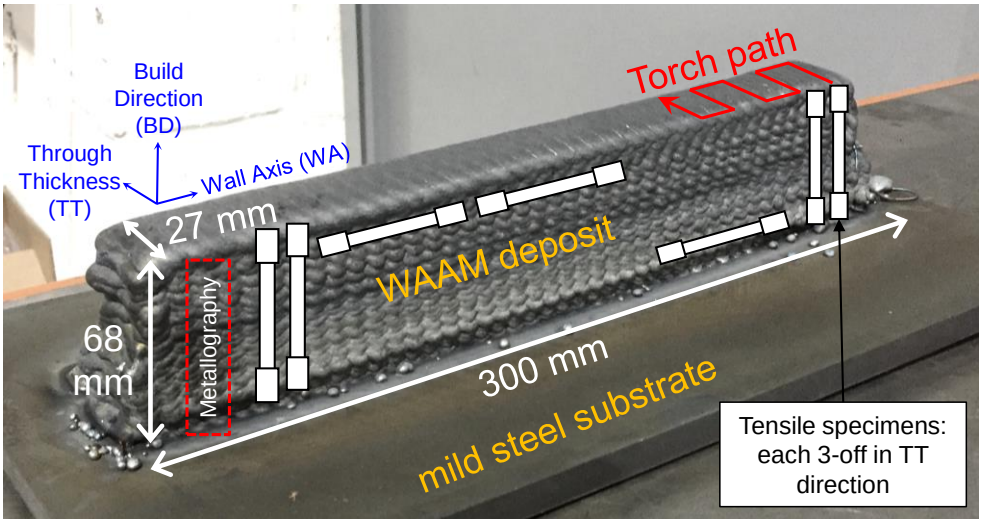

Figure 3.2: WAAM IN718 wall labelled with build dimensions, direction axes, oscillating torch path and extraction locations of metallographic slice and tensile specimens.

3.2.2 Heat treatment strategies

Heat treatments were performed using a vacuum furnace. The samples were positioned near the centre of the furnace chamber, using a stainless steel jig assembly. Samples were placed on a ceramic tile alongside titanium getters. Two thermocouples were placed in contact with the jig assembly to measure the internal temperature during the heat treatment. A photograph of the setup is shown in Figure 3.3.

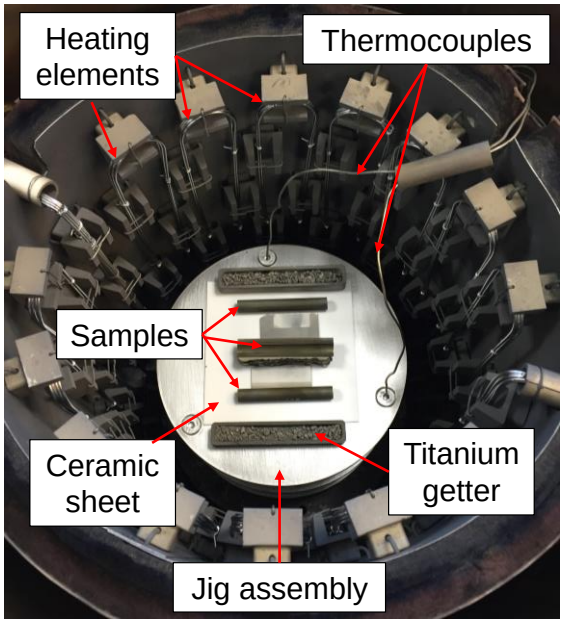

Figure 3.3: Internal chamber of vacuum furnace used to perform heat treatments.

Two separate homogenisation treatments were investigated, (i) AMS 5383 [164] homogenisation treatment at 1100 °C for 1 h, air cool, and solution treatment at 980 °C for 1 h, air cool (Standard HSA) and (ii) a modified homogenisation treatment at 1186 °C for 40 min, air cool (Modified HA). The latter treatment is a novel modification of the homogenisation treatment of AMS 5383 [164], designed based on the Laves phase eutectic temperature at 1185°C [174], [175], used here for the first time on WAAM IN718 material. The modified homogenisation treatment also has a shorter hold time to reduce grain growth. Both treatments were followed by a standard double aging treatment, (720 °C for 8 h, furnace cool, and 620 °C for 8 h, air cool). In addition, one set of samples were aged without any homogenisation or solution treatment (Aging only). The temperature traces for the Standard HSA and Modified HA materials are shown in Figure 3.4.

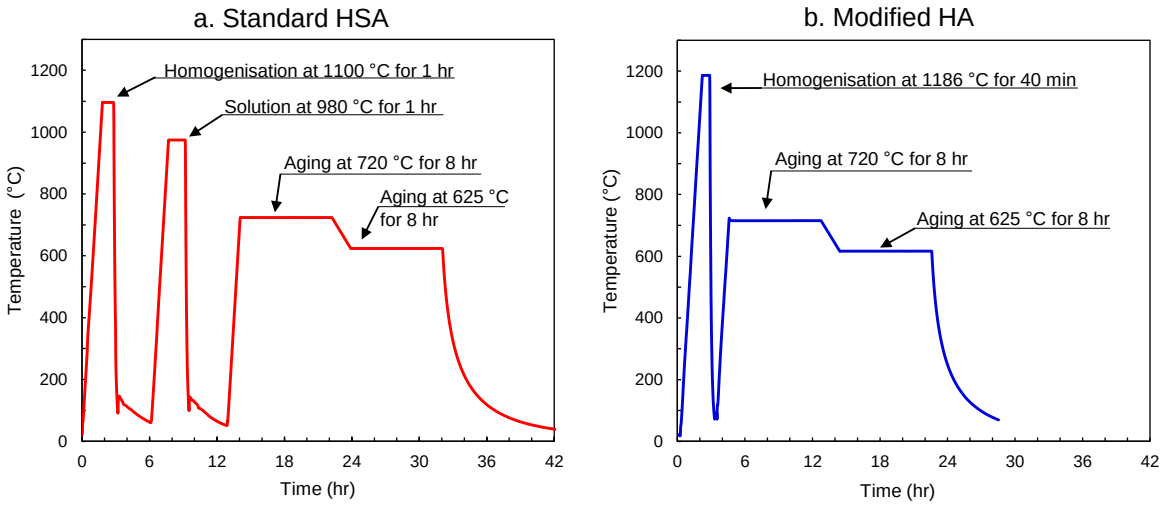

Figure 3.4: Measured temperature traces for (a) standard homogenised and solution-aged and (b) modified homogenised and aged WAAM IN718 materials.

3.2.3 Metallographic preparation and analysis

Metallographic specimens were mounted, ground and polished to 0.25 µm. They were etched electrolytically with 20 % H_2SO_4 at 3 V for 10 s. For Electron Backscatter Diffraction (EBSD), samples were given a final polishing with colloidal silica suspension. Light micrographs were taken using an optical microscope. Backscatter electron (BSE) images were taken using a ZEISS EVO Scanning Electron Microscope (SEM). Energy Dispersive X-ray Spectroscopy (EDX) analysis were also conducted using the SEM with an accelerating voltage of 20 keV. Point analyses were performed using a spot size of 1 µm. The EBSD analysis used a ZEISS SIGMA Field

Emission Gun SEM and an Oxford Instruments Nordlys detector, using an accelerating voltage of 30 keV, aperture of 60 μm and step size between 3-5 μm.

3.2.4 Hardness and tensile testing methods

Vickers hardness testing was performed in compliance with BS EN ISO 6507-1 [176], using a load of 10 kg. Measurements were made at varying distances from the substrate. Standard tensile tests were performed using specimens with dimensions in Figure 3.5, to BS EN ISO 6892-1 [177] at room temperature and BS EN ISO 6892-2 [178] at 650 °C. For the latter, a high temperature extensometer was used to measure strain. Elongation at 650 °C was determined using the total length of the specimen, as gauge markings were masked by the discolouration of specimen surface during the high temperature test.

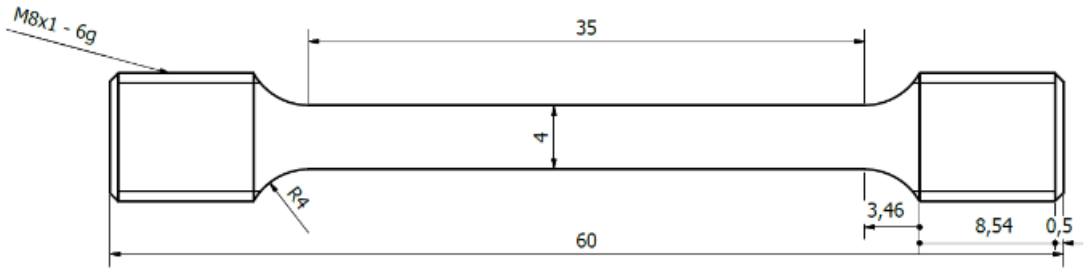

Figure 3.5: Tensile specimen dimensions in mm.

3.2.5 Characterisation of wire feedstock

The chemical composition of the IN718 wire feedstock is within the specifications of SAE International AMS5383 [164] and AMS5662 [165], as shown in Table 3.1, measured using Inductively Coupled Plasma Optical Emission Spectroscopy (ICP-OES) for major elements and inert gas fusion elemental analysis for C, N and O. Ti- and Nb-rich inclusions were found in the wire cross section, as shown in the Backscatter Electron (BSE) image and corresponding EDX spectra in Figure 3.6. Spot 1 is likely to be a carbo-nitride containing both Ti and Nb, whose morphology and elemental composition is discussed further in Section 3.3.1. Spot 2 is likely to be MC-type carbide NbC, which is typically found in IN718. The distribution of the particles in the wire (streaks aligned with the wire axis) suggest that they might have been introduced during thermomechanical processes, such as rolling or extrusion, which are commonly used in wire production.

Table 3.1: Chemical composition of INCO Alloy IN718 (wt %).

Element	Ni	Cr	Fe	Nb	Mo	Al	Ti	C	N (ppm)	O (ppm)
Wire	53.54	19.31	17.16	4.88	3.02	0.53	1.03	0.03	112	<50

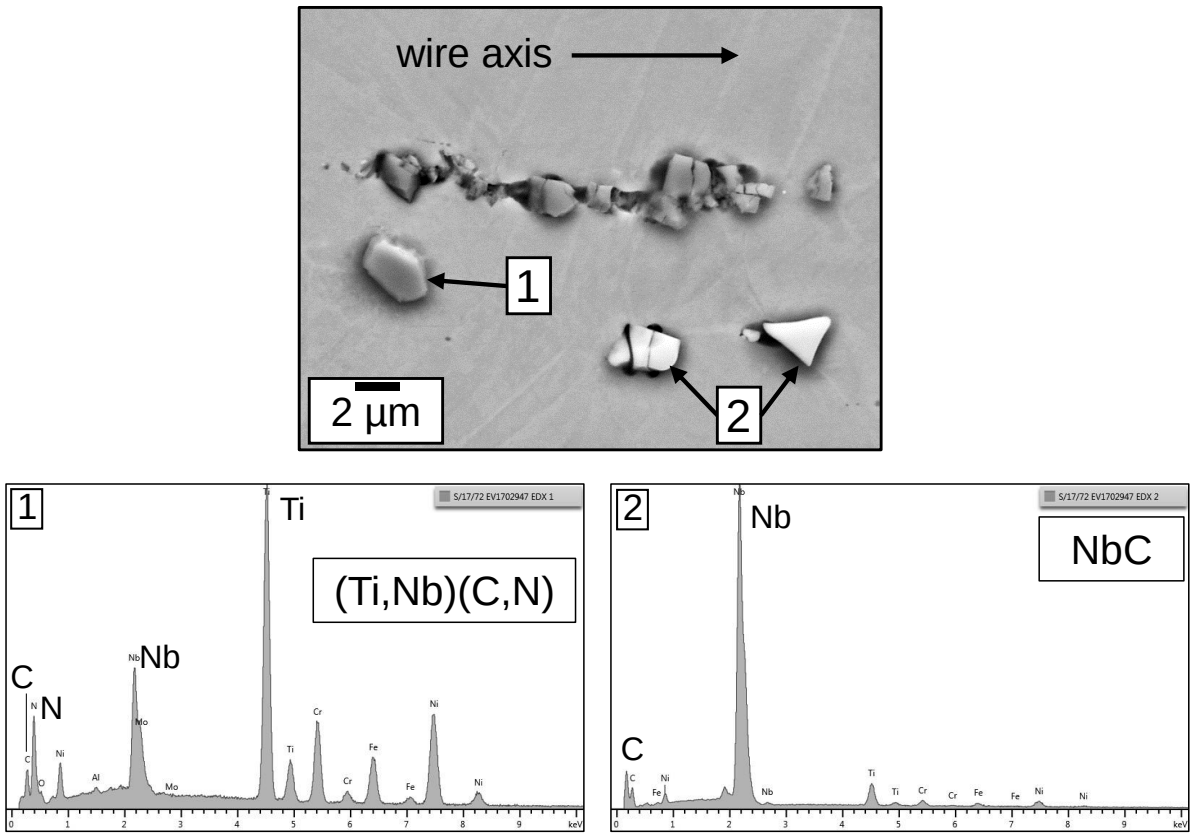

Figure 3.6: SEM backscatter electron image and corresponding EDX spectra showing TiN and NbC particles in the wire feedstock.

3.3 Results

3.3.1 As-deposited microstructure

The as-deposited (As-Dep) WAAM IN718 etched metallographic specimen (Figure 3.7) revealed alternating light and dark bands which seem to correlate with newly deposited material and re-heated zones. The interface between the bands is referred to as the interlayer boundary. The macrograph insert (Figure 3.7) also shows epitaxial dendrite growth from the substrate plate generally in line with the build direction, indicating that the thermal gradient is the largest in this direction. Some dendrites have grown across interlayer boundaries and can be several millimetres long. The interlayer boundaries were observed to correspond to differences in dendrite patterns in the light micrographs (Figure 3.8), but may be also be caused by a combination of weak segregation banding and solute partitioning in the heat affected zones, which has been recently observed in WAAM titanium alloys [95]. The curvature of the interlayer boundaries in Figure 3.7 and Figure 3.8 are likely to be partially due to the spreading of the molten pool towards the edge during deposition. The slightly outward-angled dendrite growth direction at the edges of the sample (shown in Figure 3.8a and c) suggests that there was a small shift in the thermal gradient, which could be due to heat dissipation from the edges of the deposit.

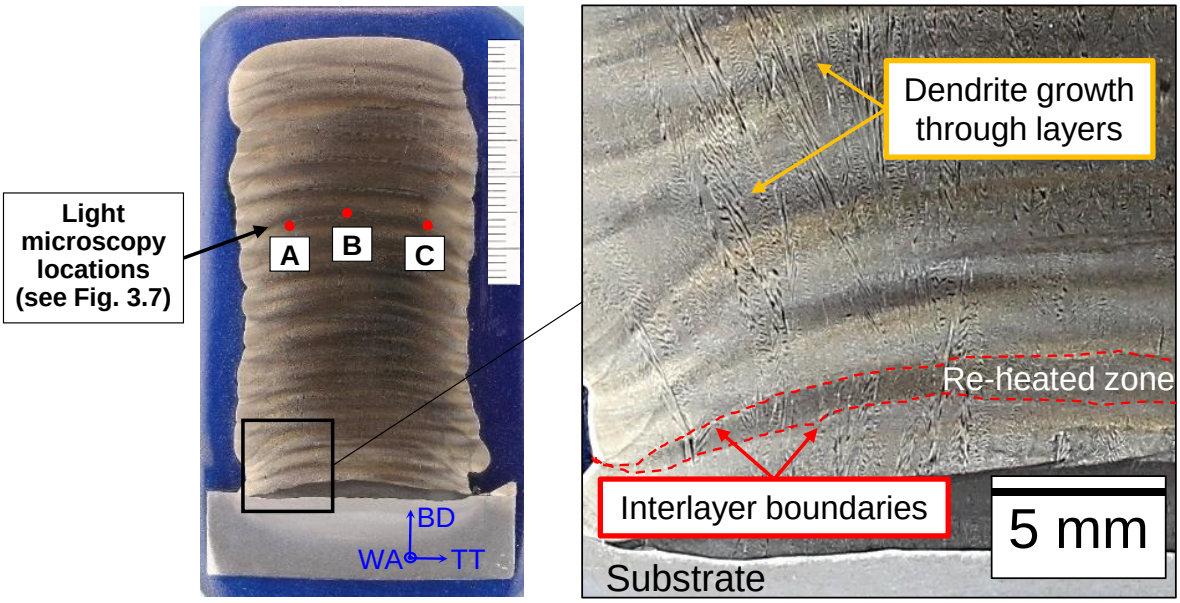

Figure 3.7: Macrograph showing locations of light micrographs A, B, C in Figure 3.8, dendritic features, re-heated zone and interlayer boundaries.

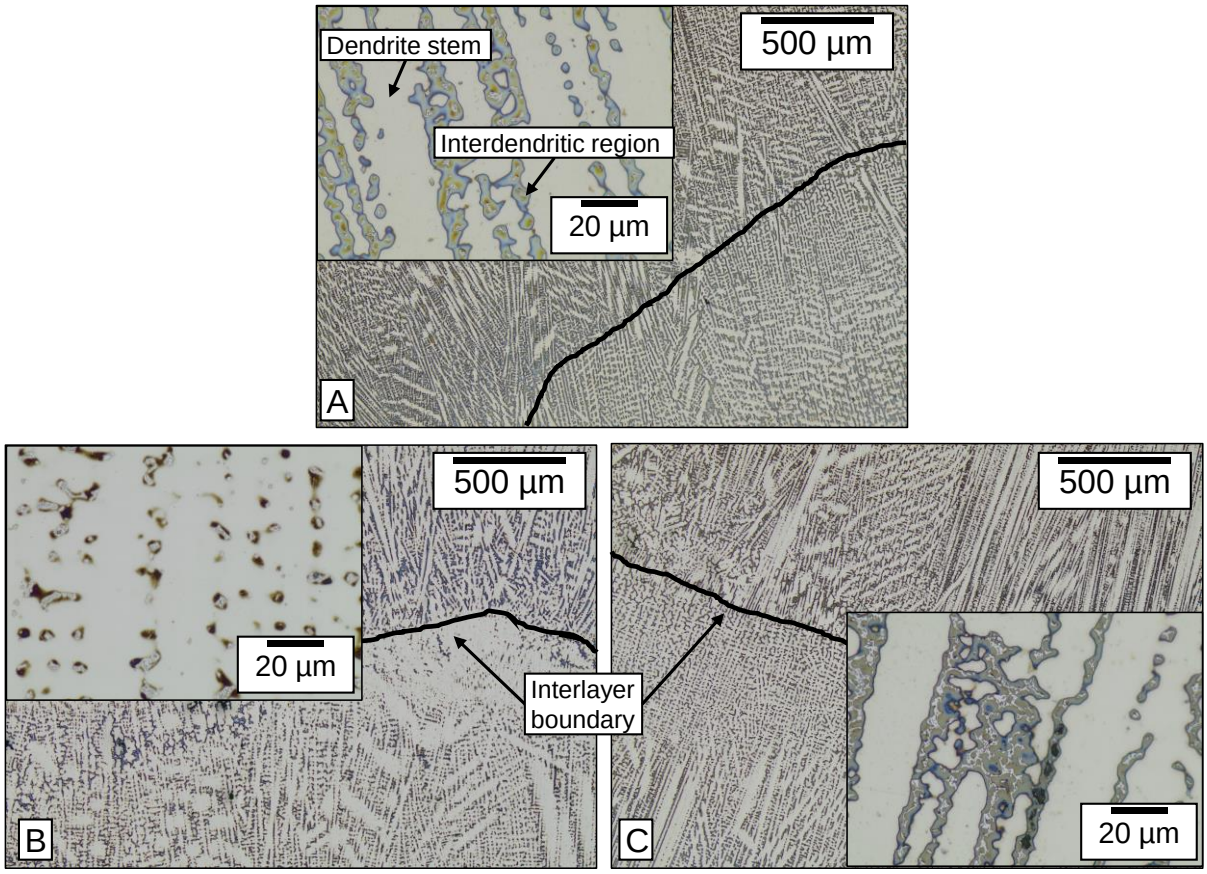

Figure 3.8 : Optical micrographs of As-Dep WAAM Inconel 718 material in the through-thickness section at locations shown in Figure 3.7.

Laves phase, along with Ti- and Nb-rich inclusions (also found in the wire feedstock described in Section 3.2.5), were found in the As-Dep microstructure. The contrast of the SEM BSE images (Figure 3.9), which is contributed by topography and elemental differences [179], show particle morphology and elemental contrast in the microstructure. Elements in the phase particles were identified from EDX spot analysis spectra. The main elements in the γ-matrix, which is represented by Area 1 in Figure 3.9, are Ni, Cr and Fe, as shown by their large peaks in the corresponding EDX spectrum. Smaller peaks were observed for Nb and Mo, as would be normally expected for IN718, whose chemical composition is detailed in Section 3.2.5.

Laves phase, appearing as light spots with island-like morphology (Spot 2 in Figure 3.9), were found to be richer in Nb and Mo than the matrix, inferred from the larger Nb and Mo peaks in Spectrum 2. These observations of Laves phase are consistent with those reported in observations of direct laser deposited IN718 [180], where the authors have confirmed the

identity of Laves phase using Transmission Electron Microscopy (TEM). The presence of Laves phase is evidence of elemental segregation caused by a high heat input and slow cooling rate [181] during WAAM deposition. The role of Laves phase in mechanical properties, and strategies to mitigate its formation are discussed in Section 3.4.1.

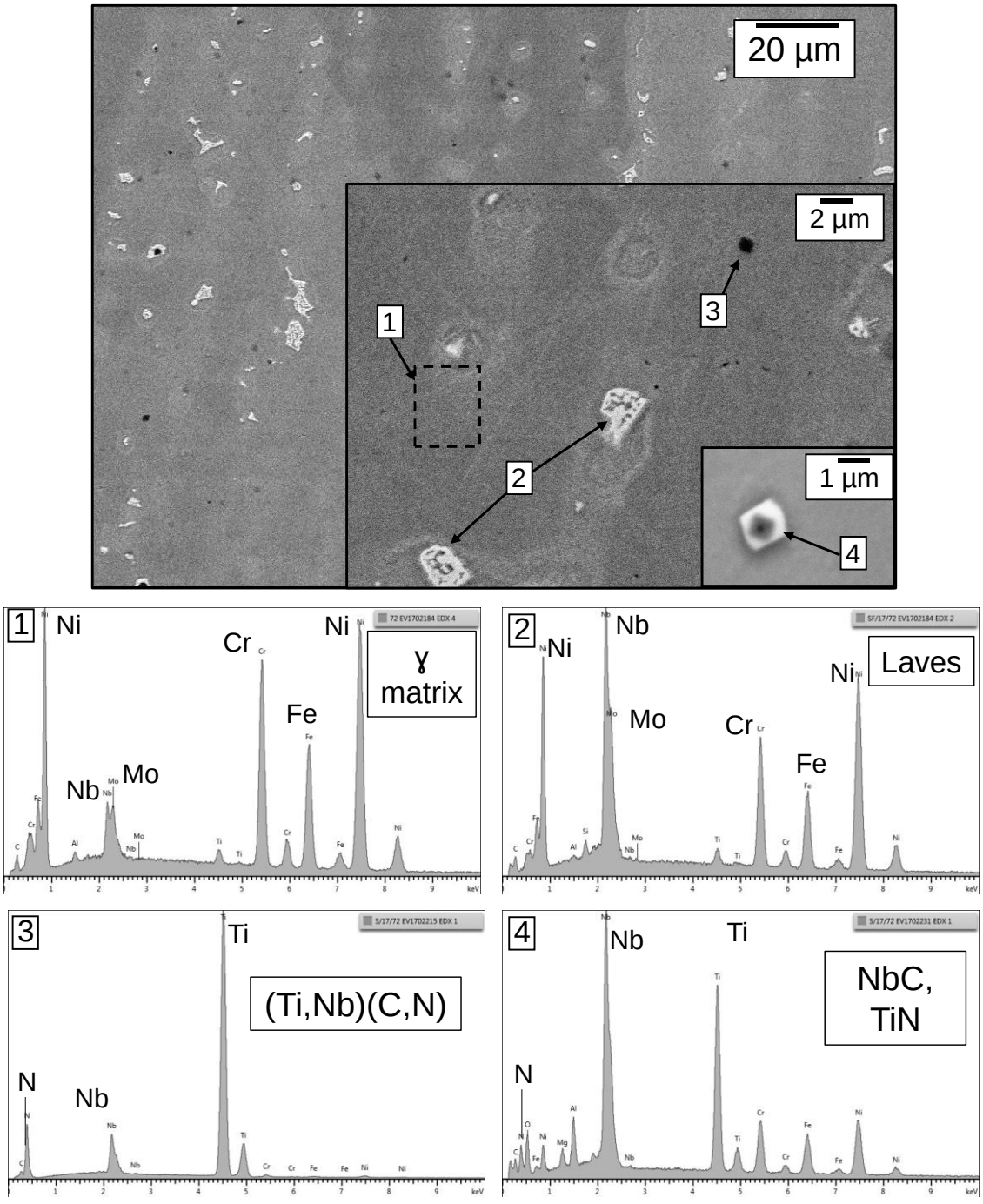

Figure 3.9: Backscatter electron images of as-Dep WAAM Inconel 718 material and corresponding EDX spectra of spot analysis.

Ti- and Nb-rich inclusions, have block-like morphology and can appear as dark or light spots (Spots 3 and 4 in Figure 3.9) depending on their proportions of Ti and Nb (dark spots are richer in Ti than Nb and vice versa). The smaller peaks in Spectra 3 and 4 are likely to have been contributed by the matrix, as the minimum spot size for EDX analysis (1 μm) is larger than the particles in Spots 3 and 4. Spot 4 in particular appears to be a Ti-rich core with a Nb-rich shell, consistent with TEM observations of similar particles in IN625 fusion welds [182], which the authors identified to be carbo-nitrides with a TiN core and NbC shell. TiN particles can act as nucleation sites for the formation of carbides like NbC [183], [184], resulting in this type of complex particles. NbC is expected in the microstructure as it forms before Laves phase in the IN718 solidification sequence [185]. In contrast, TiN is likely to have come from the wire feedstock as its melting point (2950 °C [186]) is much higher than the temperature of the melt pool, therefore remains in the solid state throughout the WAAM deposition. This type of Ti- and Nb-rich carbo-nitride has also been previously reported in various IN718 materials: WAAM [173], [82], cast ingots [187] hot-rolled bars [188], fusion welds [189] and claddings [190], indicating that these inclusions may have come from melting or thermomechanical processes commonly used to produce IN718 products.

3.3.2 Heat-treated microstructures

One purpose of the heat treatments is to dissolve Laves phase into the matrix. To this end, the starting WAAM IN718 microstructure has responded well to both the Standard HSA and Modified HA treatments, as shown by the BSE micrographs in Figure 3.10a and b respectively, which show little to no trace of Laves phase in the microstructures. Laves dissolves by diffusion of atoms into the matrix, at a rate dependent on the temperature and hold time of the homogenisation treatment [175]. Without any homogenisation treatment, the Aging only BSE micrograph (Figure 3.10c) looks more similar to that of As-Dep WAAM IN718 (Figure 3.9), with Laves phase largely unchanged. This is due to the lower temperatures in the aging treatment, which are insufficient for dissolving Laves phase into the matrix. However, the Standard HSA treatment also precipitated δ phase, whose identity has been inferred from its needle-like morphology and location at the grain boundaries, as shown in Figure 3.10a.

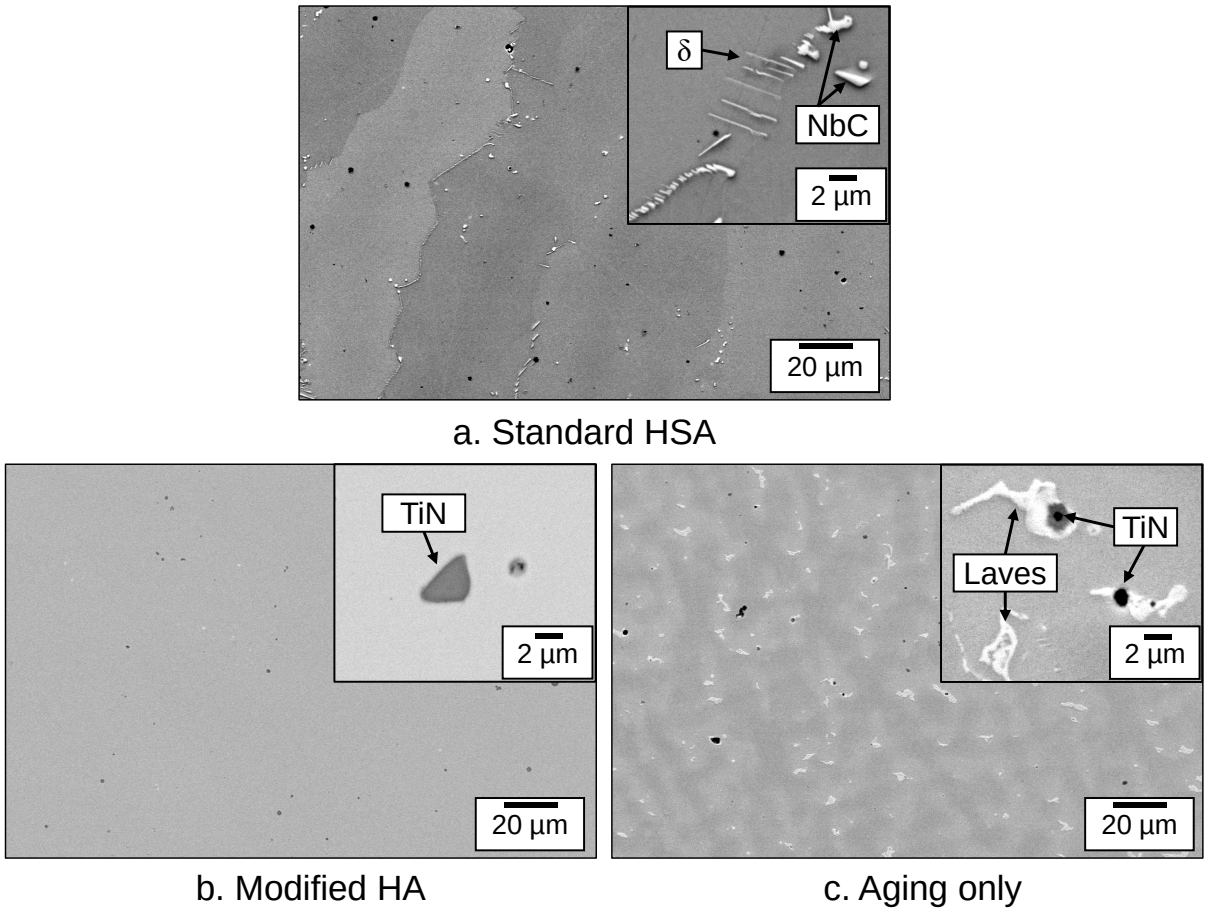

Figure 3.10: Backscatter electron images of WAAM IN718 after (a) Standard HSA, (b) Modified HA and (c) Aging only heat treatments.

Similar observations of δ phase have been made in forged IN718 by Valle et al. [191], who confirmed using TEM diffraction patterns that δ phase has a needle-like morphology, which can be clearly distinguished from spherical γ' and elliptical γ''. In wrought IN718, the precipitation of δ occurs between 860 °C to 995 °C [163] and requires Nb content of around 6-8% [192]. This implies that δ phase is likely to have precipitated during the 980 °C , 1 hr solution treatment, which has been observed in selectively laser melted IN718 [193], [194]. In addition, the dissolution of Laves phase during the homogenisation treatment may have created Nb-enriched regions in the microstructure, at which δ is more likely to precipitate. This has been previously observed in 980 °C , 1 hr solution treated WAAM IN718 (no homogenisation treatment) [82], [173], with δ phase precipitation around partially dissolved Laves phase. The acceptance of δ phase in the microstructure is dependent on several factors, which are discussed in Section 3.4.2. Ti and Nb-rich particles were found to remain in the heat-treated microstructures. Ti-rich nitrides and Nb-rich carbides are unlikely to be affected significantly by these heat treatments

as their saturation-solubility [184] and eutectic [185] temperatures are higher than the treatment temperatures.

3.3.3 Hardness and tensile properties

Another purpose of the heat treatments is to strengthen WAAM IN718 through precipitation hardening. Whilst the three heat-treated samples have undergone the same aging treatment, their response may differ due to the difference in microstructures prior to the aging treatment. Vickers hardness, which is one indication of the material's response to the aging treatment, was found to have almost doubled in the heat-treated samples (Standard HSA, Modified HA and Aging only), as summarised in Figure 3.11. This shows that the aging treatments are largely responsible for the hardening effect, which is likely to be due to the precipitation of γ" particles in the matrix. In addition, measured hardness values were relatively uniform across the build height in all four samples (Figure 3.11).

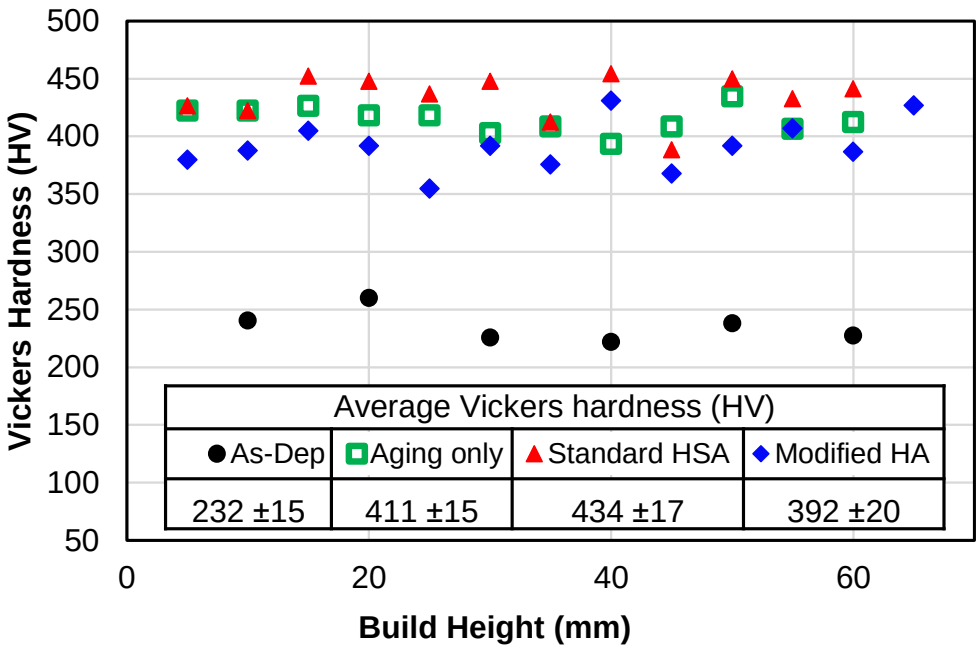

Figure 3.11: Vickers hardness of WAAM IN718 with increasing build height and a summary of the average and standard deviation.

Amongst the heat-treated samples there is a small variation in Vickers hardness values. The hardest at 434 HV is the Standard HSA sample, followed by Aging only at 411 HV, and the lowest is Modified HA at 392 HV. From the microstructures described in Section 3.3.2, the Modified

HA material would be expected to have the best response to the aging treatment due to the lack of Laves or δ phases, which diminish available Nb for γ" precipitation. However, this was not reflected in the results and one possible explanation for this is described in Section 3.3.4. The higher hardness of the Standard HSA sample than the Aging only sample suggests that despite the precipitation of δ, the dissolution of Laves phase improves the material's response to aging.

The strengthening effects from the aging treatment can also be observed in the tensile properties of the materials, shown by the stress-strain curves in Figure 3.12. The yield strength ($YS_{0.2}$), obtained using 0.2% proof stress, and ultimate tensile strength (UTS) for all three heat-treated samples are at least 250 MPa higher than that of the As-Dep samples.

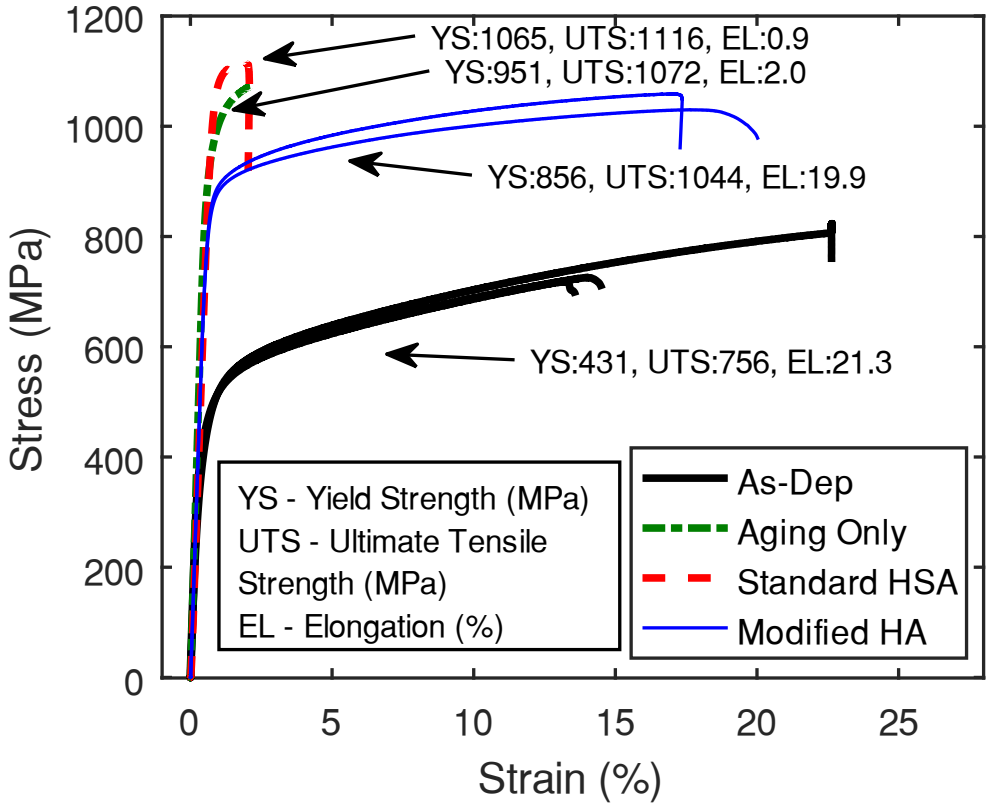

Figure 3.12: Engineering stress-strain curves from WAAM IN718 samples loaded in the build direction at room temperature.

However, the elongation (EL) of the Standard HSA and Aging only samples were just one-tenth that of the As-Dep samples. The poor elongation in the Standard HSA and Aging only samples could be due to Laves and δ phases acting as stress concentrators in the precipitation-hardened matrix. Although the As-Dep material also contains Laves phase, it is more ductile matrix may

have compensated for the stress concentration effect. Overall, the Modified HA samples showed the best combination of $YS_{0.2}$, UTS and EL.

3.3.4 Grain morphology and texture

Grains in the As-Dep sample were found to be columnar with long axis in the build direction. The grains are coarse, with length up to several mm, as shown in EBSD maps in Figure 3.13a. Columnar grain structures have also been observed in materials built from other AM processes, such as selectively laser melted IN718 [195], [196] and electron beam melted IN718 [197] and Ti-6Al-4V [65].

In the Modified HA sample, grains were found to have coarsened to more than three times the size of those in the As-Dep sample (Figure 3.13b). Grain coarsening is likely to be a result of the high homogenisation temperature used in the Modified HA treatments. The grains retain some of their previous morphology, longer in the build direction than in the other directions. Equivalent grain diameters in the TT, WA and BD directions are shown in Table 3.2. The coarse grains in the Modified HA sample could be a reason for its lower hardness, YS and UTS compared to the Standard HSA and Aging only samples, as described in Section 3.3.3.

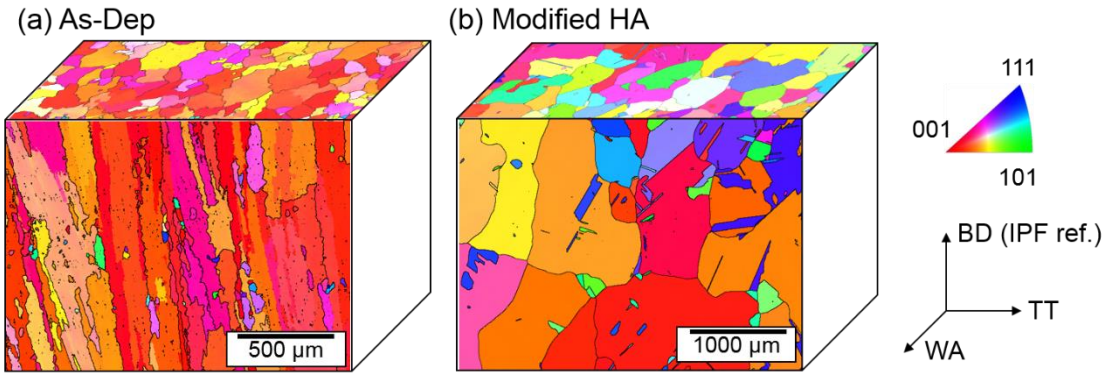

Figure 3.13: Inverse pole figure EBSD maps of (a) As-Dep and (b) Modified HA materials, with IPF colouring reference in BD showing high angle (>15°) grain boundaries.

Table 3.2: Average grain diameters for As-dep and Modified HA materials, measured using line intercept method [198].

	Average grain size (μm)	
	As-Dep	**Modified HA**
TT	76.9 ± 24.0	365.4 ± 91.8
WA	93.8 ± 29.6	297.2 ± 109.9
BD	250.0 ± 365.2	766.7 ± 200

The As-Dep material has a strong fibre texture, indicated by the colouring of the EBSD maps (Figure 3.13a) and pole figure (Figure 3.14a). The colouring of the EBSD maps shows the strong crystallographic texture of the As-Dep material, where the grains have a preferential orientation in the build direction. The pole figure shows a high intensity in the centre of the figure, indicating that most of the grains have one of their <100> directions well-aligned with the build direction. The scattered intensity along the rim of the pole figure, indicates that the grains are randomly rotated about the build direction. In contrast, the texture of the Modified HA sample is weaker than that of the As-Dep sample, shown by the more random colouring of the EBSD maps in Figure 3.13b and the scattered spots in Figure 3.14b. The intensity of the spots in the latter is likely to be due to the large grain size and limited number of grains used in the analysis.

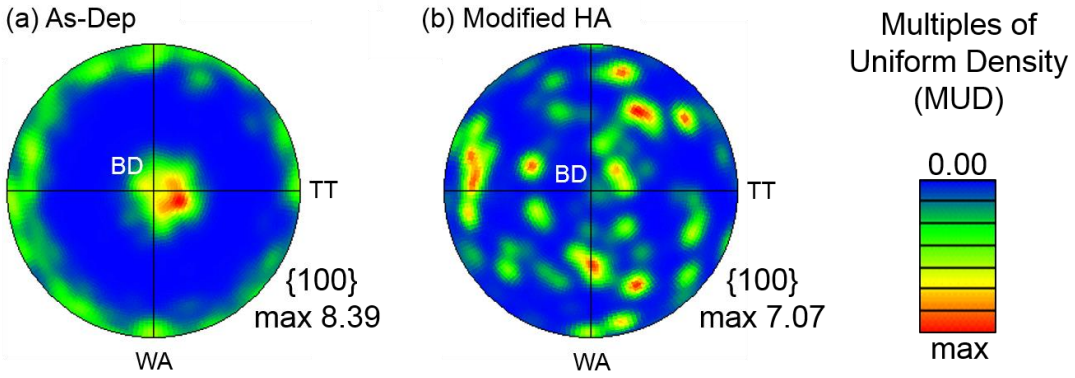

Figure 3.14: Pole figures of (a) As-Dep and (b) Modified HA materials, determined from EBSD.

3.3.5 Tensile properties

Tensile properties, from As-Dep and Modified HA materials in the build and wall axis directions, were obtained from the stress-strain curves shown in Figure 3.15 and are summarised in Table 3.3. The As-Dep material displays weak direction dependency in tensile properties at

room and elevated temperatures. Direction dependency manifests in UTS at room temperature, but in $YS_{0.2}$ at elevated temperature, both of which are higher in the build direction. These observations can be attributed to the columnar grains and fibre texture of the As-Dep material, as described in Section 3.3.4. Although the As-Dep samples displayed good ductility (EL of at least 9%) the scatter in the results are large.

The Modified HA material displays tensile properties with weak direction dependency at room temperature, and almost no direction dependency at elevated temperature. Direction dependency at room temperature manifests as higher $YS_{0.2}$ in the wall axis direction. This could be due to the elliptical grain morphology and weak texture as described in Section 3.3.4. The UTS in both directions are relatively similar. At elevated temperature, direction dependency is greatly reduced, where the average $YS_{0.2}$ and UTS in each direction differ by not more than 21 MPa. The Modified HA material is also less ductile at elevated temperature than at room temperature, indicated by the poorer elongation. The extent of anisotropy for both the As-Dep and Modified HA materials is described in Section 3.3.6. A comparison of the measured tensile properties at room temperature with those from conventional material are shown and discussed in Section 3.4.3.

Dynamic strain aging (DSA) behaviour was observed to be more extensive in the Modified HA material the As-Dep material, indicated by early onset of the serrations in the stress-strain curves shown in the insert of Figure 3.15b. DSA behaviour, which occurs when diffusing solute atoms and mobile dislocations interact, can be influenced by hardening precipitates γ'' in wrought IN718 [199], and has been observed in electron beam melted IN718 containing γ'' [200]. In addition, the unique fibre texture of the As-Dep material could also have contributed to the absence of DSA behaviour, which has been observed in laser deposited IN625 [201].

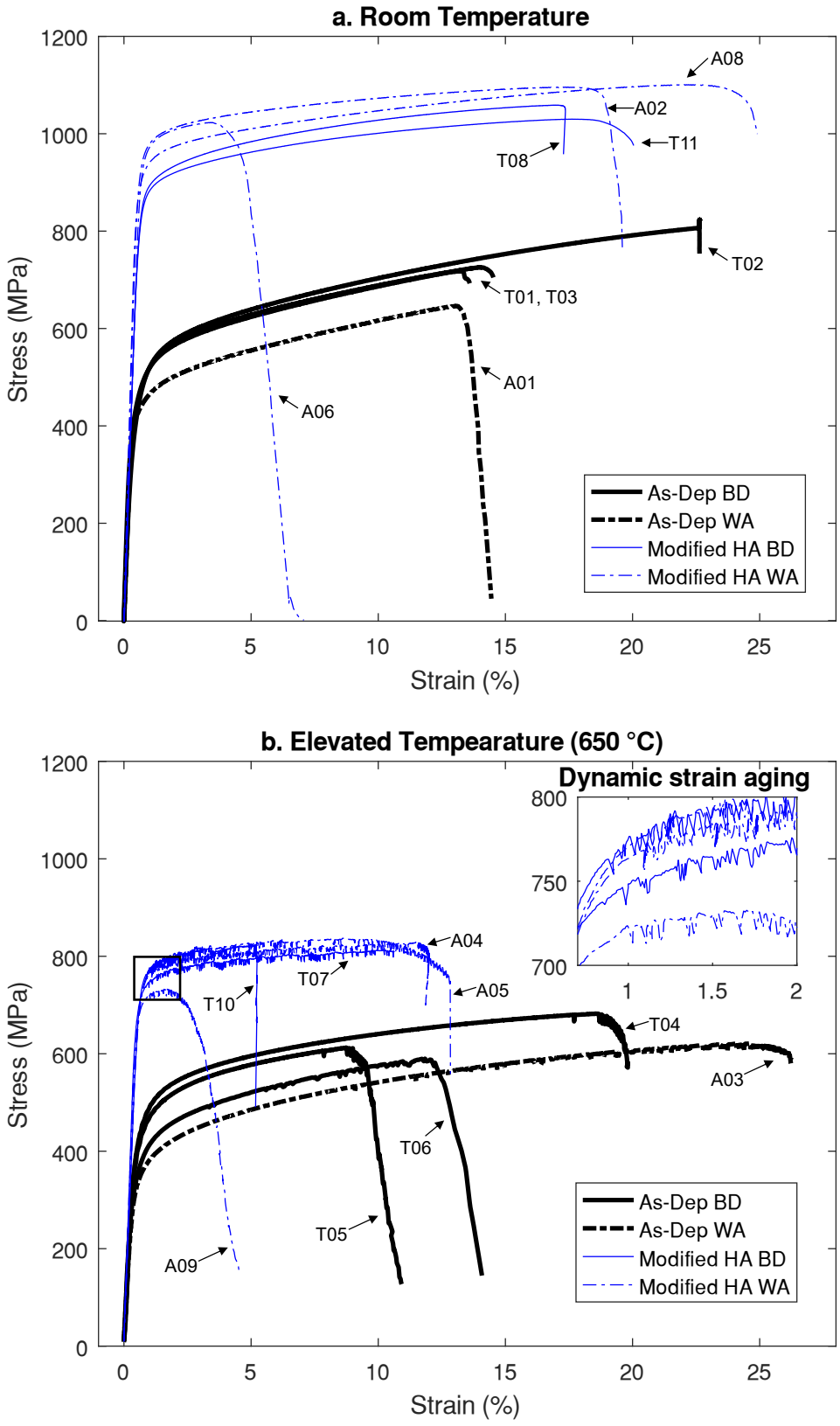

Figure 3.15: Engineering stress-strain curves of As-Dep and Modified HA tensile specimens loaded separately in the build and wall axis directions (BD and WA respectively), at (a) room and (b) elevated temperature (650 °C). See Table A.2 for specimen ID and test details.

Table 3.3: Summary of tensile properties of WAAM IN718.

	Room temperature					
	As-Dep		Aging only	Standard HSA	Modified HA	
Loading direction	BD*	WA*	BD	BD	BD	WA
UTS (MPa)	756 ± 47	646	1072	1116	1044 ± 14	1073 ± 36
$YS_{0.2}$ (MPa)	431 ± 39	421	951	1065	856 ± 6	932 ± 2
EL (%)	21.3 ± 7	17.7	2.0	0.9	19.9 ± 1	21.1 ± 8

	Elevated temperature (650 °C)			
	As-Dep		Modified HA	
Loading direction	BD	WA	BD	WA
UTS (MPa)	628 ± 39	621	821 ± 2	800 ± 51
$YS_{0.2}$ (MPa)	395 ± 38	338	734 ± 18	720 ± 21
EL (%)	9.0 ± 3	13.9	6.7 ± 3	5.9 ± 3

*BD and WA refer to build direction and wall axis respectively.

3.3.6 The extent of anisotropy

The extent of anisotropy can be represented as a ratio of the material properties in one direction over the properties in another. The further the property ratio is from 1, the more anisotropic the material is. The property ratio, R, for $YS_{0.2}$, is given by $R_{\sigma_{YS}} = \sigma_{YS_{WA}}/\sigma_{YS_{BD}}$, where σ_{YS} refers to $YS_{0.2}$ and subscripts WA and BD refer to wall axis and build direction respectively. R for YS and UTS of the As-Dep and Modified HA materials at room and elevated temperatures, is shown in Figure 3.16. For comparison, tensile properties of WAAM IN718 reported by Xu et al. [173] have also been included.

The R-values shown in Figure 3.16 are relatively close to 1, indicating that the tensile properties (YS and UTS) of WAAM IN718 material are only weakly anisotropic. The As-Dep materials displayed R-values furthest from 1, with the largest at 1.236 (As-Dep RT Wire B [173]), and smallest with 0.855 (As-Dep RT and As-Dep 650). From this, it can be concluded that the YS and UTS of As-Dep material in the wall axis direction is at least 0.85 that of the build direction. However, it must be noted that for the As-Dep RT and 650 materials, only one sample was tested in the WA direction, therefore the R-values may be influenced by material scatter. Of the heat-treated materials (i.e. Modified HA and Standard STA [173]), the Modified HA material displayed almost isotropic properties at elevated temperature, with R-values for both YS and UTS closest to 1.

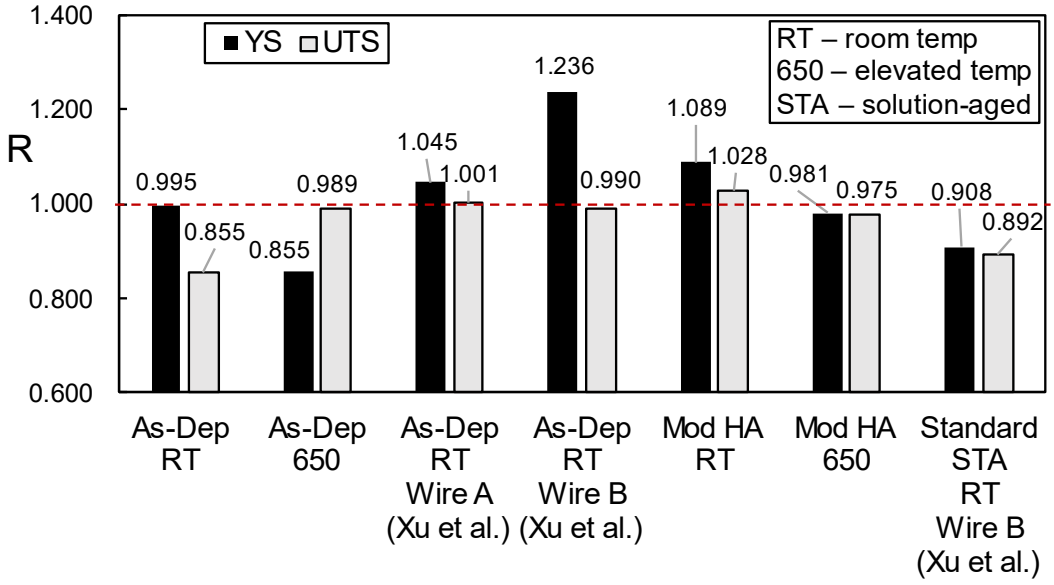

Figure 3.16: Property ratios (R) for yield strength (YS) and ultimate tensile strength (UTS) of WAAM IN718 materials from this work and reported values from Xu et al. [173]. Note that for the As-Dep RT and 650 samples, only one sample was tested in the WA direction.

3.4 Discussion

3.4.1 Laves phase mitigation

Despite the presence of Laves phase in the microstructure (as described in Section 3.3.1), the As-Dep material displayed good tensile properties comparable to equivalent conventional material (discussed in Section 3.4.3). However, poor elongation was observed in the Aging only tensile sample (reported in Section 3.3.3), which has been attributed to the embrittling effect of Laves phase within a precipitation-hardened matrix. Therefore, if WAAM IN718 material is to be used in a precipitation-hardened condition, post-deposition heat treatments should include a suitable homogenisation heat treatment to address Laves phase prior to precipitation hardening.

Further, the effectiveness of the homogenisation treatment may be dependent on the size and distribution of Laves phase in the As-Dep microstructure. As described in Section 3.3.4, the use of a high homogenisation temperature designed to address Laves phase has led to undesirable grain coarsening. Mitigating the formation of Laves phase during deposition could help in the design of homogenisation heat treatments to dissolve Laves phase without significant grain coarsening. This can be achieved by lowering the homogenisation treatment temperature and

shortening the hold time, or both. For example, Laves phase dissolution was achieved in electron beam weld fusion zones with a 980 °C , 1hr solution treatment [181] and selective laser melted samples with 1180 °C , 15 min homogenisation treatment [202], as both materials (in the as-welded/as-deposited condition) had finer and more sparsely distributed Laves phase than As-Dep WAAM IN718 material. In addition, partial dissolution of Laves phase was achieved in laser powder fed additively manufactured IN718 [203] with 1050 °C , 15 min homogenisation treatments, which changed the morphology of Laves from long striped to granular, thereby improving the tensile properties of the material.

Although it is difficult to monitor and control the thermal conditions during deposition, strategies have been adopted in welding to mitigate the formation of Laves phase. In arc welding, the use of pulsed as opposed to continuous current sources have been found to produce weld fusion zones with smaller and less densely distributed Laves phase particles [204], [192], due to decreased heat input. Further, increasing weld cooling rates have been shown to decrease the segregation of Nb in the weld fusion zone [205]. Adopting these techniques in WAAM may help in minimising the formation of Laves phase in the as-deposited microstrucure.

3.4.2 Role of δ phase in ductility

It has been assumed that the presence of δ phase in a precipitation-hardened matrix was largely responsible for poor elongation in the Standard HSA sample (reported in Section 3.3.3). The possibility of poor elongation being caused by other factors such as defects is small, as all other tensile samples with loading axis in the build direction (except the Aging only sample, discussed in Section 3.4.1), displayed elongation above 5%. Nonetheless, the effect of δ phase on mechanical properties is largely debated in the literature and is often discussed in the context of hot working formability [206], [207], where ductility prior to precipitation hardening is of more interest. It is generally accepted that large amounts of δ phase depletes the matrix of Nb for γ" precipitation, which results in decrease in strength. However, in the range of 0.3 to 1.4 % volume fraction, δ phase has been found to have no effect on the yield and ultimate tensile strength, but decreased ductility by up to 10% in precipitation-hardened IN718 [191]. Apart from tensile properties, δ phase also has effects on stress rupture and creep properties. In wrought IN718 samples without δ phase, the stress rupture life and creep elongation to failure was found to be twice and four to five times those containing δ phase [208]. Whilst it is specified in AMS5662 [165] that the presence of Laves phase within the microstructure is not acceptable, that of δ depends on specific requirements. Owing to the complex effects of δ phase on

mechanical properties, heat treatment strategies for WAAM IN718 material should be designed with careful consideration of the effects of δ phase.

3.4.3 Grain structure – tensile property relationship

Despite the columnar and elliptical grain morphology of the As-Dep and Modified HA materials (described in Section 3.3.4), the tensile properties of both materials (Section 3.3.5) do not appear to be significantly direction dependent. Although this observation has been reported in another study [173] of WAAM IN718 material, the reasons behind this observation remain unclear. For the As-Dep material, it would be expected that both the grain shape and fibre texture would contribute to anisotropic tensile properties. For the Modified HA material, contributions from the elliptical grain shape would be expected to be higher given the reduced texture. Nonetheless, the property ratios for both the As-Dep and Modified HA materials as described in Section 3.3.6 were found to be close to 1, indicating that the relationship between grain structure and tensile properties is indirect.

3.4.4 Tensile fracture surface morphology

Ductile fracture was observed to be the main failure mechanism of the As-Dep and Modified HA tensile samples, which is consistent with the observed tensile properties described in Section 3.3.5. This is evidenced by the dimples observed on the fracture surfaces of the samples, shown in Figure 3.17a, which are characteristic of microvoid coalescence. The As-Dep and Modified HA samples tested at both room and elevated temperatures, displayed similar dimple morphology at high magnification. Particles within the dimples were found to be rich in Nb. Given their size (~1 μm), they are likely to be either Nb-rich carbides or Laves phase (for the As-Dep material). At a lower magnification, a difference in dimple patterns was observed between the samples loaded in the wall axis and build directions, as shown in Figure 3.17b and c. The former displays dimples neatly arranged in rows much like the interdendritic patterns shown in Figure 3.8b, whereas the latter displays dimples in a random pattern. This implies that microvoids have initiated at inhomogeneities in the microstructure, such as carbides, nitrides and Laves phase, as described in Section 3.3.1. As these inhomogeneities tend to form in the interdendritic region, their distribution probably resulted in the patterns observed in in Figure 3.17b,c and may be a contributing factor to the weakly anisotropic tensile properties of WAAM materials.

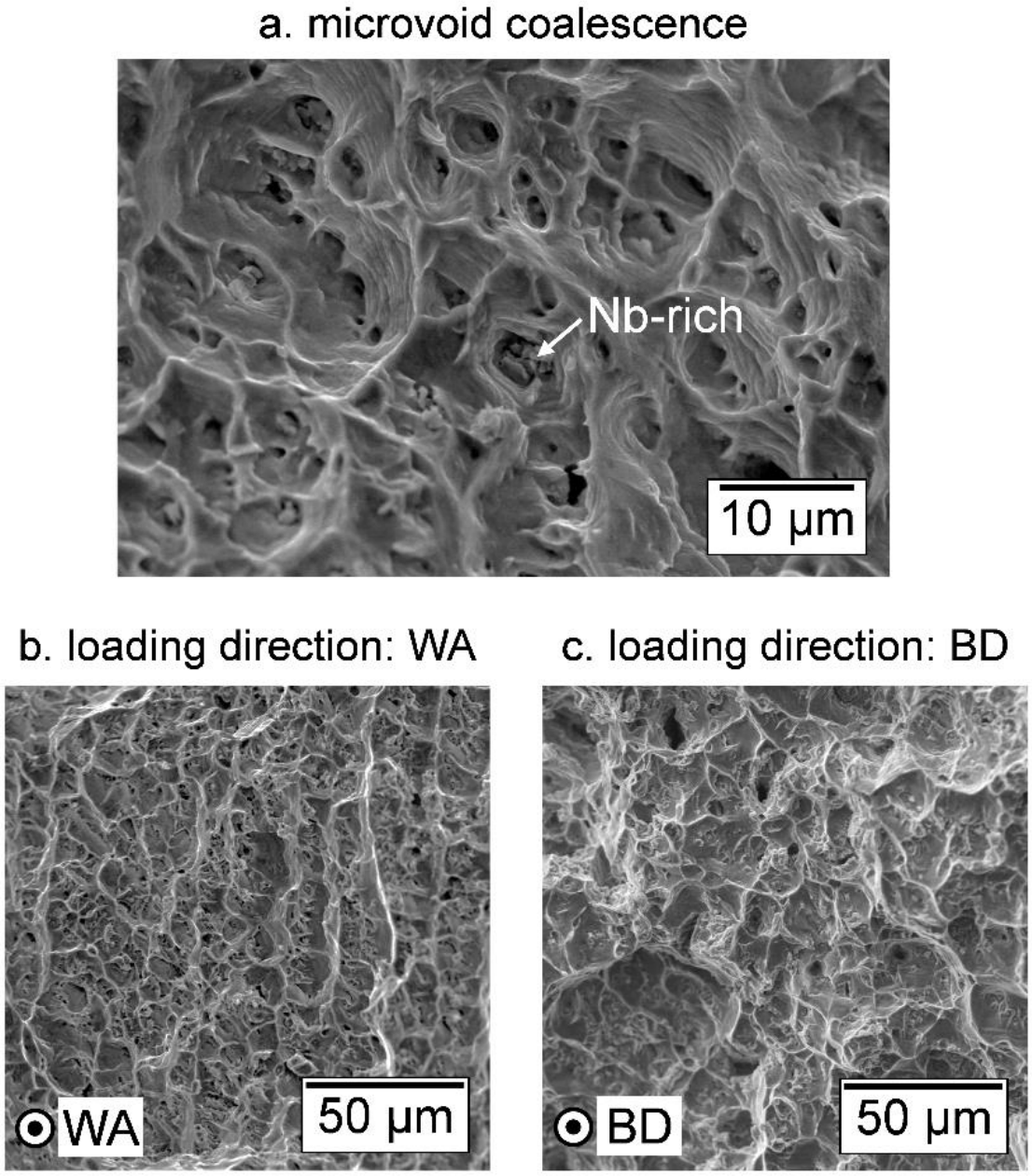

Figure 3.17: Secondary electron images of fracture surfaces from tested tensile specimens (stress strain curves in Figure 3.15), showing (a) dimples indicating microvoid coalescence characteristic of ductile fracture, and differences in dimple patterns observed in fracture surfaces normal to (b) wall axis and (c) build directions.

3.4.5 Comparison of tensile properties with conventional materials

The overall tensile performance of WAAM IN718 can be judged by comparison with conventional material. For the As-Dep material, a reasonable comparison would be all-weld-

metal properties in the as-welded condition, and for the Modified HA material, precipitation hardened cast (AMS 5383 [164]) and wrought (AMS 5662 [165]) materials. The respective tensile properties are shown in Table 3.4.

Table 3.4: Comparison of tensile properties with equivalent conventional materials.

	Room temperature				
Condition	**As-Dep[a]**	**As-welded[b]**	**Modified HA[a]**	**Cast[c]**	**Wrought[d]**
UTS (MPa)	729 ± 63	833	1062 ± 32	827	1241
$YS_{0.2}$ (MPa)	430 ± 6	565	901 ± 41	724	1034
EL (%)	20.4 ± 6	28	20.7 ± 7	3	12

	Elevated (650 °C) temperature			
Condition	**As-Dep[a]**	**Modified HA[a]**	**Cast[e]**	**Wrought[d]**
UTS (MPa)	627 ± 34	808 ± 38	576	1000
$YS_{0.2}$ (MPa)	381 ± 41	726 ± 20	517	862
EL (%)	10.2 ± 3	6.2 ± 3	13.7	12

[a] Average of 4-5 tensile samples from both BD and WA directions.

[b] Reported values from tests of samples from manual gas tungsten arc process welded plates [209].

Minimum values specified in [c]AMS 5383 [164] Table 3 and [d]AMS 5662 [165] Table 2B and 3B.

[e] Reported results [210] from tests of castings homogenised at 1200 °C, 48 h followed by standard solution aging treatments.

At room temperature, the As-Dep material is weaker and less ductile than as-welded IN718, likely due to the coarser grains and more extensive Laves phase distribution in the former. The Modified HA material exceed the minimum specifications for cast IN718, not that of wrought IN718. One contribution to the inferior YS and UTS of the Modified HA material is its large grain size (described in Section 3.3.4) as compared to the maximum grain size allowable in AMS 5662 [165] (ASTM 2). At elevated temperature, tensile properties of the Modified HA material do not meet the minimum specified for wrought IN718. As AMS 5383 [164] does not specify minimum tensile properties for elevated temperatures, reported results from IN718 castings [210] were used instead for comparison. The YS and UTS of the Modified HA material exceeded that of the castings, but EL did not.

Considering that IN718 is most commonly used at elevated temperatures, the tensile properties of WAAM IN718 material are insufficient to replace conventional wrought material like for like. Whilst post-deposition heat treatments can improve the tensile properties from the As-Dep

condition, the properties after a Modified HA treatment remain lower than the minimum specifications for wrought IN718. Although there is potential in optimising the temperature and hold time of the post-deposition homogenisation treatment to achieve finer grains which may improve tensile properties, the As-Dep microstructure provides an unfavourable starting point for improvement of mechanical properties through post-deposition heat treatments to the same level as conventional wrought material. Nonetheless, post-deposition heat treatments are crucial in optimising the mechanical properties of WAAM IN718 material.

3.5 Conclusions

The following conclusions can be drawn from this work:

1. As-deposited Wire + Arc Additive Manufactured IN718 material has a dendritic microstructure containing Laves phase, Ti- and Nb-rich inclusions. The presence of Laves phase provides evidence for the occurrence of micro-segregation during the deposition process.
2. A standard aging treatment does not dissolve Laves phase into solid solution. A standard homogenisation and solution treatment dissolves Laves phase, but precipitates acicular δ phase at the grain boundaries. A modified homogenisation treatment was found to achieve dissolution of Laves phase without precipitating δ. Ti-and Nb-rich inclusions seem to be largely unaffected by the heat treatments.
3. The as-deposited material has columnar grains with long axis in the build direction and displays a fibre texture, where the <100> direction is preferentially aligned with the build direction. The grain size of modified homogenised and aged material is almost three times larger than in the as-deposited state and displays a weaker texture.
4. As-deposited WAAM IN718 displays weakly anisotropic properties at room and elevated temperatures. The yield and ultimate tensile strength measured perpendicular to the build direction are at least 0.85 of that parallel to the build direction. Modified homogenised and aged WAAM IN718 material displays weakly anisotropic properties at room temperature, but almost isotropic tensile properties at elevated temperature.

Chapter 4 Crack-like defects in WAAM Alloy 718 and their effects on fracture toughness

This chapter describes the characteristics of crack-like defects, which can form in WAAM Alloy 718 under unfavourable deposition conditions. These defects have hot cracking characteristics and result in "semi-stable" crack extension during fracture testing. Toughness values were found to be direction dependent and have been attributed to interaction of the main crack with defects, which was observed through X-ray computed tomography on post-test fracture samples.

This chapter is based on the following publication:

Seow C E, Zhang J, Coules H E, Wu G, Jones C, et al. (2020) 'Effect of crack-like defects on the fracture behaviour of Wire + Arc Additively Manufactured nickel-base Alloy 718', Additive Manufacturing, 36, p. 101578. doi: 10.1016/j.addma.2020.101578.

4.1 Introduction

Wire + Arc Additive Manufacturing (WAAM) is a high-deposition rate, directed energy deposition technique which can be used to build large structures of low to medium complexity [7]. In WAAM, an electric arc is used to simultaneously melt and deposit wire feedstock in a layer-by-layer manner to create a desired geometry. The resulting parts are near-net shape,

therefore requiring significantly fewer machining operations in comparison to parts manufactured by conventional methods. This provides material savings and shorter lead times, which are particularly useful for low volume production.

Several alloys can be deposited with WAAM techniques, such as steels [53], [211], [59], aluminium [70], [212], [213], titanium [114], [50], [102], [63], [47], and nickel-base superalloys [46], [171], [55], [172], [173]. Nickel-base Alloy 718 is widely used in the aerospace, nuclear, oil and gas industries, due to its high temperature strength and corrosion resistance. The use of WAAM to produce Alloy 718 components is particularly attractive to industry, due to its high raw material cost and difficulty in machining. Alloy 718 is also one of the most weldable (of the commercially available nickel-base superalloys) due to its low Al and Ti contents [214], [215], and therefore well-suited for WAAM. The deposition of Alloy 718 has been demonstrated to be viable by several authors. Baufeld [55] and Xu et al. [173] deposited single-pass walls and found that the tensile properties are higher than cast but slightly lower than that of wrought material. Seow et al. [216] reported deposition of thicker sections built using an oscillating deposition strategy, that displayed mechanical properties comparable to cast material. However, all three studies also identified that Alloy 718 is susceptible to micro-segregation during WAAM deposition, which results in microstructural inhomogeneity. Under unfavourable conditions, these can lead to various forms of cracking which may not normally occur in welding.

Severe crack-like defects have been shown to form in WAAM Alloy 718 under unfavourable deposition conditions. Clark et al. [46] reported sinuous crack-like defects in metal-inert-gas (MIG) deposits of Alloy 718. As these defects were found to occur in the overlap region between two deposition passes and did not extend into the final layer, the authors postulated that they had resulted from reheating of previously deposited layers. They also attributed the defect path to the deposited microstructure, specifically the Laves phase “micro-stringers” which formed in the interdendritic regions. Although several suggestions relating to process improvements were made, the authors did not investigate the effects of these defects on mechanical properties of the deposited metal. This is especially important in the development of the WAAM technique for the manufacture of safety critical components.

Interestingly, the occurrence of crack-like defects under unfavourable deposition conditions are not unique to WAAM Alloy 718. Chen et al. [217] reported similar defects in powder-feed laser directed energy deposited (i.e. laser metal deposition) Alloy 718, and attributed their formation to the liquation of low melting point constituents like Laves phase in the microstructure. On

the other hand, for Alloy 718 manufactured via powder bed fusion (PBF), crack-like defects are rarely reported as porosity tends to be the dominant defect type [218]. The occurrence of porosity under unfavourable deposition conditions has been demonstrated in laser based [219] and electron beam [220] PBF.

One important mechanical property that drives the design and assessment of safety critical components is fracture toughness. Usually high strength materials have lower toughness, therefore tensile properties alone are insufficient in assessing the suitability of additively manufactured materials. However, there are very few published works on fracture toughness of additively manufactured materials, and most of the published work is on powder-based methods. In a recent review paper, Lewandowski and Seifi [32] reported that although there has been extensive research on uniaxial tensile properties, there are much fewer studies on fracture-critical properties. In addition, most of these studies are on Ti-6Al-4V, and there are only very few for other alloys such as Alloy 718. Reviewing these, the authors found conflicting results from different studies, attributing them to competing contributions to toughness from microstructure- and defect-dominated effects.

There are a handful of fracture toughness studies of WAAM materials, which report results with varying levels of anisotropy. The toughness of WAAM Ti-6Al-4V, reported by Zhang et al. [107], was found to be weakly anisotropic; and comparable to that of wrought alloy of the same specimen thickness. The toughness of WAAM high strength low alloy steels, reported by Dirisu et al. [221], was found to be moderately anisotropic, owing to grain size variations in the samples with different notch orientations. Charpy impact toughness of low alloy carbon manganese steels, reported by Sridharan et al. [222], was found to be significantly lower in one build orientation. Although not thoroughly investigated, the authors attributed this to the formation of brittle zones in the microstructure, arising from differences in cooling rates for the different build orientations. The authors of all three studies attributed toughness anisotropy to microstructural effects, but none of them have rigorously investigated the contribution from defect-dominated effects to the fracture toughness results in their studies.

The importance of defect-dominated effects may sometimes be overshadowed by the prospect of eliminating defects in WAAM materials, either through process optimisation or post-deposition treatments. Often, process parameters or deposition strategies can be easily optimised to achieve good deposition. However, under some circumstances these may not be suitable and the complete elimination of defects through process optimisation becomes reliant

on trial-and-error, which may vary significantly with deposition equipment and systems. More robust ways of process optimisation require significant advances in in-process monitoring and an in-depth understanding of microstructural features that control the formation of these defects [32], which are currently only just starting to be investigated. Furthermore, whilst post-deposition treatments like hot isostatic pressing have been demonstrated to reduce defects [223] and result in higher toughness [224], careful consideration of the treatment parameters are necessary to limit undesirable microstructural changes. Such techniques also often have size limitations and will be impractical for the scale of structures that WAAM is intended for. Therefore, pre-existing defects in WAAM may not always be eliminated, and understanding their effects on fracture properties is crucial in assessing their fitness for purpose.

Therefore, the main objectives of this study are to: (i) investigate the microstructural characteristics of crack-like defects formed in WAAM Alloy 718 under unfavourable deposition conditions, (ii) assess the extent to which they form, and (iii) determine their effects on the resulting apparent fracture properties.

4.2 Methodology

4.2.1 Material manufacture

WAAM wall samples were manufactured by simultaneously melting and depositing IABCO ERNiFeCr-2 (Alloy 718 filler) wire of 1.14 mm diameter onto a 20 mm thick mild steel substrate plate, using the setup shown in in Figure 4.1a. The wire was fed through a wire guide and melted using a plasma torch powered by an EWM Tetrix 352 Synergic plasma controller. A Fanuc Arc mate 120iB robot was programmed to perform the deposition in an oscillating path about the wall axis, as illustrated in Figure 4.1b. The robotic arm, plasma torch, deposited sample and sample table were situated within an argon-filled tent. The current and wire feed speed used was 240 A and 2.2 m min^{-1} for the first 10 layers. These were gradually changed to 225 A and 3.1 m/min for the remaining layers. The travel speed of the torch was maintained at 6 mm/s throughout the build. The shielding and plasma gas flows were 8 L min^{-1} and 0.6 L min^{-1} respectively. The current and wire feed speed used was 240 A and 2.2 m/min for the first 10 layers. These parameters were demonstrated to be viable for deposition in previous work [82], [173] [216] on similar material, although they are not the optimal deposition parameters. Parameter optimisation was not conducted as part of this study. The final build dimensions are shown in Figure 4.1b.

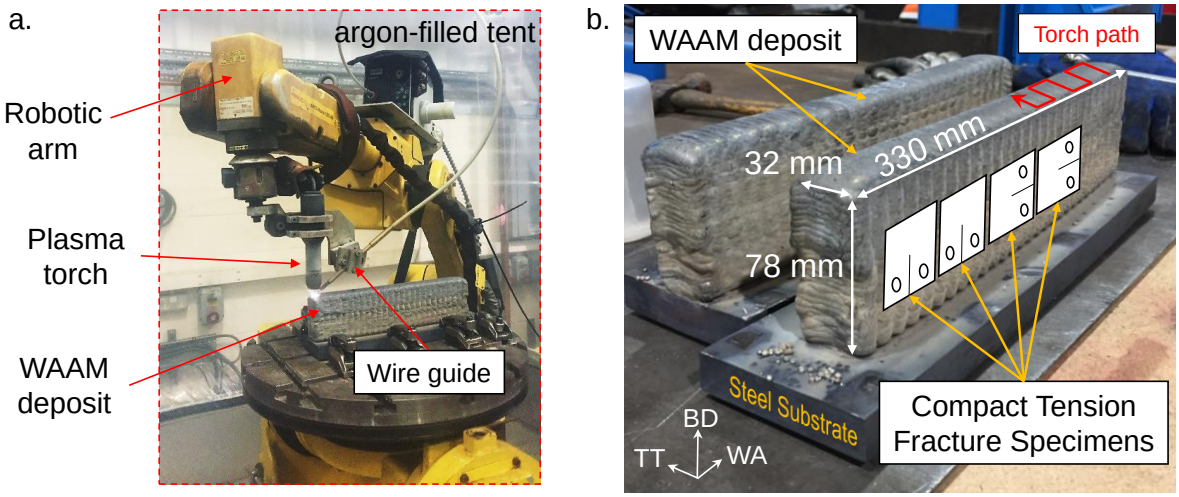

Figure 4.1: (a) WAAM equipment and (b) deposited WAAM walls with illustrations of oscillating torch path and fracture specimen extraction locations.

The chemical composition of the wire, measured using Inductively Coupled Plasma Optical Emission Spectroscopy (ICP-OES) for major elements and inert gas fusion elemental analysis for C, N and O, is shown in Table 4.1.

Table 4.1: Measured chemical composition of IABCO ERNiFeCr-2 filler metal (wt%).

	Ni	Cr	Fe	Nb	Mo	Al	Ti	C	N (ppm)	O (ppm)
IBACO ERNiFeCR-2	55.06	18.02	17.06	4.82	2.82	0.57	0.98	0.04	60	200

This composition is within the SAE International specifications for AMS5383 [164] and AMS5662 [165].

4.2.2 Defect characterisation

Crack-like defects were identified using dye penetrant inspection, conventional ultrasonic testing, digital X-ray radiography and metallographic techniques. All techniques were performed on wall slices without any post-deposition heat treatment. They were sectioned from the WAAM wall at locations where crack-like defects were the most prominent, shown in Figure 4.2. Measurements of crack-like defects were made using image analysis for both techniques.

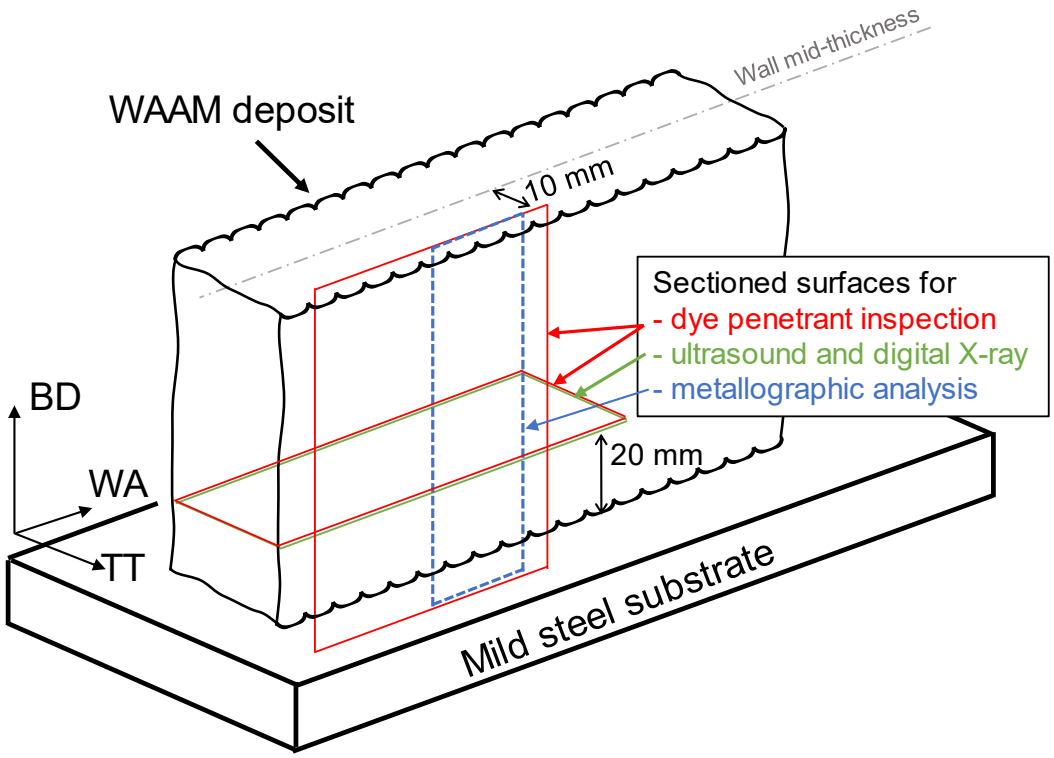

Figure 4.2: Schematic showing locations of wall sections extracted for dye penetrant inspection, ultrasonic testing and metallographic analysis.

A water-washable fluorescent dye liquid penetrant (sensitivity level 2) was applied to the surfaces of the WAAM wall sections after they were cleaned in an ultrasonic acetone bath. The walls were soaked for 30 min, then rinsed under clean running water to wash off the excess dye. A developer was applied to the surface and images were taken after 3 min.

Ultrasound measurements were taken using an ultrasonic array (manufactured by Imasonic, Besancon, France) which has 64 elements, a central frequency of 5 MHz, an element width of 0.53 mm and a pitch distance of 0.63 mm. A commercial array controller (Micropulse MP5PA, Peak NDT, Ltd., Derby, UK) was used to capture the time-domain. The captured data was then exported and processed using MATLAB (The MathWorks, Inc., Natick, MA) to generate ultrasonic total focusing images [225].

Metallographic specimens were mounted, ground and polished to 0.25 µm. Macro specimens were etched in two parts: (i) electrolytically using 20% H_2SO_4 at 3 V for 10 s for the Alloy 718 deposit, (ii) 3% nital swab for 10 s for the steel substrate. Specimens used in the Scanning Electron Microscope (SEM) were given a final polishing with colloidal silica suspension. Light micrographs were taken using an optical microscope on etched samples. A ZEISS SIGMA field

emission gun SEM was used for Energy Dispersive X-ray Spectroscopy (EDX) mapping and Electron Backscatter Diffraction (EBSD). The latter was performed with an Oxford Instruments Nordlys detector, using an accelerating voltage of 30 kV, aperture 60 µm and step size of 3.2 µm.

4.2.3 Fracture specimens

Fracture samples were heat treated using a modified homogenisation and aging heat treatment (1186 °C for 40 min, argon fast cool, 720 °C for 8 h, furnace cool and 620 °C for 8 h, air cool). This heat treatment reduces the microstructural inhomogeneity in WAAM Alloy 718 [216]. As the resulting room temperature tensile properties are weakly anisotropic, the respective direction-specific tensile properties were used in the toughness evaluation described in Section 4.3.4.

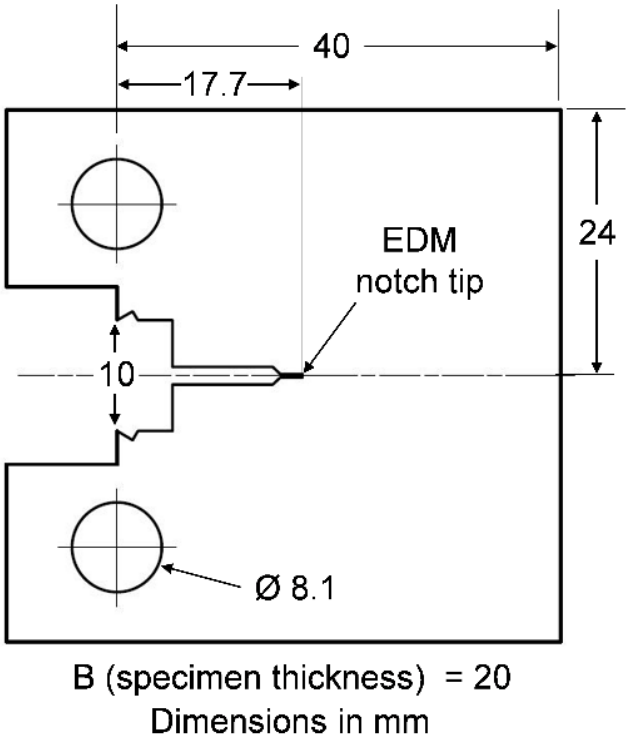

Figure 4.3: C(T) specimen machining dimensions before fatigue pre-cracking.

Compact tension (C(T)) specimens, with dimensions shown in Figure 4.3, were designed based guidelines in ASTM E1820-18ae1 [226] and ISO 12135:2016 [227], and sub-sized to optimise the number of specimens extracted per WAAM wall. A pin diameter of 8 mm was used (i.e. Ø 0.2W instead of 0.188W or 0.25W as specified the standards), to achieve a compromise between the

(i) amount of material between the integral knife edges and pin holes, and (ii) load bearing capacity of the pins. The specimens were notched in two orientations, parallel and perpendicular to the build direction (i.e. Notch // and Notch ⊥ respectively), as illustrated in Figure 4.1b. In addition, C(T) specimens with the same dimensions were extracted from wrought Alloy 718 material (NACE MR0175 [228], Ø 82.55 mm round bar, solution-treated and age hardened). The C(T) specimens were fatigue pre-cracked to a crack length of 20 mm (a_0/W = 0.5). Specimens tested with the basic procedure were plain sided, while specimens tested with the unloading compliance method were side-grooved as per ASTM E1820-18ae1 recommendations [226] (i.e. 10% thickness on each side).

4.2.4 Fracture testing

Fracture tests were carried out following the procedures outlined in ASTM E1820-18ae1 [226] and ISO 12135:2016 [227], at room temperature. Two test methods were used: the (i) basic procedure and (ii) unloading compliance resistance curve procedure. The former is typically used to obtain single-point fracture toughness values of brittle materials, while the latter is used to determine an engineering estimate of toughness at a small amount of crack extension for ductile materials. For the latter, side-grooved specimens were used. After the test, specimens were heat-tinted, broken open and their fracture surfaces were measured using optical techniques. A summary of test methods and specimens is shown in Table 4.2.

Table 4.2: Summary of fracture test methods and parameters evaluated.

Test method	Side-grooves	Toughness parameter[a]	Material	Notch orientation[b]	No. of Specimens
Basic procedure	No	J_m, J_u	WAAM	//	6
				⊥	3
			Wrought	-	6
Unloading compliance resistance curve procedure	Yes	J_m, $J_{0.2BL}$, J_Q	WAAM	//	2
				⊥	2
			Wrought	-	1

[a] for 20 mm specimen thickness

[b] with respect to the WAAM build direction (BD)

Toughness measurements were evaluated according to each specimen's response during fracture tests. However, the fracture behaviour of some WAAM C(T) specimens could not be classified as fracture instability or stable crack extension as defined in ASTM E1820-18ae1 [226]

and ISO 12135:2016 [227]. Instead, their behaviour can be described as variable decreases in load with increasing displacement, after the attainment of a maximum force, as shown in Figure 4.4. This type of behaviour is termed "semi-stable" crack extension throughout this work. Force-displacement curves from WAAM C(T) specimens tested in this work is shown in Figure 4.5.

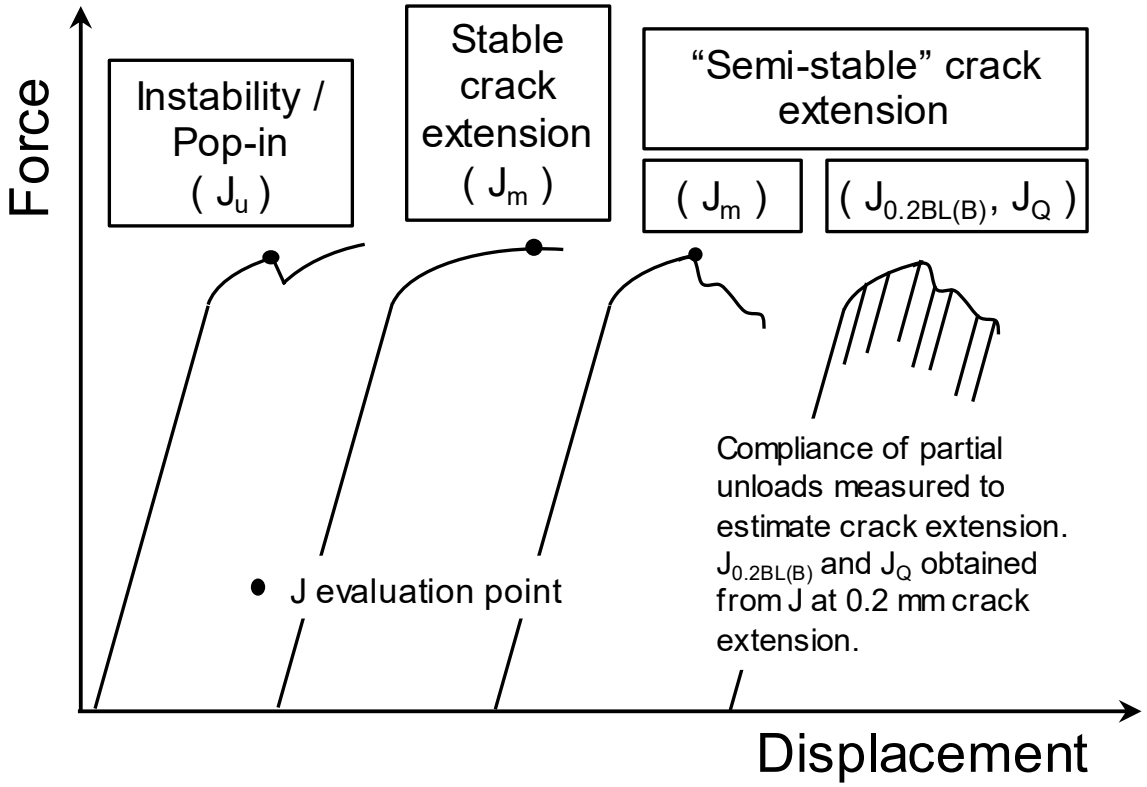

Figure 4.4: Summary of the different types of force-displacement responses from WAAM fracture tests and the corresponding J which were evaluated as per ASTM E1820-18ae1 [226] and ISO 12135:2016 [227].

Nonetheless, toughness parameters $J_{m(B)}$, $J_{0.2BL(B)}$ and J_Q were evaluated for the WAAM specimens. The significance of each of these parameters is discussed in Section 4.3.5. $J_{m(B)}$ was evaluated for specimens tested using the basic procedure and unloading compliance methods $J_{0.2BL(B)}$ and J_Q were evaluated for specimens tested using the unloading compliance method. $J_{u(B)}$ was evaluated for one specimen which displayed pop-in behaviour. The Young's Modulus, E, of WAAM Alloy 718 was assumed to be 155 GPa in both directions, based on tensile test results reported in Chapter 3. The accuracy of E and its impact on the fracture toughness results, are discussed in Section 4.3.5. A summary of toughness parameters evaluated is shown in Table 4.2.

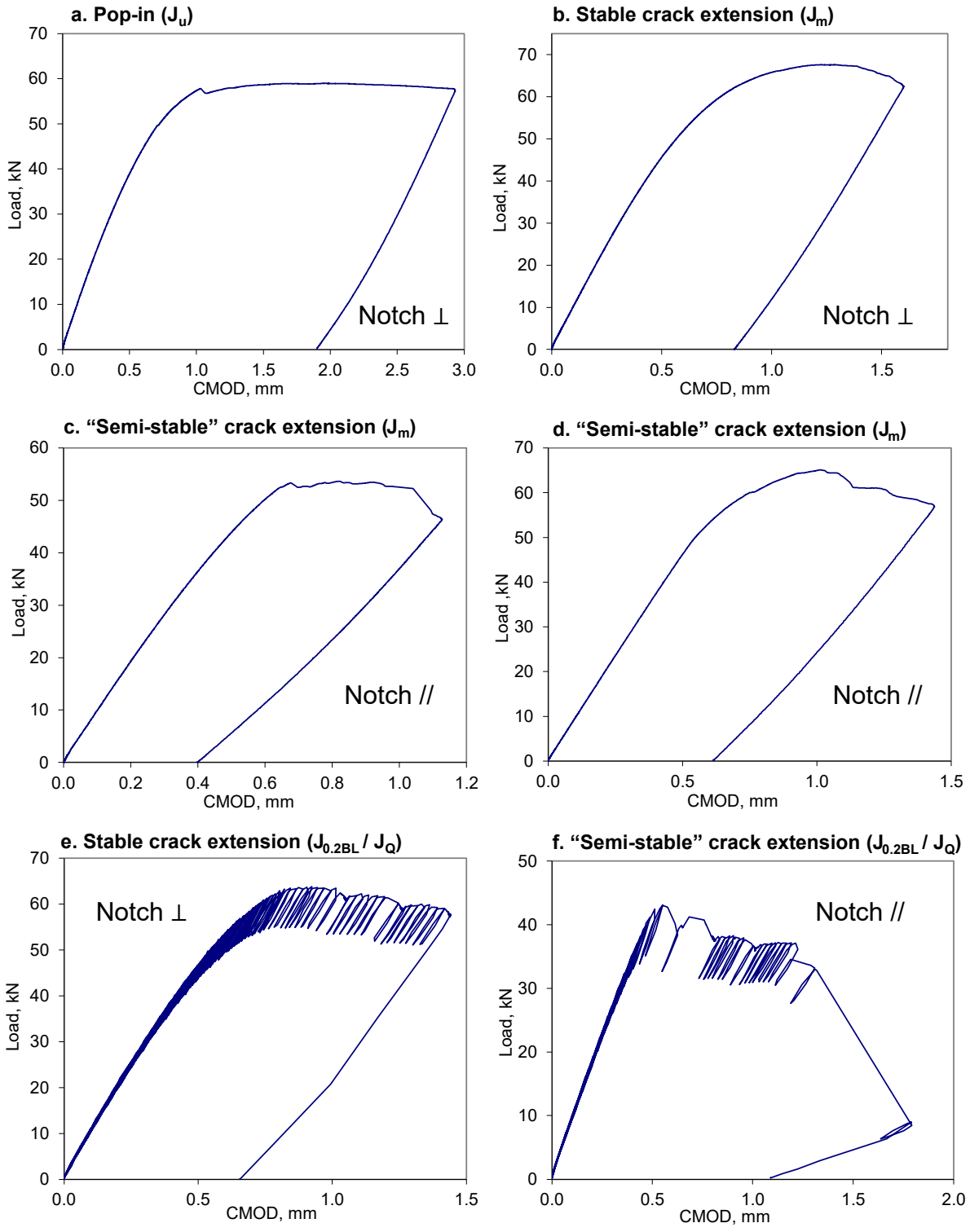

Figure 4.5: Force-displacement curves from fracture tests with WAAM C(T) specimens, showing (a) pop-in, (b) stable crack extension, (c-d) "semi-stable" crack extension, for tests using the basic procedure, and (e) stable crack extension and (f) "semi stable" crack extension, for tests using the unloading compliance procedure.

Three of five fracture samples tested using the unloading method displayed an initial decrease in compliance, leading to an apparent "negative crack extension". This has been observed in fracture tests of ductile materials, attributed to crack tip blunting [229] and specimen rotation [230]. Where apparent "negative crack extension" was observed, the vertical axis was shifted to the most negative Δa value, effectively resetting the Δa-axis. Although this method is arbitrary, it has been shown to result in the most conservative value of toughness [231]. This adjustment results in toughness values not qualified to the standards. Qualification of toughness values is discussed in Section 4.3.5.

4.2.5 Post-test analysis

Prior to being broken open, post-test C(T) specimens were scanned using X-ray computed tomography to visualise the interaction of the main crack with defects through the thickness of the C(T) specimen. Specimens were scanned using a Zeiss XRadia 520 Versa operating at 160kV, 10W, with a HE 36 filter, 15 s exposure per projection, and a 100 μm pixel size. Filtered back projection was used to reconstruct a 3D stack showing the internal structure in a non-destructive capability. From this dataset, specific tomogram slices were selected to highlight the crack propagation within the material. After the specimens were scanned, they were heat tinted and broken open. Fractured surfaces of the C(T) specimens were observed using optical techniques, SEM secondary electron imaging and EDX analysis.

4.3 Results

4.3.1 Defect morphology and location

Crack-like defects, with a planar morphology normal to the WA direction, were observed to follow a periodic pattern throughout the WAAM walls. They measure up to 16 mm in the TT direction and occur every 12 mm along the wall axis, as shown in the dye penetrant images in Figure 4.6a and b. Some defects were also observed to alternate between two TT positions, (i.e. occurring on different sides of the wall), as marked in Figure 4.6a. It is important to note that the defects are parallel to the local welding direction in single deposited layer (see illustration in Figure 4.6a). Possible reasons for the periodicity and alternating nature of the defects are discussed in Section 4.4.1. The defects measure up to 53 mm in BD, as shown in the metallographs in Figure 4.7. The stronger fluorescence from the defects Figure 4.6a can be attributed to the fact that the defects are longer in the BD direction. The defects were also found located in the centre of the weld bead, as shown in Figure 4.7, which is characteristic of weld centreline solidification cracking. The characteristics of the defects in relation to the material's microstructure are described in Section 4.3.3.

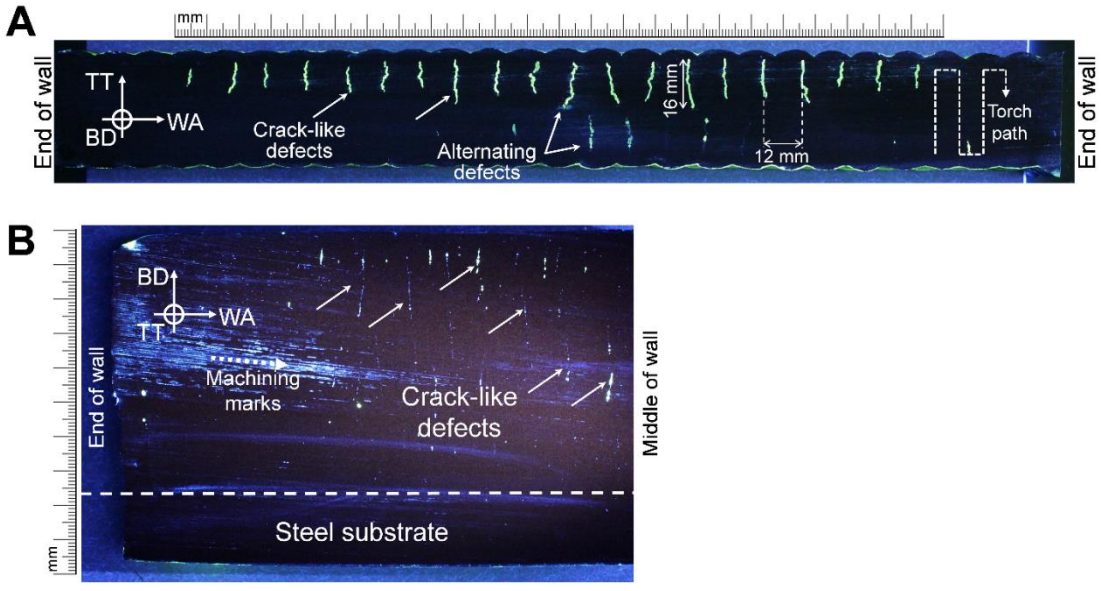

Figure 4.6: Images from fluorescent dye penetrant testing of WAAM wall sections with planes normal to the (a) build direction (BD) and (b) through thickness (TT) directions.

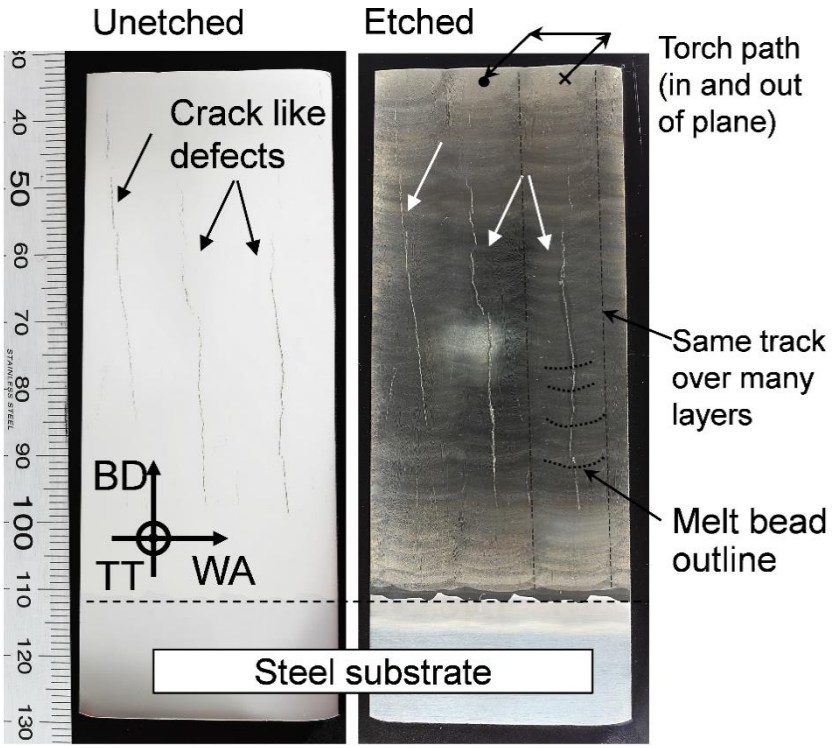

Figure 4.7: Metallographs of unetched and etched WAAM wall sections showing the length of the defects in the build direction.

4.3.2 Non-destructive detectability

The non-destructive detectability of sub-surface crack-like defects in WAAM materials is important for quality inspection purposes and crucial to the safe use of components in industry. Two techniques, ultrasound and digital X-ray radiography, were found to be viable in detecting crack-like defects in WAAM Alloy 718. Results from both techniques were found to be in good agreement with measurements from dye penetrant inspection described in Section 4.3.1.

An illustration of the ultrasound probe and WAAM material setup is shown in Figure 4.8a. For ultrasound, the main indicator of the presence of a defect is an amplitude reduction in back wall images. This indication was present in the measurement from a WAAM sample (with defects) but absent in the measurement from a wrought sample (no defects). A plot of the corresponding image amplitudes (at depth of 20 mm) is shown in Figure 4.8b. The ultrasound images from the wrought and WAAM materials (i.e. without and with defects) are shown in Figure 4.8c and d respectively. Note that the images at a depth around 20 mm is from the back

surface of the specimen. As shown, the crack-like defects disturbed the back-surface image and caused a reduction in the image amplitude at a few locations.

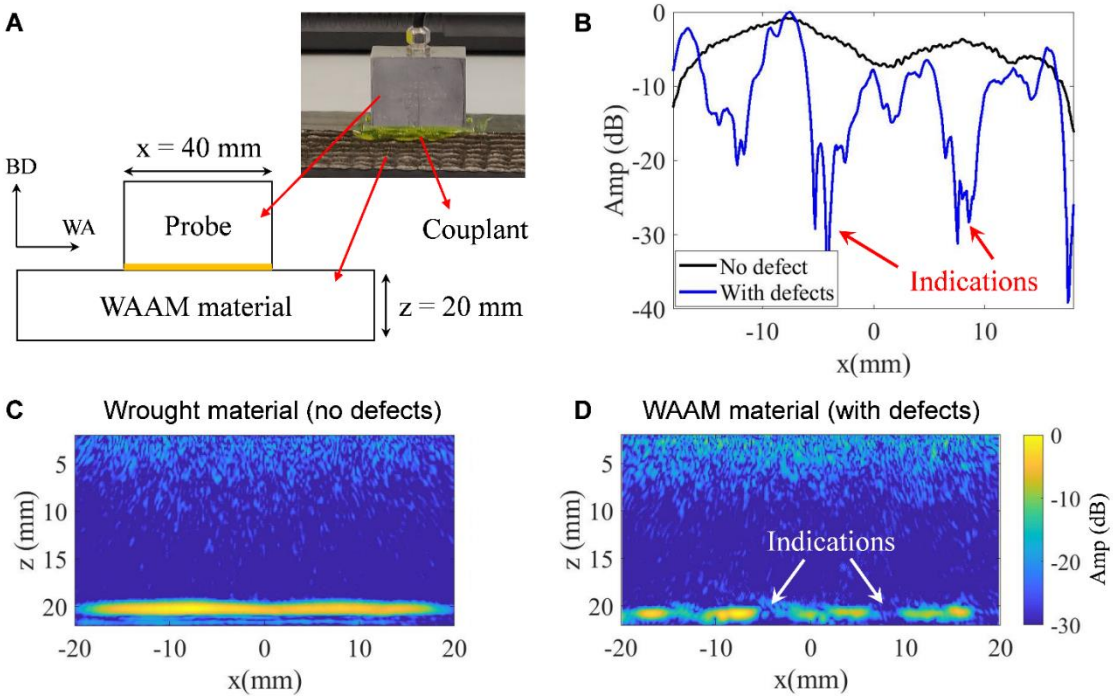

Figure 4.8: (a) Illustration of measurement probe and WAAM material setup; (b) ultrasound image amplitude distribution at depth of 20 mm and corresponding ultrasound images of (c) wrought (no defects) and (d) WAAM material (with defects).

The locations with local minimum amplitude in the blue curve indicate the positions of the crack-like defects in the WAAM material. These measurements were repeated on the WAAM slice used for dye penetrant testing. Eight consecutive measurements were made along the WA direction and the combined image amplitude at a depth of 20 mm is shown in Figure 4.9b. As shown, the separation distance between the locations with local minimum amplitude is around 12 mm, which is in good agreement with the measurements from dye penetrant testing.

For digital X-ray radiography, indications of the defects were found in the edge-filtered image. The separation distance between the indications is in good agreement with those measured from the dye penetrant image and ultrasound.

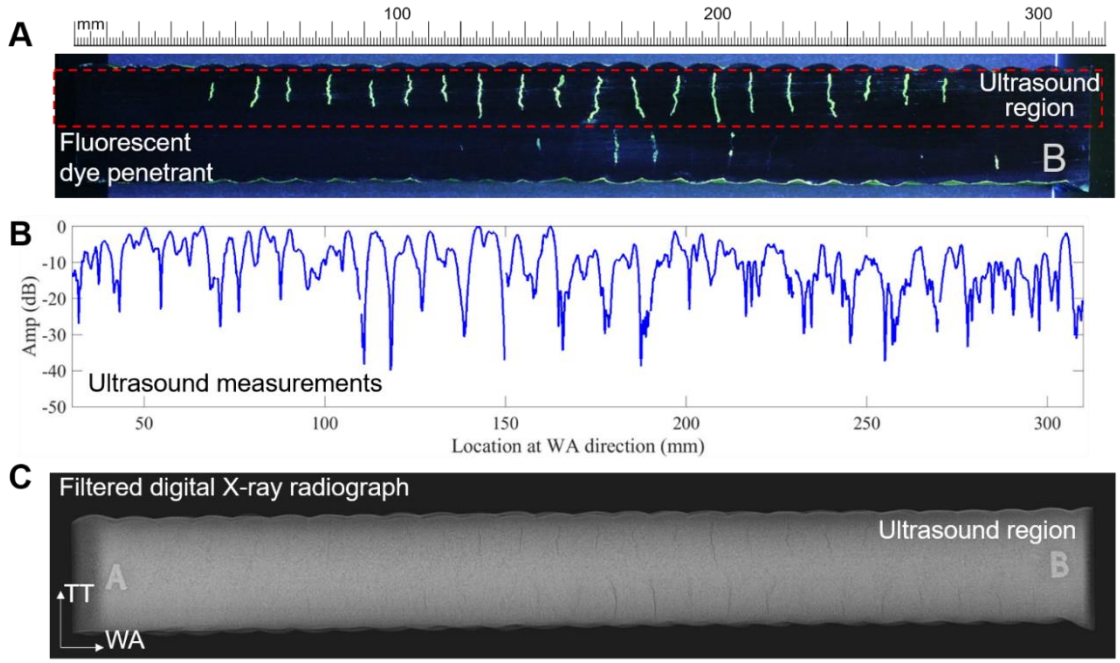

Figure 4.9: Non-destructive inspection of crack-like defects; (a) original dye penetrant inspection as shown in Figure 4.6a, corresponding (b) combined image amplitude distribution from ultrasound measurements at a depth of 20mm from 8 consecutive measurements along WA, and (c) edge-filtered digital X-ray radiograph.

4.3.3 Microstructural characteristics

WAAM Alloy 718 (with or without crack-like defects) has a unique microstructure. The material is made up of long (several mm) columnar grains with strong texture aligned with the build direction. On a sub-grain level, the microstructure can be described as dendritic, with Laves phase decorating the interdendritic regions [82], [173], [216]. The microstructure of WAAM Alloy 718 deposited under more favourable conditions are described in more detail in Chapter 3. The following paragraphs will describe the characteristics of crack-like defects in relation to these microstructural features.

The defects were observed to be intergranular, occurring along high-angle grain boundaries, as shown in the EBSD maps in Figure 4.10. It is important to note that the strong texture represented in Figure 4.10a is with reference to BD. The material has a weaker texture in the other directions (WA and TT), as represented in Figure 4.10b. This is known as fibre texture, which has been observed in WAAM Alloy 718 [216]. Figure 4.10b shows the defects occurring at high-angle grain boundaries, which are more susceptible to hot cracking [232]. In addition, intragranular misorientation, which is indicative of relative plastic strain [233], was observed in

the grains at the tips of the defects (shown in Figure 4.10b). This misorientation may have resulted from the rebalancing of strains at the defect tip, shortly after formation of the crack-like defect. The contribution of local strains to the formation of crack-like defects in WAAM is discussed in Section 4.4.1.

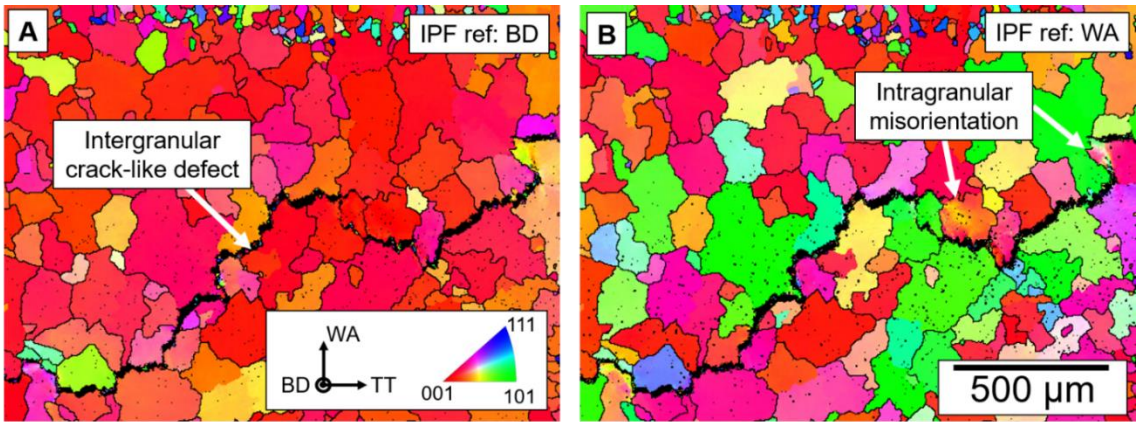

Figure 4.10: EBSD maps of crack-like defects with inverse pole figure (IPF) references in (a) build direction, showing strong texture and intergranular nature of defect; and (b) wall axis direction, showing intragranular misorientations at the tips of the defects.

On the sub-grain level, the defects were found in the interdendritic regions of the microstructure, with island-like particles lining their edges, as shown in the optical micrographs in Figure 4.11. The defects were observed to extend into these particles, and join up with microvoids in the vicinity, as shown in the backscatter electron (BSE) image in Figure 4.12a. The EDX maps in Figure 4.12b and c confirm that (i) the island-like particles are rich in Nb, characteristic of Laves phase observed in WAAM Alloy 718 [173], [216], [82]; and (ii) the dark spots in the BSE image ahead of the microfissure are microvoids and not Ti-rich inclusions. These features indicate the presence of intergranular liquid films which are characteristic of hot cracking [214]. The possible mechanisms of hot cracking in WAAM Alloy 718 are discussed in Section 4.4.1.

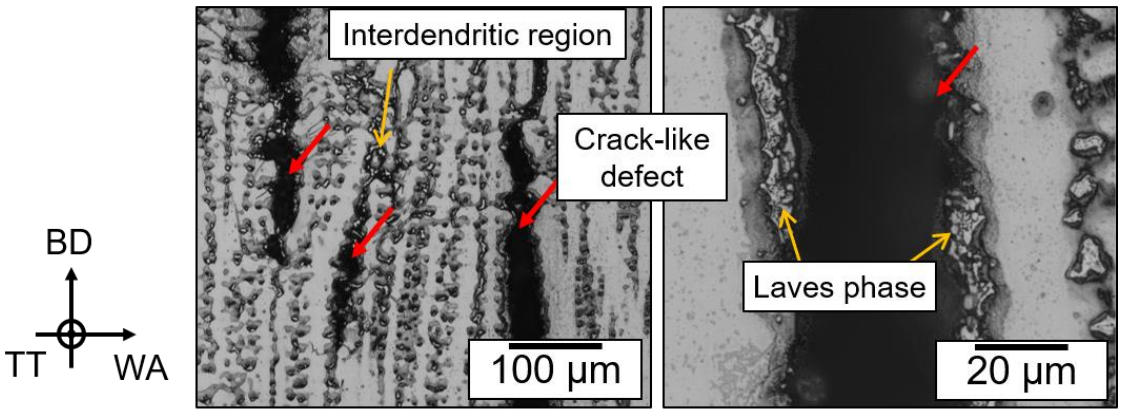

Figure 4.11: Optical micrographs of crack-like defects, showing their location in the interdendritic region, and Laves phase particles lining the edges of a defect.

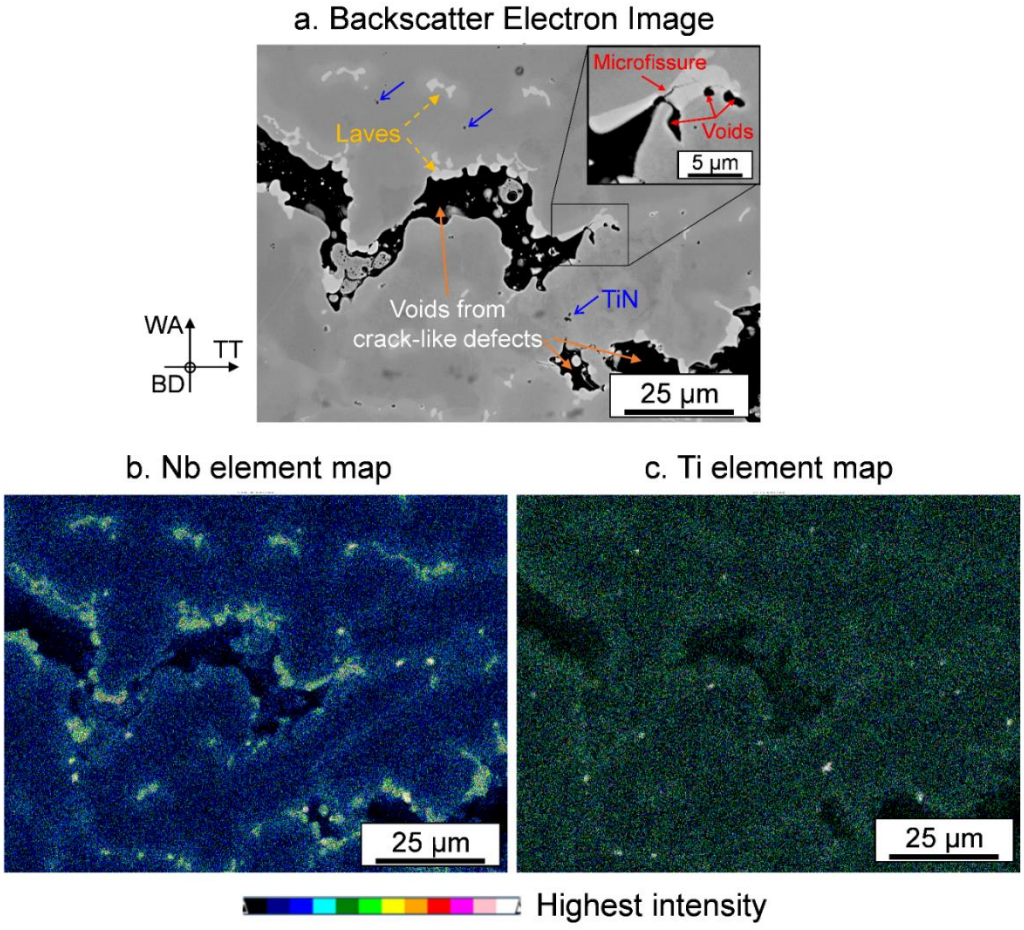

Figure 4.12: SEM images of a crack-like defect. (a) BSE image showing a defect extending into Laves phase and joining up with microvoids, (b) and (c) EDX element maps of Nb and Ti respectively.

4.3.4 Fracture toughness measurements

The fracture toughness of WAAM Alloy 718 was found to be direction dependent. $J_{m(20)}$, $J_{0.2BL(20)}$ and J_Q, of Notch ⊥ WAAM Alloy 718 were found to be higher than that of Notch // WAAM Alloy 718. The toughness measurements are plotted in Figure 4.13 and summarised in Table 4.3. The average $J_{m(20)}$, $J_{0.2BL(20)}$ and J_Q of Notch ⊥ WAAM Alloy 718 were found to be 160, 84 and 101 kJ m^{-2} respectively higher than that of Notch // WAAM Alloy 718. One contributing factor to this direction dependency in toughness is the interaction of crack-like defects with the main crack in the fracture specimens. As the crack-like defects have a plane normal to the WA direction, they are plane parallel and plane perpendicular to the main crack in the Notch // and Notch ⊥ specimens respectively. The directionality of the crack-like defects with respect to the notch orientation was observed in the fracture surface and X-ray computed tomography slices of the fracture specimens, shown in Section 4.3.6. Other contributing factors to the direction dependency of toughness are discussed in Section 4.4.4.

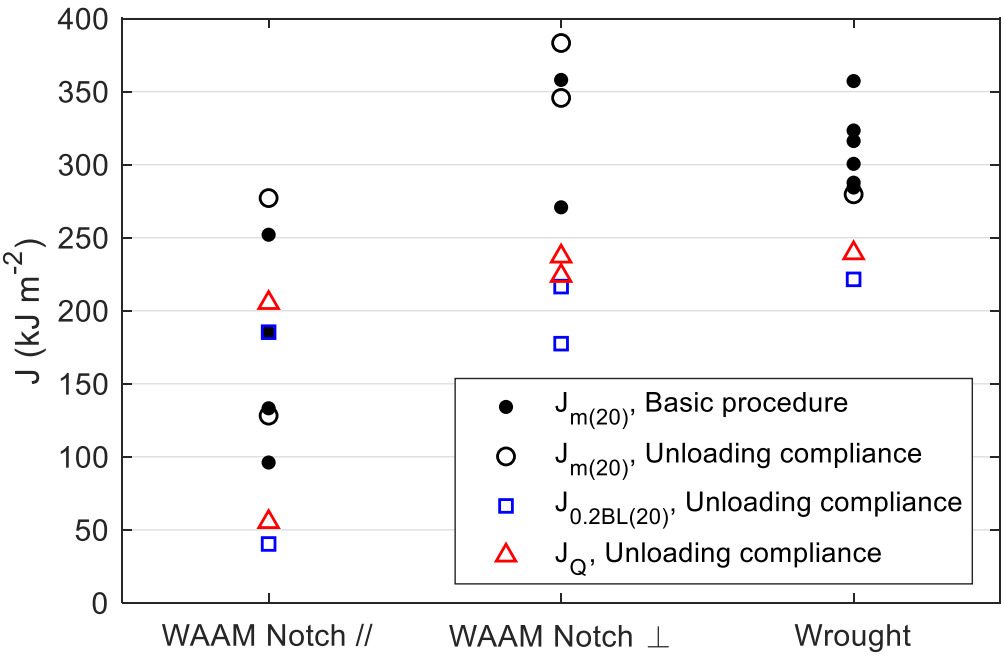

Figure 4.13: Toughness measurements of WAAM Alloy 718 and wrought specimens. Notch orientations as indicated with respect to the build direction.

The toughness of Notch ⊥ WAAM Alloy 718 was found to be comparable to that of wrought Alloy 718. The average $J_{m(20)}$, $J_{0.2BL(20)}$ and J_Q for Notch ⊥ WAAM Alloy 718, are 110 %, 89 % and 97 % that of wrought Alloy 718. In contrast, the average $J_{m(20)}$, $J_{0.2BL(20)}$ and J_Q of Notch // WAAM Alloy 718 are just 58 %, 51 % and 54 % that of wrought Alloy 718. The higher apparent toughness displayed by Notch ⊥ WAAM Alloy 718 can be attributed to crack branching effects caused by interactions between the crack-like defects and the main crack. This interaction is discussed in Section 4.3.6.

Across all specimens, measures of $J_{m(20)}$ are higher than those of $J_{0.2BL(20)}$ and J_Q. This is expected as $J_{m(20)}$ represents the toughness at the attainment of maximum load, whereas $J_{0.2BL(20)}$ and J_Q represent the toughness at 0.2 mm crack extension, which typically occurs before the specimen attains maximum load. One WAAM Notch ⊥ specimen displayed pop-in behaviour and the corresponding J_u is 221 kJ m^{-2}, which is comparable to measures of $J_{0.2BL(20)}$ and J_Q of the other Notch ⊥ specimens.

Table 4.3: Summary of toughness measurements for B = 20 mm (kJ m^{-2}).

Material	$J_{m(20)}$	%*	$J_{0.2BL(20)}$	%*	J_Q	%*	$J_{u(20)}$
WAAM Notch //	179 ± 73	58	113 ± 103	51	130 ± 106	54	-
WAAM Notch ⊥	339 ± 48	110	197 ± 28	89	231 ± 9	97	221
Wrought	307 ± 28	100	221	100	239	100	-

Note: values listed here refer to the mean and standard deviation of measurements, where applicable.

* percentage of respective wrought properties

The WAAM and wrought specimens displayed rising resistance curves, which is characteristic of ductile materials [234]. Example resistance curves for each material type and notch orientation are shown in Figure 4.14. Although the corresponding $J_{0.2BL(B)}$ values for the three specimens are similar, they display different resistance curve parameters. The WAAM Notch ⊥ specimen (Figure 4.14b) has a positive vertical intercept and the highest power coefficient. This indicates that the Notch ⊥ specimen displays the most toughening characteristics with increasing crack extension. In contrast, the WAAM Notch // specimen has a large negative vertical intercept and a power coefficient almost equal to zero. The wrought specimen has resistance curve parameters in-between those of the Notch // and Notch ⊥ specimens.

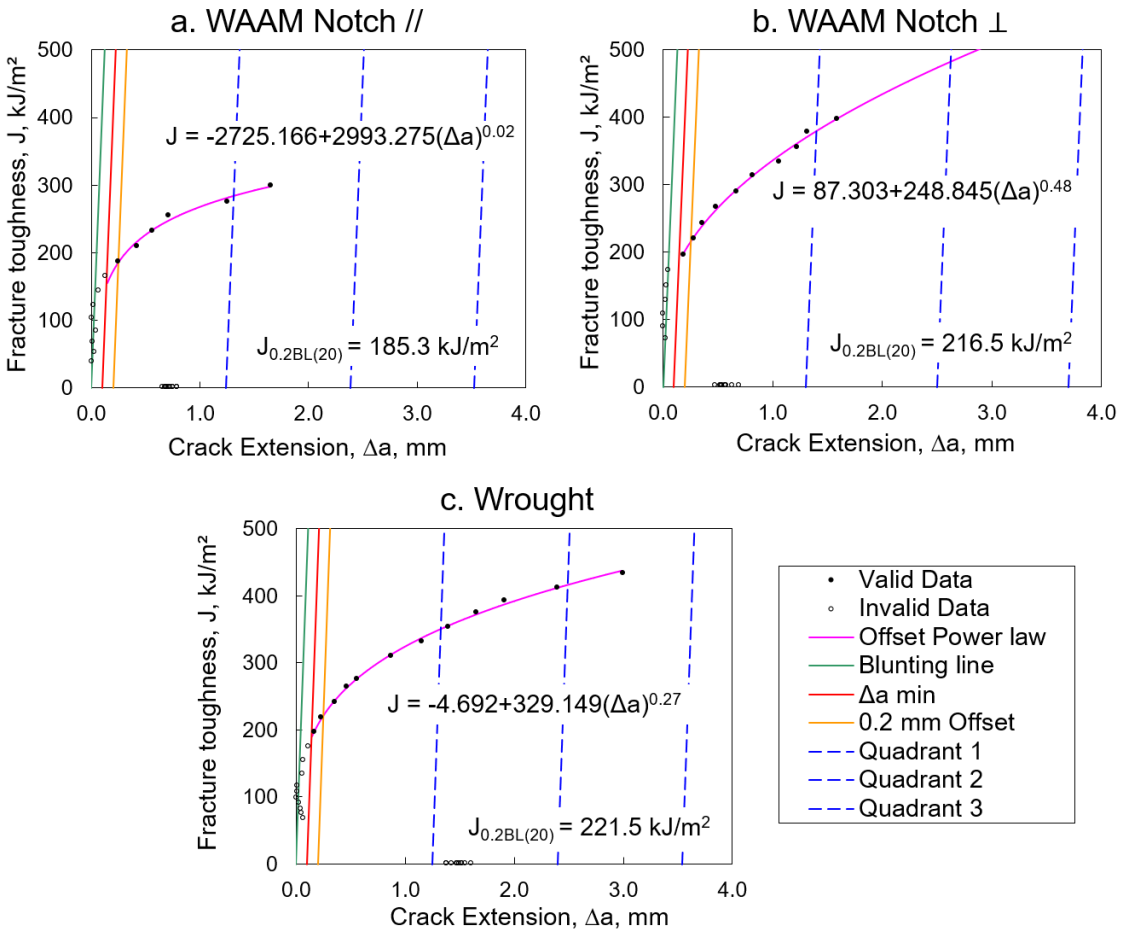

Figure 4.14: Resistance curves from WAAM (a) Notch //, (b) Notch ⊥ and (c) wrought specimens which displayed similar $J_{0.2BL(20)}$.

4.3.5 Qualification and significance of toughness measurements

The significance of toughness values reported in Section 4.3.4 is dependent on the qualification of these values to the criteria outlined in the standards (i.e. ISO 12135:2016 [227] and ASTM E1820-ae1 [226]). None of the toughness values are fully qualified to their respective standards, and the unmet qualification criteria are discussed separately for each toughness parameter. The corresponding specimen description, J values and possible reasons are detailed in Table 4.4 to Table 4.6.

The main issues with qualification of $J_{m(B)}$ (ISO 12135:2016 [227]) were observed in the WAAM specimens and are associated with the fatigue pre-crack and final crack shape. Both can be attributed to the effects of microstructure and crack-like defects. The final crack shape does not directly affect the values of J. In terms of significance, $J_{m(B)}$ represents the "size sensitive fracture

resistance J at the first attainment of a maximum force plateau for fully plastic behaviour". It is size sensitive even if all qualification criteria are met.

Issues with qualification of $J_{0.2BL(20)}$ as $J_{0.2BL}$ (ISO 12135:2016 [227]) were observed in both the WAAM and wrought specimens, and are associated with: (i) insufficient data in the third and fourth quadrants, which is a result of ending the fracture tests prematurely due to semi-stable fracture behaviour; (ii) data offset due to apparent "negative crack extension", which is due to crack tip blunting and the offset methodology is described in Section 4.2.4; and (iii) discrepancies between measured and estimated compliance and crack length, which can be attributed to inaccuracies with the estimated Young's modulus, E, used in the calculations. The tensile tests reported in Chapter 3 provide an "engineering value" of E for WAAM Alloy 718. A more accurate measurement of E can be obtained using a dedicated tensile setup focusing only on the elastic part of the stress-strain curve, involving high quality averaging strain measurement and data analysis procedures; or can be obtained using dynamic methods, described by Lord and Morrell [235].

Failing these qualification checks, the toughness values cannot be qualified as $J_{0.2BL}$, but they can be represented as $J_{0.2BL(B)}$, which represents the "size sensitive fracture resistance at 0.2 mm stable crack extension offset from the construction line". This can also be interpreted as a thickness-specific engineering estimate of toughness for ductile materials at 0.2 mm of stable crack extension.

As data from the same specimen set was used for the evaluation of J_Q, qualification of J_Q as J_{IC} (ASTM E1820-ae1 [226]) also faced similar issues, associated with insufficient data, data offset along Δa-axis and discrepancies between estimated and measured compliance. Therefore, the toughness values cannot be qualified as J_{IC}, which represents the "toughness of a material near the onset of crack extension from a pre-existing fatigue crack". The significance of J_Q is not outlined in the standard.

Nonetheless, the measures of toughness from the WAAM and wrought specimens described in Section 4.3.4 can be compared against one another, as they have been obtained from specimens of the same thickness (B = 20 mm).

Table 4.4: Summary of qualification criteria which were not met during fracture toughness evaluation of J_m (ISO 12135:2016 [227]) of WAAM and wrought specimens.

J_m (ISO 12135:2016 [227])	**Specimen description**	**J (kJ m^{-2})**	**Actual**	**Allowed**	**Reason**
From basic procedure					
Minimum fatigue pre-crack length (5.8.2 c) (mm)	WAAM Notch //	133	0.7	1.3	Interaction of pre-crack with crack-like defect
Fatigue pre-crack within envelope (5.8.2 d)	WAAM Notch //	252	-	-	Effect of microstructure
Final crack shape (5.8.3)	All WAAM specimens	-	-	-	Interaction of crack extension with crack like defect and effect of microstructure
From unloading compliance					
Initial K-rate between 0.2 and 3.0 MPa.m$^{0.5}$ s^{-1} (5.7.5)	WAAM Notch //	128	0.02	0.2 – 3	Specimens tested at slower loading rate than the other specimens
	WAAM Notch ⊥	346	0.02	0.2 – 3	
	Wrought	280	0.14	0.2 – 3	Loading rate decreased due to pin shear challenges
Fatigue pre-crack within envelope (5.8.2 d)	WAAM Notch ⊥	346	-	-	Effect of microstructure on the path of the fatigue pre-crack
	Wrought	280	-	-	

Table 4.5: Summary of qualification criteria which were not met during fracture toughness evaluation of $J_{0.2BL}$ (ISO 12135:2016 [227]) of WAAM and wrought specimens.

$J_{0.2BL}$ (**ISO 12135:2016** [227])	**Specimen description**	**J (kJ m^{-2})**	**Actual**	**Allowed**	**Reason**
Fit coefficient α greater or equal to 0.0 (7.4.2.2)	WAAM Notch //	185	-2725	≥0.0	A result of "negative" crack extension, which affects the shape of the R-curve and hence fitting parameters
	WAAM Notch ⊥	177	-172	≥0.0	
	Wrought	211	-4.7	≥0.0	
At least 1 valid data point in each quadrant (7.4.2.2)	WAAM Notch //	185	-	-	Insufficient data. Test stopped before crack extension reached third quadrant due to (i) fracture instabilities, (ii) specimen peak load achieved before sufficient crack extension
	WAAM Notch ⊥	177	-	-	
	WAAM Notch ⊥	217	-	-	
	Wrought	211	-	-	
Estimated final crack length (7.2.3) (mm)	WAAM Notch //	185	0.93	1.58 – 2.14	Inaccuracies in estimated E and/or measured compliance reduced by crack-like defect
	WAAM Notch ⊥	177	1.95	2.05 – 2.78	
	Wrought	221	1.52	2.36 – 3.19	
Data offset along Δa axis (mm)	WAAM Notch //	185	-0.73	0	To address "negative" crack extension caused by crack tip blunting
	WAAM Notch ⊥	217	-0.57	0	
	Wrought	211	-1.48	0	
λ within 10% of specimen unloading compliance (H.5.1)	All specimens	-	-	-	Inaccuracies in estimated E and/or measured compliance reduced by crack-like defect

Table 4.6: Summary of qualification criteria which were not met during fracture toughness evaluation of J_{IC} (ASTM E 1820-ae1 [226]) of WAAM and wrought specimens.

J_{IC} (**ASTM E 1820-ae1** [226])	**Specimen description**	**J (kJ m^{-2})**	**Actual**	**Allowed**	**Reason**
Correlation coefficient of fit ≥ 0.96 (A9.3.3.2)	WAAM Notch //	55	0.12	≥ 0.96	Differences between measured and estimated initial specimen compliance
	WAAM Notch ⊥	224	0.70	≥ 0.96	
No of points used to calculate a0q ≥ 3 between 0.4J_Q and J_Q (A9.3.3.2)	WAAM Notch //	205	0	≥ 3	Insufficient data. Test stopped as peak load achieved before reaching maximum crack extension capacity of specimen.
	WAAM Notch ⊥	237	2	≥ 3	
	Wrought	239	0	≥ 3	
Data offset along Δa axis (mm)	WAAM Notch //	205	-0.73	0	To address “negative” crack extension caused by crack tip blunting
	WAAM Notch ⊥	237	-0.56	0	
	Wrought	239	-1.48	0	

4.3.6 Post-test crack tip morphology

Evidence of interaction between the crack-like defects and main crack was observed in the fracture surfaces of the WAAM samples, as shown in Figure 4.15. The bronze-coloured regions are surfaces affected by heat-tinting. This normally consists of the fatigue pre-crack (marked B) and crack extension (marked C), which are typically slightly C-shaped as seen from the wrought specimen. However, in the WAAM specimens, this bronze-coloured region is connected to irregular features (marked E) of the same colour, such as "islands" in the Notch // specimen and out-of-plane cracks in the Notch ⊥ specimen. These features are likely to be crack-like defects which were exposed to the atmosphere during heat-tinting. This interaction between the main crack and defects is confirmed by X-ray computed tomographic slices of the fracture specimen, described in Section 4.3.6. Not all crack-like defects were observed to have interacted with the crack extension. The non-interacting defects (marked F) are mostly in the remaining ligament (marked D) of the fracture specimens.

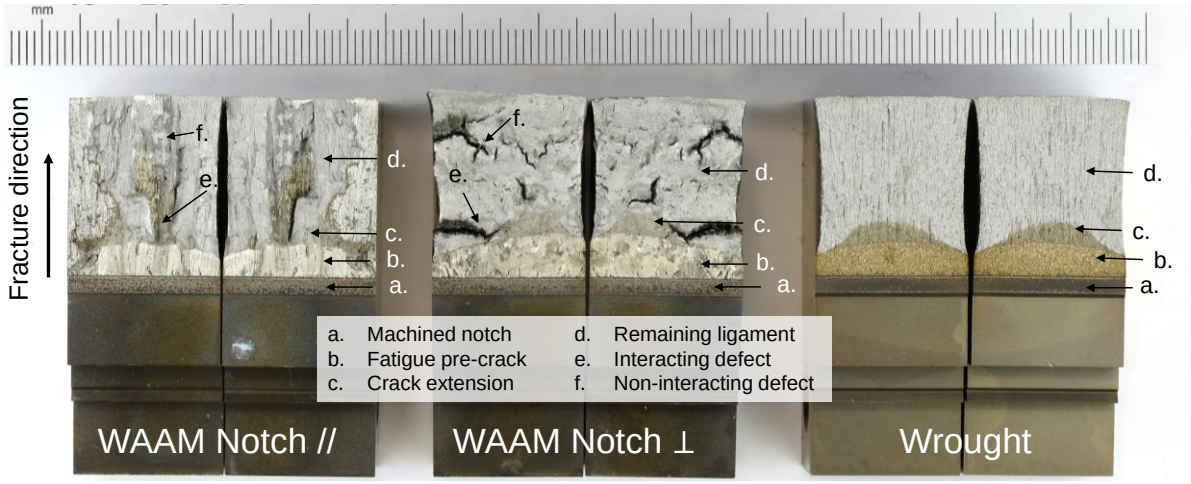

Figure 4.15: Fracture surfaces of WAAM and wrought C(T) specimens. Bronze colour indicates exposed surfaces during heat-tinting (i.e. fatigue pre-crack, crack extension and defects).

Smooth, liquid-like features were observed on SEM fractographs of a Notch // specimen, as shown in Figure 4.16. These features are characteristic of hot cracks, where liquid films form due to liquation of low melting point constituents such as Laves phase or carbides. The possible formation mechanisms of crack-like defects in WAAM Alloy 718 are discussed in Section 4.4.1. In the post-test WAAM specimens, crack-like defects were observed to be situated plane parallel and perpendicular with respect to the main crack, for the Notch // and Notch ⊥ specimens

respectively as shown in Figure 4.17. This indicates that in the Notch // specimen, the crack-like defects close to the propagating crack front results in an extension of the main crack. This secondary crack extension (due to crack-like defects) is essentially a large area of unfused material, which does not contribute to the material's resistance to fracture, thereby leading to a lower apparent fracture toughness. In contrast, these crack-like defects result in deflection of the main crack in the Notch ⊥ specimen. Crack deflection, which is one of several toughening mechanisms in materials [236], effectively reduces the crack driving force [237], leading to a higher apparent fracture toughness.

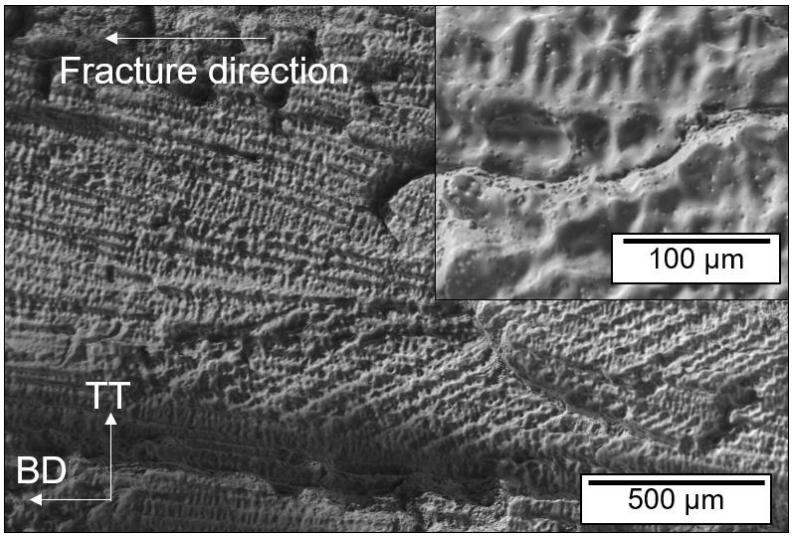

Figure 4.16: SEM secondary electron image of a crack-like defect from the fracture surface of Notch // specimen, showing solidified liquid film characteristic of hot cracking.

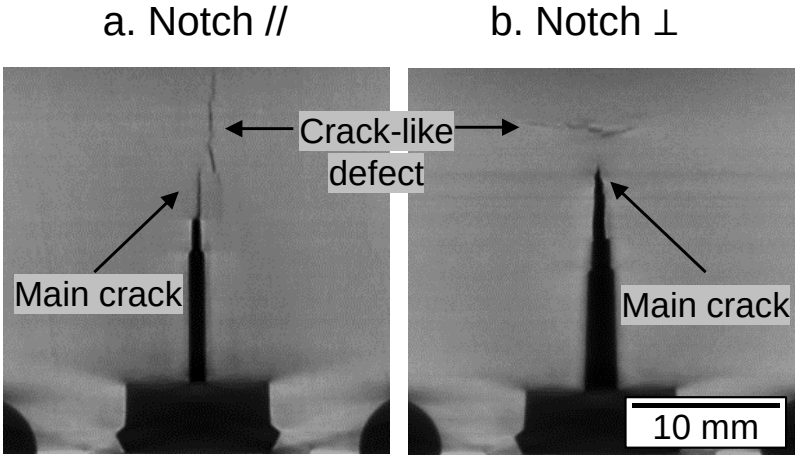

Figure 4.17: X-ray computed tomography slice of post test WAAM (a) Notch // and (b) Notch ⊥ specimens.

4.4 Discussion

4.4.1 Formation of crack-like defects

The periodic and alternating nature of the defects (see Figure 4.18a) can be attributed to the oscillating torch path used in the WAAM deposition. The spacing of alternating defects in WA is 6 mm, which is close to the length of the step advancement, as illustrated in Figure 4.18b. The defects alternate above and below the centre-line, and most likely initiated on the returning pass, where the melt pool is enlarged from residual heat of the preceding outward pass [238]. This variation in melt pool geometry may also have an effect on the local strain distribution, which has been observed in numerical models of SLM materials with a similar deposition pattern [239]. This indicates that the implications on defect rate and directionality should be carefully considered when designing a deposition path for WAAM.

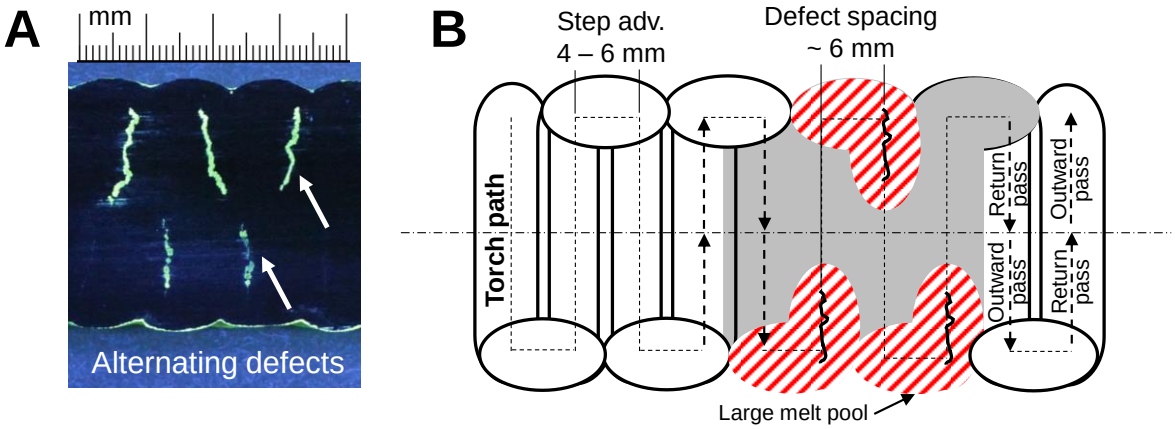

Figure 4.18: (a) Insert from Figure 4.6 showing alternating defects. (b) Schematic of possible hot and cool zones resulting from the oscillating tool path, leading to alternating defect pattern.

The characteristics of the crack-like defects described in Section 4.3 resemble aspects of hot cracking in welds, which can be attributed to two mechanisms – solidification and liquation cracking. Both mechanisms are associated with the presence of intergranular liquid films, but the former usually results from weld restraint, which in the case of WAAM can be large due to the thickness of the WAAM wall section (32 mm). The latter, which results from liquation of low melting point constituents in the microstructure [240], can occur in WAAM due to the reheating of deposited material. WAAM Alloy 718 is especially susceptible to liquation cracking due to the presence of Laves phase and NbC in the microstructure. The Nb-rich Laves phase

along the edges of the defects described in Section 4.3.3 could be a product of the re-solidification of liquated low-melting-point constituents [241]. The hot cracking mechanism in WAAM Alloy 718 is likely to be a combination of both solidification and liquation cracking. Therefore, strategies to mitigate the formation intergranular liquid films and restraint must be adopted to minimise the formation of crack-like defects. Some of these strategies are discussed in Section 4.4.3.

4.4.2 Detecting crack-like defects

The non-destructive detectability of crack-like defects in WAAM Alloy 718 is important for quality inspection purposes. Although dye penetrant inspection, conventional ultrasound testing and X-ray radiography were shown in Section 4.3.2 to be suitable for detection of crack-like defects, each technique has its limitations. Dye penetrant testing is limited to surface-breaking defects and can be sensitive to surface artefacts. Conventional ultrasonic testing requires a smooth surface for good acoustic coupling and is limited in characterising defect size. X-ray radiography may not be feasible for large parts or thick sections. In addition, for all three techniques defect size and orientation can also affect the inspection results, therefore quality inspections must be conducted considering these factors.

Non-destructive defect detection techniques can also be beneficial for process optimisation when conducted in-situ with deposition. There are a few monitoring and inspection techniques suitable for implementation during the WAAM process, which have been broadly reviewed by Lopez et al. [242]. They include eddy current, electromagnetic and laser ultrasonic testing, which may provide a way forward for production quality feedback control.

4.4.3 Mitigating crack-like defects

Mitigation of crack-like defects is mainly dependent on the ability to limit two effects: (i) the formation of low melting point constituents such as Laves phase and carbides in the microstructure; and (ii) the build-up of localised strain in the deposited material. Both are strongly affected by thermal conditions during deposition. One way to manage this is to lower the heat input, which has been observed to reduce hot cracking susceptibility in multi-pass weldments of cast Alloy 718 [243]. Control of heat input can be achieved by adjusting the WAAM primary input process parameters (i.e. current, contact-tip-to-work distance, travel speed, wire feed speed and gas flow rates.), although changing these parameters can also alter weld bead geometry, requiring re-optimisation to maintain process stability and geometric

control. An alternative which circumvents this is to limit the inter-pass temperature, which has been observed to reduce porosity in WAAM Al alloy [74]. However, this may introduce a wait time between each pass, which adds to the overall build time. There are also various ancillary processes that can be implemented in-situ to control thermal conditions. These have been comprehensively reviewed by Cunningham et al. [61] and Oliveira et al. [35], and are based on the following general principles: (i) reducing heat input into the workpiece – through pulsed current [244] and hot-wire deposition [245] techniques; (ii) dissipating heat away from the workpiece – through local cooling to the weld pool [246], [247], substrate cooling [100], [248], or inter-layer forced cooling [249], [250]; (iii) weld pool agitation – through ultrasonic vibration [251], [252] and arc oscillation [253], [254] techniques.

The build-up of localised strain can also be mitigated by reducing restraint and residual stress build up. Some techniques that address these are based on the following principles: (i) plastic deformation and grain refinement – through inter-layer high pressure cold rolling [76] and laser shock peening [255] and (ii) geometrical considerations – through deposition path optimisation [66], [67], [68], or component and build design optimisation [256].

At present, optimisation of parameters of primary and ancillary processes relies heavily on trial-and-error, which is not feasible at production scales. Feedback control of such parameters is crucial in process optimisation. One way of achieving feedback control is through in-situ temperature monitoring. Transient thermal profiles of WAAM deposits have been achieved with infrared thermography [257], although the technique was unable to accurately capture the thermal profile of the weld pool. Lastly, although costly and time consuming, modifications to the alloy composition can be made to further manipulate solidification kinetics.

4.4.4 Other factors influencing the direction dependence of fracture toughness

The direction dependence of fracture toughness reported in Section 4.3.4 has been largely attributed to the interaction between crack-like defects and the main propagating crack of the fracture specimen. Whilst this has been shown to occur in the post-test analysis described in Section 4.3.6, there may be other sources contributing to the direction dependency of toughness measurements. From a microstructural viewpoint, the grain structure of the WAAM Alloy 718 material (after heat treatment) is anisotropic, as shown in Figure 4.19. The main crack in a WAAM Notch // specimen propagates along the long axis of the grains. Therefore, in the

absence of crack-like defects in the WAAM Alloy 718 material, toughness measurements are still likely to be direction dependent.

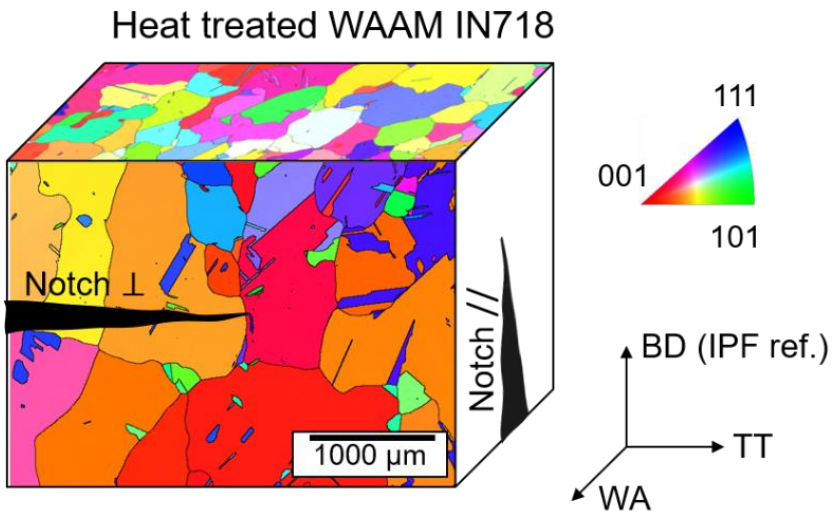

Figure 4.19: Notch orientations of WAAM C(T) fracture specimens in relation to WAAM Alloy 718 material grain structure. EBSD maps show high-angle grain boundaries and grain orientation in IPF colouring.

4.5 Conclusions

This work demonstrates that the orientation of crack-like defects can have a large effect on the resulting apparent fracture toughness of WAAM Alloy 718. The effect of direction dependence should be an important consideration at various stages of materials characterisation for WAAM materials. In addition, direction dependent fracture properties may have implications on structural integrity assessments. The following conclusions can be drawn from this work:

1. Crack-like defects with planar morphology can form in WAAM Alloy 718 under unfavourable deposition conditions. The defect pattern can be attributed to the WAAM deposition path.
2. These defects have hot cracking characteristics. They occur in the centre of the melt bead, along high-angle grain boundaries and have edges lined with Laves phase.
3. Non-destructive detection of these defects is feasible using dye penetrant, conventional ultrasonic and X-ray radiography techniques.
4. The fracture toughness of WAAM Alloy 718 was observed to be anisotropic, depending on notch orientation with respect to the defects. When notched plane perpendicular to defects,

WAAM Alloy 718 has apparent toughness comparable to wrought Alloy 718. However, when notched plane parallel to defects, toughness of WAAM Alloy 718 is half that of wrought Alloy 718.

Chapter 5 Measuring strain fields around a crack tip in WAAM nickel-base superalloys

This chapter first introduces the importance of direct measurement of crack tip strain fields, using surface and sub-surface experimental techniques, such as Digital Image Correlation (DIC) and neutron diffraction. The challenges posed by the unfavourable grain structure of WAAM materials when using neutron diffraction techniques with in-situ loading is discussed. A novel crystallite tracking experimental method is presented as a means of minimising the uncertainties caused by sample movement from the measurement gauge volume. Experimental results are presented on three length-scales: macro- (load-displacement curves), meso- (total surface strain from DIC) and lattice- (elastic lattice strain from neutron diffraction) scale. The results demonstrate that the new method is effective in accounting for sample movement (with respect to the measurement gauge volume). In addition, anisotropic meso-scale behaviour was observed in WAAM IN625 but not WAAM IN718; and in both materials, clusters of similarly oriented crystallite(s) appear to have similar elastic (lattice) strain behaviour (i.e. "grouped" behaviour). The reasons behind these observations are discussed in relation to the material's microstructure, in consideration of the limitations of an angle dispersive diffractometer. Lastly, the evolution of measured total and lattice strains is compared against those obtained from a crystal plasticity finite element model and their agreements and discrepancies are discussed.

This chapter is based on the following publication:

Seow C E, Coules H and Khan R (2018) 'Effect of Crack Orientation on Fracture Behaviour of Wire + Arc Additively Manufactured (WAAM) Nickel-Base Superalloy', in American Society of Mechanical Engineers, Pressure Vessels and Piping Division (Publication) PVP, p. V005T10A016. doi: 10.1115/pvp2018-84090.

Acknowledgement: The Crystal Plasticity Finite Element (CPFE) modelling results described in Section 5.6.4 were provided by H.E. Coules. This work on CPFE is unpublished at the time of writing this Chapter, and the results are used in this Chapter as a means of comparison and discussion only.

5.1 Introduction

The behaviour of a crack is strongly influenced by the stress field around the crack tip. Using fracture mechanics approaches, this can be represented by single parameters, such as the stress intensity factor, K, for linear elastic behaviour; and the J-integral, J, for elastic-plastic behaviour. The critical values of K and J at which fracture occurs can be measured through standardised fracture toughness testing (as described in Chapter 4). However, these parameters have a limited range of validity, and do not account for effects of geometrical constraint and strength mismatch (e.g. in weldments), which require additional parameters such as T-stress, Q and M to account for these effects [258]. Although analytical and numerical methods can be used to determine these fracture mechanics parameters, they may be unreliable when the crack tip is susceptible to crack path deviation or strain partitioning, or has complex boundary conditions [259]. In WAAM materials, the varying levels of microstructural anisotropy and inhomogeneity can lead to crack path deviation and strain partitioning, which may result in crack tip stress fields that deviate from the analytical or numerical predictions based on generalised materials properties and models.

Experimental methods provide a direct measurement of crack tip strain or displacement fields, from which the stress fields can be inferred. For surface measurements, Digital Image Correlation (DIC) is currently widely used due to its ability to capture full field elastic-plastic displacement around the crack tip [260]. If captured with the appropriate measurement parameters (e.g. subset size, field of view and area of interest) [261], reliable estimates of fracture mechanics parameters can be obtained from DIC data [259], [262]–[264]. For sub-surface

measurements, diffraction methods using synchrotron X-rays [265] and neutrons [266], [267] have been used to determine the stress field around a crack tip deep (several mm) within a cracked specimen. Elastic lattice strains are determined from the shift in positions of diffraction peaks, and the strains measured in three orthogonal directions (or at least two, assuming plane-strain conditions) can be used to calculate the corresponding stress. Plastic deformation can also be inferred from the broadening of the diffraction peaks [268].

Sub-surface strain measurements can also be taken during in-situ loading to observe the evolution of crack tip strain fields under monotonic and cyclic loading. For example, Sun et al. [269] and Lee et al. [270] investigated the effects of tensile overloads on fatigue crack growth rates, by carrying out neutron and synchrotron X-ray diffraction measurements ahead of the crack tip along the crack centreline in a C(T) specimen, at different load levels immediately following a single tensile overload. Using synchrotron X-ray diffraction Steuwer et al. [271] carried out high resolution two-dimensional crack-tip strain maps, to examine the evolution of residual stresses during various fatigue stages before and after an overload event. Combining two-dimensional synchrotron X-ray strain mapping with DIC, Lopez-Crespo et al. [272] obtained both surface and sub-surface strain measurements to estimate the effective crack driving force of a fatigue crack tip before, during and after overload events. Coules et al. also combined two-dimensional synchrotron X-ray [273], [274] and neutron [275] strain mapping with DIC, and examined the R-curve behaviour of residually stressed (by local indentation) C(T) specimens and the effects of residual stress on crack extension during unloading compliance fracture testing.

At present, little is known about crack tip strain fields in WAAM materials. One challenge with obtaining neutron or synchrotron X-ray diffraction measurements in many WAAM materials is that their coarse-grained and strongly-textured microstructure can result in inherently inaccurate measurements. Unlike powder diffraction where all crystallites contribute evenly to the diffraction pattern, coarse-grained materials contain larger crystallites that can contribute disproportionately to the diffraction pattern [276]. This inaccuracy can be exacerbated by the random positioning of large grains within the measurement gauge volume [276], [277]. Holden et al. [278] found that the uncertainty in such measurements can be as high as ±200 με, and that rotating the gauge volume by 180° can minimise this uncertainty. However, under in-situ loading, it may not always be practical to perform such rotations. Furthermore, in-situ loading can cause a sample to distort by several millimetres, resulting in movement of the sampled

gauge volume from the measurement gauge volume. In uniaxial tensile experiments, this movement is easily compensated for by a linear adjustment of the measurement gauge volume [279], [280]. However, fracture samples also undergo some degree of rotation which is dependent on the crack length, and this cannot simply be adjusted for with a linear adjustment in measurement coordinates. Although the magnitude of rotation is small, and is generally assumed to have a negligible effect on strain measurements in fine-grained materials, the effects of rotation may result in significant shifts in the gauge volume centroid in coarse grained materials.

This study presents, for the first time, a method of obtaining two-dimensional neutron strain measurements around a crack tip in a coarse grained WAAM material under in-situ loading. The effects of specimen movement have been compensated for using DIC to trace the positions of the sampled gauge volumes, from the start to the end of the loading regime, thereby minimising the uncertainty in strain measurements caused by specimen rotation. The evolution of crack tip strain fields (surface and sub-surface) is discussed in consideration of the material's microstructure and specimen orientation.

5.2 Materials and microstructure

Specimens were extracted from WAAM IN625 and heat treated WAAM IN718 materials. The manufacture and microstructure of heat treated WAAM IN718 is described in Chapter 3. For WAAM IN625, cold metal transfer (Fronius CMT advanced 4000R GMAW system, see Figure 5.1a) was used to deposit IN625 wire (Ø 1 mm, nominal composition in Table 5.1) onto a mild steel substrate plate. An oscillating torch path (see Figure 5.1b) was used and suitable deposition parameters were determined by trial and error. A slice of the deposited wall (dimensions shown in Figure 5.1b) was used in this study.

Table 5.1: Nominal composition of IN625 welding wire (wt%) [281].

Ni	Cr	Fe	Nb(+Ta)	Mo	Al/Ti	C	Mn/Si	P/S	Co
58 min.	20.0-23.0	5.0 max.	3.15-4.15	8.0-10.0	0.40 max.	0.10 max.	0.50 max.	0.015 max.	1.0 max.

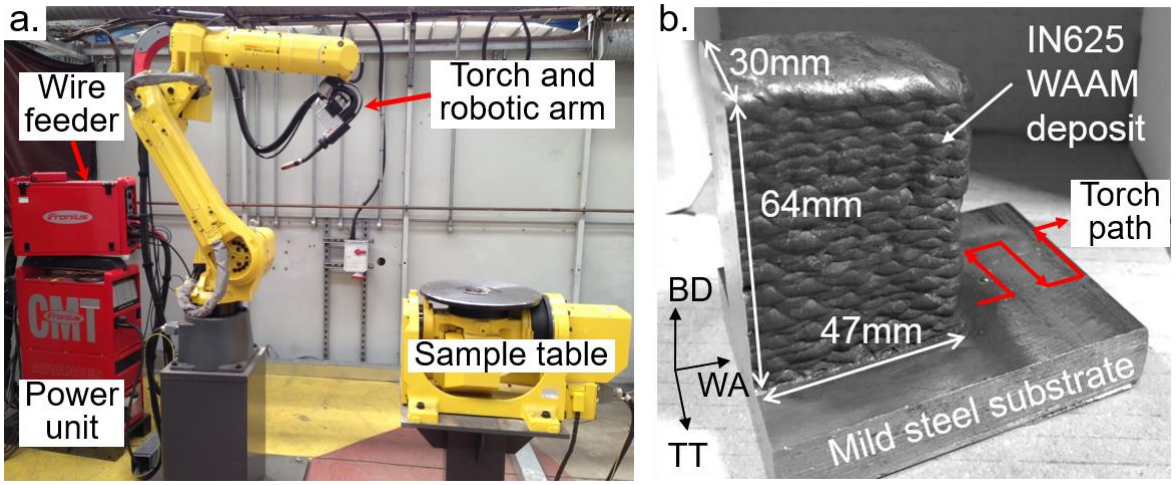

Figure 5.1: (a) WAAM Deposition equipment (courtesy of TWI Ltd) and (b) WAAM IN625 wall.

WAAM IN625 has a dendritic microstructure with long columnar grains (see Figure 5.2a and b respectively). The material also as a fibre texture, where grains are rotated about their long axis (i.e. build direction). This microstructure is similar to that of as-deposited WAAM IN718 (described in Chapter 3). Samples were prepared using conventional metallography techniques (mounted, ground, and polished to 0.25 µm). The material's microstructure was observed using optical microscopy, on samples etched electrolytically using 20% H_2SO_4 at 3 V for 10 s. The material's grain structure was observed using Electron Backscatter Diffraction (EBSD), which was performed on samples polished with colloidal silica suspension. EBSD was performed using

a ZEISS SIGMA field emission gun (FEG) scanning electron microscope (SEM) with an Oxford Instruments Nordlys detector, using an accelerating voltage of 30 kV, a 60 µm aperture and a step size of 1.25 µm.

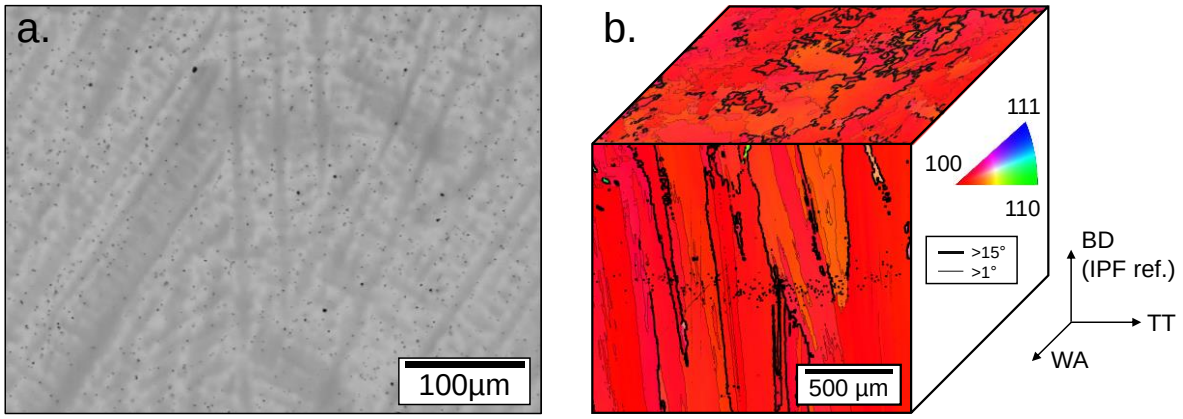

Figure 5.2: (a) Optical micrograph and (b) EBSD maps of WAAM IN625.

Due to the limited amount of WAAM IN625 material available, tensile properties were determined through small-scale tensile testing. Dog-bone specimens (dimensions in Figure 5.3a) were used and strain was measured using DIC. All specimens fractured in the gauge length (see Figure 5.3b). The stress strain curves are shown in Figure 5.3c.

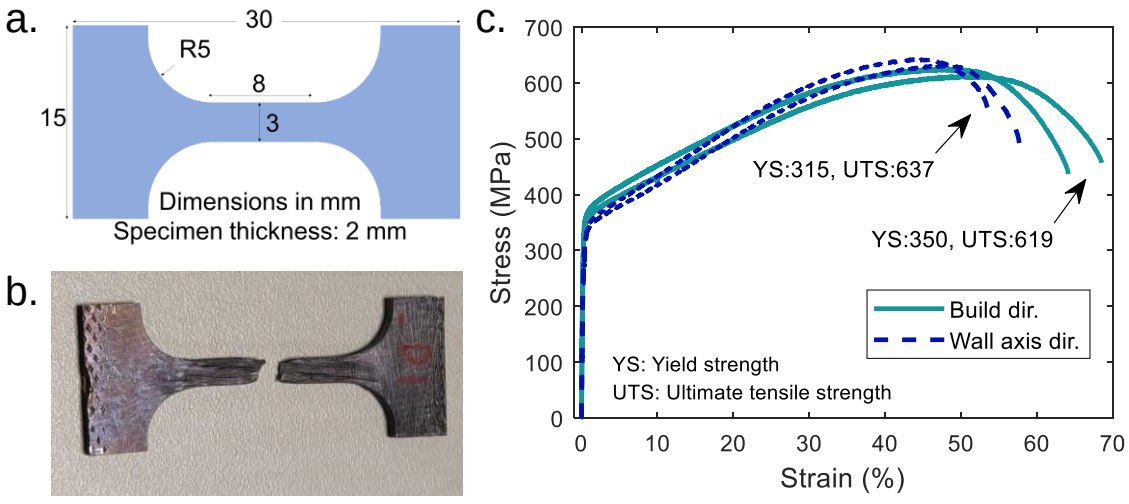

Figure 5.3: (a) Dimensions of small-scale tensile specimens; (b) specimen tested to failure; (c) stress-strain curves from small-scale tensile tests of WAAM IN625 conducted at room temperature.

5.3 Fracture testing

Five compact tension (C(T)) fracture specimens were extracted from WAAM IN625 and IN718 materials. The WAAM IN718 C(T) specimens were extracted from Wall 1, which is the same material batch reported in Chapter 3, see Table A.3 for full C(T) specimen list. The specimens were notched in two orientations, parallel and perpendicular to the build direction (Notch // and Notch ⊥ respectively). For WAAM IN625, due to the limited amount of material, sub-size C(T) specimens (dimensions in Figure 5.4) were extracted. The integral knife edges were positioned at the surface of the specimen (i.e. 8.75 mm, 0.25 W from the load line). These specimens were fatigue pre-cracked to 17.5 mm ($a_0/W = 0.5$). For WAAM IN718, C(T) specimens with dimensions detailed in Chapter 4 were extracted. The integral knife edges were positioned along the load line and therefore would be equivalent to Crack Mouth Opening Displacement (CMOD) as per ASTM E1820-18ae1 [110], or notch opening displacement, V, as per ISO 12135:2016 [227]. These specimens were fatigue pre-cracked to 26 mm ($a_0/W = 0.65$). For simplicity, clip gauge measurements on both WAAM IN625 and IN718 specimens are referred to as clip displacement in this work.

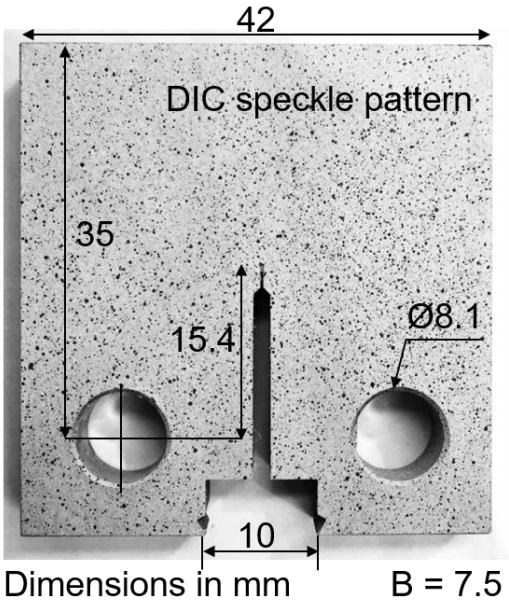

Figure 5.4: Dimensions and DIC speckle pattern of WAAM IN625 C(T) specimen. B refers to specimen thickness. Machined crack length of 15.4 mm excludes fatigue pre-crack.

Four C(T) specimens were tested at the European facility for neutron scattering, Institut Laue-Langevin (ILL), Grenoble, on the instrument SALSA [282], [283]. One WAAM IN625 specimen was tested at TWI Ltd, Cambridge. Three of the five C(T) specimens were tested using the unloading compliance method (as described in Chapter 4). Fracture toughness parameters J_m, $J_{0.2BL(B)}$ (ISO 12135:2016 [227]) and J_Q (ASTM E1820-18ae1 [110]) were evaluated where applicable. These parameters could not be obtained from the WAAM IN625 sample tested using this method as the specimen displayed toughness higher than the validity limit for the specimen dimensions, which is discussed further in Section 5.5.1. Specimens tested using this method were broken open post-test for crack length measurements.

The remaining two WAAM IN625 specimens were loaded monotonically at fixed increments of grip displacement. These two specimens were not broken open post-test, but were sectioned along the mid-plane for EBSD analysis. Therefore, single-point toughness values evaluated from these two specimens are based on the initial crack length measured from the WAAM IN625 specimen which was broken open.

A summary of the fracture specimens and their test details is shown in Table 5.2.

Table 5.2: Summary of fracture test specimens and measurements obtained.

Testing facility	Side-grooves	Material	a_o/W	Loading regime	Types of Measurements	No. of Spec.	Toughness parameter
ILL, SALSA	No	IN718 HT[a]	0.65 - 0.7	Unloading compliance	Macro load-disp, total strain (DIC), lattice strain (ND)	2 (∥, ⊥)	$J_{m(B)}$, $J_{0.2BL(B)}$, J_Q
		IN625	0.5	Mono-tonic	Macro load-disp, total strain (DIC), lattice strain (ND)	2 (∥, ⊥)[b]	J_{max}, J_{4mm}[c]
TWI	Yes	IN625	0.5	Unloading compliance	Macro load-disp	1 (∥)	J_{max}, J_{4mm}

[a]HT refers to modified homogenisation and aging treatment as described in Chapter 3.

[b]Notch orientation (with respect to the build direction).

[c]J_{4mm} refers to single point J evaluated at 4mm of clip displacement.

5.4 Experimental methods

5.4.1 General principles

5.4.1.1 Digital Image Correlation (DIC)

DIC methods detect and measure displacements by comparing digital images of the surface of an object, taken before and after deformation. The images are compared by searching for a unique image subset (see Figure 5.5). The uniqueness of the image subset can affect the accuracy of the matching, therefore an artificial random pattern (i.e. speckle pattern) is typically applied on the surface of the specimen. An image subset contains several pixels, each with a discrete grey level (i.e light intensity). The area is matched when the grey level distribution of the unique image subset (in the image before deformation) is maximally correlated with an area in the image after deformation. To obtain displacements with subpixel resolution, grey levels between discrete pixels (see Figure 5.6) are interpolated using bilinear and bicubic functions. The displacements are then determined by solving nonlinear simultaneous equations. Differentiation of the measured displacements provides strains at different positions, giving the strain map for the deformed specimen. The basic principle of DIC explained in more detail by Yoneyama [284]. As DIC is a surface technique, it is not influenced by grain structure or other microstructural effects. The effectiveness of the technique is dependent on the quality of the speckle pattern, the camera set up and calibration methods. DIC is typically used for strain mapping at the meso-scale (i.e. mm) but bespoke techniques involving microscopes can be used to achieve micro- or nano-scale strain maps [285].

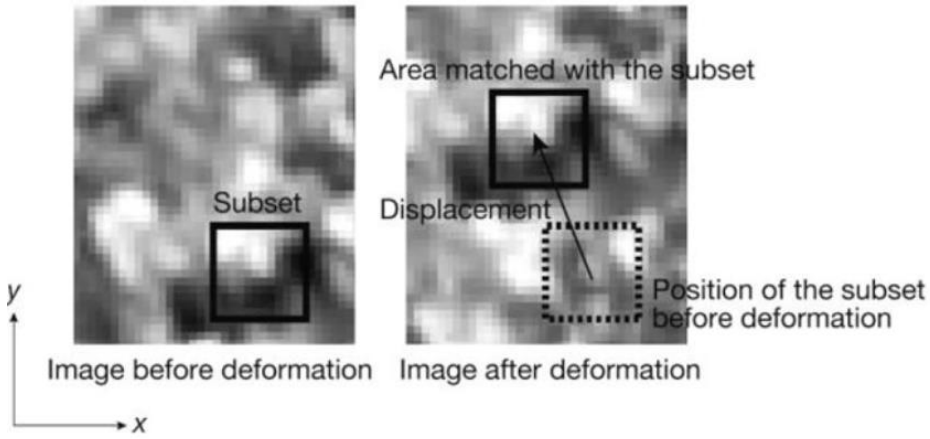

Figure 5.5: Comparisons of digital images before and after deformation, showing the matching image subset in both images and the resulting displacement that can be calculated. Image taken from [284].

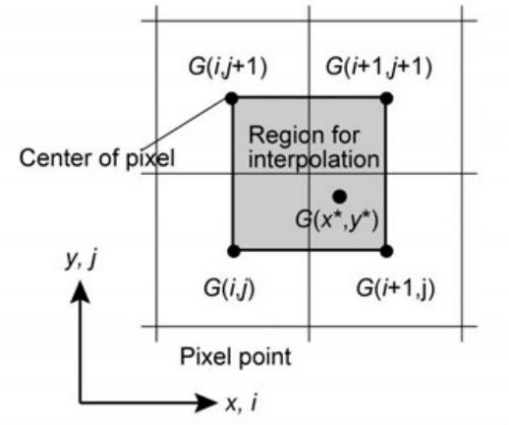

Figure 5.6: Schematic of discrete pixels and their centre points. The region between these points interpolated can be using bilinear and bicubic functions to obtain subpixel resolution. Image taken from [284].

5.4.1.2 Angle dispersive neutron diffraction

Neutron diffraction is a form of elastic scattering where the neutrons existing the experiment have approximately the same energy as the incident neutrons. Angle dispersive neutron diffraction involves the use of thermal neutrons from a reactor source that provides a wide spectrum of neutron flux as a function of wavelength. A monochromator crystal is used to extract a small range of wavelengths for specific instruments. One example of such an instrument is SALSA, ILL (see Figure 5.7). The small range of wavelengths is then passed through a series of slits and collimators before reaching the sample. The incoming beam is diffracted by a family of crystal planes within the sample, and the diffracted beam is passed through another collimator before arriving at the detector. When a specimen undergoes tensile or compressive loading, deformation leads to changes the distances between crystal planes, therefore lattice-scale strain measurements can be measured. The method of calculating strains from diffraction data is described in Section 5.4.4. Strain measurements from neutron methods are sensitive to grain structure variations within the sample.

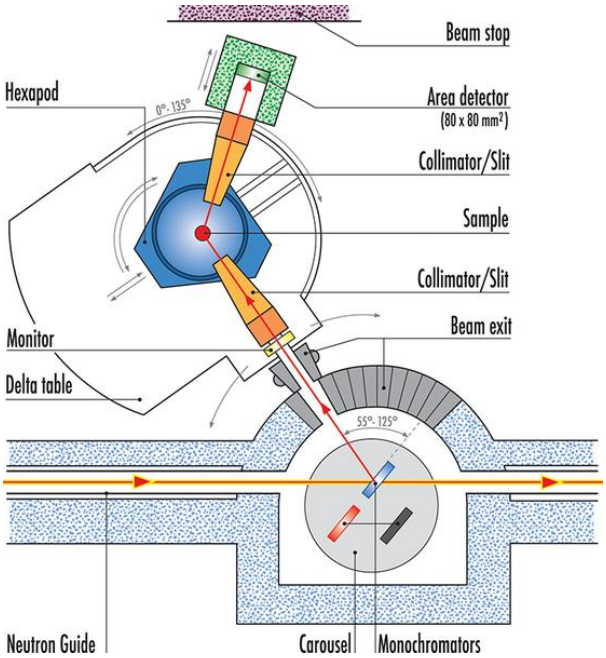

Figure 5.7: Instrument layout at SALSA, ILL. Image taken from [286] , courtesy of ILL.

5.4.2 In-situ loading on SALSA

All in-situ loading neutron experiments were conducted on SALSA, a monochromatic powder diffractometer comprising a hexapod sample positioner, two primary collimators, a secondary collimator and an area detector [282]. An Instron 50 kN servo-hydraulic stress rig was used to load the specimens uniaxially in Mode I (crack transverse, tension). A Dantec Systems Q400 System with two cameras were used for DIC measurements. Specifications of the cameras, lenses and analysis software are as described by Coules et al. [275]. The stress rig and DIC cameras were mounted onto the hexapod sample positioner, as illustrated in Figure 5.8, to minimise specimen movement relative to the cameras. A photograph of the setup is shown in Figure 5.9. Clip displacement was measured using a clip gauge with 10 mm gauge length and 4 mm travel.

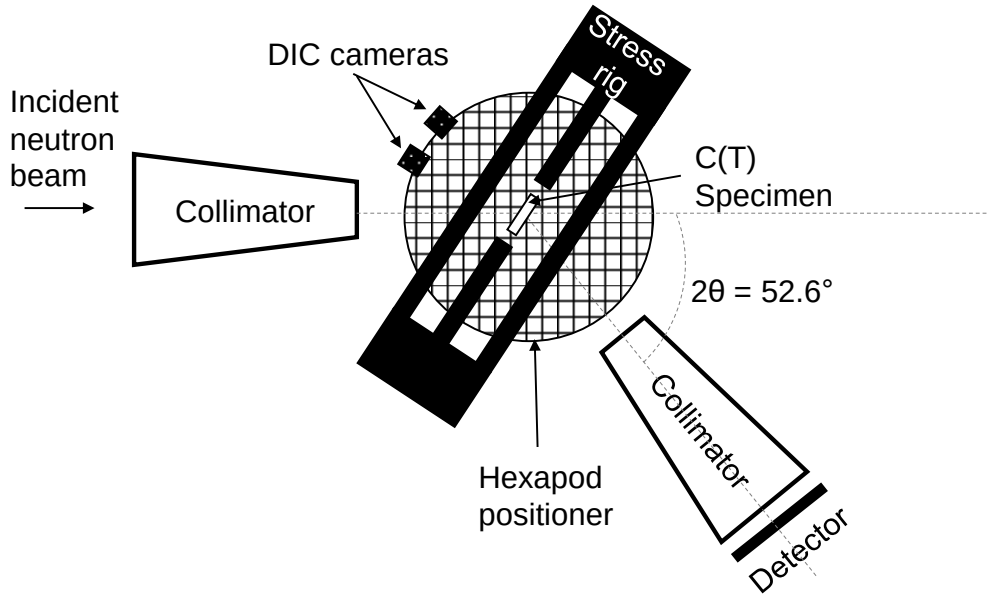

Figure 5.8: Illustration of experimental setup on SALSA (plan view).

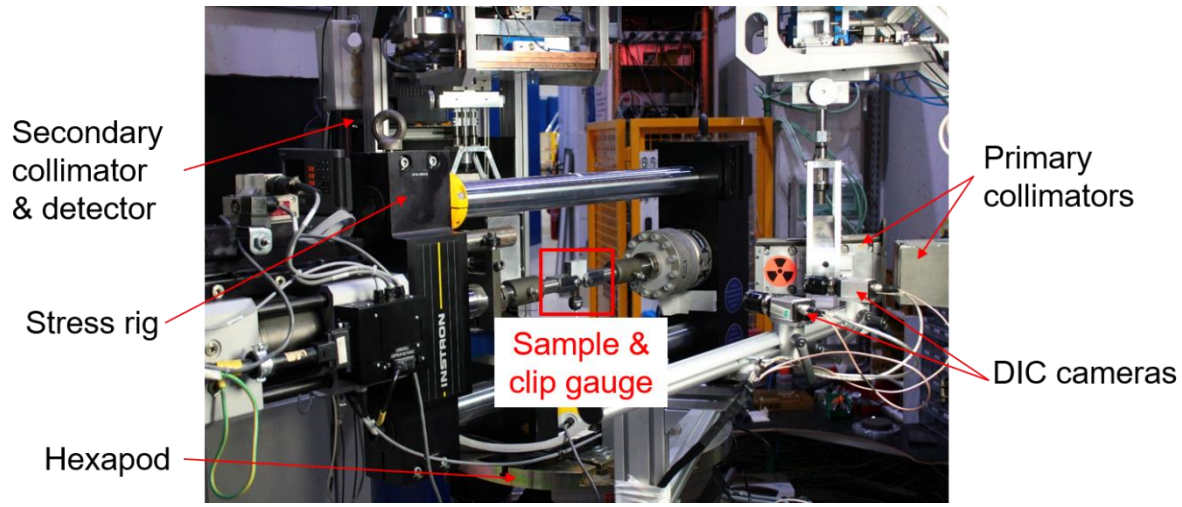

Figure 5.9: Photograph of stress rig and DIC camera setup on hexapod sample positioner on SALSA, ILL.

5.4.3 Crystallite tracking methodology

Under in-situ loading, a C(T) specimen undergoes lateral and rotational displacement. This displacement can cause a shift in the scattering grains relative to the measurement gauge volume, resulting in uncertainty in lattice strain measurements. The effect of specimen displacement under load is illustrated in Figure 5.10.

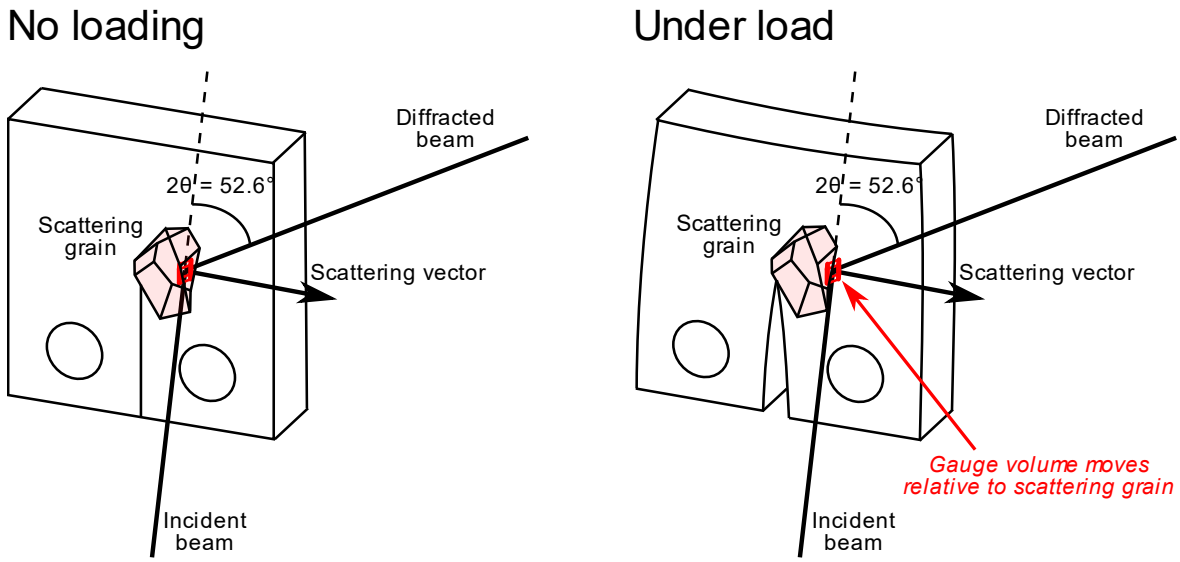

Figure 5.10: Schematic of C(T) specimen during neutron measurement. Under load, scattering grain moves with respect to the measurement gauge volume.

The goal of crystallite tracking is to compensate for specimen displacement due to loading, by first measuring the lateral and rotational components of displacement using two-dimensional techniques such as DIC, then accounting for this deformation in the measurement gauge volume coordinates. The displacements measured by DIC is exported and processed in a MATLAB script which applies the displacements to the original neutron measurement coordinates, and outputs a set of updated measurement coordinates. An example of the original and updated measurement grids is shown in Figure 5.11. The updated measurement coordinates are then imported into SALSA's sample positioning software, NOMAD, and the neutron measurements are carried out. This is repeated after each loading step, which keeps the neutron diffraction gauge volume in the same position relative to each scattering grain throughout the experiment. A summary of the crystallite tracking method is shown in Figure 5.12.

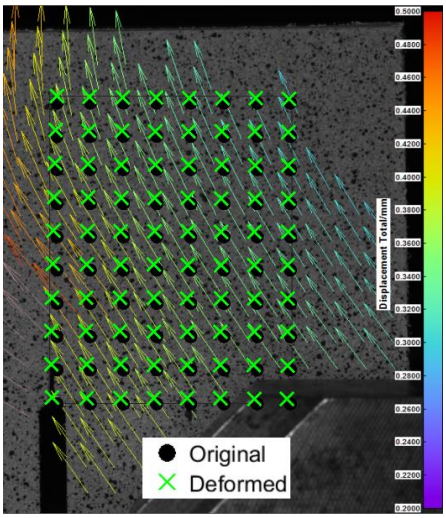

Figure 5.11: Original and deformed (i.e. updated) measurement grid overlaid on a DIC image with a displacement quiver map.

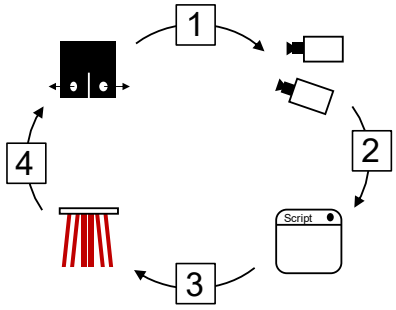

1. Loading step starts, specimen moves. DIC starts recording.
2. Specimen stops, DIC stops recording. DIC data transferred into a MATLAB script.
3. Sample table (hexapod) coordinates updated.
4. Neutron measurements taken. Next loading step begins.

Figure 5.12: Breakdown of crystallite tracking method steps for a single loading step

5.4.4 Neutron measurements and data treatment

All neutron measurements were made with an incoming neutron wavelength of 1.61 Å and a gauge volume of 2×2×2 mm^3. The measured lattice strain direction was aligned with the loading axis of the sample (i.e. crack transverse direction). Due to the texture of the WAAM materials (see Figure 5.2), the specimens produced observable Bragg peaks from the {200} reflection in the strain direction of interest, and hence this reflection was used for all measurements.

The WAAM IN625 specimens were measured using an 8×10-point grid with 2.5 mm spacing, positioned about the crack tip (see Figure 5.13) at the specimen mid-thickness. A reduced grid (21 points) was used for the Notch // specimen, which displayed fewer suitable scattering grains, likely due to the material's fibre texture. A high spatial resolution line scan at each measurement point was used to determine whether the measurement gauge volume was

located completely within a scattering grain. Measurement points which displayed a large reduction in intensity and shift in Bragg peak, relative to other measurement points in the same line scan, were inferred to be only partially filled with suitable scattering grains, and were therefore removed from the measurement grid.

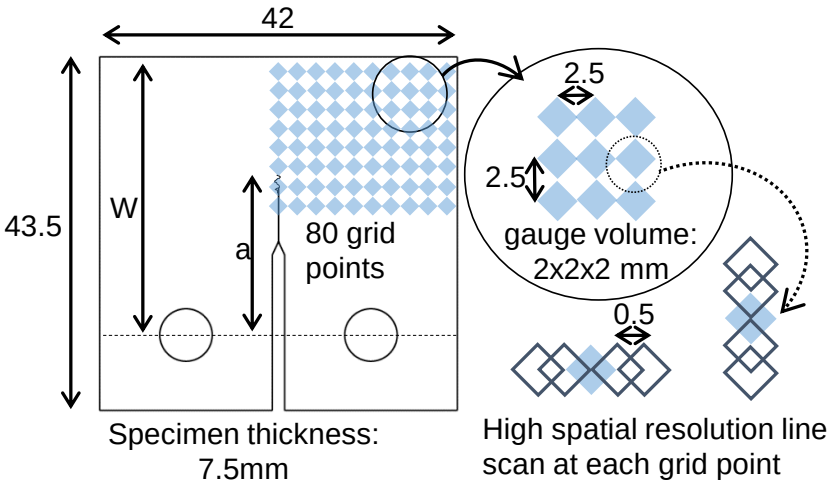

Figure 5.13: Neutron measurement grid for WAAM IN625 specimens, taken at the mid-thickness of the specimen

Due to the coarse grain structure and weaker texture of heat treated WAAM IN718 (described in Chapter 3), not every part of the specimens contained grains which scattered off the {200} reflection in the crack transverse direction. Therefore, the measurement grid was selected based on the positions of suitable scattering grains. These grains were identified using a preliminary grid scan (19×20 grid, 1 mm spacing), taken at three different thickness planes (mid-plane and ± 5 mm). The positions of suitable scattering grains were deduced from the intensity of fixed time measurements (30 s), as shown in Figure 5.14. A count threshold was set for each specimen to optimise the number of points used for the refined measurement grid.

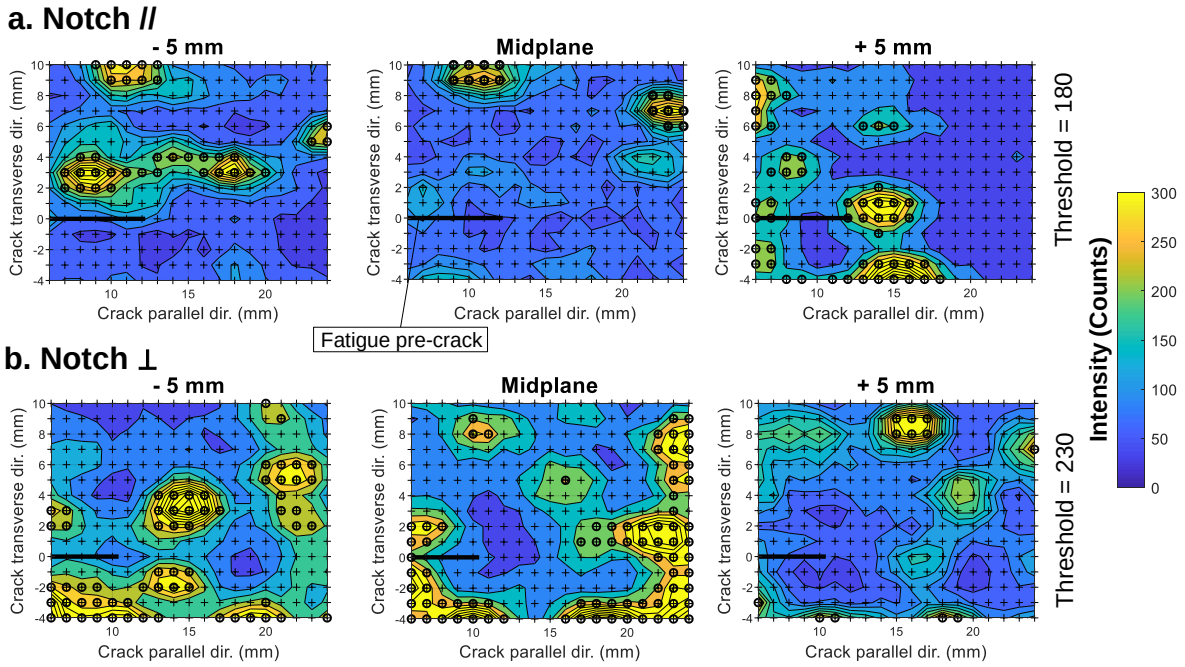

Figure 5.14: Intensity of {200} reflection from WAAM IN718 (a) Notch // and (b) Notch ⊥ specimens at different specimen thicknesses. Circled points indicate selected coordinates.

All neutron measurements used for determining lattice strains were made with a monitor count of at least 600 neutron detection events over the detector area, and crystallite tracking between each loading step. Suitable fitting parameters (i.e. model and background) were used to determine peak positions from the respective diffraction patterns from the WAAM IN625 and WAAM IN718 specimens (shown in Figure 5.15). For the measurements from WAAM IN718 specimens, a pseudo-Voigt peak fitting function was found to be more suitable than a conventional Gaussian fit, due to the narrow and sharp peaks observed experimentally. The peak positions were used to obtain lattice spacing, d, using Bragg's equation, given by

$$n\lambda = 2d\ sin\theta \tag{1}$$

where λ and θ are the incoming neutron wavelength and diffraction angle respectively, and n is an integer. Lattice strain, ε , was calculated using

$$\varepsilon = \frac{d_n - d_0}{d_0} \tag{2}$$

where d_n and d_0 refer to the lattice spacing at the nth loading step and the reference lattice spacing respectively. The lattice spacings from the first grid scan (i.e. before the first loading

step) were used as the reference measurements, which means that d_0 for each point on the grid is unique. This was done to circumvent effects of variations between the local microstructure of a stress-free specimen and the measurement locations on the C(T) specimens.

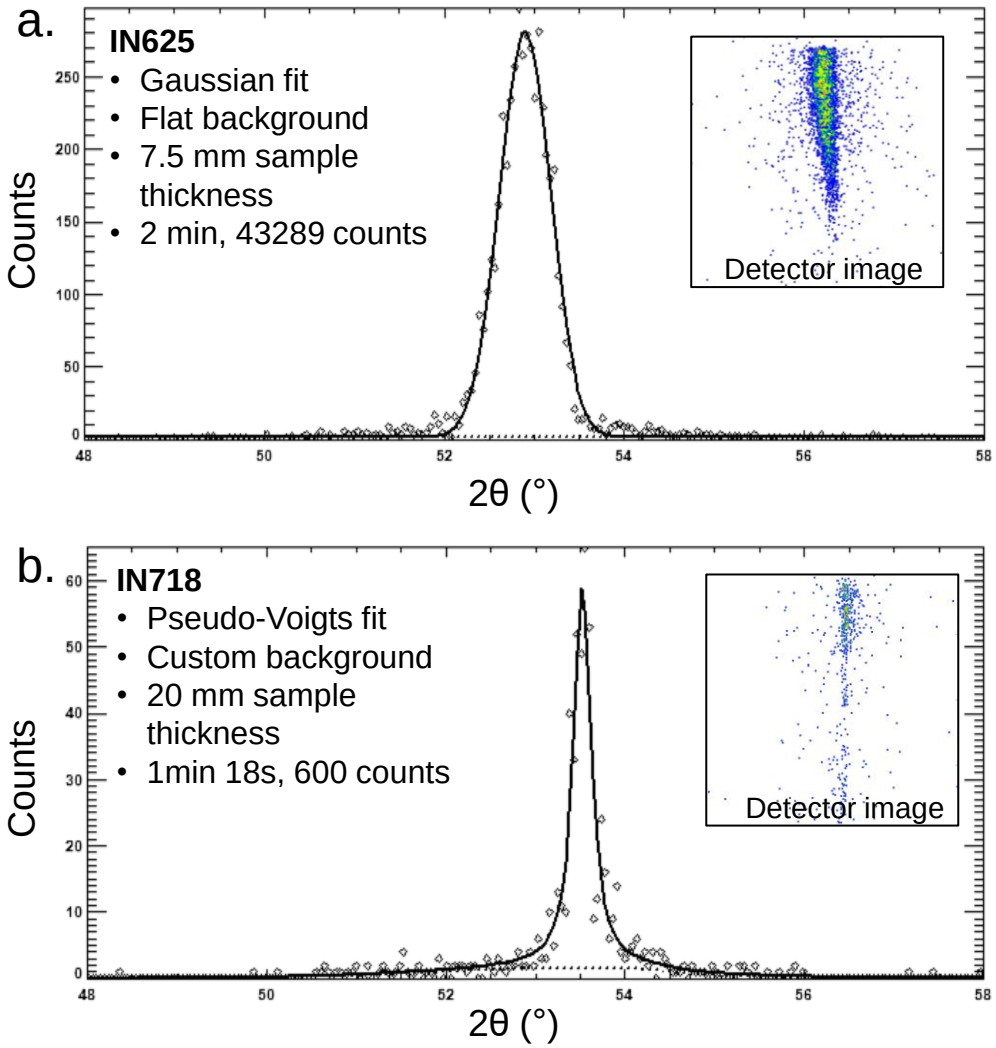

Figure 5.15: Diffraction patterns and fitting from WAAM (a) IN625 and (b) IN718 samples. Note the smaller sample thickness in (a), resulting in a higher neutron count rate than in (b).

5.5 Results and discussion

5.5.1 Macro-scale fracture behaviour

The macro-scale fracture behaviour of the WAAM IN625 specimens can be described by slow stable crack extension, characterised by a force plateau in the load-displacement curves (see Figure 5.16a and Figure 5.17a). This behaviour, which was observed in all three WAAM IN625 specimens, is distinct from the fracture behaviour of WAAM IN718 specimens described in Chapter 4.

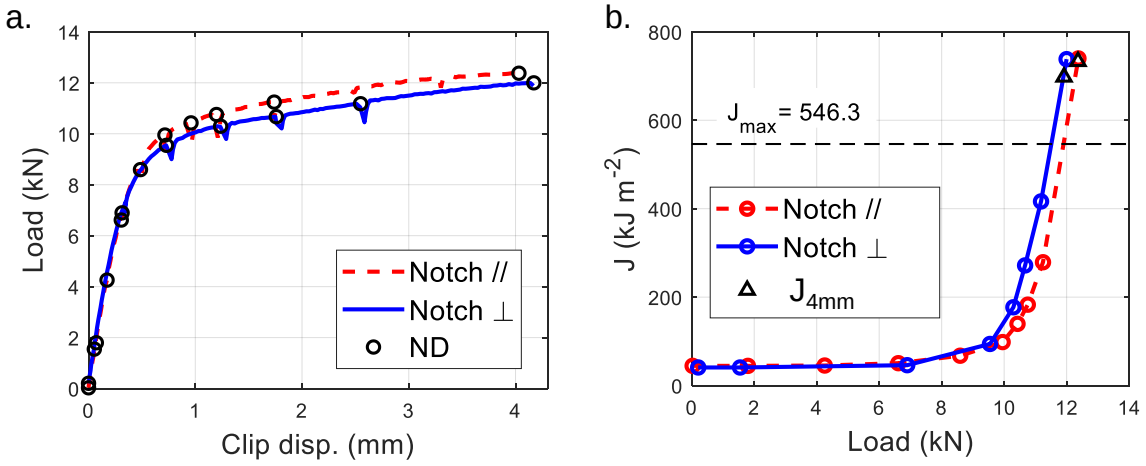

Figure 5.16: (a) Load-displacement and (b) J-load curves of WAAM IN625 specimens loaded in-situ on the SALSA neutron diffractometer. ND refers to neutron diffraction measurement point.

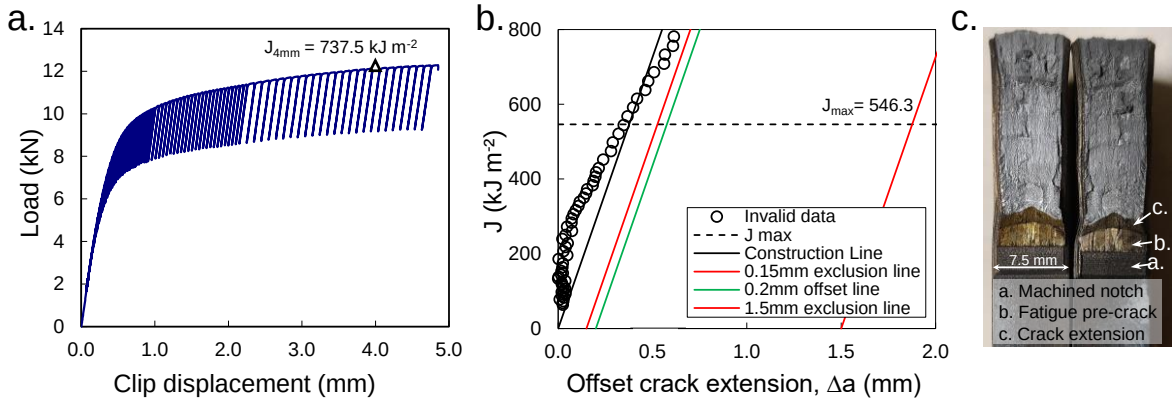

Figure 5.17: From the WAAM IN625 Notch // specimen tested using the unloading compliance procedure at TWI Ltd: (a) Load-displacement curves, (b) calculated J-Δa data points, and (c) fracture surface of heat-tinted specimen.

WAAM IN625 displayed high toughness in both notch orientations. The evolution of J for the specimens tested on SALSA is shown in Figure 5.16b. The average single-point J_{4mm} (i.e. J evaluated at a clip displacement of 4mm) across the three specimens is 722.8 kJ m^{-2}. However, due to the specimen geometry, the measurement validity is limited by J_{max}[2] of 546.3 kJ m^{-2}. It is also important to note that for this specimen geometry, clip displacement was measured at a distance from the load line, therefore the single-point values of J reported here may be an over-estimate of the true J of the material. Other J parameters (e.g. $J_{0.2BL}$, J_{IC}) could not be evaluated from the unloading compliance test, as the combination of the material's high toughness and the low J_{max} resulted in measurement points lying outside the exclusion lines (see Figure 5.17b). A summary of J values is shown in Table 5.3.

Table 5.3: Summary of fracture toughness measured from WAAM IN625 and IN718 specimens.

WAAM material	B (mm)	B_N[a] (mm)	Notch Orien.[b]	Fracture toughness (kJ m^{-2})			Crack ext.(mm)[e]
				J_{max}[c]	J_{4mm}[d]		
IN625	7.5	-	//	546.3	733.0		-
			⊥		697.8		
		6.4	//		737.5		1.085
				$J_{m(B)}$[f]	$J_{0.2BL(B)}$[f]	J_Q[g]	
IN718	20	-	//	257.9	229.7	208.1	2.796
			⊥	286.1	287.1	332.2	2.486

[a] Net specimen thickness after sidegrooving.

[b] With respect to the build direction, as described in Chapter 4.

[c] Maximum J measurement capacity for the specimen geometry.

[d] J evaluated at 4 mm of clip displacement.

[e] Weighted crack extension.

[f] As defined in ISO 12135:2016 [227].

[g] As defined in ASTM E1820-18ae1 [110].

WAAM IN718 displayed "semi-stable" crack extension, characterised by the variable load drops with increasing displacement, as described in Chapter 4 and shown in Figure 5.18a. The Notch ⊥ specimen displayed a higher toughness than the Notch // specimen, for three measures of J (i.e. J_m, $J_{0.2BL(B)}$, and J_Q), as summarised in Table 5.3. Although these values are unqualified as size-insensitive parameters (i.e. $J_{0.2BL}$, and J_{IC}), they can be treated as size-sensitive measures of fracture toughness. The significance and validity of these parameters are

[2] J_{max} is the maximum J capacity for a specimen geometry.

discussed in Chapter 4. The resistance curves of the WAAM IN718 Notch // and ⊥ specimens are shown in Figure 5.18b and c respectively.

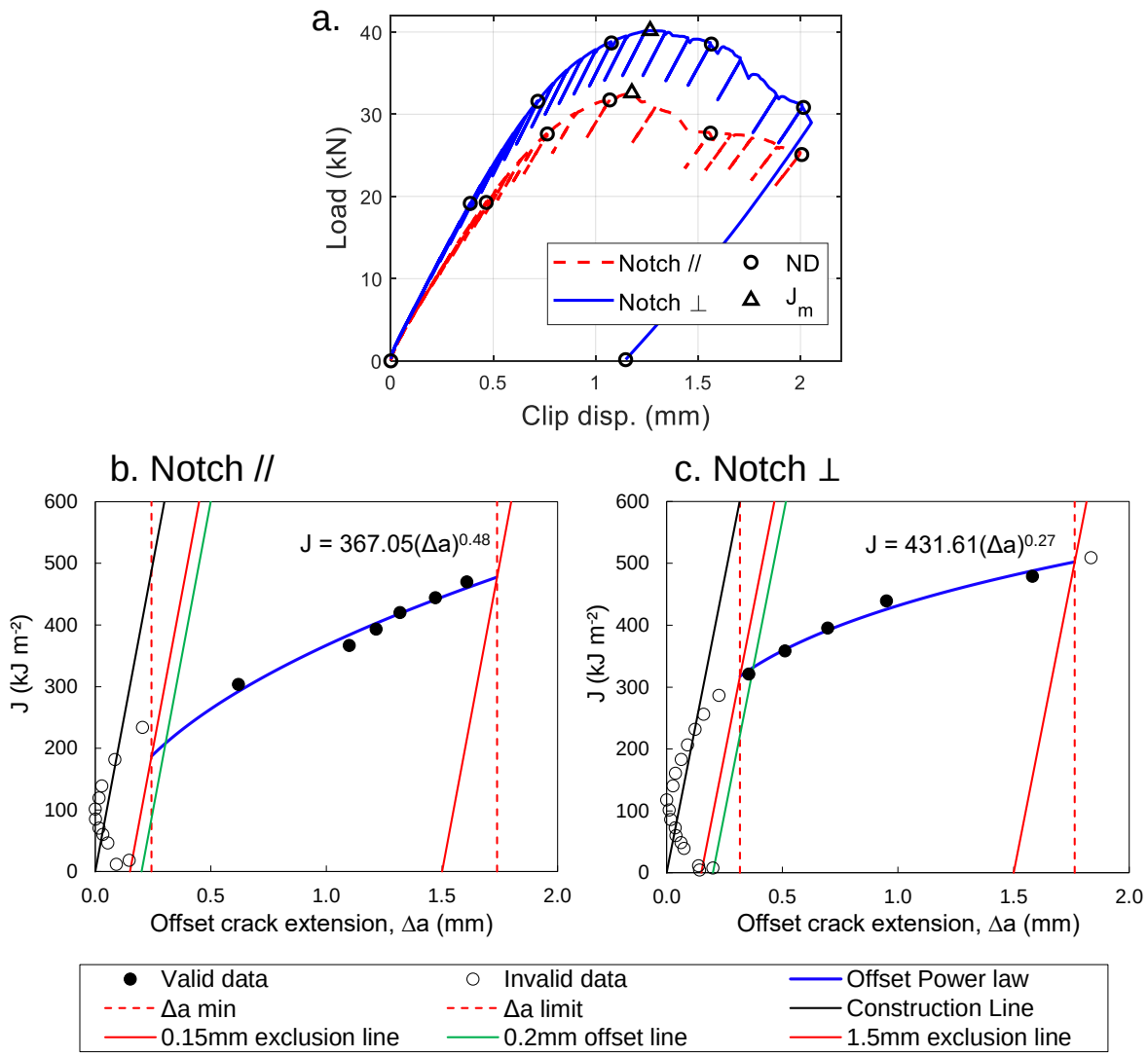

Figure 5.18: (a) Load-displacement curves from WAAM IN718 specimens tested on the SALSA neutron diffractometer; and the corresponding resistance curves for (b) Notch // and (c) Notch ⊥ specimens.

Unlike the specimens reported in Chapter 4, severe crack-like defects were not observed in the fracture surfaces of WAAM IN718 samples tested on SALSA. The specimen fracture surfaces as observed after post-test analysis (i.e. heat tinted and broken open) are shown in Figure 5.19. Therefore, the higher toughness of the Notch ⊥ specimen is likely due to microstructural effects, which are discussed in Section 5.6.2. Crack front measurements at the three planes of

specimen thickness used for neutron measurements are shown in Figure 5.20. The final crack length at -5 mm, midplane and +5 mm of specimen thickness are very similar, for both specimens.

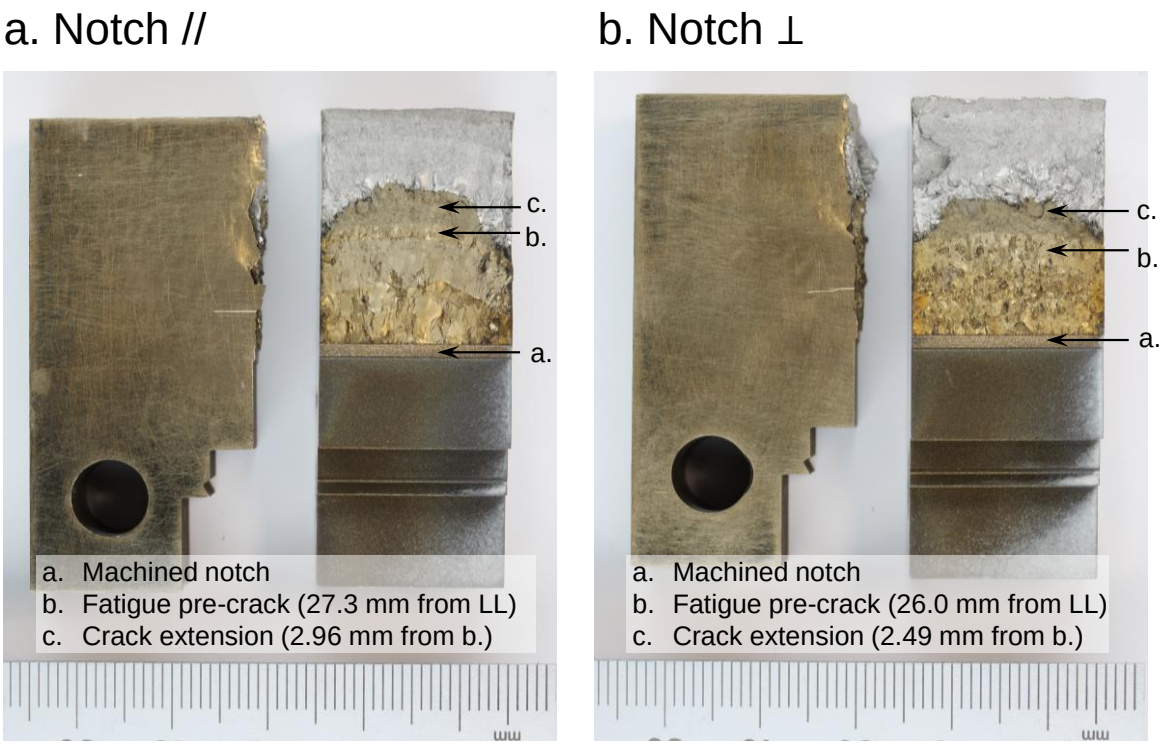

Figure 5.19: Fracture surfaces of WAAM IN718 (a) Notch // and (b) Notch ⊥ specimens.

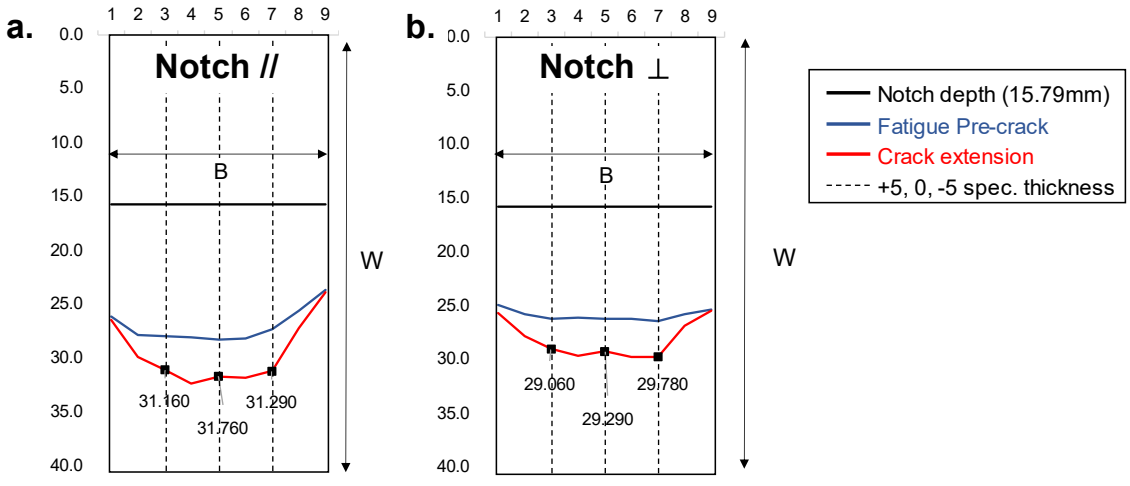

Figure 5.20: Crack front measurements for WAAM IN718 (a) Notch // and (b) Notch ⊥ specimens. Data labels show crack front measurements at the -5 mm, midplane and +5 mm of specimen thickness.

5.5.2 Meso-scale fracture behaviour

WAAM IN625 display meso-scale behaviour around the crack tip that are different in the Notch // and Notch ⊥ orientations, as can be observed in the crack tip deformation patterns (see Figure 5.21) and the total surface strain measured by DIC (see Figure 5.22).

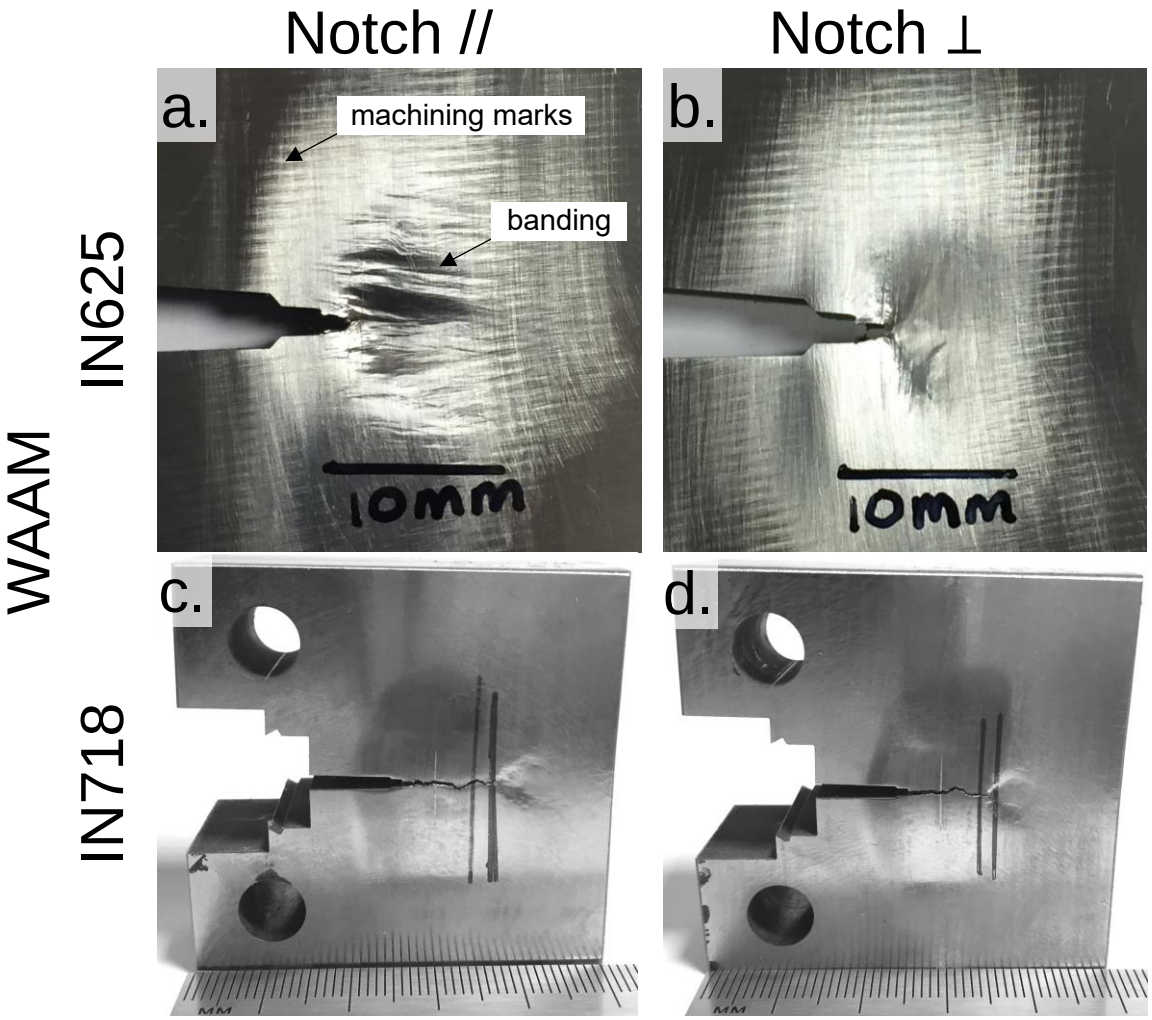

Figure 5.21: Crack-tip macrographs of post-test C(T) specimens of WAAM IN625 (a, b) and IN718 (c, d) with Notch // (a, c) and Notch ⊥ (b, d) to the build direction. Note that speicmens here are in the fully unloaded state.

Around the crack tip, banding was observed on the surface of the Notch // specimen in both the deformation and strain distributions, occurring parallel to the crack propagation direction (also WAAM build direction for Notch //). In contrast, this banding behaviour was not observed in the Notch ⊥ specimen. This may be attributed to differences in notch orientation

with respect to the material's grain structure, which are discussed in Section 5.6.1. Banding behaviour was also absent in WAAM IN718. This can be attributed to the different grain structure of the IN718 specimens, which is a result of the modified homogenisation and aging heat treatment as described in Chapter 3.

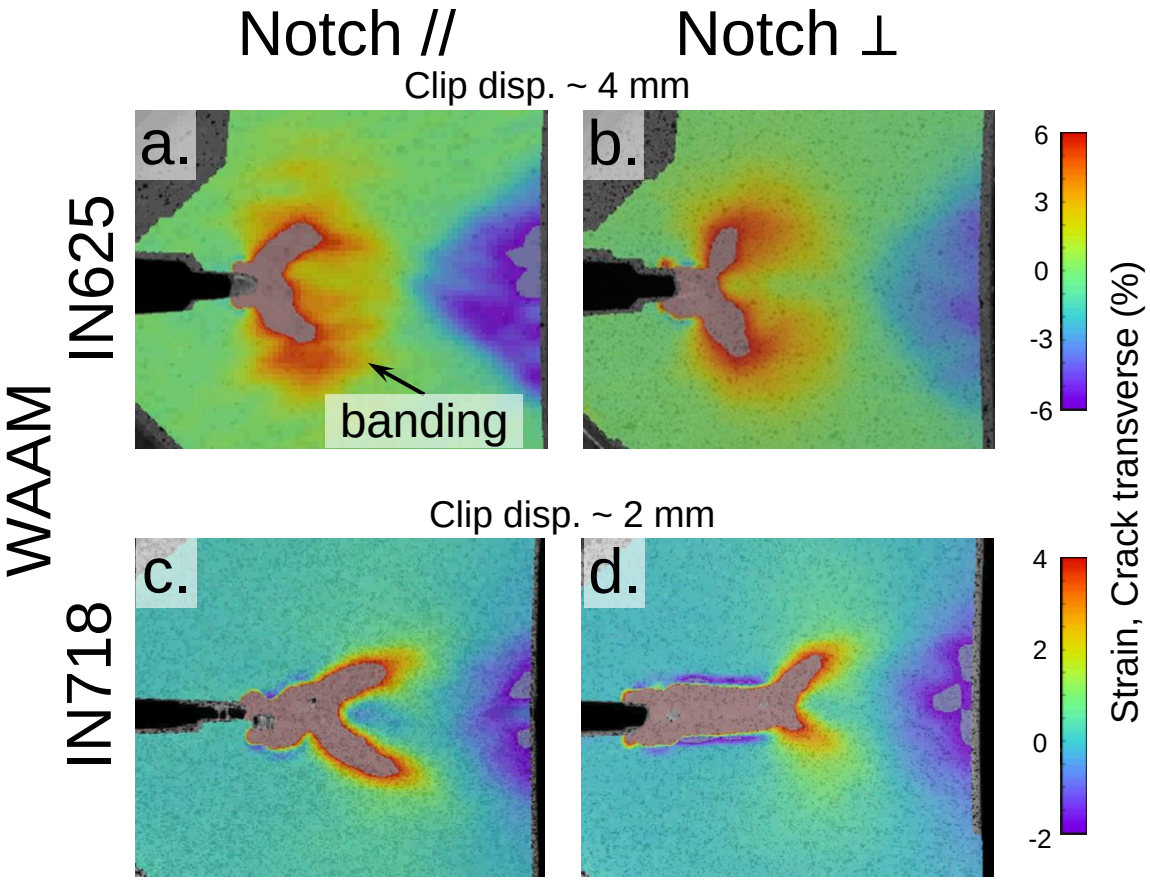

Figure 5.22: Total strain (measured by DIC) in crack transverse direction (ε_{yy}) of WAAM IN625 (a, b) and IN718 (c, d) specimens, Notch // (a, c) and Notch ⊥ (b, d) to the build direction, at their maximum clip displacements. Grey areas correspond to regions which have exceeded the max/min strain values indicated in the colour bars (note that these are different for a,b and c,d).

5.5.3 Lattice-scale behaviour

5.5.3.1 Lattice strain distribution

The lattice strain distributions for both WAAM IN625 and IN718 materials (see Figure 5.23 Figure 5.24 respectively) are in good general agreement with the total strain distributions (shown in Section 5.5.2), where there is a region of tension ahead of the crack tip and compression at the back face of the specimen. The lattice strain magnitudes were found to be

in good agreement with those[3] in the published literature (i.e. ~4000 με for IN625 [287], ~8000 με for IN718 [288], [289], [290] for the {200} reflection). It is important to note that, under in-situ loading, lattice strains are expected to be higher than residual lattice strains; and the larger lattice strain magnitudes are expected for WAAM IN718, due to the higher yield and ultimate tensile strengths than WAAM IN625.

The lattice strain distributions at different loading steps for WAAM IN625 and IN718 are shown in Figure 5.23 and Figure 5.24 respectively. As instantaneous crack length was not measured for the WAAM IN625 specimens, the length of the initial crack (fatigue pre-crack) is illustrated on the lattice strain maps in Figure 5.23. Nonetheless, the crack extension in these specimens is likely to be small, as the maximum lattice strain measured just ahead of the initial crack tip intensifies without shifting towards the right throughout the loading regime. In addition, an estimate of the crack extension in these specimens can be taken from the WAAM IN625 specimen tested at TWI Ltd. It displayed 1.085 mm of total crack extension, which is slightly over half the width of the neutron gauge volume. Therefore, similar levels of crack extension in the WAAM IN625 specimens tested on SALSA would not manifest in the lattice strain distributions.

For the WAAM IN718 specimens, the instantaneous crack length was measured from the partial unloads, and is illustrated on the lattice strain maps in Figure 5.24. Evidence of crack extension can also be observed from these lattice strain maps, which manifests as an intensification of strain as the crack tip approaches and subsequent progression into compression when the crack extends past the measurement points. Note that the strain maps in Figure 5.24 show strain measurements from three specimen thickness planes (i.e. -5 mm, midplane, +5 mm). Most of the measurement points were non-overlapping (i.e. different coordinates). For the few that were overlapping an average strain is shown instead.

Lattice strain was measured to be more than 8,000 με for a few measurement points in the WAAM IN718 specimens. There are two possible causes for this: the first, observed in the Notch // specimen, is the occurrence of "double spots" in the detector image (example shown in Figure 5.25a) from the neutron measurement, which is indicative of the neutron gauge volume encompassing two clusters of scattering crystallites. For the affected measurement points, strains were found to be around 10,000-12,000 με, which is beyond what is expected for

[3] Refers to the maximum lattice strains measured in uniaxial tensile tests.

the material's strength, and have been greyed out in Figure 5.24a. The second, observed in the Notch ⊥ specimen, can be attributed to localised areas of very high strain, possibly due to specific crystallites taking up a larger share of load. These measurement points, which displayed lattice strains around 8,000-8,500 με, lacked the aforementioned "double spots" (see Figure 5.25b). In addition, they are located close to the crack tip, which is where the strains are expected to be the highest.

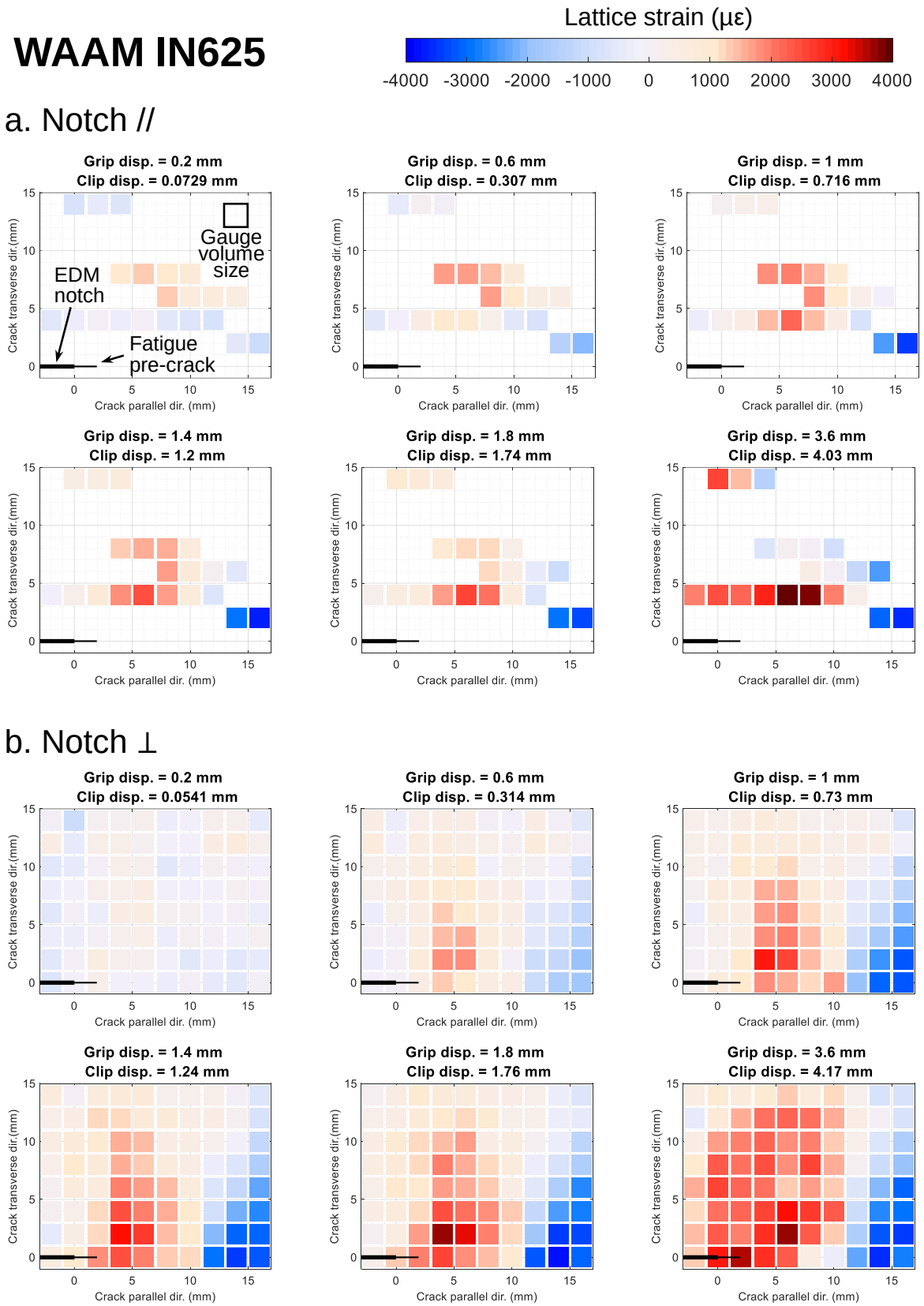

Figure 5.23: Lattice strain maps from WAAM IN625 (a) Notch // and (b) Notch ⊥ specimens, measured on SALSA with in-situ loading and crystallite tracking.

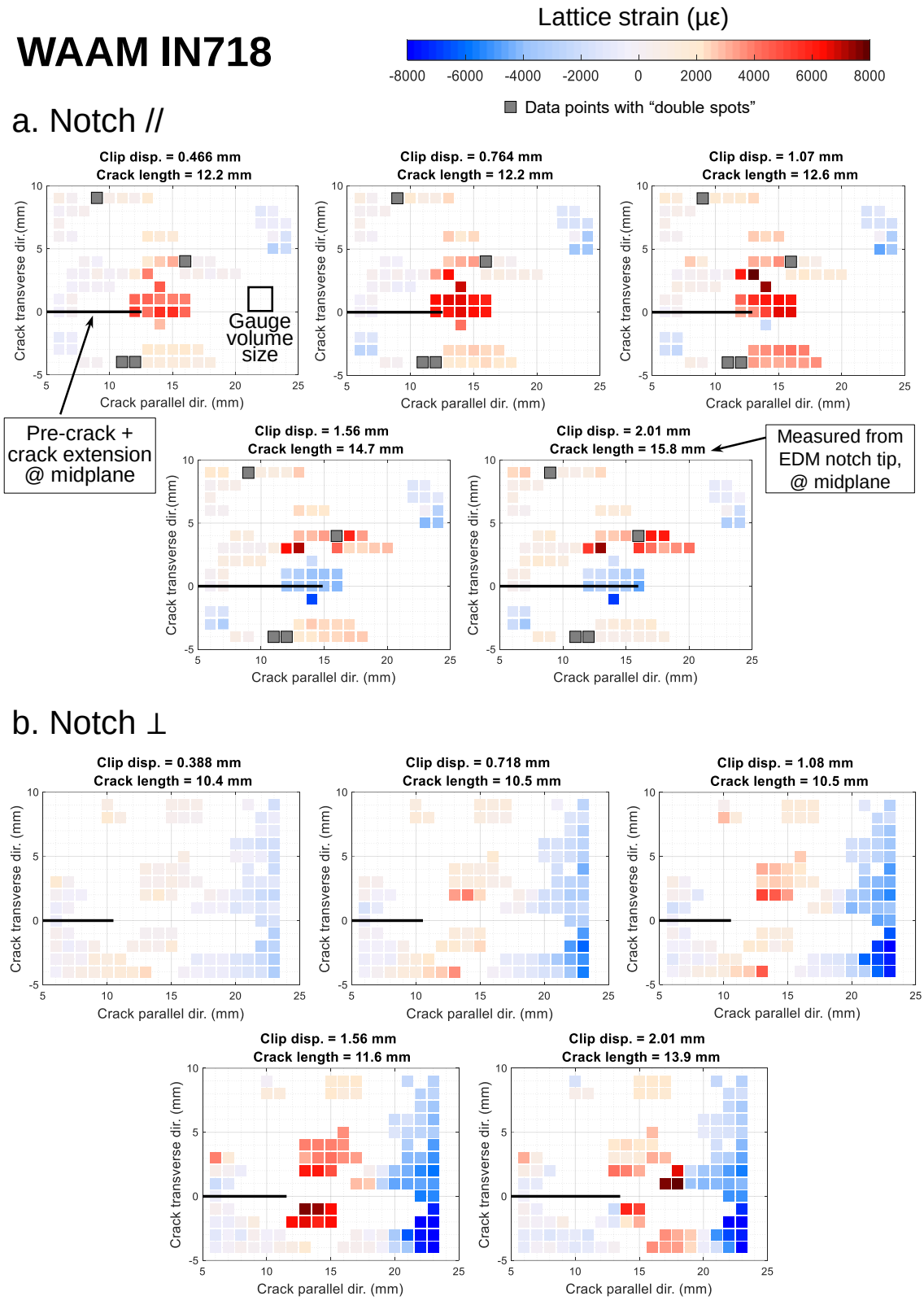

Figure 5.24: Lattice strain maps from WAAM IN718 (a) Notch // and (b) Notch ⊥ specimens, showing strain measurements from three specimen thickness planes. Note that the crack length stated here is the length at the midplane of the specimen.

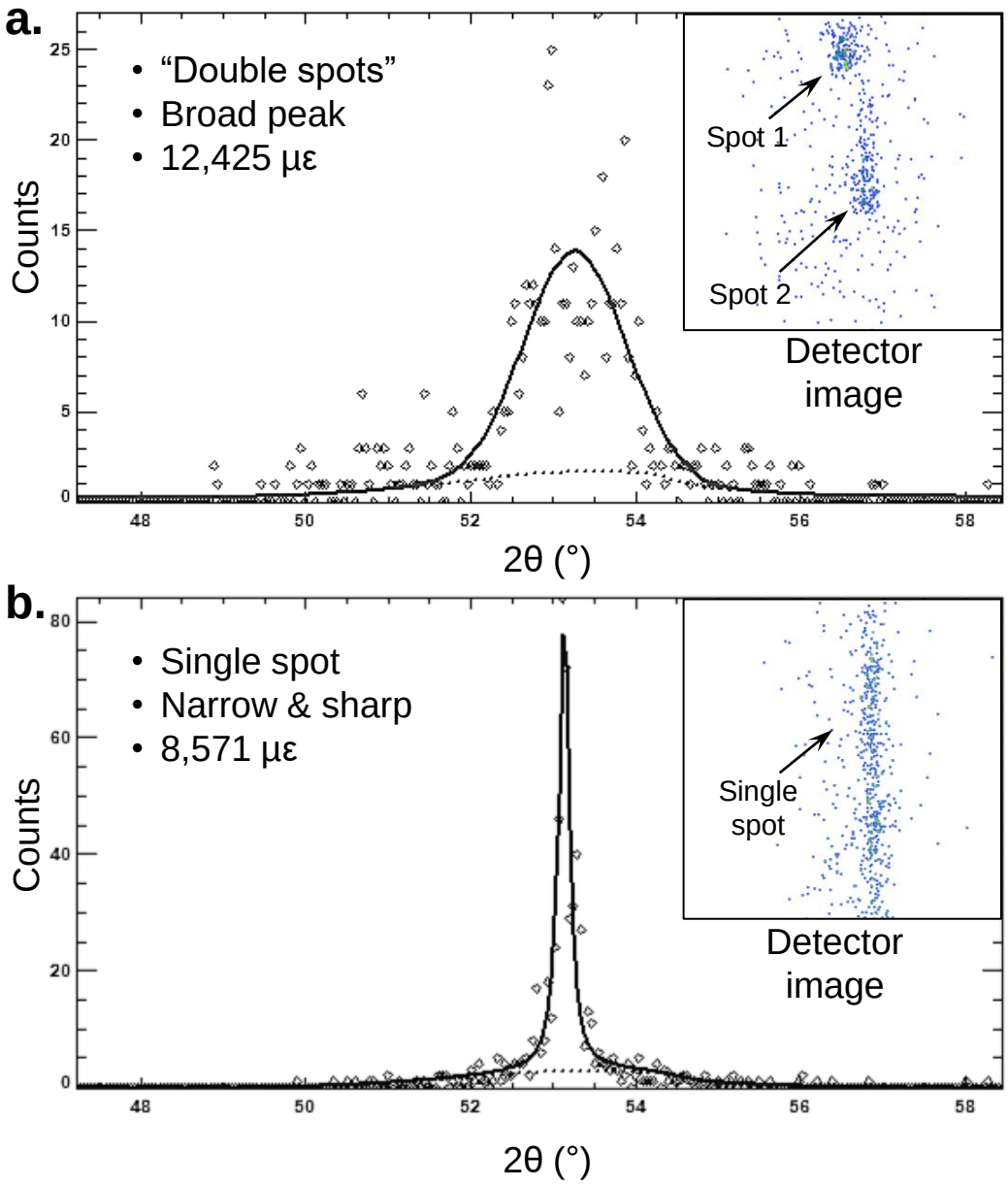

Figure 5.25: Example detector images and fitting patterns from WAAM IN718 measurement points with high lattice strains, (a) with and (b) without "double spots".

5.5.3.2 *Lattice strain evolution*

The lattice strain evolution in both WAAM IN625 and IN718 materials display "grouped" behaviour, where distinct evolution patterns can be observed from different groups of measurement points. This lattice strain evolution is shown in Figure 5.26(a, b) and Figure 5.27(a, b) for the WAAM IN625 and IN718 specimens respectively. The "grouping" of these measurement points corresponds to clusters of similarly oriented crystallite(s), deduced from the respective intensity plots, as shown in Figure 5.26(c, d) and Figure 5.27(c, d).

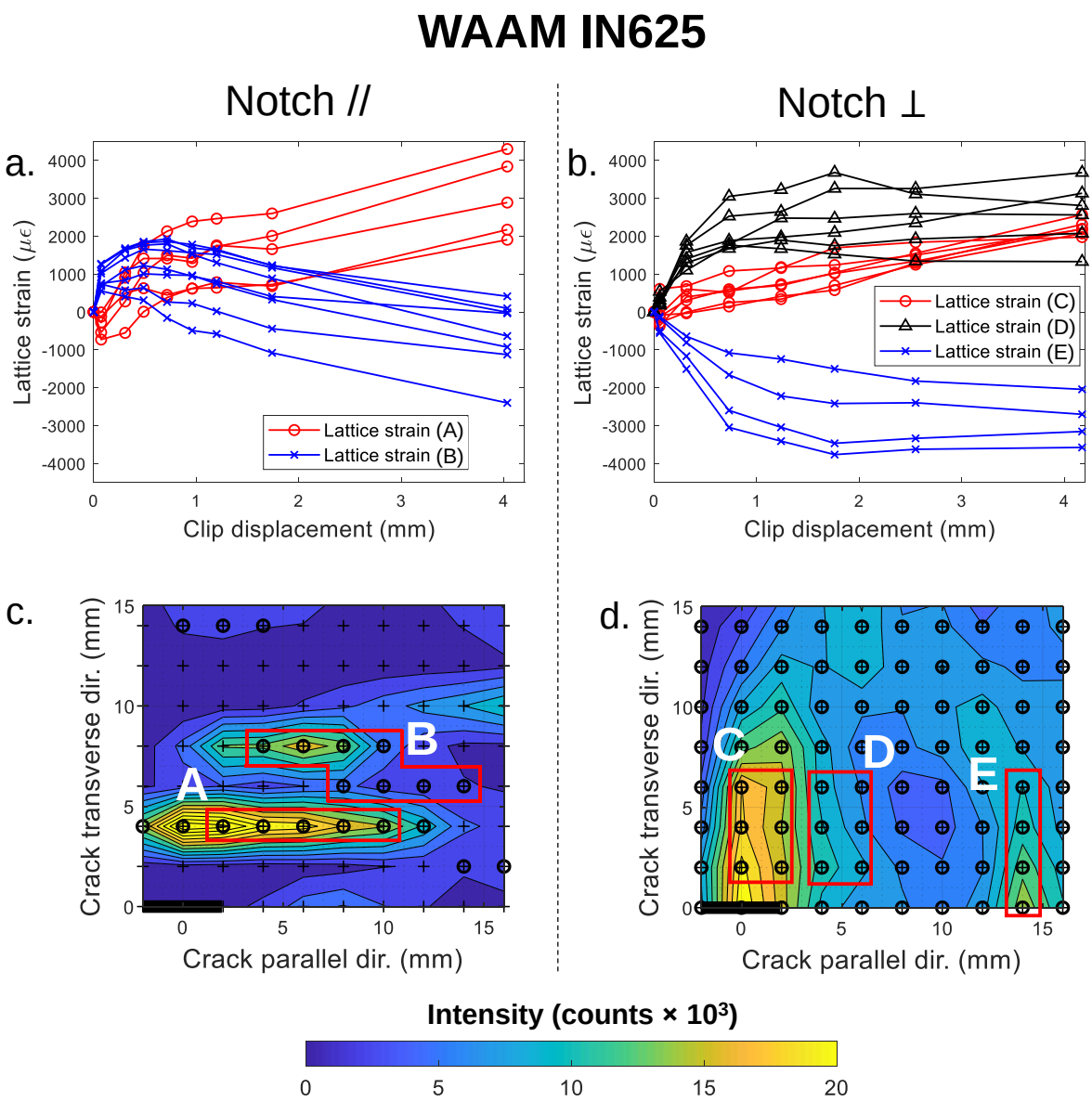

Figure 5.26: Lattice strain evolution of Groups A, B, C, D and E, (a) Notch // and (b) Notch ⊥ WAAM IN625 specimens, and their corresponding lattice strain intensity (c, d) maps.

For the WAAM IN625 specimens, the lattice strain evolution of most of the measurement points are monotonic. However, the lattice strains in Group B (see Figure 5.26a) initially increase in tension, then decrease into compression towards the end of the loading regime. Although non-monotonic lattice strain evolution is usually observed when a crack extends past a measurement point, this is unlikely to be the cause as the crack extension in this specimen is small. One possible reason for the non-monotonic behaviour of Group B is intergranular interaction between clusters of crystallites, causing load to be shed away from this cluster of crystallite(s) to another. Deformation of neighbouring crystallites could also cause these crystallites to go into compression.

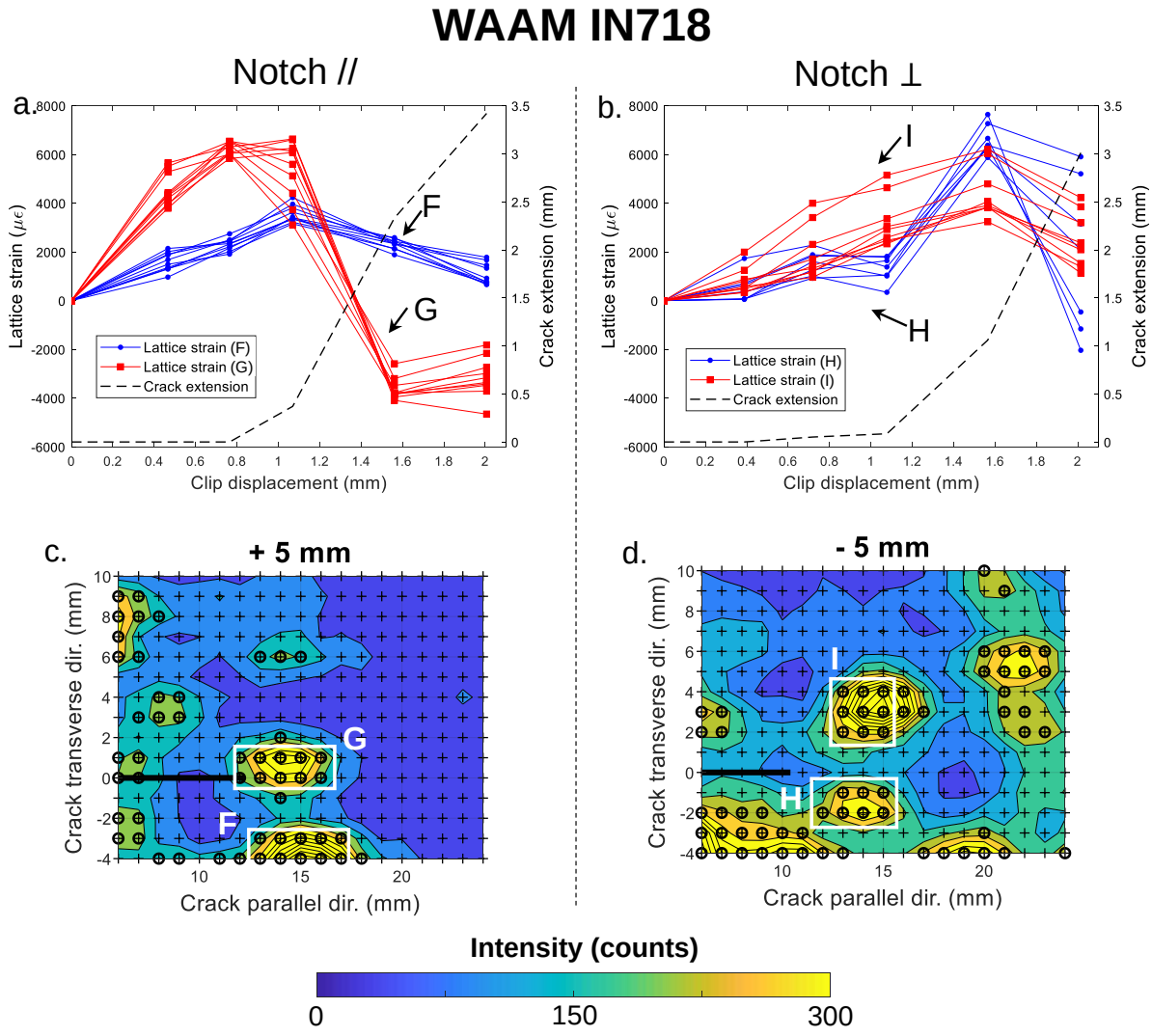

Figure 5.27: Lattice strain of Groups F, G, H and I, in (a) Notch // and (b) Notch ⊥ WAAM IN718 specimens, and their corresponding intensity maps (c, d).

In addition, lattice strains in Groups C, D and E in Figure 5.26b display an evolution pattern dependent on their proximity to the crack tip. Groups C and D, which are nearer to the crack tip, display tensile lattice strains which increase with load. However, Group E, which is the furthest from the crack tip, and hence nearer to the back face of the specimen, display compressive lattice strains which increase in magnitude with increasing load.

For the WAAM IN718 specimens, the lattice strain evolution patterns were observed to be non-monotonic as shown in Figure 5.27(a, b). The onset of non-monotonic behaviour in the lattice strains is closely aligned with the start of crack extension, indicating that the relaxation and redistribution of elastic strain caused by the propagating crack has contributed to the lattice strain evolution patterns.

5.6 Discussion

5.6.1 Microstructural effects in WAAM IN625

One explanation for the banding in the deformation and total strain distribution around the crack tip in the WAAM IN625 Notch // specimen, described in Section 5.5.2, is the orientation of the notch with respect to the material's grain structure. The grain structure of the post-test WAAM IN625 specimens are shown in Figure 5.28. The Notch // specimen is notched parallel to the long axis of the columnar grains, and the direction of the strongest texture (fibre texture). In contrast, the Notch $\perp$ specimen is notched perpendicular to the long axis of the grains and in the direction of the weaker texture. Sub-grain boundaries, which are indicative of stored dislocations caused by intergranular strain, were observed to form in the appearance of slip bands along the columnar grains. The positions of these slip bands can be more easily visualised in the Local Misorientation (LM) maps shown in Figure 5.28(b, d). These suggest that the slip bands cluster in horizontal bands in the Notch // specimen, and are more spread out in the Notch $\perp$ specimen. Although direct quantitative comparisons between the total strain (measured by DIC) and the dislocation densities from LM maps cannot be made [291], these dislocation patterns are in good general agreement with the banding observations discussed in Section 5.5.2.

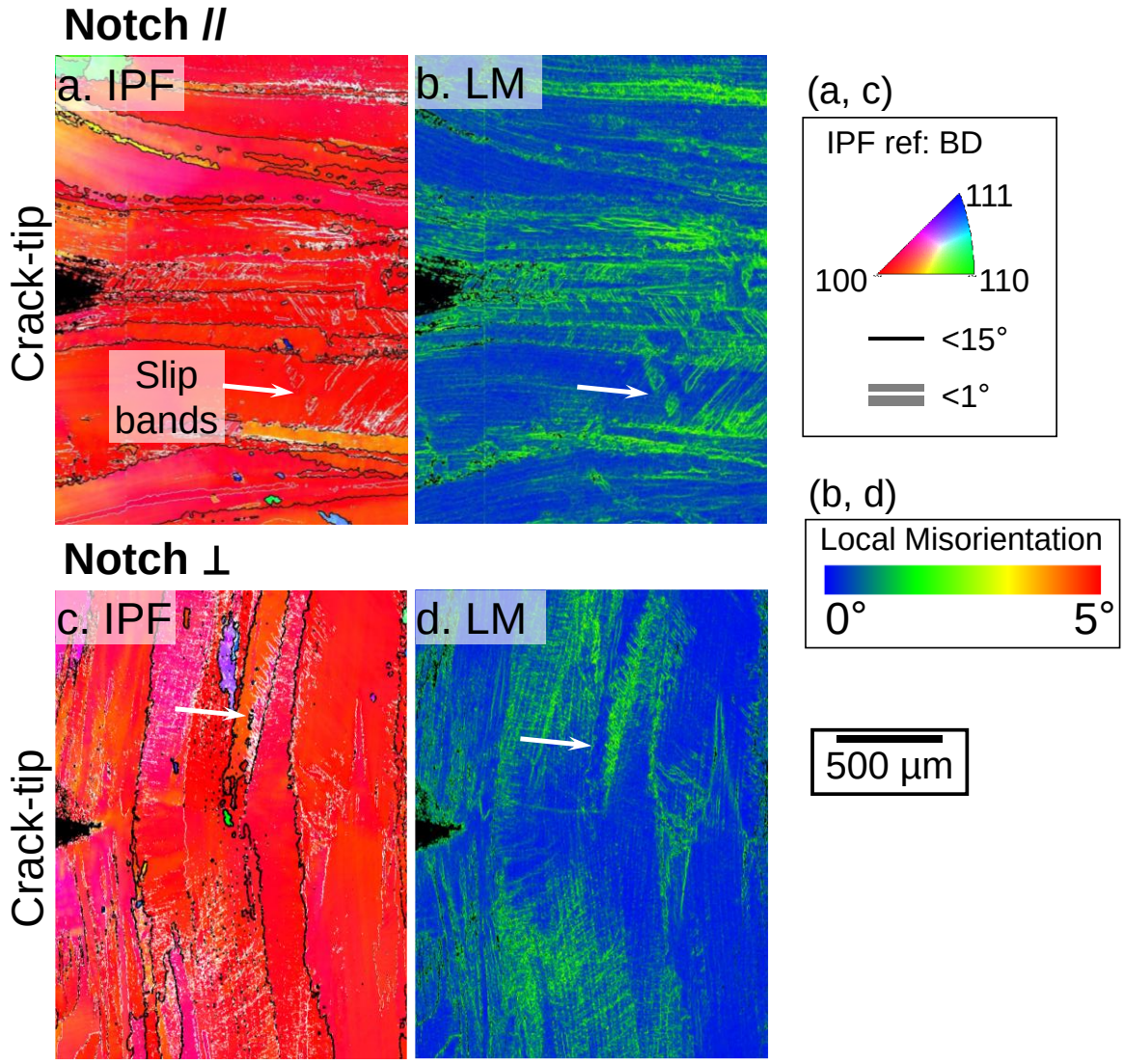

Figure 5.28: EBSD (a, c) and local misorientation (b, d) maps of post-test WAAM IN625 specimens, taken at specimen midplane, Notch // (a, b) and Notch ⊥ (c, d) to the build direction.

5.6.2 Influence of crack-like defects in WAAM IN718

The WAAM IN718 samples reported here were extracted from Wall 1 (ie same material batch used in Chapter 3 and Chapter 5, which unlike those in Chapter 4, did not show indications of severe crack-like defects on the fracture surface. This can be attributed to the more favourable deposition conditions used during the manufacture of this batch of material (described in Chapter 3), which are different to those used for the characterisation of crack-like defects and their resulting fracture toughness (described in Chapter 4). Nonetheless, there is a possibility that micro-scale hot cracking may have taken place in these fracture specimens, as indicated by the presence of small areas of liquid films and dendritic features found in the fractographs from

these specimens (see Figure 5.29). However, the contribution of these micro-scale hot cracks is likely to be smaller than that of anisotropy of grain structure, due to them being an order of magnitude smaller than the grain size of the material.

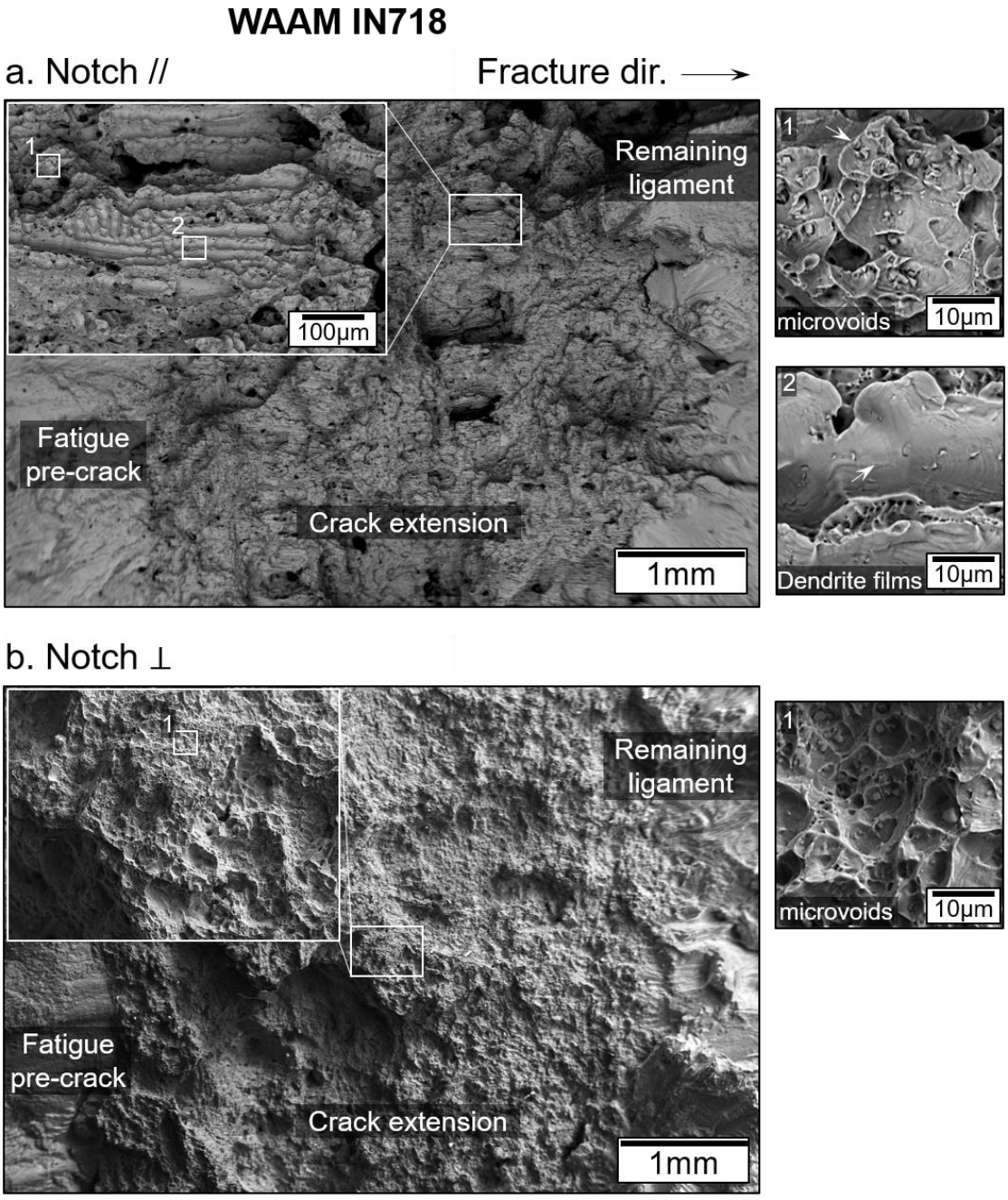

Figure 5.29: Fractographs from WAAM IN718 (a) Notch // and (b) Notch ⊥ specimens.

5.6.3 Limitations of angle dispersive diffraction

In this study, two types of WAAM microstructures are considered, WAAM IN625 is columnar grained and strongly textured, whereas WAAM IN718 (in the heat-treated condition) is coarse grained and weakly textured. Both types of microstructures were found to be unfavourable for angle dispersive neutron diffraction, due to the lack of suitably scattering grains around the crack tip, in the strain direction of interest (i.e. crack transverse direction), for the selected diffraction plane. This is demonstrated in the intensity plots in Figure 5.14.

However, the presence of a strong texture was observed to mitigate the unavailability of suitably scattering grains. In both the WAAM IN625 and IN718 materials, the Notch $\perp$ specimens displayed more measurement points with high intensity counts than their Notch // counterparts, indicating that there were more suitably scattering grains in those specimens. This can be attributed to the stronger texture in the build direction, which coincides with the strain direction of interest in these specimens.

Using angle dispersive diffraction methods, single-peak measurements are obtained from a fraction of the measurement gauge volume. In fine-grained polycrystalline materials, there are usually many suitably-oriented crystallites within the gauge volume. However, in large-grained materials, there are far fewer suitably-oriented crystallites for each diffraction plane. This is the main limitation of using angle dispersive diffraction methods on such materials. Although it is possible to obtain measurements from several diffraction planes using angle dispersive methods, (e.g. using either multiple detectors or taking measurements at various detector angles), this is not currently practical or time-efficient to implement with in-situ loading. Alternatively, time-of-flight diffraction provides the benefit of measuring several peaks in the diffraction spectrum, potentially avoiding the issue of unavailability of suitably scattering grains.

5.6.4 Comparisons with a Crystal Plasticity Finite Element model

The interpretation of lattice strain distribution and evolution can be aided by Crystal Plasticity Finite Element (CPFE) modelling [292]. A preliminary analysis was conducted for WAAM IN625 and the workflow is shown in Figure 5.30. A Finite Element (FE) model of a C(T) specimen relies on three key inputs: (i) a polycrystal material model, (ii) specimen geometry and (iii) applied load data. Material models for conventional materials are not applicable to WAAM materials due to their unique microstructures and weakly anisotropic tensile properties [293]. Therefore, a WAAM-specific polycrystal material model was tuned using crystallographic orientation data and tensile properties measured from WAAM IN625. This polycrystal material model assumes that the WAAM material has a perfect fibre texture, (i.e. grains are rotated randomly about their long axis). From the FE model of the C(T) specimen, total strain at a point (on the surface of the specimen) was extracted and compared against the experimental surface strains measured from DIC. Although lattice strains cannot be derived directly from the FE model of a C(T) specimen, the total strain at any point within the specimen can be applied to a single crystal material model, from which the crystal's stress state was derived. This stress state was then converted into elastic lattice strain and compared against experimental elastic lattice strain data measured from neutron diffraction.

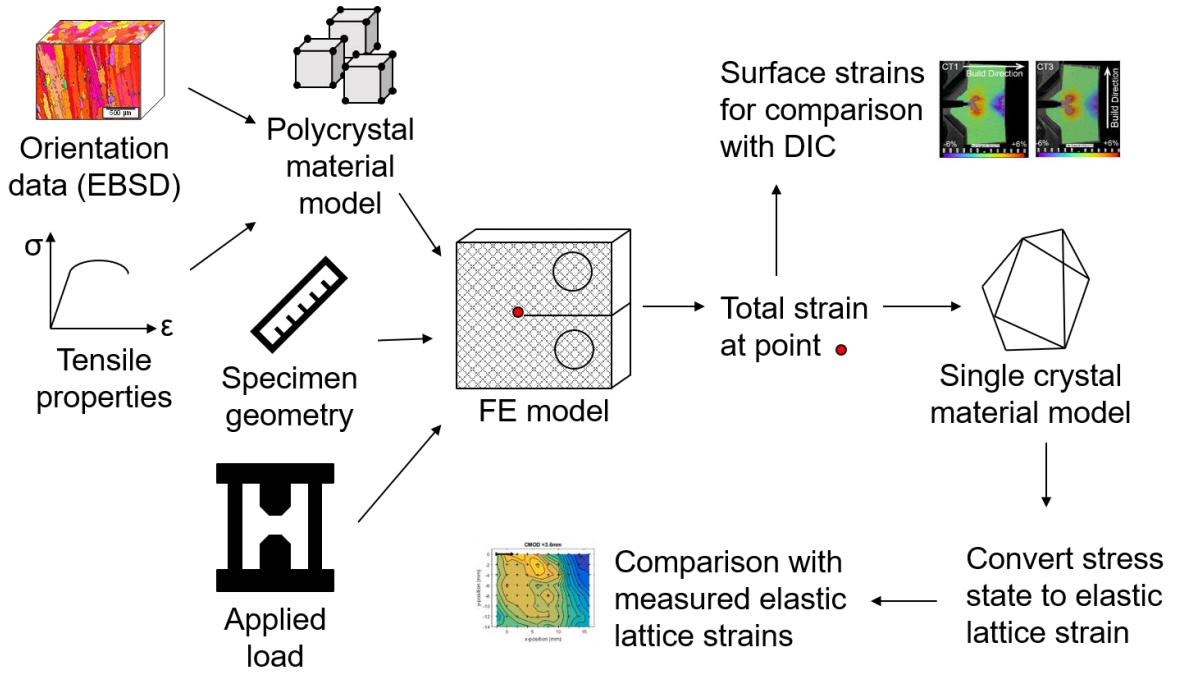

Figure 5.30: Data flow in and out of CPFE model used for comparison with total (surface) and lattice strains.

The results of CPFE reflect similar trends to the experimental measurements for both the total (surface) and elastic lattice strains. The surface strain comparisons between the CPFE results and DIC measurements for the WAAM IN625 C(T) specimens at 4 mm clip displacement is shown in Figure 5.31. Around the crack tip, the region of tensile surface strain predicted by CPFE is similar to that measured by DIC, for both specimens. CPFE also predicts that the region of high tensile strain (i.e. > 5%), is smaller in the Notch // specimen than the Notch ⊥ specimen, in agreement with the measured surface strains. The surface strain distribution predicted by the CPFE model does not display banding patterns for the Notch // specimen (described in Section 5.5.2 and shown in the DIC map in Figure 5.3la), as the CPFE model is based on continuum mechanics and treats the specimen as a continuous distribution of material points, which does not account for point-to-point variations caused by grain-level interactions that are likely to be the cause of the banding patterns observed in the experimental measurements.

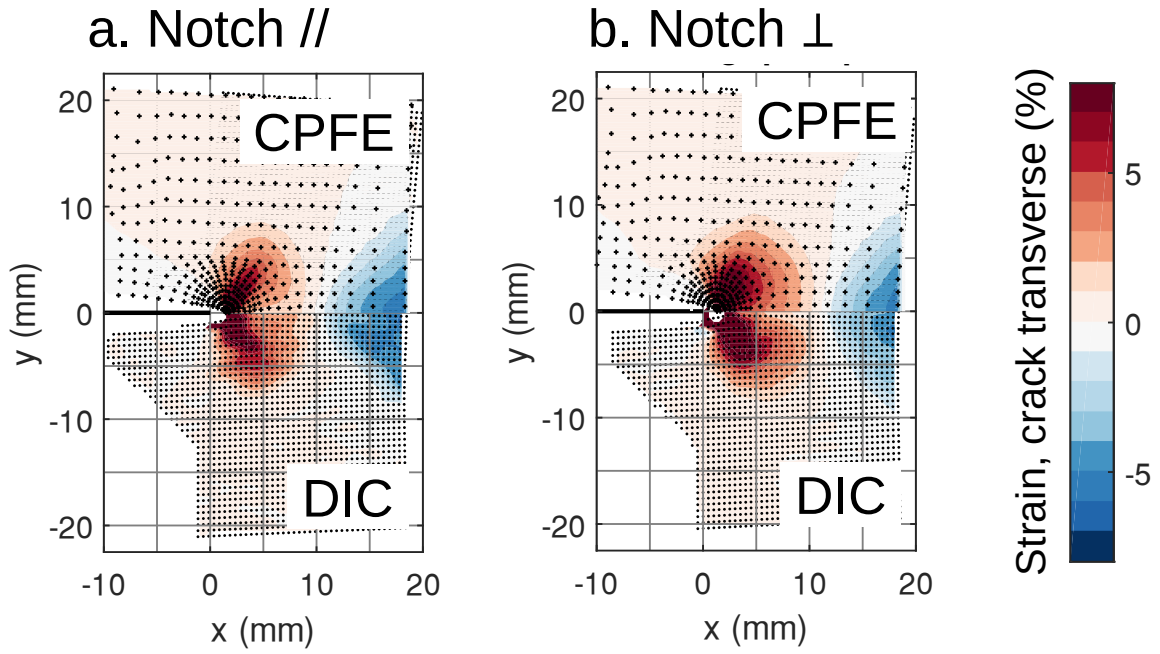

Figure 5.31: Surface total strain predicted by CPFE and measured by DIC, of WAAM IN625 C(T) specimens with (a) Notch // and (b) Notch ⊥, at clip displacement of 4mm.

The elastic lattice strain evolution predicted by CPFE for the WAAM IN625 Notch // and Notch ⊥ specimens display the same trend as the experimental results, as shown in Figure 5.32 and Figure 5.33 respectively. However, as the predictions by CPFE do not account for point-to-point variations caused by grain-level interactions, "grouped" behaviour described in Section

5.5.3.2 is not displayed in the CPFE results. This discrepancy between the CPFE and experimental data demonstrating this is most obvious in Groups A, B and C (see Figure 5.32a,b and Figure 5.33a). These results indicate that the crystallite tracking method for experiments, combined with CPFE is a viable way forward for investigating the lattice strain behaviour in WAAM materials.

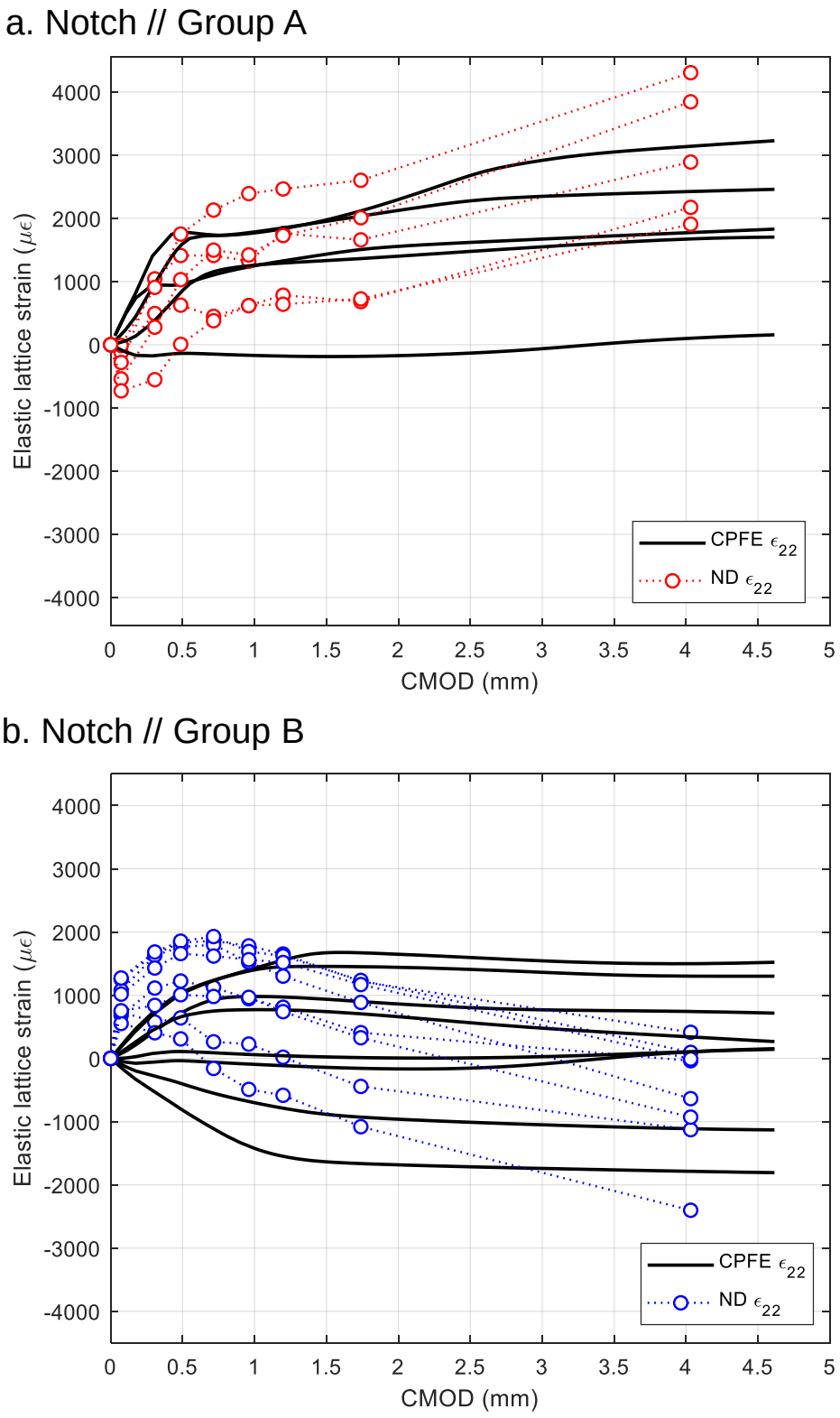

Figure 5.32: Elastic lattice strain evolution of Groups (a) A and (b) B in the WAAM IN625 Notch // specimen, extracted from CPFE and measurements from neutron diffraction experiment. Each line represents the strain evolution of one measurement point. The solid line represents data extracted from the CPFE and the circular markers represent measured lattice strain data.

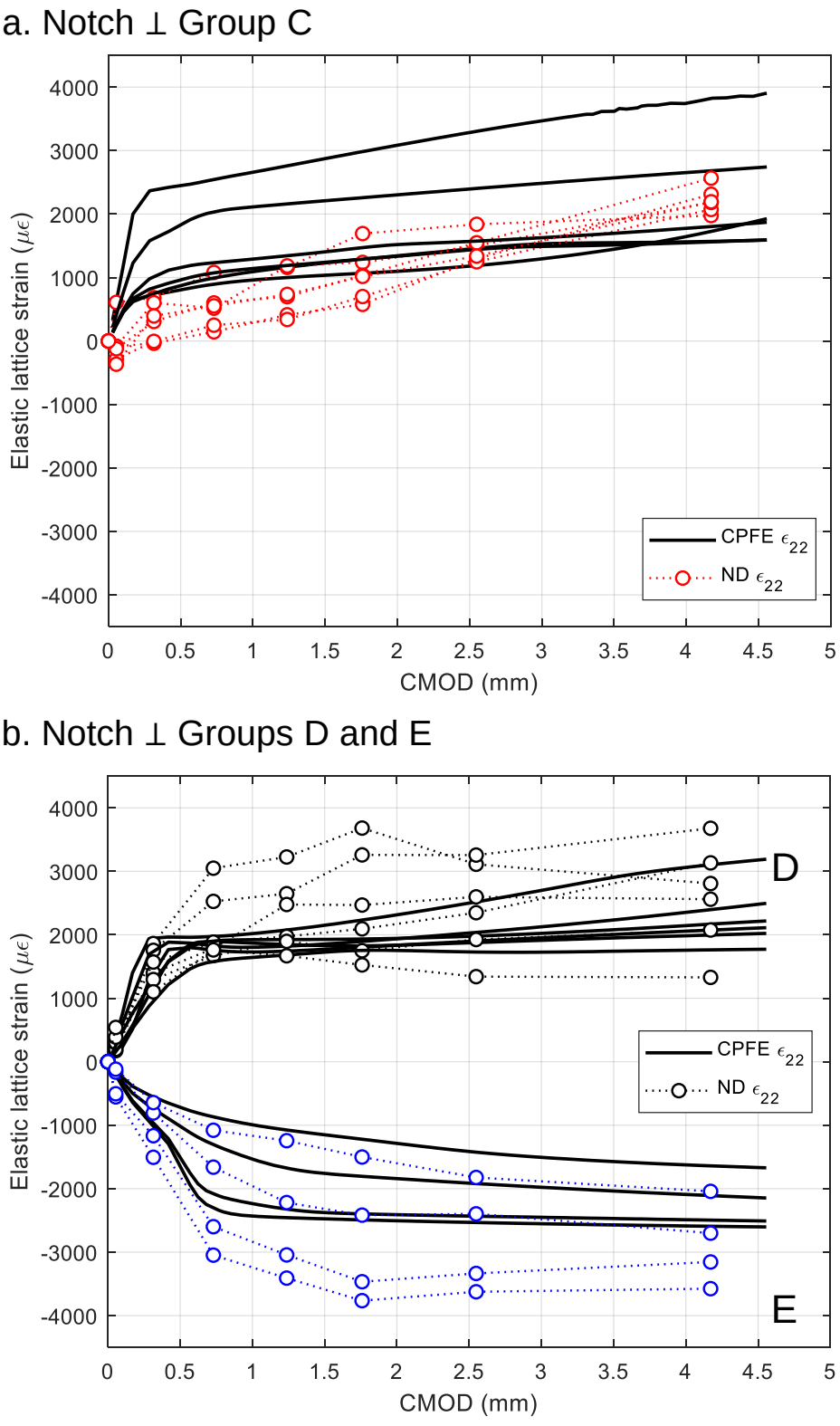

Figure 5.33: Elastic lattice strain evolution of Groups (a) A and (b) B in the WAAM IN625 Notch ⊥ specimen, extracted from CPFE and measurements from neutron diffraction experiment. Each line represents the strain evolution of one measurement point. The solid line represents data extracted from the CPFE and the circular markers represent measured lattice strain data.

5.7 Conclusions

This work has shown that the coarse-grained microstructures of WAAM IN625 and IN718 materials present challenges for experimental determination of strain fields around a crack tip, using conventional methods, during in-situ loading. A novel crystallite tracking methodology has been found to be effective in accounting for the movement of the sample with respect to the measurement gauge volume. In addition, the following conclusions can be drawn from this work:

1. The macro-scale behaviour of WAAM IN625, notched parallel and perpendicular to the build direction, was relatively similar. In both notch orientations, WAAM IN625 displayed stable ductile crack extension and had a high resistance to fracture.
2. The meso-scale behaviour of WAAM IN625, observed from total surface strain (i.e. DIC) measurements, was found to be anisotropic. Banding patterns were observed only in the specimen notched parallel to the build direction. The meso-scale behaviour of WAAM IN718 was similar in both notch orientations.
3. On the lattice-scale, "grouped" elastic (lattice) strain behaviour was observed in both WAAM IN625 and IN718 materials, where clusters of similarly oriented crystallite(s) appear to display similar elastic (lattice) strain evolution.
4. The experimental measurements of total surface strain and elastic (lattice) strain for WAAM IN625 were found to be in good agreement with a crystal plasticity finite element model based on measured material properties.

These findings demonstrate that WAAM IN625 and IN718 materials display behaviour that is inherently different, on various length-scales, to conventional materials of the same composition. Therefore, it may not be appropriate to treat WAAM materials as homogeneous or isotropic continua, providing a basis for further investigation into the effects of material anisotropy on the micromechanics of WAAM materials.

Conclusions and further work

Wire and Arc Additively Manufactured (WAAM) nickel-base superalloys, Inconel (IN) 625 and 718, have micro-, meso- and macro-scale characteristics that are inherently different from their conventional (e.g. cast and wrought) equivalents. In the as-deposited condition, WAAM IN625 and IN718 have dendritic microstructures containing Nb-rich Laves phase and Ti-rich inclusions. They have coarse-columnar grain structures with a fibre texture, with <100> preferentially aligned in the build direction. They have weakly anisotropic tensile properties at both room and elevated (650 °C) temperatures.

Specialised post-deposition heat treatments, which address the unique microstructure of WAAM IN718, are crucial to achieving optimal mechanical properties. Several post-deposition heat treatment regimes were trialled to investigate their effects on the microstructure and tensile properties of WAAM IN718. Without any homogenisation heat treatments, standard aging heat treatments did not dissolve Laves phase into solid solution. Although standard homogenisation and solution heat treatments dissolved Laves phase, acicular δ phase precipitated at the grain boundaries, and resulted in poor elongation. A new modified homogenisation heat treatment successfully dissolved Laves phase without precipitating δ phase, resulting in a good combination of strength and ductility. The modified heat treatment also reduced the anisotropy in grain structure, leading to almost isotropic elevated temperature tensile properties, which meet minimum specifications for conventional cast material but not for wrought material.

Crack-like defects can occur in WAAM IN718 deposited under unfavourable conditions. The defects observed had hot cracking characteristics – they were found along high angle grain boundaries and had edges lined with Laves phase. The defects also had a planar morphology which was attributable to the WAAM deposition path; and were detectable using conventional non-destructive techniques (i.e. liquid penetrant, ultrasonic testing, X-ray radiography). The fracture behaviour of WAAM IN718 containing these defects was "semi-stable" – a mixture of fracture instability and stable crack extension. The apparent fracture toughness of WAAM IN718 containing these defects is anisotropic and can be attributed to the interaction of the notched crack with pre-existing defects. WAAM IN718 displayed an apparent fracture toughness comparable to that of wrought IN718 when notched perpendicular to the defects; but only half that of wrought when notched parallel to the defects. This demonstrates that the orientation of crack-like defects can have a large effect on the resulting apparent fracture toughness of WAAM Alloy 718. The effect of direction dependence should be an important consideration at various stages of materials characterisation for WAAM materials. This suggests that anisotropic fracture properties may need to be accounted for in the structural integrity assessment of parts made using WAAM superalloys.

Owing to the coarse-grained microstructures of WAAM IN625 and IN718, the experimental determination of strain fields around a crack tip under in-situ loading using conventional neutron diffraction methods is challenging in these materials. Nonetheless, a novel crystallite tracking methodology incorporating the use of Digital Image Correlation (DIC) with neutron diffraction is effective in accounting for the movement of the sample with respect to the measurement gauge volume, and experimental results on the macro-, meso- and lattice-scales were obtained. The results have demonstrated that it may not be appropriate to treat WAAM materials as homogeneous or isotropic continua, providing a basis for further investigation into the effects of material anisotropy on the micromechanics of WAAM materials. The macro-scale fracture behaviour of WAAM IN625 is similar in both notch orientations, characterised by stable ductile crack extension and a high resistance to fracture. The fracture behaviour of WAAM IN718 (in the absence of severe crack-like defects) is anisotropic, where the apparent fracture toughness when notched perpendicular to the build direction is higher across three different measures of J. Meso-scale behaviour, observed from total surface strain (i.e. DIC) measurements, was anisotropic in WAAM IN625 but isotropic in WAAM IN718, likely due to the differences in the grain structures. On the lattice-scale, clusters of similarly oriented crystallite(s) appear to have similar elastic (lattice) strain behaviour (i.e. "grouped" behaviour)

in both materials. The experimental measurements of total surface strain and elastic (lattice) strain for WAAM IN625 were found to be in good agreement with a crystal plasticity finite element model based on measured WAAM IN625 material properties.

Following on from these conclusions, there are several avenues for further work. Firstly, as this work has demonstrated the importance of specialised heat treatments to optimise the materials properties of WAAM IN718, it suggests that optimisation of heat treatment parameters to achieve various tailored microstructures and mechanical properties of WAAM IN625 and IN718 to suit the intended applications, for example in high temperature applications or corrosive environments. This knowledge could contribute to standards development for appropriate heat treatments for WAAM materials. One example for thermal powder bed fusion is ASTM F3301-18a [294].

Secondly, as it has been demonstrated that crack-like defects can occur in WAAM IN718 when deposited under unfavourable conditions. There is room for optimisation of WAAM process parameters, and there is also a possibility that the current chemical composition of the wire feedstock may not be suitable for WAAM deposition and may be tailored to achieve more favourable deposition quality and microstructures. Furthermore, as crack-like defects can affect the resulting apparent fracture toughness, it is important for suitable defect acceptance criteria to be determined for WAAM materials, depending on their intended applications. It is also important to determine the true fracture toughness of WAAM materials deposited with a defect rate that is acceptable under the appropriate acceptance criteria.

Lastly, as demonstrated in this work, WAAM IN625 and IN718 have inhomogeneous and anisotropic microstructures, which could affect other mechanical properties such as fatigue and creep properties. Understanding the effect of these characteristics on the fatigue or creep behaviour of WAAM materials could help inform whether current methods of structural integrity assessment are appropriate for WAAM materials. Another important input into structural integrity assessments is residual stress. However, the unique microstructure of WAAM IN625 and IN718 has been demonstrated to be unfavourable for experimental determination of residual stresses using diffraction methods. Therefore, residual stress characterisation using non-destructive techniques should be investigated.

List of References

[1] ISO / ASTM 52900-15, "Standard Terminology for Additive Manufacturing - General Principles - Technologies." ASTM International, West Conshohocken, PA, 2015.

[2] D. L. Bourell, "Perspectives on Additive Manufacturing," *Annu. Rev. Mater. Res.*, vol. 46, no. 1, pp. 1–18, 2016.

[3] R. Baker, "Method of Making Decorative Articles," US Patent 1533300A, 14-Apr-1925.

[4] C. W. Hull, "Apparatus for production of three-dimensional objects by stereolithography," US Patent 4575330, 08-Aug-1984.

[5] 3D Systems, "3D Printers, 3D Scanning, Software, Manufacturing and Healthcare Services | 3D Systems," 2020. [Online]. Available: https://www.3dsystems.com/. [Accessed: 22-Apr-2020].

[6] Stratasys Ltd, "What is FDM?: Fused Deposition Modeling Technology for 3D Printing | Stratasys," 2020. [Online]. Available: https://www.stratasys.com/fdm-technology. [Accessed: 16-Jun-2020].

[7] S. W. Williams, F. Martina, A. C. Addison, J. Ding, G. Pardal, and P. Colegrove, "Wire + arc additive manufacturing," *Mater. Sci. Technol.*, vol. 32, no. 7, pp. 641–647, 2016.

[8] EOS GmbH, "Press Releases about EOS and 3D Printing." [Online]. Available: https://www.eos.info/en/about-us/press-releases. [Accessed: 13-Jul-2020].

[9] "SLM Solutions Group AG: About us." [Online]. Available: https://www.slm-solutions.com/en/about-slm/about-slm/about-us/. [Accessed: 17-May-2020].

[10] T. Wohlers and T. Gornet, "History of Additive Manufacturing," in *Wohlers Report 2016*, Fort Collins, CO: Wohlers Associates, Inc, 2016.

[11] T. Maconachie *et al.*, "SLM lattice structures: Properties, performance, applications and challenges," *Materials and Design*, vol. 183. Elsevier Ltd, p. 108137, 05-Dec-2019.

[12] I. Gibson, D. Rosen, and B. Stucker, "Introduction and Basic Principles," in *Additive Manufacturing Technologies*, 2nd ed., New York, NY: Springer, 2015, pp. 1–18.

[13] A. Gisario, M. Kazarian, F. Martina, and M. Mehrpouya, “Metal additive manufacturing in the commercial aviation industry: A review,” *J. Manuf. Syst.*, vol. 53, pp. 124–149, Oct. 2019.

[14] X. Zhang and E. Liang, “Metal additive manufacturing in aircraft: Current application, opportunities and challenges,” *IOP Conf. Ser. Mater. Sci. Eng.*, vol. 493, no. 1, 2019.

[15] P. Liu, S. H. Huang, A. Mokasdar, H. Zhou, and L. Hou, “The impact of additive manufacturing in the aircraft spare parts supply chain: Supply chain operation reference (scor) model based analysis,” *Prod. Plan. Control*, vol. 25, no. 13–14, pp. 1169–1181, Oct. 2014.

[16] W. Ya, C. Goulas, K. Hamilton, M. Hermans, G.-W. Römer, and I. Richardson, “Microstructure and mechanical properties of CuAl8Ni6 produced by Wire Arc Additive Manufacturing for marine applications,” in *European Congress and Exhibition on Advanced Materials and Processes, EUROMAT 2017*, 2017.

[17] T. He, S. Yu, Y. Shi, and A. Huang, “Forming and mechanical properties of wire arc additive manufacture for marine propeller bracket,” *J. Manuf. Process.*, vol. 52, pp. 96–105, Apr. 2020.

[18] A. Taşdemir and S. Nohut, “An overview of wire arc additive manufacturing (WAAM) in shipbuilding industry,” *Ships and Offshore Structures*. Taylor and Francis Ltd., pp. 1–18, 2020.

[19] C. Greer *et al.*, “Introduction to the design rules for Metal Big Area Additive Manufacturing,” *Addit. Manuf.*, vol. 27, pp. 159–166, May 2019.

[20] M. Attaran, “Additive Manufacturing: The Most Promising Technology to Alter the Supply Chain and Logistics,” *J. Serv. Sci. Manag.*, vol. 10, no. 03, pp. 189–206, 2017.

[21] I. Gibson, D. Rosen, and B. Stucker, “Development of Additive Manufacturing Technology,” in *Additive Manufacturing Technologies*, 2nd ed., New York, NY: Springer, 2015, pp. 19–42.

[22] W. E. Frazier, “Metal additive manufacturing: A review,” *J. Mater. Eng. Perform.*, vol. 23, no. 6, pp. 1917–1928, 2014.

[23] W. J. Sames, F. A. List, S. Pannala, R. R. Dehoff, and S. S. Babu, "The metallurgy and processing science of metal additive manufacturing," *Int. Mater. Rev.*, vol. 61, no. 5, pp. 315–360, Jul. 2016.

[24] T. DebRoy *et al.*, "Additive manufacturing of metallic components – Process, structure and properties," *Prog. Mater. Sci.*, vol. 92, pp. 112–224, 2018.

[25] Z. E. Tan, J. H. L. Pang, J. Kaminski, and H. Pepin, "Characterisation of porosity, density, and microstructure of directed energy deposited stainless steel AISI 316L," *Addit. Manuf.*, vol. 25, pp. 286–296, Jan. 2019.

[26] H. Gong, K. Rafi, H. Gu, T. Starr, and B. Stucker, "Analysis of defect generation in Ti-6Al-4V parts made using powder bed fusion additive manufacturing processes," *Addit. Manuf.*, vol. 1, pp. 87–98, Oct. 2014.

[27] B. Wu *et al.*, "A review of the wire arc additive manufacturing of metals: properties, defects and quality improvement," *J. Manuf. Process.*, vol. 35, pp. 127–139, Oct. 2018.

[28] P. Liu, Z. Wang, Y. Xiao, M. F. Horstemeyer, X. Cui, and L. Chen, "Insight into the mechanisms of columnar to equiaxed grain transition during metallic additive manufacturing," *Addit. Manuf.*, vol. 26, pp. 22–29, Mar. 2019.

[29] P. Mohammadpour, A. Plotkowski, and A. B. Phillion, "Revisiting solidification microstructure selection maps in the frame of additive manufacturing," *Addit. Manuf.*, vol. 31, p. 100936, Jan. 2020.

[30] F. Yan, W. Xiong, and E. J. Faierson, "Grain structure control of additively manufactured metallic materials," *Materials (Basel).*, vol. 10, no. 11, p. 1260, Nov. 2017.

[31] D. Herzog, V. Seyda, E. Wycisk, and C. Emmelmann, "Additive manufacturing of metals," *Acta Mater.*, vol. 117, pp. 371–392, Sep. 2016.

[32] J. J. Lewandowski and M. Seifi, "Metal Additive Manufacturing: A Review of Mechanical Properties," *Annu. Rev. Mater. Res.*, vol. 46, no. 1, pp. 151–186, 2016.

[33] Y. Kok *et al.*, "Anisotropy and heterogeneity of microstructure and mechanical properties in metal additive manufacturing: A critical review," *Mater. Des.*, vol. 139, pp. 565–586, Feb. 2018.

[34] A. Dass and A. Moridi, "State of the art in directed energy deposition: From additive manufacturing to materials design," *Coatings*, vol. 9, no. 7. MDPI, p. 418, 29-Jun-2019.

[35] J. P. Oliveira, T. G. Santos, and R. M. Miranda, "Revisiting fundamental welding concepts to improve additive manufacturing: From theory to practice," *Prog. Mater. Sci.*, vol. 107, p. 100590, Jan. 2020.

[36] S. Gorsse, C. Hutchinson, M. Gouné, and R. Banerjee, "Additive manufacturing of metals: a brief review of the characteristic microstructures and properties of steels, Ti-6Al-4V and high-entropy alloys," *Science and Technology of Advanced Materials*, vol. 18, no. 1. Taylor and Francis Ltd., pp. 584–610, 31-Dec-2017.

[37] M. Seifi, A. Salem, J. Beuth, O. Harrysson, and J. J. Lewandowski, "Overview of Materials Qualification Needs for Metal Additive Manufacturing," *JOM*, vol. 68, no. 3, pp. 747–764, 2016.

[38] E. Herderick, "Additive manufacturing of metals: A review," *Mater. Sci. Technol. Conf. Exhib. 2011, MS T'11*, vol. 2, no. 176252, pp. 1413–1425, 2011.

[39] J. R. Yates, P. Efthymiadis, A. A. Antonysamy, C. Pinna, and J. Tong, "Do additive manufactured parts deserve better?," *Fatigue Fract. Eng. Mater. Struct.*, vol. 42, no. 9, pp. 2146–2154, Sep. 2019.

[40] D. Dye, O. Hunziker, and R. C. Reed, "Numerical analysis of the weldability of superalloys," *Acta Mater.*, vol. 49, no. 4, pp. 683–697, Feb. 2001.

[41] S. Kou, "Fusion Welding Processes," in *Welding Metallurgy*, 2nd ed., John Wiley & Sons, Inc., 2003, pp. 3–34.

[42] Y. A. Song, S. Park, D. Choi, and H. Jee, "3D welding and milling: Part I-a direct approach for freeform fabrication of metallic prototypes," *Int. J. Mach. Tools Manuf.*, vol. 45, no. 9, pp. 1057–1062, Jul. 2005.

[43] F. B. Prinz and L. E. Weiss, "Method and apparatus for fabrication of three-dimensional metal articles by weld deposition," US Patent 5207371A, 04-May-1993.

[44] Y. M. Zhang, Y. Chen, P. Li, and A. T. Male, "Weld deposition-based rapid prototyping: A preliminary study," *J. Mater. Process. Technol.*, vol. 135, no. 2-3 SPEC., pp. 347–357, Apr.

2003.

[45] S. Suryakumar, K. P. Karunakaran, U. Chandrasekhar, and M. A. Somashekara, “A study of the mechanical properties of objects built through weld-deposition,” *Proc. Inst. Mech. Eng. Part B J. Eng. Manuf.*, vol. 227, no. 8, pp. 1138–1147, Aug. 2013.

[46] D. Clark, M. R. Bache, and M. T. Whittaker, “Shaped metal deposition of a nickel alloy for aero engine applications,” *J. Mater. Process. Technol.*, vol. 203, no. 1–3, pp. 439–448, 2008.

[47] B. Baufeld, O. Van der Biest, and R. Gault, “Manufacturing of Ti-6Al-4V components by shaped metal deposition: Microstructure and mechanical properties,” *Mater. Des.*, vol. 31, no. SUPPL. 1, 2010.

[48] C. H. Amon, J. L. Beuth, L. E. Weiss, R. Merz, and F. B. Prinz, “Shape deposition manufacturing with microcasting: Processing, thermal and mechanical issues,” *J. Manuf. Sci. Eng. Trans. ASME*, vol. 120, no. 3, pp. 656–665, 1998.

[49] P. Graff, B. Ståhlbom, E. Nordenberg, A. Graichen, P. Johansson, and H. Karlsson, “Evaluating Measuring Techniques for Occupational Exposure during Additive Manufacturing of Metals: A Pilot Study,” *J. Ind. Ecol.*, vol. 21, no. S1, pp. S120–S129, Nov. 2017.

[50] F. Wang, S. Williams, and M. Rush, “Morphology investigation on direct current pulsed gas tungsten arc welded additive layer manufactured Ti6Al4V alloy,” *Int. J. Adv. Manuf. Technol.*, vol. 57, no. 5–8, pp. 597–603, 2011.

[51] K. S. Derekar, “A review of wire arc additive manufacturing and advances in wire arc additive manufacturing of aluminium,” *Mater. Sci. Technol.*, vol. 34, no. 8, pp. 895–916, May 2018.

[52] W. Ya and K. Hamilton, “On-Demand Spare Parts for the Marine Industry with Directed Energy Deposition: Propeller Use Case,” in *Industrializing Additive Manufacturing - Proceedings of Additive Manufacturing in Products and Applications - AMPA2017*, Springer International Publishing, 2018, pp. 70–81.

[53] C. V. Haden, G. Zeng, F. M. Carter, C. Ruhl, B. A. Krick, and D. G. Harlow, “Wire and arc

additive manufactured steel: Tensile and wear properties," *Addit. Manuf.*, vol. 16, pp. 115–123, Aug. 2017.

[54] P. Colegrove, "High deposition rate high quality metal additive manufacture using wire + arc technology," *Cranf. Univ.*, 2010.

[55] B. Baufeld, "Mechanical properties of INCONEL 718 parts manufactured by shaped metal deposition (SMD)," *J. Mater. Eng. Perform.*, vol. 21, no. 7, pp. 1416–1421, 2012.

[56] G. Posch, K. Chladil, and H. Chladil, "Material properties of CMT—metal additive manufactured duplex stainless steel blade-like geometries," *Weld. World*, vol. 61, no. 5, pp. 873–882, 2017.

[57] M. Eriksson *et al.*, "Additive manufacture of superduplex stainless steel using WAAM," in *MATEC Web of Conferences*, 2018, vol. 188, p. 03014.

[58] X. Xu, J. Ding, S. Ganguly, C. Diao, and S. Williams, "Preliminary Investigation of Building Strategies of Maraging Steel Bulk Material Using Wire + Arc Additive Manufacture," *J. Mater. Eng. Perform.*, vol. 28, no. 2, pp. 594–600, Feb. 2019.

[59] X. Xu, S. Ganguly, J. Ding, S. Guo, S. Williams, and F. Martina, "Microstructural evolution and mechanical properties of maraging steel produced by wire + arc additive manufacture process," *Mater. Charact.*, vol. 143, pp. 152–162, Sep. 2018.

[60] G. Marinelli, F. Martina, S. Ganguly, and S. Williams, "Microstructure, hardness and mechanical properties of two different unalloyed tantalum wires deposited via wire + arc additive manufacture," *Int. J. Refract. Met. Hard Mater.*, vol. 83, p. 104974, Sep. 2019.

[61] C. R. Cunningham, J. M. Flynn, A. Shokrani, V. Dhokia, and S. T. Newman, "Invited review article: Strategies and processes for high quality wire arc additive manufacturing," *Additive Manufacturing*, vol. 22. pp. 672–686, Aug-2018.

[62] I. Tabernero, A. Paskual, P. Álvarez, and A. Suárez, "Study on Arc Welding Processes for High Deposition Rate Additive Manufacturing," in *Procedia CIRP*, 2018, vol. 68, pp. 358–362.

[63] F. Martina, J. Mehnen, S. W. Williams, P. Colegrove, and F. Wang, "Investigation of the benefits of plasma deposition for the additive layer manufacture of Ti-6Al-4V," *J. Mater.*

Process. Technol., vol. 212, no. 6, pp. 1377–1386, Jun. 2012.

[64] E. Aldalur, F. Veiga, A. Suárez, J. Bilbao, and A. Lamikiz, "Analysis of the wall geometry with different strategies for high deposition wire arc additive manufacturing of mild steel," *Metals (Basel).*, vol. 10, no. 7, pp. 1–19, Jul. 2020.

[65] A. A. Antonysamy, J. Meyer, and P. B. Prangnell, "Effect of build geometry on the β-grain structure and texture in additive manufacture of Ti6Al4V by selective electron beam melting," *Mater. Charact.*, vol. 84, pp. 153–168, Oct. 2013.

[66] M. A. Somashekara, M. Naveenkumar, A. Kumar, C. Viswanath, and S. Simhambhatla, "Investigations into effect of weld-deposition pattern on residual stress evolution for metallic additive manufacturing," *Int. J. Adv. Manuf. Technol.*, vol. 90, no. 5–8, pp. 2009–2025, 2017.

[67] G. Venturini, F. Montevecchi, A. Scippa, and G. Campatelli, "Optimization of WAAM Deposition Patterns for T-crossing Features," in *Procedia CIRP*, 2016, vol. 55, pp. 95–100.

[68] F. Michel, H. Lockett, J. Ding, F. Martina, G. Marinelli, and S. Williams, "A modular path planning solution for Wire + Arc Additive Manufacturing," *Robot. Comput. Integr. Manuf.*, vol. 60, pp. 1–11, Dec. 2019.

[69] S. Ríos, P. A. Colegrove, and S. W. Williams, "Metal transfer modes in plasma Wire + Arc additive manufacture," *J. Mater. Process. Technol.*, vol. 264, pp. 45–54, Feb. 2019.

[70] B. Cong, J. Ding, and S. Williams, "Effect of arc mode in cold metal transfer process on porosity of additively manufactured Al-6.3%Cu alloy," *Int. J. Adv. Manuf. Technol.*, vol. 76, no. 9–12, pp. 1593–1606, 2015.

[71] L. Wang, J. Xue, and Q. Wang, "Correlation between arc mode, microstructure, and mechanical properties during wire arc additive manufacturing of 316L stainless steel," *Mater. Sci. Eng. A*, vol. 751, pp. 183–190, Mar. 2019.

[72] J. Xiong, Y. Li, R. Li, and Z. Yin, "Influences of process parameters on surface roughness of multi-layer single-pass thin-walled parts in GMAW-based additive manufacturing," *J. Mater. Process. Technol.*, vol. 252, pp. 128–136, Feb. 2018.

[73] M. Dinovitzer, X. Chen, J. Laliberte, X. Huang, and H. Frei, "Effect of wire and arc additive

manufacturing (WAAM) process parameters on bead geometry and microstructure," *Addit. Manuf.*, vol. 26, pp. 138–146, Mar. 2019.

[74] K. Derekar, J. Lawrence, G. Melton, A. Addison, X. Zhang, and L. Xu, "Influence of Interpass Temperature on Wire Arc Additive Manufacturing (WAAM) of Aluminium Alloy Components," *MATEC Web Conf.*, vol. 269, p. 05001, 2019.

[75] B. Shassere, A. Nycz, M. W. Noakes, C. Masuo, and N. Sridharan, "Correlation of microstructure and mechanical properties of Metal Big Area Additive Manufacturing," *Appl. Sci.*, vol. 9, no. 4, p. 787, Feb. 2019.

[76] P. A. Colegrove *et al.*, "Microstructure and residual stress improvement in wire and arc additively manufactured parts through high-pressure rolling," *J. Mater. Process. Technol.*, vol. 213, no. 10, pp. 1782–1791, Oct. 2013.

[77] J. Gu, J. Ding, S. W. Williams, H. Gu, P. Ma, and Y. Zhai, "The effect of inter-layer cold working and post-deposition heat treatment on porosity in additively manufactured aluminum alloys," *J. Mater. Process. Technol.*, vol. 230, pp. 26–34, 2016.

[78] F. Martina, P. A. Colegrove, S. W. Williams, and J. Meyer, "Microstructure of Interpass Rolled Wire + Arc Additive Manufacturing Ti-6Al-4V Components," *Metall. Mater. Trans. A*, vol. 46, no. 12, pp. 6103–6118, Dec. 2015.

[79] A. R. McAndrew *et al.*, "Interpass rolling of Ti-6Al-4V wire + arc additively manufactured features for microstructural refinement," *Addit. Manuf.*, vol. 21, pp. 340–349, May 2018.

[80] J. Donoghue, A. A. Antonysamy, F. Martina, P. A. Colegrove, S. W. Williams, and P. B. Prangnell, "The effectiveness of combining rolling deformation with Wire-Arc Additive Manufacture on β-grain refinement and texture modification in Ti-6Al-4V," *Mater. Charact.*, vol. 114, pp. 103–114, 2016.

[81] X. Xu *et al.*, "Improving mechanical properties of wire plus arc additively manufactured maraging steel through plastic deformation enhanced aging response," *Mater. Sci. Eng. A*, vol. 747, pp. 111–118, Feb. 2019.

[82] X. Xu, S. Ganguly, J. Ding, C. E. Seow, and S. Williams, "Enhancing mechanical properties of wire + arc additively manufactured INCONEL 718 superalloy through in-process

thermomechanical processing," *Mater. Des.*, vol. 160, pp. 1042–1051, Dec. 2018.

[83] J. Gu *et al.*, "The strengthening effect of inter-layer cold working and post-deposition heat treatment on the additively manufactured Al-6.3Cu alloy," *Mater. Sci. Eng. A*, vol. 651, pp. 18–26, Jan. 2016.

[84] Z. Qi, B. Qi, B. Cong, H. Sun, G. Zhao, and J. Ding, "Microstructure and mechanical properties of wire + arc additively manufactured 2024 aluminum alloy components: As-deposited and post heat-treated," *J. Manuf. Process.*, vol. 40, pp. 27–36, Apr. 2019.

[85] A. Vahedi Nemani, M. Ghaffari, and A. Nasiri, "On the Post-Printing Heat Treatment of a Wire Arc Additively Manufactured ER70S Part," *Materials (Basel).*, vol. 13, no. 12, p. 2795, 2020.

[86] L. Ji *et al.*, "Research on mechanisms and controlling methods of macro defects in TC4 alloy fabricated by wire additive manufacturing," *Materials (Basel).*, vol. 11, no. 7, p. 1104, Jun. 2018.

[87] X. Xu, J. Ding, S. Ganguly, C. Diao, and S. Williams, "Oxide accumulation effects on wire + arc layer-by-layer additive manufacture process," *J. Mater. Process. Technol.*, vol. 252, pp. 739–750, Feb. 2018.

[88] F. Xu *et al.*, "Realisation of a multi-sensor framework for process monitoring of the wire arc additive manufacturing in producing Ti-6Al-4V parts," *Int. J. Comput. Integr. Manuf.*, vol. 31, no. 8, pp. 785–798, 2018.

[89] G. Pardal, F. Martina, and S. Williams, "Laser stabilization of GMAW additive manufacturing of Ti-6Al-4V components," *J. Mater. Process. Technol.*, vol. 272, pp. 1–8, Oct. 2019.

[90] G. Mathers, "Weld defects and quality control," in *The Welding of Aluminium and its Alloys*, Cambridge, England: Woodhead Publishing, 2002, pp. 199–215.

[91] E. M. Ryan, T. J. Sabin, J. F. Watts, and M. J. Whiting, "The influence of build parameters and wire batch on porosity of wire and arc additive manufactured aluminium alloy 2319," *J. Mater. Process. Technol.*, vol. 262, pp. 577–584, Dec. 2018.

[92] K. S. Derekar *et al.*, "Effect of pulsed metal inert gas (pulsed-MIG) and cold metal transfer

(CMT) techniques on hydrogen dissolution in wire arc additive manufacturing (WAAM) of aluminium," *Int. J. Adv. Manuf. Technol.*, vol. 107, no. 1–2, pp. 311–331, Mar. 2020.

[93] P. M. Sequeira Almedia, "Process Control and Development in Wire and Arc Additive Manufacturing," Cranfield University, 2012.

[94] C. E. Seow, H. Coules, and R. Khan, "Effect of Crack Orientation on Fracture Behaviour of Wire + Arc Additively Manufactured (WAAM) Nickel-Base Superalloy," in *American Society of Mechanical Engineers, Pressure Vessels and Piping Division (Publication) PVP*, 2018, vol. 5, p. V005T10A016.

[95] A. Ho, H. Zhao, J. W. Fellowes, F. Martina, A. E. Davis, and P. B. Prangnell, "On the origin of microstructural banding in Ti-6Al4V wire-arc based high deposition rate additive manufacturing," *Acta Mater.*, vol. 166, pp. 306–323, Mar. 2019.

[96] J. F. Wang, Q. J. Sun, H. Wang, J. P. Liu, and J. C. Feng, "Effect of location on microstructure and mechanical properties of additive layer manufactured Inconel 625 using gas tungsten arc welding," *Mater. Sci. Eng. A*, vol. 676, pp. 395–405, 2016.

[97] F. J. Xu, Y. H. Lv, B. S. Xu, Y. X. Liu, F. Y. Shu, and P. He, "Effect of deposition strategy on the microstructure and mechanical properties of Inconel 625 superalloy fabricated by pulsed plasma arc deposition," *Mater. Des.*, vol. 45, pp. 446–455, Mar. 2013.

[98] F. Xu, Y. Lv, Y. Liu, F. Shu, P. He, and B. Xu, "Microstructural Evolution and Mechanical Properties of Inconel 625 Alloy during Pulsed Plasma Arc Deposition Process," *J. Mater. Sci. Technol.*, vol. 29, no. 5, pp. 480–488, 2013.

[99] A. N. M. Tanvir *et al.*, "Heat treatment effects on Inconel 625 components fabricated by wire + arc additively manufacturing (WAAM)—part 2: mechanical properties," *Int. J. Adv. Manuf. Technol.*, 2020.

[100] X. Lu, Y. F. Zhou, X. L. Xing, L. Y. Shao, Q. X. Yang, and S. Y. Gao, "Open-source wire and arc additive manufacturing system: formability, microstructures, and mechanical properties," *International Journal of Advanced Manufacturing Technology*, vol. 93, no. 5–8, pp. 1–10, 2017.

[101] Z. Lin, C. Goulas, W. Ya, and M. J. M. Hermans, "Microstructure and mechanical

properties of medium carbon steel deposits obtained via wire and arc additive manufacturing using metal-cored wire," *Metals (Basel).*, vol. 9, no. 6, p. 673, Jun. 2019.

[102] F. Wang, S. Williams, P. Colegrove, and A. A. Antonysamy, "Microstructure and mechanical properties of wire and arc additive manufactured Ti-6Al-4V," *Metall. Mater. Trans. A*, vol. 44, no. 2, pp. 968–977, 2013.

[103] Y. Xie *et al.*, "Anisotropy of fatigue crack growth in wire arc additive manufactured Ti-6Al-4V," *Mater. Sci. Eng. A*, vol. 709, pp. 265–269, Jan. 2018.

[104] O. Oguntuase, O. A. Ojo, and J. Beddoes, "Influence of Post-deposition Heat Treatments on the Microstructure and Mechanical Properties of Wire–Arc Additively Manufactured ATI 718Plus," *Metall. Mater. Trans. A Phys. Metall. Mater. Sci.*, vol. 51, no. 4, pp. 1846–1859, Apr. 2020.

[105] A. Waqas, Q. Xiansheng, X. Jiangtao, Y. Chaoran, and L. Fan, "Impact toughness of components made by GMAW based additive manufacturing," in *Procedia Structural Integrity*, 2018, vol. 13, pp. 2065–2070.

[106] A. Waqas, X. Qin, J. Xiong, C. Zheng, and H. Wang, "Analysis of ductile fracture obtained by charpy impact test of a steel structure created by robot-assisted GMAW-based additive manufacturing," *Metals (Basel).*, vol. 9, no. 11, p. 1208, Nov. 2019.

[107] X. Zhang, F. Martina, J. Ding, X. Wang, and S. W. Williams, "Fracture toughness and fatigue crack growth rate properties in wire + arc additive manufactured Ti-6Al-4V," *Fatigue Fract. Eng. Mater. Struct.*, vol. 40, no. 5, pp. 790–803, May 2017.

[108] ASTM International, "ASTM E399-20 Standard Test Method for Linear-Elastic Plane-Strain Fracture Toughness of Metallic Materials." ASTM International, West Conshohocken, PA, 2020.

[109] A. Ermakova, A. Mehmanparast, S. Ganguly, J. Razavi, and F. Berto, "Investigation of mechanical and fracture properties of wire and arc additively manufactured low carbon steel components," *Theor. Appl. Fract. Mech.*, vol. 109, p. 102685, Oct. 2020.

[110] E1820-18ae1, "Standard Test Method for Measurement of Fracture Toughness," *ASTM Stand.*, p. E 1820 – 01, 2019.

[111] P. Dirisu, S. Ganguly, A. Mehmanparast, F. Martina, and S. Williams, "Analysis of fracture toughness properties of wire + arc additive manufactured high strength low alloy structural steel components," *Mater. Sci. Eng. A*, vol. 765, p. 138285, Sep. 2019.

[112] J. V. Gordon, C. V. Haden, H. F. Nied, R. P. Vinci, and D. G. Harlow, "Fatigue crack growth anisotropy, texture and residual stress in austenitic steel made by wire and arc additive manufacturing," *Mater. Sci. Eng. A*, vol. 724, pp. 431–438, May 2018.

[113] E. Brandl, B. Baufeld, C. Leyens, and R. Gault, "Additive manufactured Ti-6Al-4V using welding wire: Comparison of laser and arc beam deposition and evaluation with respect to aerospace material specifications," *Phys. Procedia*, vol. 5, no. PART 2, pp. 595–606, 2010.

[114] B. Baufeld, E. Brandl, and O. Van Der Biest, "Wire based additive layer manufacturing: Comparison of microstructure and mechanical properties of Ti-6Al-4V components fabricated by laser-beam deposition and shaped metal deposition," *J. Mater. Process. Technol.*, vol. 211, no. 6, pp. 1146–1158, 2011.

[115] J. Gordon, J. Hochhalter, C. Haden, and D. G. Harlow, "Enhancement in fatigue performance of metastable austenitic stainless steel through directed energy deposition additive manufacturing," *Mater. Des.*, vol. 168, p. 107630, Apr. 2019.

[116] R. Biswal *et al.*, "Interrupted fatigue testing with periodic tomography to monitor porosity defects in wire + arc additive manufactured Ti-6Al-4V," *Addit. Manuf.*, vol. 28, pp. 517–527, Aug. 2019.

[117] P. Dirisu, G. Supriyo, F. Martina, X. Xu, and S. Williams, "Wire plus arc additive manufactured functional steel surfaces enhanced by rolling," *Int. J. Fatigue*, vol. 130, p. 105237, Jan. 2020.

[118] J. Zhang *et al.*, "Crack path selection at the interface of wrought and wire + arc additive manufactured Ti-6Al-4V," *Mater. Des.*, vol. 104, pp. 365–375, Aug. 2016.

[119] J. Zhang, X. Wang, S. Paddea, and X. Zhang, "Fatigue crack propagation behaviour in wire+arc additive manufactured Ti-6Al-4V: Effects of microstructure and residual stress," *Mater. Des.*, vol. 90, pp. 551–561, 2016.

[120] T. Ron, G. K. Levy, O. Dolev, A. Leon, A. Shirizly, and E. Aghion, "The effect of microstructural imperfections on corrosion fatigue of additively manufactured ER70S-6 alloy produced by wire arc deposition," *Metals (Basel).*, vol. 10, no. 1, p. 98, Jan. 2020.

[121] J. R. Hönnige, S. Williams, M. J. Roy, P. Colegrove, and S. Ganguly, "Residual Stress Characterization and Control in the Additive Manufacture of Large Scale Metal Structures," *Eur. Conf. Residual Stress. 2016*, vol. 2, pp. 455–460, Jan. 2017.

[122] F. Martina, S. W. Williams, and P. Colegrove, "Improved microstructure and increased mechanical properties of additive manufacture produced TI-6AL-4V by interpass cold rolling," in *24th International SFF Symposium - An Additive Manufacturing Conference, SFF 2013*, 2013, pp. 490–496.

[123] F. Martina *et al.*, "Residual stress of as-deposited and rolled wire+arc additive manufacturing Ti–6Al–4V components," *Mater. Sci. Technol. (United Kingdom)*, vol. 32, no. 14, pp. 1439–1448, Sep. 2016.

[124] B. A. Szost *et al.*, "A comparative study of additive manufacturing techniques: Residual stress and microstructural analysis of CLAD and WAAM printed Ti-6Al-4V components," *Mater. Des.*, vol. 89, pp. 559–567, Jan. 2016.

[125] J. R. Hönnige *et al.*, "Residual stress and texture control in Ti-6Al-4V wire + arc additively manufactured intersections by stress relief and rolling," *Mater. Des.*, vol. 150, pp. 193–205, 2018.

[126] S. Srivastava, R. K. Garg, V. S. Sharma, and A. Sachdeva, "Measurement and Mitigation of Residual Stress in Wire-Arc Additive Manufacturing: A Review of Macro-Scale Continuum Modelling Approach," *Arch. Comput. Methods Eng.*, 2020.

[127] J. Ding, P. Colegrove, J. Mehnen, S. Williams, F. Wang, and P. S. Almeida, "A computationally efficient finite element model of wire and arc additive manufacture," *Int. J. Adv. Manuf. Technol.*, vol. 70, no. 1–4, pp. 227–236, 2014.

[128] Q. Wu, T. Mukherjee, A. De, and T. DebRoy, "Residual stresses in wire-arc additive manufacturing – Hierarchy of influential variables," *Addit. Manuf.*, vol. 35, p. 101355, Oct. 2020.

[129] M. J. Donachie and S. J. Donachie, *Superalloys: a technical guide*, 2nd ed. Materials Park, OH: ASM International, 2002.

[130] J. N. DuPont, J. C. Lippold, and S. D. Kiser, *Welding Metallurgy and Weldability of Nickel Based Alloys*. Hoboken, New Jersey: John Wiley & Sons, Inc., 2009.

[131] R. C. Reed, *The Superalloys: Fundamentals and Applications*. Cambridge: Cambridge University Press, 2006.

[132] R. Schlatter, "Melting and Refining Technology of High-Temperature Steels and Superalloys a Review of Recent Process Developments," in *Superalloys 1972*, 1972, pp. A1–A40.

[133] R. L. Kennedy, R. M. Forbes Jones, R. M. Davis, M. G. Benz, and W. T. Carter, "Superalloys made by conventional vacuum melting and a novel spray forming process," *Vacuum*, vol. 47, no. 6–8, pp. 819–824, 1996.

[134] V. Weber *et al.*, "A Comprehensive model of the electroslag remelting process: Description and validation," *Metall. Mater. Trans. B Process Metall. Mater. Process. Sci.*, vol. 40, no. 3, pp. 271–280, 2009.

[135] C. E. Shamblen, D. R. Chang, and J. A. Corrado, "Superalloy Melting and Cleanliness Evaluation," in *Proc. 5th Int. Symp. on Superalloys*, 1984, pp. 509–520.

[136] X. Wang, R. M. Ward, M. H. Jacobs, and M. D. Barratt, "Effect of variation in process parameters on the formation of freckle in INCONEL 718 by vacuum arc remelting," *Metall. Mater. Trans. A Phys. Metall. Mater. Sci.*, vol. 39, no. 12, pp. 2981–2989, 2008.

[137] D. X. Wen, Y. C. Lin, H. Bin Li, X. M. Chen, J. Deng, and L. T. Li, "Hot deformation behavior and processing map of a typical Ni-based superalloy," *Mater. Sci. Eng. A*, vol. 591, pp. 183–192, Jan. 2014.

[138] N. K. Park, I. S. Kim, Y. S. Na, and J. T. Yeom, "Hot forging of a nickel-base superalloy," *J. Mater. Process. Technol.*, vol. 111, no. 1–3, pp. 98–102, Apr. 2001.

[139] J. W. Brooks, "Forging of superalloys," *Mater. Des.*, vol. 21, no. 4, pp. 297–303, Aug. 2000.

[140] E. Alabort, R. C. Reed, and D. Barba, "Combined modelling and miniaturised

characterisation of high-temperature forging in a nickel-based superalloy," *Mater. Des.*, vol. 160, pp. 683–697, Dec. 2018.

[141] J. E. Kanyo, S. Schafföner, R. S. Uwanyuze, and K. S. Leary, "An overview of ceramic molds for investment casting of nickel superalloys," *Journal of the European Ceramic Society*, vol. 40, no. 15. Elsevier Ltd, pp. 4955–4973, 01-Dec-2020.

[142] D. Wang, B. He, S. Liu, C. Liu, and L. Fei, "Dimensional shrinkage prediction based on displacement field in investment casting," *Int. J. Adv. Manuf. Technol.*, vol. 85, no. 1–4, pp. 201–208, Jul. 2016.

[143] Y. W. Dong, X. L. Li, Q. Zhao, J. Yang, and M. Dao, "Modeling of shrinkage during investment casting of thin-walled hollow turbine blades," *J. Mater. Process. Technol.*, vol. 244, pp. 190–203, Jun. 2017.

[144] X. G. Zheng, Y. N. Shi, and L. H. Lou, "Healing Process of Casting Pores in a Ni-based Superalloy by Hot Isostatic Pressing," *J. Mater. Sci. Technol.*, vol. 31, no. 11, pp. 1151–1157, Nov. 2015.

[145] S. F. Gao, L. Liu, N. Wang, X. B. Zhao, J. Zhang, and H. Z. Fu, "Grain selection during casting Ni-base, single-crystal superalloys with spiral grain selector," *Metall. Mater. Trans. A Phys. Metall. Mater. Sci.*, vol. 43, no. 10, pp. 3767–3775, 2012.

[146] L. Tan, Y. Li, G. He, F. Liu, Y. Nie, and L. Jiang, "Optimized hot workability of a powder metallurgy nickel-base superalloy," *Mater. Charact.*, vol. 147, pp. 340–352, Jan. 2019.

[147] G. Raisson, "Evolution of PM nickel base superalloy processes and products," *Powder Metall.*, vol. 51, no. 1, pp. 10–13, 2008.

[148] O. T. Ola, O. A. Ojo, P. Wanjara, and M. C. Chaturvedi, "Analysis of microstructural changes induced by linear friction welding in a nickel-base superalloy," *Metall. Mater. Trans. A Phys. Metall. Mater. Sci.*, vol. 42, no. 12, pp. 3761–3777, Dec. 2011.

[149] M. B. Henderson, D. Arrell, R. Larsson, M. Heobel, and G. Marchant, "Nickel based superalloy welding practices for industrial gas turbine applications," *Sci. Technol. Weld. Join.*, vol. 9, no. 1, pp. 13–21, 2004.

[150] M. D. Rowe, "Ranking the resistance of wrought superalloys to strain-age cracking,"

Weld. J., vol. 85, no. 2, pp. 27s-33s, 2006.

[151] A. Lingenfelter, "Welding of Inconel Alloy 718: A Historical Overview," in *Superalloy 718*, 1989, pp. 673–683.

[152] R. Vincent, "Precipitation around welds in the nickel-base superalloy, Inconel 718," *Acta Metall.*, vol. 33, no. 7, pp. 1205–1216, Jul. 1985.

[153] H. L. Eiselstein and D. J. Tillack, "The Invention and Definition of Alloy 625," in *Superalloys 718, 625 and Various Derivatives*, 1991, pp. 1–14.

[154] H. L. Eiselstein, "Age-hardenable Nickel Alloy," US3046108A, 24-Jul-1962.

[155] T. Dai, R. A. Wheeling, K. Hartman-Vaeth, and J. C. Lippold, "Precipitation behavior and hardness response of Alloy 625 weld overlay under different aging conditions," *Weld. World*, vol. 63, no. 4, pp. 1087–1100, Jun. 2019.

[156] B. Dubiel and J. Sieniawski, "Precipitates in additively manufactured inconel 625 superalloy," *Materials (Basel).*, vol. 12, no. 7, pp. 1–11, 2019.

[157] M. A. Shaikh, M. Ahmad, K. A. Shoaib, J. I. Akhter, and M. Iqbal, "Precipitation hardening in Inconel 625," *Mater. Sci. Technol.*, vol. 16, no. 2, pp. 129–132, 2000.

[158] M. Sundararaman, P. Mukhopadhyay, and S. Banerjee, "Carbide Precipitation in Nickel Base Superalloys 718 and 625 and Their Effect on Mechanical Properties," in *Superalloys 718, 625, 706 and Various Derivatives*, 1997, pp. 367–378.

[159] A. Mitchell, "Primary carbides in alloy 718," in *7th International Symposium on Superalloy 718 and Derivatives 2010*, 2010, vol. 1, pp. 161–167.

[160] C. Radhakrishna and K. Prasad Rao, "The formation and control of Laves phase in superalloy 718 welds," *J. Mater. Sci.*, vol. 32, no. 8, pp. 1977–1984, 1997.

[161] D. Srinivasan, "Effect of long-time exposure on the evolution of minor phases in Alloy 718," *Mater. Sci. Eng. A*, vol. 364, no. 1–2, pp. 27–34, 2004.

[162] J. N. DuPont, J. C. Lippold, and S. D. Kiser, "Repair Welding of Ni-base Alloys," in *Welding Metallurgy and Weldability of Nickel-Base Alloys*, John Wiley & Sons, Inc., 2009, pp. 281–326.

[163] H. E. Chandler, *Heat treater's guide: practices and procedures for nonferrous alloys*. ASM International, 1996.

[164] SAE International, "AMS5383F Nickel Alloy, Corrosion and Heat-Resistant, Investment Castings 52.5Ni - 19Cr - 3.0Mo - 5.1Cb(Nb) - 0.90Ti - 0.60Al - 18Fe Vacuum Melted Homogenization and Solution Heat Treated." SAE International, 2018.

[165] SAE International, "AMS5662N Nickel Alloy, Corrosion and Heat-Resistant, Bars, Forgings, and Rings 52.5Ni - 19Cr - 3.0Mo - 5.1Cb (Nb) - 0.90Ti - 0.50AI - 18Fe Consumable Electrode or Vacuum Induction Melted 1775 °F (968 °C) Solution Heat Treated, Precipitation-Hardenable." SAE International, 2016.

[166] X. Shi, S. Duan, W. Yang, H. Guo, and J. Guo, "Solidification and segregation behaviors of superalloy IN718 at a slow cooling ratess," *Materials (Basel).*, vol. 11, no. 12, p. 2398, Nov. 2018.

[167] A. N. M. Tanvir, M. R. U. Ahsan, C. Ji, W. Hawkins, B. Bates, and D. B. Kim, "Heat treatment effects on Inconel 625 components fabricated by wire + arc additive manufacturing (WAAM)—part 1: microstructural characterization," *Int. J. Adv. Manuf. Technol.*, 2019.

[168] R. M. Kindermann, M. J. Roy, R. Morana, and P. B. Prangnell, "Process response of Inconel 718 to wire + arc additive manufacturing with cold metal transfer," *Mater. Des.*, vol. 195, p. 109031, Oct. 2020.

[169] J. Hönnige *et al.*, "Study of residual stress and microstructural evolution in as-deposited and inter-pass rolled wire plus arc additively manufactured Inconel 718 alloy after ageing treatment," *Mater. Sci. Eng. A*, p. 140368, Oct. 2020.

[170] T. Artaza, T. Bhujangrao, A. Suárez, F. Veiga, and A. Lamikiz, "Influence of heat input on the formation of laves phases and hot cracking in plasma arc welding (PAW) additive manufacturing of inconel 718," *Metals (Basel).*, vol. 10, no. 6, pp. 1–17, Jun. 2020.

[171] D. Clark, M. R. Bache, and M. T. Whittaker, "Microstructural characterization of a polycrystalline nickel-based superalloy processed via tungsten-inert-gas-shaped metal deposition," *Metall. Mater. Trans. B*, vol. 41, no. 6, pp. 1346–1353, 2010.

[172] G. Asala, A. K. Khan, J. Andersson, and O. A. Ojo, "Microstructural Analyses of ATI 718Plus® Produced by Wire-ARC Additive Manufacturing Process," *Metall. Mater. Trans. A*, vol. 48, no. 9, pp. 4211–4228, 2017.

[173] X. Xu, J. Ding, S. Ganguly, and S. Williams, "Investigation of process factors affecting mechanical properties of INCONEL 718 superalloy in wire + arc additive manufacture process," *J. Mater. Process. Technol.*, vol. 265, pp. 201–209, Mar. 2019.

[174] M. J. Cieslak, G. a. Knorovsky, T. J. Headley, and A. D. Romig, Jr, "The Solidification Metallurgy of Alloy 718 and Other Nb-Containing Superalloys," *Superalloys 718 Metall. Appl.*, pp. 59–68, 1989.

[175] M. J. Sohrabi, H. Mirzadeh, and M. Rafiei, "Solidification behavior and Laves phase dissolution during homogenization heat treatment of Inconel 718 superalloy," *Vacuum*, vol. 154, pp. 235–243, Aug. 2018.

[176] BSI, "BS EN ISO 6507-1:2018 Metallic materials. Vickers hardness test. Test method." BSI, 2018.

[177] BSI, "BS EN ISO 6892-1:2016 Metallic materials — Tensile testing Part 1 : Method of test at room temperature." BSI, 2016.

[178] BSI, "BS EN ISO 6892-2:2018 Metallic materials — Tensile testing Part 2 : Method of test at elevated temperature." BSI, 2018.

[179] J. I. Goldstein, D. E. Newbury, J. R. Michael, N. W. M. Ritchie, J. H. J. Scott, and D. C. Joy, "SEM Image Interpretation," in *Scanning Electron Microscopy and X-Ray Microanalysis*, New York, NY: Springer New York, 2018, pp. 111–121.

[180] R. G. Ding, Z. W. Huang, H. Y. Li, I. Mitchell, G. Baxter, and P. Bowen, "Electron microscopy study of direct laser deposited IN718," *Mater. Charact.*, vol. 106, pp. 324–337, 2015.

[181] C. Radhakrishna and K. Prasad Rao, "The formation and control of Laves phase in superalloy 718 welds," *J. Mater. Sci.*, vol. 32, no. 8, pp. 1977–1984, 1997.

[182] C. C. Silva, H. C. de Miranda, M. F. Motta, J. P. Farias, C. R. M. Afonso, and A. J. Ramirez, "New insight on the solidification path of an alloy 625 weld overlay," *J. Mater. Res.*

Technol., vol. 2, no. 3, pp. 228–237, Jul. 2013.

[183] A. Mitchell, A. J. Schmalz, C. Schvezov, and S. L. Cockroft, "The Precipitation of Primary Carbides in Alloy 718," in *Superalloys 718, 625, 706 and Various Derivatives (1994)*, 1994, pp. 65–78.

[184] S. L. Cockcroft, T. Degawa, A. Mitchell, D. W. Tripp, and A. Schmalz, "Inclusion Precipitation in Superalloys," *Superalloys 1992*, pp. 577–586, 1992.

[185] G. A. Knorovsky, M. J. Cieslak, T. J. Headley, A. D. Romig, and W. F. Hammetter, "INCONEL 718: A solidification diagram," *Metall. Trans. A*, vol. 20, no. 10, pp. 2149–2158, 1989.

[186] H. O. Pierson, "Interstitial Nitrides: Properties and General Characteristics," in *Handbook of Refractory Carbides and Nitrides*, William Andrew Publishing, 1996, pp. 181–208.

[187] C. I. Garcia, A. K. Lis, E. A. Loria, and A. J. DeArdo, "Thermomechanical Processing and Continuous Cooling Transformation Behavior of IN-718," in *Superalloys 1992*, 1992, pp. 527–536.

[188] S. Benhadad, N. L. Richards, and M. C. Chaturvedi, "The influence of minor elements on the weldability of an INCONEL 718-type superalloy," *Metall. Mater. Trans. A Phys. Metall. Mater. Sci.*, vol. 33, no. 7, pp. 2005–2017, 2002.

[189] R. Vincent, "Precipitation around welds in the nickel-base superalloy, Inconel 718," *Acta Metall.*, vol. 33, no. 7, pp. 1205–1216, 1985.

[190] O. T. Ola and F. E. Doern, "A study of cold metal transfer clads in nickel-base INCONEL 718 superalloy," *Mater. Des.*, vol. 57, pp. 51–59, May 2014.

[191] L. C. M. Valle, L. S. Araújo, S. B. Gabriel, J. Dille, and L. H. de Almeida, "The Effect of δ Phase on the Mechanical Properties of an Inconel 718 Superalloy," *J. Mater. Eng. Perform.*, vol. 22, no. 5, pp. 1512–1518, May 2013.

[192] G. D. Janaki Ram, A. Venugopal Reddy, K. Prasad Rao, and G. Madhusudhan Reddy, "Control of Laves phase in Inconel 718 GTA welds with current pulsing," *Sci. Technol. Weld. Join.*, vol. 9, no. 5, pp. 390–398, 2004.

[193] J. Li *et al.*, "Microstructural evolution and mechanical properties of IN718 alloy fabricated by selective laser melting following different heat treatments," *J. Alloys Compd.*, vol. 772, pp. 861–870, Jan. 2019.

[194] Z. Wang, K. Guan, M. Gao, X. Li, X. Chen, and X. Zeng, "The microstructure and mechanical properties of deposited-IN718 by selective laser melting," *J. Alloys Compd.*, vol. 513, pp. 518–523, Feb. 2012.

[195] N. Nadammal *et al.*, "Effect of hatch length on the development of microstructure, texture and residual stresses in selective laser melted superalloy Inconel 718," *Mater. Des.*, vol. 134, pp. 139–150, Nov. 2017.

[196] V. A. Popovich, E. V. Borisov, A. A. Popovich, V. S. Sufiiarov, D. V. Masaylo, and L. Alzina, "Functionally graded Inconel 718 processed by additive manufacturing: Crystallographic texture, anisotropy of microstructure and mechanical properties," *Mater. Des.*, vol. 114, pp. 441–449, Jan. 2017.

[197] A. Strondl, R. Fischer, G. Frommeyer, and A. Schneider, "Investigations of MX and γ′/γ″ precipitates in the nickel-based superalloy 718 produced by electron beam melting," *Mater. Sci. Eng. A*, vol. 480, no. 1–2, pp. 138–147, 2008.

[198] ASTM E112-13, "ASTM E112-13 Standard Test Methods for Determining Average Grain Size." ASTM International, West Conshohocken, PA, 2013.

[199] W. Chen and M. C. Chaturvedi, "On the mechanism of serrated deformation in aged Inconel 718," *Mater. Sci. Eng. A*, vol. 229, no. 1–2, pp. 163–168, 1997.

[200] H. J. Lee, H. K. Kim, H. U. Hong, and B. S. Lee, "Influence of the focus offset on the defects, microstructure, and mechanical properties of an Inconel 718 superalloy fabricated by electron beam additive manufacturing," *J. Alloys Compd.*, vol. 781, pp. 842–856, Apr. 2019.

[201] A. M. Beese, Z. Wang, A. D. Stoica, and D. Ma, "Absence of dynamic strain aging in an additively manufactured nickel-base superalloy," *Nat. Commun.*, vol. 9, no. 1, 2018.

[202] W. Huang, J. Yang, H. Yang, G. Jing, Z. Wang, and X. Zeng, "Heat treatment of Inconel 718 produced by selective laser melting: Microstructure and mechanical properties,"

Mater. Sci. Eng. A, vol. 750, pp. 98–107, Mar. 2019.

[203] S. Sui *et al.*, "The influence of Laves phases on the room temperature tensile properties of Inconel 718 fabricated by powder feeding laser additive manufacturing," *Acta Mater.*, vol. 164, pp. 413–427, Feb. 2019.

[204] G. D. Janaki Ram, A. V. Reddy, K. P. Rao, and G. M. Reddy, "Improvement in stress rupture properties of Inconel 718 gas tungsten arc welds using current pulsing," *J. Mater. Sci.*, vol. 40, no. 6, pp. 1497–1500, 2005.

[205] S. G. K. Manikandan, D. Sivakumar, K. Prasad Rao, and M. Kamaraj, "Effect of weld cooling rate on Laves phase formation in Inconel 718 fusion zone," *J. Mater. Process. Technol.*, vol. 214, no. 2, pp. 358–364, Feb. 2014.

[206] M. Anderson, A.-L. L. Thielin, F. Bridier, P. Bocher, and J. Savoie, "δ Phase precipitation in Inconel 718 and associated mechanical properties," *Mater. Sci. Eng. A*, vol. 679, pp. 48–55, Jan. 2017.

[207] B. Hassan and J. Corney, "Grain boundary precipitation in Inconel 718 and ATI 718Plus," *Materials Science and Technology*, vol. 33, no. 16. pp. 1879–1889, 2017.

[208] C.-M. Kuo, Y.-T. Yang, H.-Y. Bor, C.-N. Wei, and C.-C. Tai, "Aging effects on the microstructure and creep behavior of Inconel 718 superalloy," *Mater. Sci. Eng. A*, vol. 510–511, pp. 289–294, 2008.

[209] Special Metals Corporation, "INCONEL alloy 718." Special Metals Corporation, pp. 1–28, 2007.

[210] T. Trosch, J. Strößner, R. Völkl, and U. Glatzel, "Microstructure and mechanical properties of selective laser melted Inconel 718 compared to forging and casting," *Mater. Lett.*, vol. 164, pp. 428–431, Feb. 2016.

[211] F. Martina, J. Ding, S. Williams, A. Caballero, G. Pardal, and L. Quintino, "Tandem metal inert gas process for high productivity wire arc additive manufacturing in stainless steel," *Addit. Manuf.*, vol. 25, pp. 545–550, Jan. 2019.

[212] A. Horgar, H. Fostervoll, B. Nyhus, X. Ren, M. Eriksson, and O. M. Akselsen, "Additive manufacturing using WAAM with AA5183 wire," *J. Mater. Process. Technol.*, vol. 259, pp.

68–74, Sep. 2018.

[213] P. A. Colegrove, J. Donoghue, F. Martina, J. Gu, P. Prangnell, and J. Hönnige, "Application of bulk deformation methods for microstructural and material property improvement and residual stress and distortion control in additively manufactured components," *Scr. Mater.*, vol. 135, pp. 111–118, 2017.

[214] J. N. DuPont, J. C. Lippold, and S. D. Kiser, "Precipitation-Strengthened Ni-base Alloys," in *Welding Metallurgy and Weldability of Nickel-Base Alloys*, John Wiley & Sons, Inc., 2009, pp. 157–254.

[215] M. J. Donachie and S. J. Donachie, *Superalloys: A Technical Guide, 2nd Edition*. ASM International, 2002.

[216] C. E. Seow, H. E. Coules, G. Wu, R. H. U. Khan, X. Xu, and S. Williams, "Wire + Arc Additively Manufactured Inconel 718: Effect of post-deposition heat treatments on microstructure and tensile properties," *Mater. Des.*, vol. 183, no. September, p. 108157, Dec. 2019.

[217] Y. Chen, K. Zhang, J. Huang, S. R. E. Hosseini, and Z. Li, "Characterization of heat affected zone liquation cracking in laser additive manufacturing of Inconel 718," *Mater. Des.*, vol. 90, pp. 586–594, Jan. 2016.

[218] E. Hosseini and V. A. Popovich, "A review of mechanical properties of additively manufactured Inconel 718," *Additive Manufacturing*, vol. 30. Elsevier B.V., p. 100877, 01-Dec-2019.

[219] K. Georgilas, R. H. U. Khan, and M. E. Kartal, "The influence of pulsed laser powder bed fusion process parameters on Inconel 718 material properties," *Mater. Sci. Eng. A*, vol. 769, p. 138527, Jan. 2020.

[220] A. Strondl, M. Palm, J. Gnauk, and G. Frommeyer, "Microstructure and mechanical properties of nickel based superalloy IN718 produced by rapid prototyping with electron beam melting (EBM)," *Mater. Sci. Technol.*, vol. 27, no. 5, pp. 876–883, May 2011.

[221] P. Dirisu, S. Ganguly, A. Mehmanparast, F. Martina, and S. Williams, "Analysis of fracture toughness properties of wire + arc additive manufactured high strength low alloy

structural steel components," *Mater. Sci. Eng. A*, vol. 765, Sep. 2019.

[222] N. Sridharan, M. W. Noakes, A. Nycz, L. J. Love, R. R. Dehoff, and S. S. Babu, "On the toughness scatter in low alloy C-Mn steel samples fabricated using wire arc additive manufacturing," *Mater. Sci. Eng. A*, vol. 713, pp. 18–27, Jan. 2018.

[223] L. N. Carter, C. Martin, P. J. Withers, and M. M. Attallah, "The influence of the laser scan strategy on grain structure and cracking behaviour in SLM powder-bed fabricated nickel superalloy," *J. Alloys Compd.*, vol. 615, pp. 338–347, Dec. 2014.

[224] M. Seifi, A. A. Salem, D. P. Satko, U. Ackelid, S. L. Semiatin, and J. J. Lewandowski, "Effects of HIP on microstructural heterogeneity, defect distribution and mechanical properties of additively manufactured EBM Ti-48Al-2Cr-2Nb," *J. Alloys Compd.*, vol. 729, pp. 1118–1135, 2017.

[225] C. Holmes, B. W. Drinkwater, and P. D. Wilcox, "Post-processing of the full matrix of ultrasonic transmit-receive array data for non-destructive evaluation," *NDT E Int.*, vol. 38, no. 8, pp. 701–711, Dec. 2005.

[226] ASTM International, "ASTM E1820-18ae1 Standard Test Method for Measurement of Fracture Toughness." ASTM International, West Conshohocken, PA, 2018.

[227] ISO, "ISO 12135:2016 Metallic materials — Unified method of test for the determination of quasistatic fracture toughness." ISO, Geneva, Switzerland, 2016.

[228] NACE International, "ANSI/NACE MR0175/ISO 15156-2015-SG Petroleum and natural gas industries — Materials for use in H2S-containing environments in oil and gas production." NACE International, Houston, TX, 2015.

[229] K. Weiss and A. Nyilas, "Specific aspects on crack advance during J-test method for structural materials at cryogenic temperatures," *Fatigue Fract. Eng. Mater. Struct.*, vol. 29, no. 2, pp. 83–92, 2006.

[230] M. A. Verstraete, S. Hertelé, R. M. Denys, K. Van Minnebruggen, and W. De Waele, "Evaluation and interpretation of ductile crack extension in SENT specimens using unloading compliance technique," *Eng. Fract. Mech.*, vol. 115, pp. 190–203, Jan. 2014.

[231] Y. Rosenthal, R. Tobler, and P. Purtscher, "JIc Data Analysis Methods with a 'Negative

Crack Growth' Correction Procedure," *J. Test. Eval.*, vol. 18, no. 4, p. 301, 1990.

[232] N. Wang, S. Mokadem, M. Rappaz, and W. Kurz, "Solidification cracking of superalloy single- and bi-crystals," *Acta Mater.*, vol. 52, no. 11, pp. 3173–3182, Jun. 2004.

[233] S. I. Wright, M. M. Nowell, and D. P. Field, "A review of strain analysis using electron backscatter diffraction," *Microsc. Microanal.*, vol. 17, no. 3, pp. 316–329, Jun. 2011.

[234] M. E. Launey and R. O. Ritchie, "On the Fracture Toughness of Advanced Materials," 1999.

[235] R. Morrell and J. Lord, *A National Measurement Good Practice Guide - Elastic Modulus Measurement*, no. 98. National Physical Laboratory, 2006.

[236] R. O. Ritchie, "The conflicts between strength and toughness," *Nat. Mater.*, vol. 10, no. 11, pp. 817–822, Nov. 2011.

[237] R. O. Ritchie, "Mechanisms of fatigue crack propagation in metals, ceramics and composites: Role of crack tip shielding," *Mater. Sci. Eng.*, vol. 103, no. 1, pp. 15–28, 1988.

[238] A. Plotkowski, M. M. Kirka, and S. S. Babu, "Verification and validation of a rapid heat transfer calculation methodology for transient melt pool solidification conditions in powder bed metal additive manufacturing," *Addit. Manuf.*, vol. 18, pp. 256–268, Dec. 2017.

[239] A. Ukwattage and A. Achuthan, "Development of residual stress in parts fabricated via selective laser melting (SLM) technique under different scanning strategies," in *AIAA/ASCE/AHS/ASC Structures, Structural Dynamics, and Materials Conference, 2018*, 2018, no. 210049.

[240] R. G. Thompson, D. E. Mayo, and B. Radhakrishnan, "The relationship between carbon content, microstructure, and intergranular liquation cracking in cast nickel alloy 718," *Metall. Trans. A*, vol. 22, no. 2, pp. 557–567, Feb. 1991.

[241] R. G. Thompson and S. Genculu, "Microstructural Evolution in the HAZ of Inconel 718 and Correlation with the Hot Ductility Test," *Weld. J.*, vol. 62, no. 12, pp. 337–345, 1983.

[242] A. Lopez, R. Bacelar, I. Pires, T. G. Santos, J. P. Sousa, and L. Quintino, "Non-destructive

testing application of radiography and ultrasound for wire and arc additive manufacturing," *Addit. Manuf.*, vol. 21, pp. 298–306, May 2018.

[243] X. Ye, X. Hua, M. Wang, and S. Lou, "Controlling hot cracking in Ni-based Inconel-718 superalloy cast sheets during tungsten inert gas welding," *J. Mater. Process. Technol.*, vol. 222, pp. 381–390, Aug. 2015.

[244] J. J. Lin *et al.*, "Microstructural evolution and mechanical properties of Ti-6Al-4V wall deposited by pulsed plasma arc additive manufacturing," *Mater. Des.*, vol. 102, pp. 30–40, Jul. 2016.

[245] Z. Li *et al.*, "Reducing arc heat input and obtaining equiaxed grains by hot-wire method during arc additive manufacturing titanium alloy," *Mater. Sci. Eng. A*, vol. 742, pp. 287–294, Jan. 2019.

[246] F. Montevecchi, G. Venturini, N. Grossi, A. Scippa, and G. Campatelli, "Heat accumulation prevention in Wire-Arc-Additive-Manufacturing using air jet impingement," *Manuf. Lett.*, vol. 17, pp. 14–18, Aug. 2018.

[247] E. M. Van Der Aa, "Local cooling during welding: Prediction and control of residual stresses and buckling distortion," Delft University of Technology, 2007.

[248] Y. Chen *et al.*, "Dendritic microstructure and hot cracking of laser additive manufactured Inconel 718 under improved base cooling," *J. Alloys Compd.*, vol. 670, pp. 312–321, Jun. 2016.

[249] B. Wu, Z. Pan, D. Ding, D. Cuiuri, H. Li, and Z. Fei, "The effects of forced interpass cooling on the material properties of wire arc additively manufactured Ti6Al4V alloy," *J. Mater. Process. Technol.*, vol. 258, pp. 97–105, Aug. 2018.

[250] B. Wu *et al.*, "Mitigation of thermal distortion in wire arc additively manufactured Ti6Al4V part using active interpass cooling," *Sci. Technol. Weld. Join.*, vol. 24, no. 5, pp. 484–494, Jul. 2019.

[251] R. Thavamani, V. Balusamy, J. Nampoothiri, R. Subramanian, and K. R. R. Ravi, "Mitigation of hot cracking in Inconel 718 superalloy by ultrasonic vibration during gas tungsten arc welding," *J. Alloys Compd.*, vol. 740, pp. 870–878, Apr. 2018.

[252] C. Hua, H. Lu, C. Yu, J.-M. Chen, X. Wei, and J.-J. Xu, "Reduction of ductility-dip cracking susceptibility by ultrasonic-assisted GTAW," *J. Mater. Process. Technol.*, vol. 239, pp. 240–250, Jan. 2017.

[253] N. Anbarasan, N. Narein, and S. Jerome, "Influence of Mechanical Arc Oscillation on the Microstructural and Mechanical Properties of Inconel 718 Welds," *Trans. Indian Inst. Met.*, vol. 72, no. 6, pp. 1541–1544, Jun. 2019.

[254] X. Yu *et al.*, "Reducing hot cracking tendency of dissimilar weld overlay by magnetic arc oscillation," *Mater. Sci. Technol. (United Kingdom)*, vol. 30, no. 8, pp. 930–937, Jul. 2014.

[255] R. Sun *et al.*, "Microstructure, residual stress and tensile properties control of wire-arc additive manufactured 2319 aluminum alloy with laser shock peening," *J. Alloys Compd.*, vol. 747, pp. 255–265, May 2018.

[256] H. Lockett, J. Ding, S. Williams, and F. Martina, "Design for wire + Arc additive manufacture: Design rules and build orientation selection," *J. Eng. Des.*, vol. 28, no. 7–9, pp. 568–598, Sep. 2017.

[257] D. Yang, G. Wang, and G. Zhang, "Thermal analysis for single-pass multi-layer GMAW based additive manufacturing using infrared thermography," *J. Mater. Process. Technol.*, vol. 244, pp. 215–224, Jun. 2017.

[258] U. Zerbst *et al.*, "Review on fracture and crack propagation in weldments - A fracture mechanics perspective," *Eng. Fract. Mech.*, vol. 132, pp. 200–276, Dec. 2014.

[259] S. Yoneyama, S. Arikawa, S. Kusayanagi, and K. Hazumi, "Evaluating J-integral from displacement fields measured by digital image correlation," *Strain*, vol. 50, no. 2, pp. 147–160, Apr. 2014.

[260] J. R. Yates, M. Zanganeh, and Y. H. Tai, "Quantifying crack tip displacement fields with DIC," *Eng. Fract. Mech.*, vol. 77, no. 11, pp. 2063–2076, Jul. 2010.

[261] M. Mokhtarishirazabad, P. Lopez-Crespo, B. Moreno, A. Lopez-Moreno, and M. Zanganeh, "Evaluation of crack-tip fields from DIC data: A parametric study," *Int. J. Fatigue*, vol. 89, pp. 11–19, Aug. 2016.

[262] S. Roux and F. Hild, "Stress intensity factor measurements from digital image correlation:

Post-processing and integrated approaches," *Int. J. Fract.*, vol. 140, no. 1–4, pp. 141–157, 2006.

[263] J. Tong, "Full-field characterisation of crack tip deformation and fatigue crack growth using digital image correlation—a review," *Fatigue and Fracture of Engineering Materials and Structures*, vol. 41, no. 9. Blackwell Publishing Ltd, pp. 1855–1869, 01-Sep-2018.

[264] S. M. Barhli, M. Mostafavi, A. F. Cinar, D. Hollis, and T. J. Marrow, "J-Integral Calculation by Finite Element Processing of Measured Full-Field Surface Displacements," *Exp. Mech.*, vol. 57, no. 6, pp. 997–1009, 2017.

[265] A. Steuwer and J. E. Daniels, "In-situ stress and strain measurements around cracks using synchrotron X-ray diffraction," *J. Strain Anal. Eng. Des.*, vol. 46, no. 7, pp. 593–606, 2011.

[266] J. Smith, M. N. Bassim, C. D. Liu, and T. M. Holden, "Measurement of crack tip strains using neutron diffraction," *Eng. Fract. Mech.*, vol. 52, no. 5, pp. 843–851, Nov. 1995.

[267] E. W. Huang, S. Y. Lee, W. Woo, and K. W. Lee, "Three-orthogonal-direction stress mapping around a fatigue-crack tip using neutron diffraction," *Metall. Mater. Trans. A Phys. Metall. Mater. Sci.*, vol. 43, no. 8, pp. 2785–2791, 2012.

[268] P. R. Dawson, D. E. Boyce, and R. B. Rogge, "Correlation of diffraction peak broadening to crystal strengthening in finite element simulations," *Mater. Sci. Eng. A*, vol. 399, no. 1–2, pp. 13–25, Jun. 2005.

[269] Y. Sun *et al.*, "Neutron diffraction studies on lattice strain evolution around a crack-tip during tensile loading and unloading cycles," *Scr. Mater.*, vol. 53, no. 8, pp. 971–975, Oct. 2005.

[270] S. Y. Lee *et al.*, "Neutron and X-ray microbeam diffraction studies around a fatigue-crack tip after overload," in *Metallurgical and Materials Transactions A: Physical Metallurgy and Materials Science*, 2008, vol. 39, no. 13, pp. 3164–3169.

[271] A. Steuwer, M. Rahman, A. Shterenlikht, M. E. Fitzpatrick, L. Edwards, and P. J. Withers, "The evolution of crack-tip stresses during a fatigue overload event," *Acta Mater.*, vol. 58, no. 11, pp. 4039–4052, Jun. 2010.

[272] P. Lopez-Crespo, M. Mostafavi, A. Steuwer, J. F. Kelleher, T. Buslaps, and P. J. Withers,

"Characterisation of overloads in fatigue by 2D strain mapping at the surface and in the bulk," *Fatigue Fract. Eng. Mater. Struct.*, vol. 39, no. 8, pp. 1040–1048, 2016.

[273] H. E. Coules, S. J. Oliver, G. C. M. Horne, D. G. A. Van Gelderen, M. J. Peel, and T. Connolley, "Direct observation of elastic and plastic strain fields during ductile tearing of a ferritic steel," in *American Society of Mechanical Engineers, Pressure Vessels and Piping Division (Publication) PVP*, 2016, vol. 6A-2016.

[274] H. E. Coules, G. C. M. Horne, M. J. Peel, and T. Connolley, "Localised prior strain-hardening increases the tearing resistance of ductile steel," *Int. J. Mech. Sci.*, vol. 150, no. September 2018, pp. 103–111, 2019.

[275] H. E. Coules, G. C. M. Horne, K. Abburi Venkata, and T. Pirling, "The effects of residual stress on elastic-plastic fracture propagation and stability," *Mater. Des.*, vol. 143, pp. 131–140, Apr. 2018.

[276] M. T. Hutchings, Withers.P.J, T. M. Holden, and T. Lorentzen, *Introduction to characterization of residual stress by neutron diffraction*, vol. 8. Taylor & Francis, 2005.

[277] R. C. Wimpory, U. Wasmuth, J. Rebelo-Kornmeier, and M. Hofmann, "The effect of grain size on strain determination using a neutron diffractometer," in *Materials Science Forum*, 2010, vol. 638–642, pp. 2405–2410.

[278] T. M. Holden, Y. Traore, J. James, J. Kelleher, and P. J. Bouchard, "Determination and mitigation of the uncertainty of neutron diffraction measurements of residual strain in large-grained polycrystalline material," *J. Appl. Crystallogr.*, vol. 48, no. 2, pp. 582–584, Apr. 2015.

[279] A. Baczmanski *et al.*, "Neutron time-of-flight diffraction used to study aged duplex stainless steel at small and large deformation until sample fracture," *J. Appl. Crystallogr.*, vol. 44, no. 5, pp. 966–982, Oct. 2011.

[280] J. N. Wagner, M. Hofmann, R. Wimpory, C. Krempaszky, and M. Stockinger, "Microstructure and temperature dependence of intergranular strains on diffractometric macroscopic residual stress analysis," *Mater. Sci. Eng. A*, vol. 618, pp. 271–279, Sep. 2014.

[281] Special Metals Corporation, "INCONEL alloy 625." Special Metals Corporation, pp. 1–28,

2013.

[282] D. J. Hughes, G. Bruno, T. Pirling, and P. J. Withers, “First Impressions of SALSA: The New Engineering Instrument at ILL,” *Sci. Rev.*, vol. 17, no. 3, 2006.

[283] T. Pirling, G. Bruno, and P. J. Withers, “SALSA-A new instrument for strain imaging in engineering materials and components,” *Mater. Sci. Eng. A*, vol. 437, no. 1, pp. 139–144, 2006.

[284] S. Yoneyama, “Basic principle of digital image correlation for in-plane displacement and strain measurement,” *Adv. Compos. Mater.*, vol. 25, no. 2, pp. 105–123, Mar. 2016.

[285] Y. Sun, J. H. L. Pang, F. Wei, and X. Shi, “Micro- and nano-DIC deformation analysis for electronic packaging applications,” in *Proceedings of the Electronic Packaging Technology Conference, EPTC*, 2006, pp. 290–296.

[286] Institut Laue-Langevin, “ILL Neutrons for Society - Instrument layout,” 2001. [Online]. Available: https://www.ill.eu/users/instruments/instruments-list/salsa/description/instrument-layout. [Accessed: 27-Jul-2021].

[287] Z. Wang, A. D. Stoica, D. Ma, and A. M. Beese, “Diffraction and single-crystal elastic constants of Inconel 625 at room and elevated temperatures determined by neutron diffraction,” *Mater. Sci. Eng. A*, vol. 674, pp. 406–412, 2016.

[288] U. Cihak, P. Staron, H. Clemens, J. Homeyer, M. Stockinger, and J. Tockner, “Characterization of residual stresses in turbine discs by neutron and high-energy X-ray diffraction and comparison to finite element modeling,” *Mater. Sci. Eng. A*, vol. 437, no. 1, pp. 75–82, Nov. 2006.

[289] J. von Kobylinski, R. Lawitzki, M. Hofmann, C. Krempaszky, and E. Werner, “Micromechanical behaviour of Ni-based superalloys close to the yield point: a comparative study between neutron diffraction on different polycrystalline microstructures and crystal plasticity finite element modelling,” *Contin. Mech. Thermodyn.*, vol. 31, no. 3, pp. 691–702, 2019.

[290] P. E. Aba-Perea, T. Pirling, P. J. Withers, J. Kelleher, S. Kabra, and M. Preuss, “Determination of the high temperature elastic properties and diffraction elastic

constants of Ni-base superalloys," *Mater. Des.*, vol. 89, pp. 856–863, 2016.

[291] E. Breitbarth, S. Zaefferer, F. Archie, M. Besel, D. Raabe, and G. Requena, "Evolution of dislocation patterns inside the plastic zone introduced by fatigue in an aged aluminium alloy AA2024-T3," *Mater. Sci. Eng. A*, vol. 718, pp. 345–349, Mar. 2018.

[292] E. B. Marin, "On the formulation of a crystal plasticity model.," Albuquerque, New Mexico, 2006.

[293] F. Roters, P. Eisenlohr, L. Hantcherli, D. D. Tjahjanto, T. R. Bieler, and D. Raabe, "Overview of constitutive laws, kinematics, homogenization and multiscale methods in crystal plasticity finite-element modeling: Theory, experiments, applications," *Acta Mater.*, vol. 58, no. 4, pp. 1152–1211, 2010.

[294] ASTM International, "ASTM F3301-18a Standard for Additive Manufacturing – Post Processing Methods – Standard Specification for Thermal Post-Processing Metal Parts Made Via Powder Bed Fusion," *ASTM Standards*. ASTM International, West Conshohocken, PA, pp. 4–6, 2018.

Appendix A Supplementary data

Table A.1: Summary of tensile properties for various WAAM materials.

Material	Tech.	Dir.	Condition	YS (MPa)	UTS (MPa)	Elong. (%)	Ref.
Alloy 718	TIG	BD	As-dep	473 ± 6	828 ± 8	28 ± 2	[55]
Alloy 718	PA	BD	As-dep	506 ± 2	756 ± 7	27.9 ± 1.3	[82]
Alloy 718	PA	LD	As-dep	525 ± 7	818 ± 13	33.3 ± 2.5	[82]
Alloy 718	PA	BD	As-dep, rolled	687 ± 1	1072 ± 6	26.6 ± 1.3	[82]
Alloy 718	PA	LD	As-dep, rolled	763 ± 8	1082 ± 13	26.2 ± 2.2	[82]
Alloy 718	PA	BD	STA	791 ± 14	988 ± 6	12.8 ± 1.2	[82]
Alloy 718	PA	LD	STA	790 ± 9	1102 ± 78	14.7 ± 1.3	[82]
Alloy 718	PA	BD	STA, rolled	1035 ± 20	1356 ± 10	17.4 ± 1.1	[82]
Alloy 718	PA	LD	STA, rolled	1057 ± 19	1348 ± 10	15.1 ± 3.3	[82]
Alloy 718Plus	TIG	BD	As-dep	-	954	43.8	[104]
Alloy 718Plus	TIG	LD	As-dep	-	764	35.8	[104]
Alloy 718Plus	TIG	BD	STA	-	817	7.6	[104]
Alloy 718Plus	TIG	LD	STA	-	1022.3	14.3	[104]
Alloy 718Plus	TIG	BD	Custom HT		1317	34.7	[104]
Alloy 718Plus	TIG	LD	Custom HT		1267	30.5	[104]
Alloy 625	PA	BD	As-Dep	480	771	50	[97]
Alloy 625	PA	BD	DA	495	833	38	[97]
Alloy 625	PA	BD	STA	535	851	44	[97]
Alloy 625	PA	BD	HSTA	449	732	40	[97]
Alloy 625	PA	BD	As-Dep	438	721	49	[98]
Alloy 625	TIG	BD	As-Dep	-	684 ± 23	40 ± 3	[96]
Alloy 625	TIG	TD	As-Dep	-	722 ± 17	42 ± 2	[96]
Alloy 625	CMT	BD	As-Dep	373 ± 5	658 ± 4	56 ±4	[99]
Alloy 625	CMT	BD	ST	360 ± 11	672 ± 8	43 ± 1	[99]
AA 2024	TIG	BD	As-dep	175	277	5.8	[84]
AA 2024	TIG	LD	As-dep	177	284	6	[84]
AA 2024	TIG	BD	HT-T4	294	395	5	[84]
AA 2024	TIG	LD	HT-T4	310	458	12.7	[84]
AA 2024	TIG	BD	HT-T6	352	410	2.1	[84]
AA 2024	TIG	LD	HT-T6	374	470	8.2	[84]
Ti-6Al-4V	PA	BD	As-dep	803	918	14	[102]
Ti-6Al-4V	PA	LD	As-dep	850	980	8	[102]
Ti-6Al-4V	PA	BD	As-dep	840	923	7.8	[103]
Ti-6Al-4V	PA	LD	As-dep	810	906	11.6	[103]

Continued from Table A.1

Material	Tech.	Dir.	Condition	YS (MPa)	UTS (MPa)	Elong. (%)	Ref.
Mild steel ER70S-6	MIG/MAG	BD	As-dep	404	512	-	[45]
Mild steel ER70S-6	MIG/MAG	TD	As-dep	434	560	-	[45]
Mild steel ER70S-6	MIG/MAG	LD	As-dep	470	588	-	[45]
Mild steel ER70S-6	MIG/MAG	BD	As-dep	461.5 ± 6.3	618.5 ± 10.8	28.2 ± 0.5	[100]
Mild steel ER70S-6	MIG/MAG	TD	As-dep	519.5±8.3	693.5±8.5	36.8±0.2	[100]
Structural steel, S355	MIG/MAG	BD	As-dep	545	602	11	[101]
Structural steel, S355	MIG/MAG	LD	As-dep	553	710	6.4	[101]
Steel ZG230-450	CMT	BD	As-dep	651	778	23.0	[17]
Steel ZG230-450	CMT	LD	As-dep	660	796	26	[17]
Stainless Steel, 316L	SpeedPulse	LD	As-dep	418.0	550 ± 6	-	[71]
Stainless Steel, 316L	SpeedArc	LD	As-dep	417.9	553 ± 2	-	[71]
Maraging steel	PA	BD	As-dep	833 ± 26	1026 ± 10	8.0 ± 3.8	[59]
Maraging steel	PA	LD	As-dep	904 ± 78	1118 ± 94	11.7 ± 0.8	[59]
Maraging steel	PA	BD	DA	1227 ± 31	1345 ± 19	6.0 ± 1.7	[59]
Maraging steel	PA	LD	DA	1303 ± 29	1410 ± 32	8.5 ± 3.3	[59]
Maraging steel	PA	BD	As-dep, rolled	882 ± 25	1013 ± 8	7.1 ± 0.7	[81]
Maraging steel	PA	LD	As-dep, rolled	1014 ± 102	1138 ± 118	9.2 ± 4.5	[81]
Maraging steel	PA	BD	DA, rolled	1623 ± 18	1735 ± 10	4.8 ± 0.3	[81]
Maraging steel	PA	LD	DA, rolled	1654 ± 37	1750 ± 17	4.3 ± 1.0	[81]

Notes:
BD, LD and TD refer to the build, longitudinal and thickness directions respectively.
STA – Solution treatment and Aging
DA – Direct Aging
HSTA – Homogenisation, Solution treatment and Aging
ST – Solution treatment

Table A.2: WAAM IN718 tensile specimen and result list.

Spec. ID	Slice ID	Loading Dir.	Heat treatment	Test temp.	$YS_{0.2}$ (MPa)	UTS (MPa)	Elong. (%)	E (GPa)
T01	P	BD	As-Dep	Room temp	429.3	725.6	17.0	154
T02	P	BD	As-Dep	Room temp	429.9	823.2	31.3	126
T03	P	BD	As-Dep	Room temp	433.7	717.9	15.7	160
T04	P	BD	As-Dep	650 °C	432.0	682.2	12.6	103
T05	P	BD	As-Dep	650 °C	409.8	612.5	6.3	111
T06	P	BD	As-Dep	650 °C	343.6	589.8	8.3	114
T07	Z	BD	Modified HA	650 °C	716.4	818.3	9.6	148
T08	Z	BD	Modified HA	Room temp	861.4	1058.6	19.3	155
T09	Z	BD	Standard HSA	Room temp	1065.2	1115.7	0.9	150
T10	Z	BD	Modified HA	650 °C	752.1	822.8	3.83	125
T11	Z	BD	Modified HA	Room temp	850.2	1029.9	20.55	150
T12	Z	BD	Aging only	Room temp	950.6	1072.2	1.95	175
A01	Q	WA	As-Dep	Room temp	420.5	646.3	17.7	143
A02	Q	WA	Modified HA	Room temp	945.5	1096.1	24.8	173
A03	Q	WA	As-Dep	650 °C	337.7	621.4	13.9	90
A04	Q	WA	Modified HA	650 °C	734.4	830.7	8.6	128
A05	Q	WA	Modified HA	650 °C	733.4	837.0	6.7	134
A06	Q	WA	Modified HA	Room temp	949.3	1023.2	9.0	156
A07	Y	WA	As-Dep	Room temp	436.9	437.5	1.5	155
A08	Y	WA	Modified HA	Room temp	899.9	1101.0	29.7	191
A09	Y	WA	Modified HA	650 °C	692.6	732.7	2.31	148

Note: All tensile specimens were taken from WAAM Wall 1, and have geometry shown in Figure 3.5. Tensile result from A07 is omitted from Figure 3.15 for brevity.

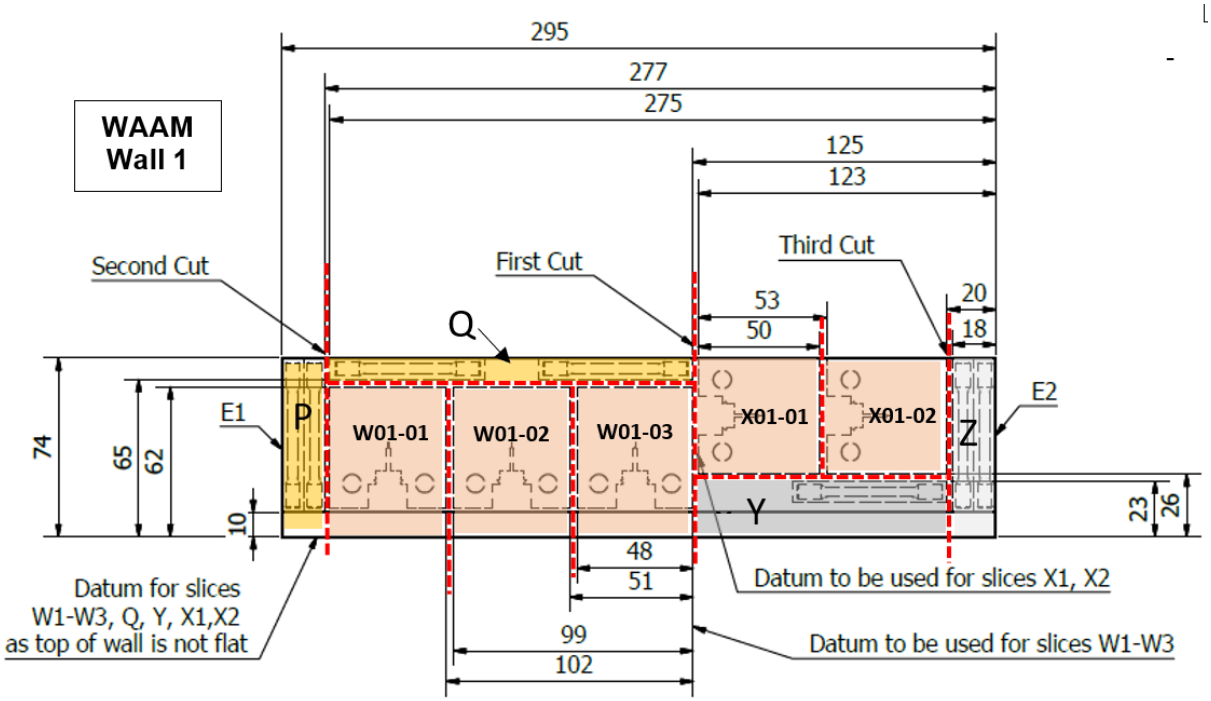

Figure A.1: Cutting plan for WAAM wall 1 indicating Slice ID for tensile specimens and Specimen IDs for compact tension specimens. Detailed list in Table A.2.

a.

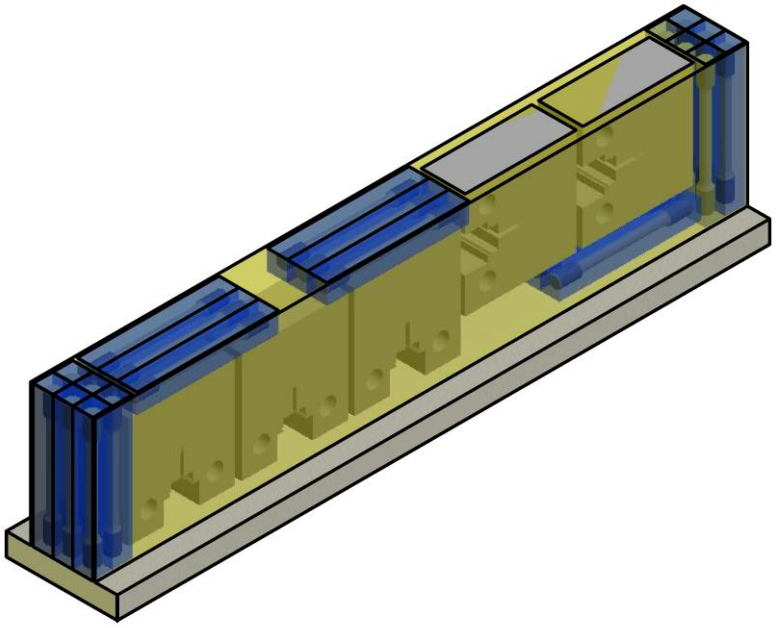

b.

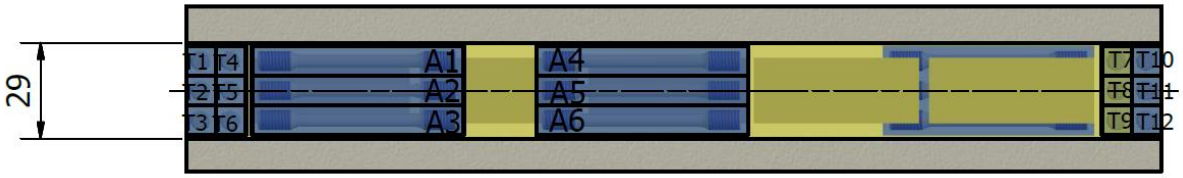

Figure A.2: Cutting plan for WAAM Wall 1, (a) 3D view and (b) top view indicating tensile specimen IDs. Detailed list in Table A.2.

Table A.3: Compact tension specimen list.

Wall No.	Spec ID	Notch Dir.	Test(s) carried out	Test facility	Comments
1	W01-01	//	Fracture tou., Neutron Diff.	ILL, SALSA	Fracture toughness and ND reported in Chapter 5.
1	W01-02	//	Fracture tou.	TWI Ltd	Reported in Chapter 4
1	W01-03	//	Fracture tou.	TWI Ltd	Reported in Chapter 4
1	X01-01	⊥	Fracture tou., Neutron Diff.	ILL, SALSA	Fracture toughness and ND reported in Chapter 5
1	X01-02	⊥	Fracture tou.	TWI Ltd	Reported in Chapter 4
2	W02-01	//	Fracture tou., Neutron Diff.	ISIS, ENGIN-X	Fracture toughness reported in Chapter 4, ND omitted from this work.
2	X02-01	⊥	Fracture tou., Neutron Diff.	ISIS, ENGIN-X	Fracture toughness reported in Chapter 4, ND omitted from this work.
2	M02-01	⊥	Fracture tou.	TWI Ltd	Reported in Chapter 4
2	M02-02	//	Fracture tou.	TWI Ltd	Reported in Chapter 4
2	M02-03	//	Fracture tou.	TWI Ltd	Reported in Chapter 4
3	M03-01	//	Fracture tou.	TWI Ltd	Reported in Chapter 4
3	M03-02	⊥	Fracture tou.	TWI Ltd	Reported in Chapter 4
3	M03-03	⊥	Fracture tou.	TWI Ltd	Reported in Chapter 4
3	M03-04	//	Fracture tou.	TWI Ltd	Reported in Chapter 4
3	M03-05	//	Fracture tou.	TWI Ltd	Reported in Chapter 4

Note: All C(T) specimens underwent Modified HA heat treatment prior to testing.

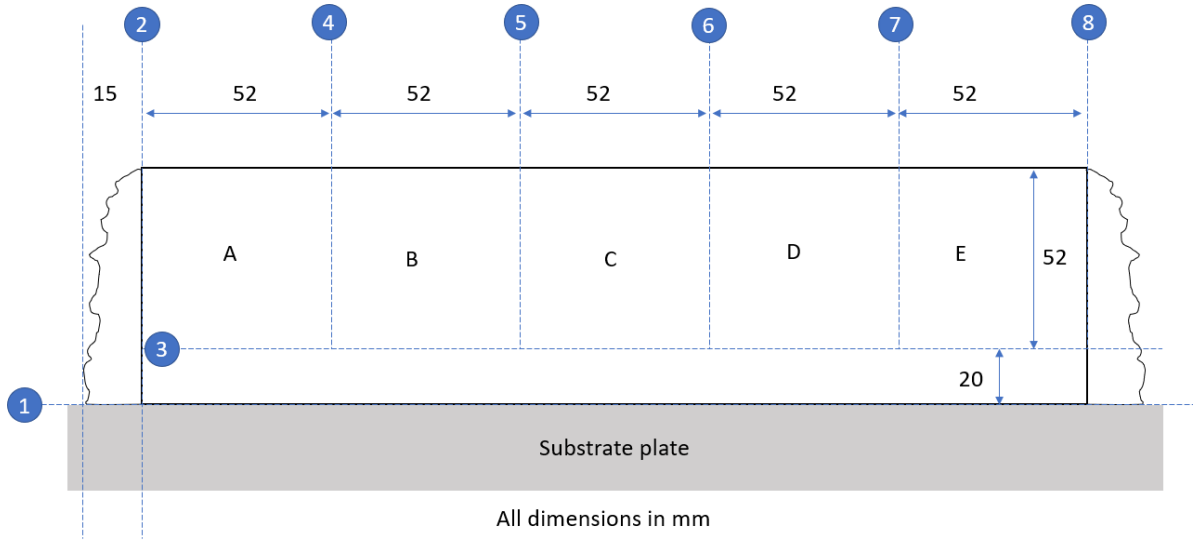

Figure A.3: Cutting plan for WAAM Walls 2 and 3. 5-off compact tension specimens were extracted from each wall, indicated by sliced.

Figure A.4: Compact tension specimen blanks (i.e. prior to machining), indicating position of notch relative to top of WAAM wall.